Optimizing the Physical Properties of Vascular Targeted Carriers for Maximum Efficacy in Inflammatory Disease

by

Margaret Brooks Fish

A dissertation submitted in partial fulfillment
of the requirements for the degree of
Doctor of Philosophy
(Chemical Engineering)
in the University of Michigan
2018

Doctoral Committee:

Professor Omolola Eniola-Adefeso, Chair
Professor Mark A. Burns
Professor Andrew J. Putnam
Assistant Professor Timothy F. Scott
Assistant Professor Greg M. Thurber

Margaret Fish

fishmarg@umich.edu

ORCID ID: 0000-0002-0995-7226

Dedication

This dissertation is dedicated to

Jack

Mom and Dad

My brother, Bryan

Acknowledgments

First, I would like to thank my advisor, Professor Omolola Eniola-Adefeso for welcoming me into her lab initially as a Masters student, and for continuing to mentor me through my entire PhD. Thank you for your guidance, support, and patience throughout my doctoral studies. Working with Lola has allowed me to grow and develop enormously as both a professional and as a research scientist. I look forward to seeing the continued work coming out of the lab in the future and I am proud be a part of that continued legacy.

I would also like to express my gratitude to my committee members, Professors Andrew Putnam, Timothy Scott, and Gregory Thurber, for their support and valuable time spent on my committee. Thank you for your candid advice and insight during my dissertation process, it undoubtedly increased the quality of my work. I wish you all the best with your future research endeavors!

Thank you to all the former and current members of the Eniola Lab- it has been truly wonderful to work with and learn from you all. Thank you in particular Alex Thompson, Peter Onyskiw, Katawut Namdee, Daniel Sobczynski, and Mariana Carrasco-Teja for your support and guidance when I was new to the lab. I want to express my gratitude in particular to Professor Cathy Fromen for her encouragement and research direction the past three years, in addition to all of the fun times. To the younger students in the lab- Billy Kelley, Genesis Lopez, Hanieh Safari, Mario Gutierrez, and Alison Banka, it has been fantastic working with you daily over the past years and it has been truly rewarding watching you grow into successful scientists. To all

those with whom I collaborated with outside the Eniola Lab, and there are many, thank you for your willingness to help expand my horizons in graduate school both experimentally and conceptually. This highly collaborative environment at the University of Michigan fueled my research to higher levels, for which I am very thankful. In particular, I would like to thank Prof. Raymond Adili and Prof. Michael Holinstat for their guidance with animal work and access to highly valuable equipment.

I am very lucky to have had two outstanding undergraduate students, Alexander Golinski and Margaret Braunreuther, work with me on research projects. You were a joy to work with and taught me invaluable lessons about how to be a better scientific mentor.

I'd like to acknowledge the funding that supported me, which includes Lola's lab funds, the Whitaker Foundation, and the National Institute of Health Predoctoral NRSA (F31) and Training Program in Translational Cardiovascular Research and Entrepreneurship (T32).

Lastly, and most importantly, I want to thank my family. Thank you to my mom and dad for supporting me unwaveringly through all of my crazy ambitions in life, a PhD being the latest. Bryan, thank you for being an older brother who made me tougher and has always celebrated everything in life with me. To my newest family member and husband, Jack, thank you for choosing to be by my side every day, and for providing the foundation of love and support that I needed to make it this far. I love you all dearly.

Table of Contents

List of Figures

List of Tables

List of Abbreviations

ACD	Acid citrate dextrose
ApoE$^{-/-}$	Apolipoprotein E–deficient
AIC	Akaike information criterion
Ant-ICAM-1	Anti-intercellular adhesion molecule-1
ALI	Acute lung injury
APC	Allophycocyanin
AUC	Area under the curve
Ca	Capillary number
CAM	Cellular adhesion molecule
CEA	2-carboxyethyl acrylate
CFL	Cell free layer
DLS	Dynamic light scattering
EC	Endothelial cell
EDC	N-(3-Dimethylaminopropyl)-N-ethylcarbodiimide hydrochloride
ELISA	Enzyme-linked immunosorbent assay
EPR	Enhanced permeability and retention
ESR	Equilibrium swelling ratio
FEA	Finite element analysis
FITC	Fluorescein isothiocyanate
FSC	Forward scatter
HUVEC	Human umbilical vein endothelial cell
IACUC	Institutional animal care and use committee
ICAM-1	Intercellular adhesion molecule-1
IL-1β	Interleukin-1β
IRB-MED	Institutional review board-of UM medical school
IVM	Intravital microscopy
LAC	Leukocyte adhesion cascade
LAM	Leukocyte adhesion molecule
LPS	Lipopolysaccharide

LR	Ligand-receptor
LSD	Least significant difference
MFI	Median fluorescent intensity
MMEC	Mouse mesentery endothelial cells
MP	Microparticle
MPS	Mononuclear phagocyte system
MW	Molecular weight
NIR	Near-infrared
n.d.	None detected
NP	Nanoparticle
n.s	Non-significant
PDI	Polydispersity index
PEG	Poly(ethylene glycol)
PEGDA	Poly(ethylene glycol) diacrylate
PI	Photoinitiator
PLGA	Poly(lactic-co-glycolic acid)
PMT	Photo-multiplier tube
PPFC	Parallel plate flow chamber
PS	Polystyrene
RBC	Red blood cell
RBC-FL	Red blood cell-free layer
RBC+p	Red blood cells + plasma
RES	Reticuloendothelial system
Rhodamine	Acryloxyethyl thiocarbamoyl rhodamine B
ROI	Region of interest
SEM	Scanning electron microscopy
sLe^A	Sialyl $Lewis^A$
SMC	Smooth muscle cell
SSC	Side scatter
TNF-α	Tumor necrosis factor-α
VCAM-1	Vascular cell adhesion molecule-1
VTC	Vascular targeted carrier
WBC	White blood cell
WSR	Wall shear rate
ZP	Zeta potential

Abstract

Vascular targeted carriers (VTCs) increase the specificity of drug delivery while also protecting drugs from degradation in the bloodstream, and therefore, have the potential to revolutionize many clinical treatments of common diseases. It has previously been shown that rigid microparticles (MPs) are significantly more efficient than rigid nanoparticles (NPs) at adhering to target vasculature from bulk blood flow; yet, despite this increased efficiency, MP VTCs have not been successfully developed for therapeutic applications, and are routinely passed over in favor of NP systems, which better evade capillary occlusion and promote tissue transport. Here, we investigate different physical properties of VTCs, including the interplay between particle modulus, size, and targeting ligand regime, to enhance the translational potential of MP VTC therapeutics and to optimize the overall design of VTCs for a range of clinical applications.

We systematically varied the physiochemical properties of particle modulus via poly(ethylene glycol) crosslinking density, targeting ligand (varied density, composition), and size (50 nm polystyrene to 2 μm hydrogels) and evaluated the impact of each property on targeted adhesion. VTC designs were evaluated *in vitro* using parallel plate flow chamber assays with inflamed human umbilical vein endothelial cells enabling controlled hemodynamic shear with primary human blood. VTC designs were evaluated *in vivo* using real time imaging of acute mouse mesentery inflammation, and full biodistribution studies following acute lung injury. The methods developed and employed here represent accurately simulated physiological conditions to encourage translatability of trends into that expected in the body.

We confirmed that MPs were significantly better in targeted adhesion than NPs for all experimental conditions, with anywhere from 50% to 5,450% increase versus NPs, depending on the hemodynamic conditions. We found that both VTC modulus and targeting ligand regime could be tailored *in vitro* and *in vivo* to optimize adhesion given known hemodynamics. More deformable particles performed better at low wall shear rate (WSR), while more rigid particles

adhered better at high WSRs. At high WSR, an increased ligand surface density improved the adhesion of deformable particles 27-fold, but not sufficiently to match the adhesion of rigid counterparts. While local shear rate dictated the optimal particle modulus, the local cellular protein expression dictated the adhesion kinetics required for optimized rigid NP and hydrogel MP adhesion. We found that a 25%-75% mix of ligand, skewed to the receptor which is lesser expressed, was consistently the most efficient at providing NP VTC adhesion, producing up to 9-fold more adhesion.

We found that the addition of targeting ligand to MPs did not significantly decrease the circulation *in vivo.* Targeted, deformable MPs showed maximal retention at the target site over time versus rigid particles of any size. Finally, we showed that hydrogel MPs can greatly increase the transport of 50 nm NPs to the vascular wall, up to 5,450% versus free 50 nm NPs. This work explores and explains trends that depend on both the physiological conditions and particle properties *in vitro* and *in vivo.* Overall, we emphasize the importance of particle size, modulus, targeting ligand regime, and the local targeted tissue environment in engineering maximally efficient VTCs. We present work from VTC formulation which concludes with applications in multiple *in vivo* models, to provide a big picture view of how multiple particle properties cooperate to affect targeted adhesion.

Chapter 1: Introduction

1.1 Publication Information

The following text is in part from the publication: **Fish, Margaret B**., Alex J. Thompson, Catherine A. Fromen, and Omolola Eniola-Adefeso. "Emergence and Utility of Nonspherical Particles in Biomedicine." *Industrial & Engineering Chemistry Research.* 2015. 54 (16): 4043-4059.

1.2 Background and Significance

The design of new drug delivery systems has garnered significant attention in recent decades with the goal to greatly improve the treatment and diagnosis of major diseases including cancer and atherosclerosis.[1,2] Systemic administration of small molecule pharmaceutics results in undirected distribution of the therapeutic throughout the body. This leads to unnecessary delivery to healthy cells, resulting in potentially severe side effects that trigger dose-limiting toxicity.[3] Paul Ehrlich coined the term "magic bullet" over a century ago, with the vision that a drug could be designed to preferentially target disease, thereby introducing the idea of drug delivery selectivity.[4,5] To overcome the non-specific delivery of free therapeutics, particulate drug delivery systems ranging in size from a few nanometers to a few micrometers have been designed to specifically accumulate in the diseased tissue of interest, simultaneously increasing the local concentration and efficacy of the drug and decreasing systemic side effects.[6]

The change in size scale from a small molecule therapeutic to a particle creates both new opportunities, along with new challenges, for improving drug efficiency and specificity. The

loading of drug cargo into or onto particle carriers[7] improves upon freely soluble systems by protecting the cargo from degradation in the blood (enzymatic and hydrolytic) while providing controlled, sustained release. Unlike small molecule drugs, particle systems larger than 3 nm are unable to pass through the tight junctions of healthy endothelial cells (ECs) to the surrounding tissue, with some dependence on vasculature type.[8,9] Particles are restricted to the circulatory system, subsequently increasing exposure to the vasculature and ECs. Capitalizing on this increased exposure, vascular targeted carriers (VTCs) have been proposed with surface ligands to actively target diseased ECs. Covalently attached ligands can complex with specific cellular membrane receptors to produce firm adhesion and can be designed with high specificity to ECs with various disease pathophysiology.[6,10] Therefore, the gold standard in this field is to engineer VTCs which simultaneously increase local therapeutic payload through specific EC-targeting while decreasing systemic exposure and related toxicity.[11,12] Realization of such a system will greatly improve the therapeutic outcome of a wide variety of treatments, impacting diseases ranging from cancer, autoimmune disorders, cardiovascular disease, and more. This work has the true potential to unlock treatments by molecules previously unavailable, due to systemic toxicity, for a broad range of ailing patients.

In the design of targeted drug carriers, it is imperative to engineer for the entire biological journey, from injection to intended site of delivery, to achieve maximal targeting efficacy. While the golden standard of VTCs sounds miraculous, there have been significant hurdles limiting translation into the clinic,[13,14] requiring the understanding of complex biological systems to progress towards successful vascular-targeting. VTCs must successfully evade immune capture, distribute to the targeted organ, localize to the endothelial layer of a blood vessel in dynamic blood flow, be taken up by cells of interest, and release drugs on an appropriate time scale for the

disease model. Given this complex series of barriers, further understanding of targeted particle delivery systems is required before they become commonplace in the clinic. Control of physical particle properties to alter particle behavior at different stages of this biological journey holds great promise for improving the efficacy of targeted particulate carriers.[15–17] While many studies have approached the concept of optimizing physical VTCs properties, often the studies are conducted in over-simplified systems, when maximally physiological experiments are needed to truly imitate the biological barriers to VTC adhesion. Here, we aim to provide a holistic view engineered VTC properties, with the hypothesis that VTC physical parameters, including the size, modulus, targeting regime, and more, interplay with each other to collectively determine the final success of VTC systems *in vivo*. Furthermore, we hypothesize that these particle properties interplay with physiological considerations, such as local hemodynamics and endothelial cell expression patterns, to result in optimized VTC properties, tailored for each different experimental condition.

1.3 Important Physiological Considerations for Vascular Targeting

By loading drugs into or onto particulate carriers, the resulting change in size scale from small molecule to particle has revealed new biological hurdles that are highly specific to certain particle sizes.[18] Injected particles face physical barriers throughout the body, including filtration by the spleen, liver, and kidney, which restrict passage of particles of varying sizes and deformabilities. Particle carriers are the ideal size to interact with the reticuloendothelial system (RES), an active network of phagocytic cells, such as monocytes and macrophages, which are responsible for clearing foreign objects rapidly from the blood stream. Macrophages of RES organs, especially in the spleen and liver, are known to clear a large number of particle carriers

from the blood stream.[19,20] Furthermore, recent work in our lab has demonstrated that circulating neutrophils, phagocytic blood cells, are also capable of actively sequestering and clearing particles from blood stream.[21] This cellular clearance has an obvious impact on the number of particles that have the chance to interact with the tissue of interest. Overall, it is imperative to understand each biological barrier individually affects our VTC efficacy in order to design particles to avoid as many clearance mechanisms as possible.

RES clearance and organ biodistribution

As VTCs travel through the blood stream, they encounter an enormous number of barriers, which must be accounted for in the particle design to ensure eventual targeted delivery. The kidney's glomerular filtration relies on the convection and mostly the diffusion of small compounds through the fenestrated capillary endothelium and across the subsequent podocyte filtration slits. The kidney freely filters hydrophilic particles and compounds with radii less than 6 nm, meaning drug delivery particle systems are typically too large for kidney filtration.[22] Overall, kidney clearance can be diminished or eliminated if at least one axis of the particle is larger than 6 nm, irrespective of the specific shape. This is in stark contrast to hydrophilic small molecule drugs, which are often limited by renal clearance and toxicity, as the drug freely filters through the fenestrated capillary endothelium.[23] Lipophilic small molecule drugs often bind to serum proteins, such as albumin, which can decrease their accumulation in the kidney until broken into more hydrophilic portions by endogenous enzymes.[24,25]

Circulating particles will rapidly encounter clearance mechanisms in the complex vasculature of the spleen. The human splenic artery branches and narrows through cords of billroth, which serve as an immunoactive filter with a pore size ~500 nm.[26] Anything caught in

the spleen is readily phagocytosed by resident macrophages.[27] Researchers widely accept spleen filtration as a mechanism to clear damaged red blood cells (RBCs) and other objects above the pore size cut-off. Whereas free drug simply passes through the spleen, the spleen pore size requires that particles larger than 200 nm deform to pass through the filtration system or risk immune clearance.[28] Larger, spherical VTCs have always shown significant accumulation in the spleen and researchers have proposed deformability as a way to mitigate this accumulation.[29]

The liver is a large organ of the digestive system but also plays a significant role in RES responses. In the context of the RES, the liver is comprised of hepatocytes and liver-specific macrophages called Kupffer cells, which both metabolize foreign or toxic substances. In the liver, blood flow splits into discontinuous sinusoids lined with fenestrated endothelium with gaps up to 150 nm. Hepatocytes form a layer behind the endothelium and phagocytic Kupffer cells, which project into blood flow to collect foreign entities in blood.[30] Kupffer cells account for 80-90% of fixed macrophages in the entire body; they use foreign surface protein patterns to identify non-endogenous entities, rendering the liver a highly immunoactive organ.[31] To avoid this well-known mechanism of liver clearance, much research has aimed at alleviating the absorption of plasma proteins onto particle surfaces.[18,19] Overall, the size of particles entrapped into the liver is controlled by both the size of capillary fenestrations and the phagocytic capabilities of resident Kupffer cells.

These interactions the innate defenses of the human body will dictate the overall fate, or biodistribution, of a VTC in an animal. Particles will continue to pass through the various filtration systems and RES mechanisms and ultimately distribute to different tissues in the body. One challenge with the implementation of injectable micro/nanocarriers is in understanding and, more importantly, controlling the fate of the carrier system. Typically, particulate drug carriers

large enough to avoid kidney clearance accumulate in the organs of the RES, with the majority of the dose removed from circulation in minutes to hours. Biodistribution can be skewed to the targeted organ by modifying the particle surfaces with various ligands.[32,33] Changes in particle material type (lipid-based, polymeric, metallic)[34], size (nanometer to micrometer scale)[35], drug loading method (encapsulated, ionic interaction, or covalently linked)[36], and surface chemistry (use of targeting ligands, surface coatings, and charge) have been explored to alleviate RES particle clearance.[37] Additionally, researchers have extensively shown that deformable VTCs remained in circulation longer, shifting the overall time horizon and biodistribution versus rigid equivalents.[38,39] Indeed, physical and chemical properties of particulate drug carriers dictate the overall biodistribution; this information is key to engineering systems which avoid the RES sufficiently to deliver a clinically viable drug delivery system.[11]

Particle margination

If particles are able to elude the clearance mechanisms of the RES, they must then navigate the vasculature, interact with the correct tissue and cell type, and release the payload for maximal therapeutic effect. Thus, VTCs must navigate the dynamic environment of the blood stream to reach the target tissue. The ability of an injected carrier to "marginate", or localize from human blood flow to adhere the periphery of the vessel, is key to ensuring properly specific EC distribution. In blood flow, a RBC core develops for two key reasons: 1. due to heterogeneous collisions between highly deformable RBCs and more rigid leukocytes, and 2. due to wall-induced lift preferentially experienced by more deformable entities in flow.[40,41] Similar to leukocytes and platelets, VTC with functionality designed to interact with the endothelium needs to also exit the RBC core of bulk blood flow and marginate under physiological conditions.

It is well known that RBCs play a role in the margination of leukocytes and platelets; thus, it is important to determine how RBCs influence particle margination. It is imperative to conduct these studies in whole blood flow, so that true margination can be experienced by the VTCs, unlike in buffer flow. Researchers have shown that for rigid and deformable particles, the ability to marginate in the presence of blood components is highly dependent on size.[10,42–46] In general, particles with diameters 2-5 micrometer, markedly about the same size as a platelet, preferentially displace to the RBC cell-free layer (RBC-FL) in the presence of RBCs, while smaller 100-500 nm particles do not experience this enhanced localization.[42–46] This difference in margination directly results in significantly better adhesion of 2 μm particles versus 500 nm particles. While size is well-established as a particle property that significantly influences hemodynamic behavior, the importance of other physical properties, such as deformability, are less understood both experimentally and computationally.

Opsonization and protein coronae

Once particles are at the vascular wall, the integrity and steric availability of the targeting ligands is key for adhesive functionality. Adsorption of plasma proteins onto the surface of particles initiates the inevitable biological clearance of VTCs by phagocytes. This rapid, unavoidable effect of intravenously delivered particles begins within seconds,[47] and directly defines the biological signature of the VTC, with significant implications for immune clearance rate. This protein corona is a function of many variables, including particle size, shape, hydrophobicity, material, exposure time, and more,[48] and it produces opsonization, or the adsorption of "opsonins", typically immunoglobulins and complement, which initiate phagocytosis and clearance of VTCs from the blood. Phagocytes in the RES then rapidly clear

VTCs from the blood stream, diminishing their clinical utility.[18,19,49,50] For this reason, the plasma protein corona is very well studied on many different particle types, mostly with the end goal of lessening or eliminating adsorption all together.

Poly(ethylene glycol) (PEG) is a hydrophilic monomer that has been reviewed and used extensively as a surface coating or ligand to mitigate plasma protein adsorption and opsonization effect and the immune recognition described above.[51] The efficiency of PEG as a coating is highly dependent on the particle surface concentration; low concentrations (mushroom regime) do not exhibit efficient repulsion of plasma proteins whereas high concentrations (brush regime) allow for the most effective immune evasion. This transition from mushroom to brush is determined by the PEG molecular weight and the spacing between monomers.[52–54] In general, PEGylated particles show longer circulation times in animal models versus non-PEGylated particles; particles with brush conformation show better immune evasion than mushroom conformation, though any amount of surface grafted PEG greatly improved the pharmacokinetic (PK) parameters versus a polymerized surface.[32] For polymerized PEG-based materials this "PEGylation" effect is lessened due to the lack of free, hydrophilic PEG end groups.[38,55] Overall, PEG was initially proposed as a hydrophilic ligand to decrease immune response, and while some clinically viable systems have been developed, the initial excitement for this strategy has faded. Therefore, it is of key interest to study and understand how other VTC properties may improve targeted adhesion.

1.4 VTC Design Parameters

The biological barriers innate to the human body, which efficiently protect against infection and disease, also prescribe certain restrictions on VTC design, however, there is an

immense parameter space of physical properties that can be optimized to maximize the accumulation at the targeted site. The efficiency of vascular targeting is determined by the amount of the particle dose that specifically accumulates in the diseased region or tissue of the body. Therefore, particles with high targeting specificity must be designed to maximally accumulate in the region of disease while minimally accumulating elsewhere in the body.

Particle fabrication and composition

There are a wide variety of fabrication methods for drug delivery particles, including top-down methods such as soft lithography, specifically particle replication in non-wetting templates (PRINT),[56] and bottom-up methods including emulsion, self-assembly, spray drying, electrospraying, any many more.[57–61] In addition, some of these methods are amenable to multiple of the traditional biomaterials, including a whole host of biocompatible polymers, such as poly(lactic-co-glycolic acid), poly(capralactone), PEG, polylactic acid, dextran, chitosan and many more.[62] Additionally, polymer chemists and physicists have engineered "smart" polymers which respond to different stimuli such a pH, temperature, magnetic fields, and much more.[63] Other than polymers, VTCs can also be composed of inorganic materials, such as iron oxide, or lipid, which are frequently seen in clinical trials. Taken together, this massive range of particle fabrication techniques, in combination with all of the possible biocompatible materials, affords an incredible range of physiochemical properties to be tuned. As such, the fabrication method and material are likely the first design parameter to consider. Simply put, this many degrees of freedom in design necessitates well-designed studies to identify key VTC properties without confounding variables.

Particle size

Size is the most-studied physical characteristic of particulate drug carriers. Indeed, the conception of particulate drug carriers was driven by the idea of tailoring particle size to exploit the leaky vasculature of cancerous tissues. Particles were designed with diameters between 20-100 nm to preferentially leak out of the abnormally fenestrated tumor vasculature while avoiding both renal and RES clearance, in a phenomenon labeled the enhanced permeation and retention (EPR) effect.[11] Since the origination of particulate drug delivery, many levels of complexity have been imparted into particle design, but particle size often still drives the overall behavior.

When detailing the RES clearance mechanisms, it is clear that particle size determines many biological interactions *in vivo*. At the organ level, particles less than 6 nm will be cleared by diffusion through the kidneys, rigid particles larger than ~500 nm will become entrapped in the spleen, and particles 1-2 μm in size range will be cleared via the liver. At the blood flow level, particle size has been shown to control the margination efficiency in bulk blood flow, with microparticles performing significantly more efficiently than nanoparticles.[10,46,64,65] Finally, on the cellular level, the radius of curvature has been identified as the key property that controls both the amount of protein opsonization and rate of phagocytosis.[18,66–68] Phagocytes use the radius of curvature to extrapolate the overall size of the object; particles with large radii of curvature induce frustrated phagocytosis and better avoid uptake,[68–70] whereas particles with a small enough radius of curvature avoid protein opsonization and are not recognized by phagocytes.[71] Overall, controlling or evading these clearance mechanisms increases the probability that the particles will accumulate at the site of interest.

On the blood flow level, particle size has been shown to control the margination efficiency in bulk blood flow.[10,46,64,65] Particle size also drives critical ligand-receptor

interactions necessary for VTCs. Targeted adhesion requires that the adhesive force between the particle and endothelium receptors is stronger than the shear removal force of the blood flow. Size affects this delicate balance in two competing ways: (1) larger particles experience larger shear removal forces that can produce particle detachment and (2) larger particles have more ligand-receptor pairs available for adhesion at the cell-particle interface due to the larger radius of curvature.

Particle size greatly affects the amount of cargo that can be loaded into the particle and the resulting release kinetics.[72,73] The exact effect depends on the physiochemical interactions between the drug and particle. Zero-order drug release kinetics have been the golden standard in drug delivery for decades; zero-order means that the drug release rate is constant independent of the amount remaining in the particles.[74] If one can achieve sustained release at a constant rate, then a therapeutic dosage can be maintained and controlled over much longer periods of time compared to free drug administration. First order release slows linearly as the concentration in the particle decreases and second order slows exponentially; these release kinetics still deliver an improvement over free drug, but are not considered truly sustained release. For spherical particles, the smaller the particle, the larger the surface area to the volume ratio, which has direct implications on the release kinetics; the more exposed surface area, the faster the particle degradation and the more of an overall burst release. Larger particles degrade slower and therefore provide more of an extended release profile. The release of drugs loaded physically or covalently into a biomaterial matrix depends on many factors, including drug-polymer interaction strength, diffusivity out of the particle, surface area to volume ratio, amount of drug loaded, and more. Size directly affects the surface area to volume ratio, and thereby greatly

changes drug release profiles. [57] Overall, particle size directly determines the amount and overall release profile out of biocompatible drug carriers.

VTC targeting ligands

VTCs achieve tissue specificity with active ligand-receptor targeting, which exploits differential expression of certain inflammatory proteins on the membranes of vascular ECs, thereby eliminating the need to rely on size for passive accumulation. Marked changes in endothelial surface expression occurs in disease;[75–77] particles are engineered to capitalize on these variations, to have high affinity in the diseased vasculature and low affinity elsewhere. For example, in generally inflamed vasculature, which is associated with many acute and chronic diseases, multiple classes of molecules are upregulated on the endothelium surface. These markers include E-selectin, P-selectin, intercellular adhesion molecule-1 (ICAM-1) and vascular cell adhesion molecule-1 (VCAM-1), which all play a different role in the leukocyte adhesion cascade (LAC).[78,79] The upregulation of inflammatory markers leads to the recruitment, adhesion, and transmigration of circulating leukocytes into the tissue space, which progresses the inflammatory disease.[80] While leukocytes typically bind to these receptors, the change in EC expression provides a platform for targeting particulate therapeutics to these receptors, and subsequently, the site of disease.

Targeting ligands come in many sizes and molecular motifs, including small molecules, aptamers, affibodies, receptors, and antibodies.[6,81–83] Researchers have evaluated selectins for their natural ligands on WBCs and contributions to the LAC and inflammation.[84] Some of the initial motivation for targeting these particular molecules arose out of observing the innate LAC. Most studies of VTCs focus on particle designs with a single ligand-receptor (LR) pair, with

emphasis on disease outcome of the delivered drug. Efficacy studies that have probed dual ligands are largely qualitative, comparing multi-ligand particles versus their single ligand counterparts with minimal control over the total ligand presentation on the particle.[85–89] Many studies have probed the importance of ligand ratios between two LR pairs in static conditions, which fail to capture the LR pair dynamics under physiologically relevant flows.[85,90] Studies involving three distinct targeting ligands delivered improvements in targeted adhesion *in vivo* over a single ligand, but not over dual targeting. Often these systems are tested in buffer under static conditions *in vitro*, and then are injected into animal models. Much more robust understanding of targeting ligand kinetics in hemodynamic blood flow is required to inform the intelligent design of VTCs for targeting.

For VTCs, the conjugation of these constructs onto the surface of particles imparts high affinity for areas of vasculature with overexpression of the targeted molecules. Ideally, the particles will freely circulate until they encounter an area of vasculature for which their targeting ligands impart high binding affinity, and then they will bind. However, adding targeting ligands changes the protein corona opsonized onto the surface and is thought to decrease the overall circulation time.[12,91] Therefore, there is still open discussion in the field about whether targeting ligands are rational *in vivo* due to their added complexity and resulting decrese in circulation time. A few strategies have been employed to try and mitigate this: PEG has been conjugated with targeting ligand to decrease immune recognition. Sterically, the targeting ligand must extend further than the PEG layer to be available for targeted receptor binding. The targeting ligand on the free end of PEG increases the amount of protein opsonization versus free PEG—researchers confirmed that the targeting moiety itself changes the pattern of proteins on the surface, regardless of brush PEG density.[92,93] *In vivo*, the amount and length of PEG must be

optimized versus the corresponding length and amount of targeting ligand present; otherwise there may be sacrifices in both stealth and targeting functionality.[94] Despite decades of research, PEG has not provided a "one size fits all" solution for decreasing the immune recognition of VTCs. An additional hurdle with PEG has been uncovered recently; humans have increasing amounts of anti-PEG antibodies in their blood stream due to the amount of PEG found in consumer products and therapeutics.[95] Thus, there is not yet a magic bullet solution that increases the circulation time of all particle systems. With all of this in mind, one is left wondering what the actual effect of targeting ligand addition is on diseased site accumulation, independent of circulation time.

Particle modulus

As more biocompatible particulate carriers are developed for commercial use, researchers have increasingly employed PEG as the bulk material, rather than just a surface coating, because of its modularity and broad range of functionalities.[96,97] Both top-down and bottom-up approaches allow for the tuning of PEG-based particle modulus, by either altering the amount of covalently cross-linked PEG (%v/v) in the synthesis or by altering the cross-linking density within the hydrogel by including monofunctional monomers. Of note, the higher the molecular weight of the PEG, the less soluble in water and hydrophilic;[98] the free end groups are key for producing the "PEGylation" effect of resisting protein opsonization, and therefore are not imparted on crosslinked PEG particles. Macrophages readily recognize polymerized PEG surfaces, which leads to rapid clearance from the blood stream.[32,38] Therefore, despite researchers' best efforts, many of these crosslinked PEG particles are afflicted with the same

issues as particles composed of other polymers, including rapid clearance and lack of accumulation into the targeted tissue.

Recently, much of the development in PEG-based particles has focused on exploring the particle modulus as a key parameter to shift the overall biodistribution and circulation profiles. Indeed, the entire field of bio-mimetic particle carriers uses mimicry of many biological features, including the highly deformable nature of most endogenous biological entities.[38,99–102] Researchers have explored particles of varying modulus to determine how the RES system responds and the resulting biodistribution. In general, more deformable particles are known to circulate longer by avoiding recognition, filtration by or interaction with the immune system, and by better squeezing through natural immune filters such as the spleen.[38,39,103] Additionally, it has been well-established that phagocytic immune cells, such as macrophages, phagocytose rigid particles significantly more rapidly than deformable particles of the same composition.[38,39,104–106] Therefore, by understanding the mechano-responsiveness of phagocytic immune cells, particles can be engineered to better avoid immune clearance. Overall, particle modulus is emerging as a key VTC physical property, with researchers interested in circulation time, biodistribution, cell uptake, and margination processes.

1.5 Opportunities in Vascular Targeting

Despite the idea of vascular targeting has existed for decades, few systems have made it through clinical trials; those particle systems that are approved are mainly non-targeted liposomes or PLGA NPs.[14,107,108] The concept of vascular targeting has the potential to revolutionize the treatment of a broad range of diseases; the main requirement being that the endothelium has a different surface protein marker pattern than healthy endothelium. In particular, diseases such as cancer and cardiovascular disease, which cause a massive number of

deaths per year and are marked by chronic inflammation, are amenable to advances in particulate drug delivery. Researchers have spent a massive amount of time and energy investigating different particulate, and more recently, VTC systems. Recurring from throughout the introduction, VTCs need to be evaluated in increasingly physiological systems. As a prime example, many VTCs are studied in the absence of shear flow and without key blood components, such as RBCs and phagocytic leukocytes. While this work provides basic insight into VTC behavior, in order to contribute the most translatable work possible, relevant physiological components should be included in studied. For instance, VTC uptake by cells in static buffer cannot accurately represent the dynamic environment of blood, which must be navigated to accomplish any cellular uptake *in vivo.* VTCs in static buffer do not have to evade immune clearance or compete with leukocytes for binding sites on the inflamed endothelium. Indeed, most research lacks the key complexity delivered by the involvement of blood. We hypothesize that through fine control of particle modulus, better-characterized ligand kinetics, and experiments designed to facilitate conclusions about the collective influence of multiple VTC properties, we have the potential to deliver significant advances in the field of VTCs based on physiologically relevant scenarios.

1.6 Organization of the Dissertation

The work presented in this dissertation is focused on the engineering of the physical properties of PEG-based particles, including size, modulus, and targeting ligand regime, for optimal targeting performance and adhesion, evaluated extensively both *in vitro* and *in vivo*. We hypothesize these parameters of the physiochemistry of the particles can dramatically increase the VTC efficiency to produce large impacts in the clinic.

Chapter 1 lays out the background and motivation for the experimental work presented in this dissertation, including a general overview of VTCs and the key design parameters to lever in engineering new systems.

Chapter 2 is a description of the materials and methods utilized to obtain the experimental data for the rest of the dissertation.

Chapter 3 is an experimental exploration of the importance of PEG-based particle modulus and size for both *in vitro* and *in vivo* targeted adhesion and drug delivery. We detail the margination, responses to physiological blood forces, and adhesion to inflamed endothelium using both a flow chamber and intravital microscopy in murine mesentery venules.

As we only focused a single ligand receptor system and a single site density in chapter 3, chapter 4 provides experimental analysis of the interplay of two different targeting ligands, their site densities, and particle modulus on hydrogel MPs to prescribe the final targeted adhesion to inflamed endothelial cells *in vitro*.

In an effort to improve the targeted adhesion of rigid NPs, chapter 5 employs two different targeting ligands on 500 nm PS particles to explain how dual targeted particles with ligands of different kinetics work together to produce maximal binding both *in vitro* and *in vivo* in a model of mesentery inflammation. This chapter is a collaborative project with Dr. Catherine Fromen; I have only included the work to which I contributed significantly.

Considering the extensive investigation into targeting ligand regime in chapters 4 and 5, chapter 6 provides a detailed *in vivo* perspective on how adding targeting ligand to PEG particles affect both their circulation time, biodistribution, and accumulation at the site of inflammation.

Chapter 7 combines much of the previous accrued knowledge to highlight how PEG-based particles can be used as Trojan Horse carriers for much smaller NPs to the vascular wall.

This experimental work provides clear head to head comparisons of how free NPs and packaged NPs accumulate at the site of inflammation both *in vitro* and *in vivo*.

Chapter 8 provides the overarching conclusions of this dissertation and the future directions and outlook for both this work and the general particulate drug delivery field.

Chapter 2: Materials and Methods

2.1 Introduction

This chapter details the materials and methods utilized to complete the experimental research described in the following five chapters of data. Details about the materials and protocols are given to allow for reproduction of results described. A range of VTCs are prepared and the ability to adhere to inflamed endothelium under a variety of hemodynamic and inflammatory conditions are investigated, both *in vitro* using a parallel plate flow chamber (PPFC) assay and *in vivo* using murine models of inflammation with a variety of tools to evaluate adhesion in real time and over longer time scales. The materials (and source) are listed within the specific subsection for which that material was utilized.

2.2 Particle Fabrication

Polystyrene (PS) particles

Fluoresbrite® YG, Carboxylated polystyrene spheres (50 nm, 500 nm, and 2 μm diameter) were purchased commercially from Bangs Laboratories (Fishers, IN).

PEG- hydrogel particle fabrication

Poly(ethylene glycol) diacrylate (PEGDA, Sigma Aldrich, St. Louis, MO), 2-carboxyethyl acrylate (CEA, Sigma Aldrich, St. Louis, MO), acryloxyethyl thiocarbamoyl Rhodamine B (Rhodamine, Polysciences, Warrington, PA), and lithium phenyl-2,4,6-

trimethylbenzoylphosphinate photoinitiator (PI) were combined into methanol at predetermined concentrations to produce a range of crosslinking densities and a range of hydrogel material properties. The PI was synthesized in house as previously published by others.[109,110] The methanol-PEG solution was emulsified into silicone oil via probe sonication at 15% intensity. The solutions were then exposed to a 365 nm UV light for 2 minutes to initiate polymerization. A series of centrifugation and filtration steps were utilized to obtain particles of desired size and monodispersity. First, the particles were filtered through 2 μm filter tips to eliminate larger particles. Then, the stocks were diluted into 15 mL conical tubes and centrifuged at 1500xg for 5 minutes; the pellets were kept and the supernatants containing smaller particles were moved to a different tube. The pellets were resuspended in 1% PVA and probe sonicated. This process was repeated twice more to remove smaller sized particles and establish a 2 μm particle stock. The collected supernatants containing smaller particles were centrifuged at 3000xg for 10 minutes three times. The pellet was kept and resuspended in 1% PVA each repetition. The final pellet was kept as the 500 nm hydrogel particle stock. The particles were covalently modified and characterized, as described in more detail later.

Loaded PEG-hydrogel fabrication

PEGDA, CEA, Rhodamine, and PI were again combined into methanol at predetermined concentrations. Unmodified, carboxylated PS nanoparticles (NPs) (Bangs Laboratories, Fishers, IN) were loaded directly into hydrogels matrices in the following way. First, the commercial stock of NPs was concentrated via centrifugation and then lyophilized to remove any residual liquid. All other components of the hydrogels were added directly to this dried NP powder to minimize any possible loss by powder transport. The resulting solution was emulsified and

polymerized such that the NPs were physically entrapped into the hydrogel matrix. All particle stocks were diluted in 1% PVA, filtered through a 2 μm filter, and washed at least 3 times before quantifying the median fluorescent intensity (MFI). The % v/v used in the hydrogel formulation, specifically 2.3%, 3.9%, 7.8%, and 15.6% v/v, is reported quantitatively in chapter 7 so that NPs of different sizes can be directly compared. To convert the MFI to a number of NPs per hydrogel microparticle (MP), a standard curve of NP concentrations was established on a Biotek microplate reader (Winooski, VT). After thorough washing to remove any free 50 nm NPs, hydrogel MPs were evaluated in a 96 well plate at a fixed concentration of 1E7 hydrogel MPs/well. The reading was converted to number of NPs loaded after subtracting out unloaded MP background and using a calibration curve of 50 nm NPs.

Particle characterization methods

Malvern Zetasizer Nano-ZS (Malvern, Westborough, MA) was used to determine the size, zeta potential, and polydispersity index (PDI) of all particle stocks. Particle samples were diluted in water for all measurements and run in triplicate. Particle morphology was monitored by scanning electron microscopy (SEM); samples were sputter-coated with 10 nm of Au (SPI-Module Carbon/Sputter Coater, West Chester, PA) and imaged dry using a Philips XL30 FEG scanning electron microscope (SEM) (Hillsboro, OR). The NP-loaded hydrogels were imaged via confocal fluorescent microscopy, to confirm the co-localization of rhodamine in the hydrogel matrix backbone and green fluorescence of the 50 nm PS NPs.

2.3 PEG Material Characterization Methods

Equilibrium swelling ratios(ESRs)

Bulk hydrogels of the same composition as particles were polymerized in polytetrafluoroethylene molds (Ted Pella, Redding, CA) and transferred into 5 mL water to swell. The water was exchanged twice to rinse out unpolymerized polymer. The hydrogels were then placed in water or blood plasma for 24 hours at 37°C. The swollen samples were weighed, rinsed of possible residual plasma proteins, lyophilized for 48 hours (Labconco Freezone 2.5, Kansas City, MO), and then weighed again dry. The ESR is calculated as shown in equation (1).

$$ESR = \frac{Swollen\ Mass}{Lyophilized\ Mass}; unitless \quad [1]$$

The experimental dried mass was directly compared to the theoretical dried mass to confirm complete polymerization of all samples.

In situ *rheometry*

In situ polymerization was performed beginning with unpolymerized hydrogel precursor solutions, whose compositions are detailed in the respective chapters. These precursor solutions were injected into a 500 µm gap between the head and stage of an AR-G2 Rheometer (TA Instruments, New Castle, DE). A 20 mm rheometer head was used for *in situ* polymerization data collection. The 365 nm UV light source, built into the stage, was turned on at an intensity of 10 mW/cm^2 at time 0 and the resulting changes in G' and G'' were recorded ~8 times/second.

Swollen rheometry

Hydrogel coupons were polymerized in polytetrafluoroethylene molds (Ted Pella, Redding, CA), allowed to swell in water overnight, and then 8 mm cylinders were punched out

for experimental sampling. For all rheometry, the same formulation was used in the bulk molds as for the particles of interest, including when loaded with NPs. For all swollen conditions, an 8 mm rheometer head was used and the % strain was altered on the AR-G2 Rheometer (TA Instruments, New Castle, DE) depending on the material properties, from 0.1% for rigid and 10% for deformable. The rheological sampling parameters were validated via frequency and amplitude sweeps, as shown in Figure 2.1, prior to gathering experimental data. To convert from shear modulus (G) to Young's modulus (E) we use equation (2), assuming a Poisson's ratio, of υ=0.5, as can be done for elastic materials such as swollen hydrogels.[111]

$$E = 2G(1 + \upsilon); Pa \quad [2]$$

The controlled shear stress experiments were conducted on swollen bulk hydrogels at a gap height of 3 mm. The rheometer swept a range of predetermined stress inputs at 37°C and determined the resulting percent strains, dependent on hydrogel condition.

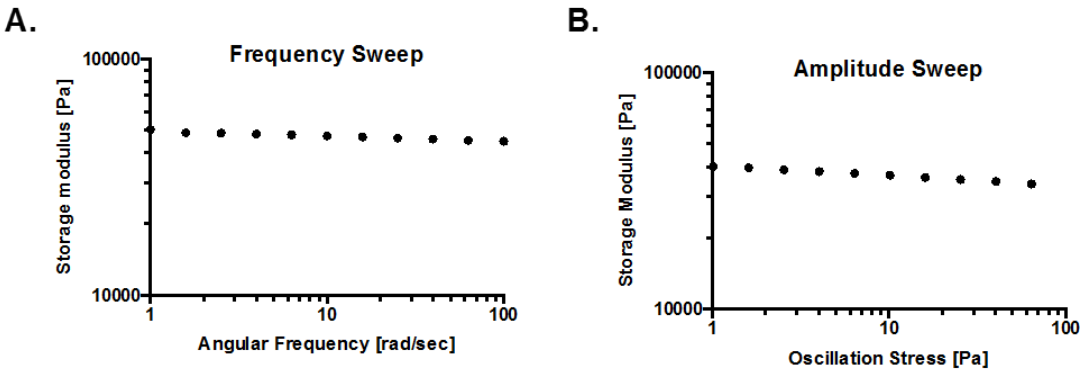

Figure 2.1 Validation of rheological sampling parameters.
(A) Frequency and (B) amplitude sweeps of a hydrogel composed of 40% solids. These sweeps ensure hydrogel integrity over sampling ranges used to test bulk materials. Across the frequency sweep, different oscillatory frequencies are tested to determine if internal structure of the gel

changes with measuring conditions; Figure 2.1A shows that the internal structure of our gels is consistent. The amplitude sweep defines the viscoelastic amplitude range for hydrogels; Figure 2.1B shows little change over a broad range of oscillatory stresses tested.

Calculated hydrogel properties

The density (kg/m^3) and pore size (nm) of our hydrogel materials were calculated as previously reported.[112] Density is calculated utilizing equilibrium volume fractions of each precursor component. Pore size depends on the bulk density, Young's modulus, temperature and polymer volume fraction.

2.4 Particle Surface Modifications and Ligand Density Quantification

Targeting for in vitro *experiments*

CEA functionality was incorporated throughout the hydrogel particles, resulting in terminal carboxylic acid functional groups. NeutrAvidin (Thermo Scientific, Waltham, MA) was covalently attached to the carboxylic acid end groups on both PS and hydrogel particles via carboiimide chemistry. Particles were washed with 2-(N-morpholino)ethanesulfonic acid buffer (Thermo Scientific, Waltham, MA) and incubated with a NeutrAvidin® solution (5 mg/ml) for 15 minutes at room temperature, after which an equal volume of N-(3-Dimethylaminopropyl)-N′-ethylcarbodiimide hydrochloride (EDC, 75 mg/ml, Thermo Scientific, Waltham, MA) was added and pH adjusted to 8.0. After incubating for 24 hours, glycine (7.5 mg/ml, Sigma Aldrich, St. Louis, MO) was added for 30 minutes to quench the reaction. NeutrAvidin®-conjugated particles were then washed with a phosphate-buffered saline (50 mM) and stored at 4°C until ligand conjugation.

Biotinylated ligands were then coupled as described previously.[46] NeutrAvidin®-conjugated particles were incubated for 45 minutes with a mixture of multivalent Sialyl Lewis^A-

PAA-biotin (sLe^A, Glycotech, Gaithersburg, MD) and/or biotinylated anti-human CD54 (R&D Systems, Minneapolis, MN) at room temperature. Following incubation, particles were washed with phosphate-buffered saline containing calcium and magnesium ions and 1% bovine serum albumin and were then stored at 4°C until same day use for flow adhesion experiments or ligand site characterization.

Targeting for in vivo *experiments*

Particles were conjugated with NeutrAvidin, as detailed above. For *in vivo* experiments, biotinylated anti-mouse CD62P (BD Biosciences, San Jose, CA), sLe^A, and/or biotinylated anti-mouse CD54 (Biolegend, London, UK) were coupled to NeutrAvidin-coated particles, by again rotating at room temperature for 45 minutes and washing. The particles were characterized by comparison to a curve of standard beads, and conjugated for final total site densities detailed in each relevant chapter.

Quantification of ligand site density

Particles with targeting moieties were stained to determine the number of ligands per surface area of particle. Anti-cutaneous-lymphocyte-associated antigen-APC/fluorescein isothiocyanate (FITC) (Miltenyi Biotec, Auburn, CA), anti-rat IgG2b-PE (Thermo Scientific, Waltham, MA), anti-rat IgG2b-APC (Biolegend, London, UK), and anti-rat IgG1-APC were used to stain sLe^A, anti-human CD54, anti-mouse CD54, and anti-mouse CD62P, respectively. The MFIs of APC, FITC, or PE were compared to both non-stained particles and either APC, FITC, or PE calibration bead curves (Bangs Laboratories, Fishers, IN). Particle surface area and MFI were used to compute the site density in # sites/μm^2, as previously described. [93,113] For dual

targeted particles, stains were selected that did not overlap in fluorescence, to obtain the site densities of both ligands concurrently. A representation of the site densities obtained on Attune NxT Focusing Flow Cytometer (Life Technologies, Carlsbad, CA) is shown in Figure 2.2.

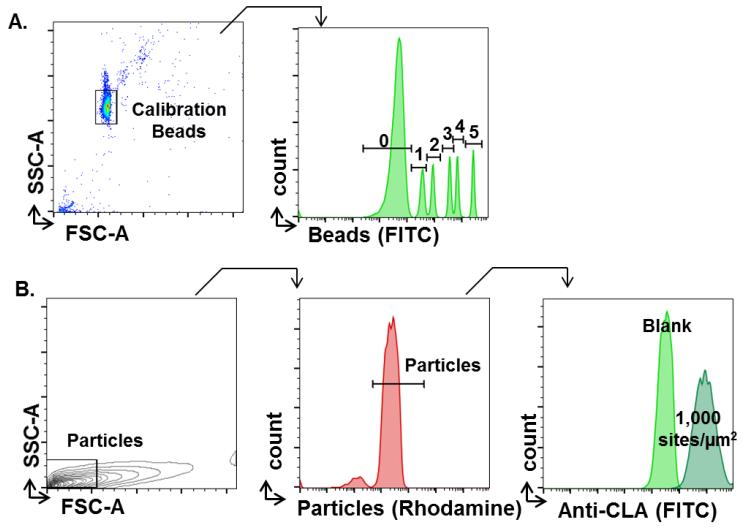

Figure 2.2 Representative gating for particle site density calibrations.
(A) Calibration beads from Bangs Laboratories were run on the flow cytometer at the same voltages as the particles tested. The median fluorescence intensity (MFI) of each bead (0-5) was recorded for FITC and a calibration curve made with known molecules of soluble fluorochrome (MESF) units provided by manufacturer. (B) Particles (2 µm shown) identified by forward (FSC) and side (SSC) area, and positive signal in the BL2 Rhodamine/PE channel. MFIs for FITC was determined for sLe^A using anti-cutaneous lymphocyte associated antigen, anti-CLA-FITC. MFIs were converted to units of MESF using the calibration curve from A.

2.5 HUVEC Culture and Characterization

HUVEC isolation and culture

Human umbilical vein endothelial cells (HUVECs) used in all assays were isolated from healthy umbilical cords (Mott Children's Hospital, Ann Arbor, MI), which were obtained via an approved human tissue transfer protocol. Briefly, the umbilical vein was filled with collagenase and incubated for 20 minutes to degrade the extracellular matrix and free the endothelial cells.

The collected cells were then plated onto a gelatin-coated T75 flask and washed until reaching confluence. Each cell batch was pooled from at least 3 umbilical cords. Isolated HUVEC were cultured in gelatin-coated T75 flasks at 37°C and 5% CO_2 until passage 5, after which they were discarded. For experiments involving flow, HUVECs were seeded onto glass coverslips coated with gelatin (cross linked with glutaraldehyde) at 37°C and 5% CO_2 with standard media until confluent density was reached.[114,115]

HUVEC surface characterization

6 well plates were coated with gelatin (cross linked with glutaraldehyde) and seeded with HUVEC at a confluent density. The cells were activated with 10 ng/mL tumor necrosis factor-α (TNF-α, Fitzgerald, Acton, MA) or 1 ng/mL interleukin-1β (IL-1β, Fitzgerald, Acton, MA) for varying time points. Following activation, the cells were trypsinized, divided into multiple samples, and stained with antibodies to CD54, CD62E, and CD62P as well as an isotype control IgG1 (R&D Systems, Minneapolis, MN) at 4°C. All subsequent steps were performed at 4°C. After 20 minutes of staining, samples were washed twice in phosphate buffered saline with 0.5% bovine serum albumin. Flow cytometry data was collected on an Attune NxT Focusing Flow Cytometer (Life Technologies, Carlsbad, CA) and analyzed using FlowJo software (Ashland, OR). Data for activated cells are presented as compared to unactivated cells. All data have the appropriate isotype controls subtracted from the MFI. The data is represented either as a fold increase over unactivated cells or as a quantitative site density.

2.6 THP-1 Culture and Uptake

THP-1 monocytes (ATCC, Manassas, VA) were seeded at $1x10^5$ cells/well in 96 well plates and incubated with particles at varied times. Cells were incubated with equivalent masses of fluorescent particles, corresponding to 2×10^6 particles/well for 2 μm hydrogels or 1.28×10^8 particles/well 500 nm hydrogels in a total well volume of 200 μL. Cells were washed 3 times with phosphate buffered saline with 2% fetal bovine serum) and assessed for particle uptake via flow cytometry. All studies were performed using Roswell Park Memorial Institute media (Thermo Scientific, Waltham, MA) with heat inactivated 10% fetal bovine serum.

2.7 Blood Collection and Preparations

Phlebotomy was performed according to Institutional Review Board-of UM Medical School (IRB-MED) approved protocols and in line with the World Medical Association Declaration of Helsinki. Written, informed consent was obtained from all donors prior to venipuncture. Anticoagulated, whole blood was obtained from healthy donors directly into acid citrate dextrose (ACD), at a ratio of 1.4 mL ACD/10 mL whole blood. White blood cell (WBC) depleted, red blood cells + plasma (RBC+plasma) medium was obtained by adding 6% dextran (1.4 mL per 10 mL whole blood) to anticoagulated blood in an inverted syringe to sediment red blood cells (RBCs) from WBCs and plasma. The RBC fraction was separated from the leukocyte rich plasma fraction and phosphate buffered saline was added to the RBCs. All was centrifuged at 2250xg for 20 minutes, 3 times. Each time the WBC pellet was discarded from the leukocyte rich plasma, and the buffy coat containing leukocytes over the RBC pellet was discarded. Finally, isolated plasma and RBCs were recombined at 40% v/v RBCs and designated “RBCs+plasma”. Reconstituted blood was put through the same processing as RBC+plasma,

except the WBCs were added back in a physiological concentration, to determine if the processing itself produced any changes in experimental outcomes.

2.8 Parallel Plate Flow Chamber (PPFC) Assay

Flow distribution studies

A 100 µm Ibidi chamber (Fitchburg, WI) was used to perfuse blood containing $1x10^7$ particles/mL. An Olympus FV 1200 Confocal Microscope (Shinjuku, Tokyo, Japan) was used to detect the number of fluorescent particles at each designated height. Particles without rhodamine were conjugated with NeutrAvidin, as described above, and then were stained with R-Phycoerythrin**,** Biotin XX conjugate (Biotin-PE, Thermo Scientific, Waltham, MA). The MFI of each particle type was matched, so to achieve uniform particle brightness. The bottom of the chamber was set by first visualizing adherent 500 nm PS particles. Images were taking using confocal microscopy with a 543 nm laser at 80% power, with the photo-multiplier tube (PMT) voltage set at 700V, 1X gain, and 0% offset. The microscope was run in a round-trip 0.488 ms/line using a 2x digital zoom and a 20x water immersive objective. Particles were processed and counted for a total of 250 images using FIJI software by setting a constant threshold and the "Analyze Particle" function. Laser, PMT, and threshold settings were optimized for blank samples (no particles) to contain less than 1% count of particle positive trials. The shutter speed was set to allow for visualization of individual particles in flow. Results presented are the number of detected particles, not simply the MFI.

Adhesion assay

HUVECs were cultured on glass coverslips as described in more detail above.[114] The coverslips were held by vacuum to the PPFC (Glycotech, Inc., Gaithersburg, MD). Blood from human donors was drawn with the anticoagulant ACD and stored at 37 °C until use. ACD chelates calcium and inhibits particle internalization for the assay duration.[116] HUVECs seeded onto gelatin-coated coverslips were activated under static conditions with either TNF-α or IL-1β, for either 4 or 24 hours, at 37°C and 5% CO_2, to induce E-selectin and ICAM-1 expression.[46] Targeted particles, with more details in each chapter and figure about the ligand and site density, at a fixed concentration, were mixed with either whole blood, RBC+plasma, or reconstituted blood and then perfused through the PPFC in a laminar flow profile for 5 minutes. Non targeted particles were avidin conjugated, with no biotinylated ligand. The volumetric flow rate through the channel (Q) was controlled via a syringe pump (Harvard Apparatus, Holliston, MA), which dictates the wall shear rate (WSR) (γ_W), as shown in equation (3),

$$\gamma_W = \frac{6Q}{h^2 w}; s^{-1} \quad [3]$$

where *h* is the channel height (0.0127 cm), *w* the channel width (0.25 cm), and *Q* the volumetric flow rate (mL/second). The *h* of 127 μm and γ_w of 200 s^{-1} were chosen to mimic the flow profile within a vein/venule of similar dimensions to those studied later via intravital microscopy (IVM).[117,118] The WSR was increased to 500 s^{-1} and 1000 s^{-1} mimic other types of vessels such as larger arteries.[119] After 5 mins of blood media perfusion, 10 images of different areas were captured, and firmly adhered particles were counted and scaled by the monolayer surface area, producing results in number bound/mm^2.

For rate of attachment experiments, images were collected every 30 seconds in the same location, including 5 minutes of blood and particle flow, representing an attachment region, and

5 minutes of buffer only flow, representing a detachment region. Adhesion data was captured using a Photometric CoolSNAP EZ digital camera sensor, and adherent particles were quantified using Metamorph®. All experiments are quantified as number of bound particles/mm^2 HUVEC.

The translation of hydrogel MP binding to NPs delivered in chapter 7 was done using a scaling factor, which was the average number of NPs loaded per 2 μm hydrogel MP. The numbers were as follows: 15% PEG low loading: 3 NPs/hydrogel MP, 15% PEG high loading: 25 NPs/hydrogel MP, and 50% PEG high loading: 16 NPs/hydrogel MP. In this way, we converted the binding of hydrogels to the delivery of NPs.

2.9 Intravital Microscopy

Animal studies were conducted in accordance with National Institutes of Health guidelines for the care and use of laboratory animals and approved by the Institutional Animal Care and Use Committee (IACUC) of University of Michigan. C57BL/6 mice were obtained from Jackson Laboratories (Bar Harbor, ME) between 3 and 6 weeks of age. All animals were maintained in pathogen-free facilities at the University of Michigan.

Visualization of mesentery vessels was performed to discern particle binding and/or rolling.[120–122] Briefly, female mice (3-4 weeks) were anesthetized and a tail vein catheter placed for delivery of particles. A midline incision in the abdominal cavity allowed for exteriorization of the mouse intestines, and therefore, the mesentery connective tissue. Mice were placed on a custom-made microscope heated stage at 37°C and the mesentery was positioned on a glass cover slip. Imaged vessels were chosen based on size, with the diameter of veins ranging from 100 - 200 μm. Following vessel selection, local injury was induced by topical application of TNF-α (10 μL of 200 μg/mL in phosphate buffered saline). Particles were injected 3 minutes

following topical TNF-α application via IV catheter and continuously imaged for another 5 minutes via both brightfield and fluorescent imaging. Particles were dosed by an equivalent mass of ~10 mg/kg, unless otherwise specified, corresponding to 4.34 x 10^7 2 μm particles and 2.78 x 10^9 500 nm particles for each mouse of about 20 g, in a 200 μL injection volume. Targeted particle adhesion in mesenteric veins was visualized under a 25x oil objective using an inverted fluorescence microscope (Zeiss Axio Observer Z1 Marianas Microscope). After 5 minutes, the data were quantified by number of individually bound particles for N=4 mice and represented as number bound or converted to ng particles /mm^2 vessel based on the calculated mass of one particle. At least 10 different imaging locations were found per mouse, using Slidebook 6 software (3i, Denver, CO). Analysis of particle number bound was performed using Slidebook 6 and ImageJ using blinded file names. Particles found in adjacent vessels but within the frame were excluded from the analysis.

In studies with information about rolling velocities, real time videos were captured in addition to still frame images. For each mouse, at least 5 distinct video locations were utilized. Particle rolling velocities were obtained using particle tracking software, and all paths were manually confirmed until at least 50 particles were tracked per experimental condition. Vessels were again measured using Slidebook 6. Particles found in adjacent vessels but within the frame were excluded from the analysis. Particles were considered adherent when they appeared in the same location for ten consecutive frames of the particle tracking. Particles were considered rolling when their tracked paths moved less than 50 μm between frames. Firmly adhered particles did not contribute to the rolling velocity data.

Long time mesentery experiments

Intravital microscopy was conducted as described above,[106,122] but modified to extend the time window of imaging. Briefly, mice were anesthetized by intraperitoneal injection of a mixture of ketamine and xylazine and opened surgically via a midline incision. A tail vein catheter was placed and the intestines were manipulated gently to position the mesentery on the custom, heated microscope stage. A vein was visualized and topical TNF-α was dropped in the area of interest. After 3 minutes, 30 mg/kg particles were injected via tail vein catheter. Firm particle adhesion was quantified every 5 minutes by taking 5 pictures in the same physical locations. In order to maintain the anesthesia of the mice, every 20 minutes 50 µL of the ketamine and xylazine mixture were dropped topically onto the exposed abdominal cavity. The data was compiled to obtain time courses of mesentery particle adhesion to an hour post particle injection, with N=3 mice for each particle type.

2.10 Acute Lung Injury (ALI) Model

Near-infrared (NIR) dye was loaded into the PEG hydrogels used for ALI studies to facilitate whole organ scans, in place of the rhodamine utilized for previous assays. Female C57BL/6 mice (Jackson, Bar Harbor, ME) were anesthetized using isoflurane and 20 µg of lipopolysaccharide (LPS) LPS at 0.4 mg/mL in phosphate buffered saline was delivered to the lungs via an orotracheal instillation to produce local inflammation, as described previously.[123–125] One hour after instillation, particles were injected through the tail vein. Mice received 2 µm MP or 500 nm NP in 200 µL injection volume in phosphate buffered saline (~30mg/kg). Depending on the time point, mice were euthanized a certain number of hours after particle injection. Blood was collected via cardiac puncture in heparin coated tubes. After the blood draw, for those mice that were perfused prior to organ harvesting, the right atrium was cut, and cold phosphate

buffered saline was injected into the left ventricle, thus perfusing the vasculature. Organs, including the lungs, liver, kidneys, spleen, and heart, were harvested and stored in phosphate buffered saline on ice until scanned. Each data point represents N=4 mice per condition and time point.

Whole organ scans were performed on an Odyssey CLx Infrared Imaging System (LI-COR, Lincoln, NE) using the 700 nm channel at 169 μm resolution. Total fluorescence for each organ was determined by drawing a region of interest (ROI) using Image Studio Software from LI-COR. Untreated samples were used to determine the background fluorescence for each organ, which was subtracted from the fluorescence obtained for each organ ROI.

To account for variability in particle brightness, standard curves of each particle type were generated using the Odyssey LI-COR Imaging System. Total fluorescence values of each organ were converted to the number of particles per organ using these standard curves. For each mouse, this value was then scaled by each organ to achieve mass of particles per mass of organ. Total recovered fluorescence was determined as the sum from each organ. The corresponding fluorescent percentage was determined as a portion of this total.

2.11 Circulation Time of Particles

Circulation time curves of both targeted and untargeted particles, again loaded with NIR dye, were established via a tail nick procedure. ALI was induced into mice by LPS instillation into the lungs; both LPS and non-LPS mice were sampled for circulation time measurements. Particles were prepped and dosed by equivalent mass (~30 mg/kg) by injection through a tail vein catheter. At each time point post tail vein injection (5 minutes, 30 minutes, 1 hour, 3 hours, and 24 hours) 10 μL of blood was collected and diluted 10X into phosphate buffered saline. The

blood samples were deposited into black-sided 96 well plates and scanned on the Odyssey CLx Infrared Imaging System. The signal intensity was converted to particle concentration by a standard curve of each particle type. These values were converted to mass circulating by multiplying by the mass of a single particle. PK analysis of the circulation time data was completed in PKSolver (Microsoft Excel). Both one and two compartment models were tested for all conditions; two compartment models were more accurate for all conditions.

2.12 Finite Element Analysis (FEA)

Spherical 2 μm particle meshes were generated in SolidWorks CAD Software (Waltham, MA) and exported to LISA (Sonnenhof Holdings, Ontario, Canada). Meshes were refined to 5425 elements and the material properties for each particle type, including Young's modulus and density, were defined with a Poisson's ratio of 0.5. Surface pressures of $8x10^{-13}$ N/ μm^2 (corresponding WSR=200 s^{-1}), $4x10^{-12}$ N/ μm^2 (corresponding WSR=1,000 s^{-1}), $2.5x10^{-11}$ N/ μm^2, $1x10^{-9}$ N/ μm^2, and $1x10^{-8}$ N/ μm^2 were applied along the X-direction on the top and bottom face of the sphere in opposing directions. The center nodes were fixed with a zero displacement in all directions. The Taylor deformability parameter, Δ, was defined as $(D_{max}-D_{min})/(D_{max}+D_{min})$ as detailed previously.[126]

2.13 Data Analysis and Statistics

For all studies, all data points were included in the analyses and no outliers were excluded in calculations of means or statistical significance. Data are plotted with standard error bars and analyzed with the statistical test indicated in figure legends. In general, (*) indicates $p<0.05$, (**) indicates $p<0.01$, (***) indicates $p<0.001$, and (****) indicates $p<0.0001$, unless

otherwise specified in the figure legend. A lack of asterisks denotes that the difference is not significant (n.s).

Rheometry data represents 3 different bulk hydrogels each, with at least 15 data points from each individual hydrogel. ESR experiments were repeated in triplicate for each condition. The loading of NPs was measured for 2 different batches of hydrogels fabricated. THP-1 uptake studies were performed in duplicate. Characterization of HUVEC expression after activation is representative of three independent experiments from different cell isolations, with two technical replicates each. All PPFC flow experiment data is an average of 10 pictures from each individual experiment, with $N \geq 3$ blood donors for each group of data presented. Flow distribution experiments were repeated with N=3 blood donors for each perfusion condition. IVM results represent at least 4 mice per group, with at least 10 images of particle adhesion quantified from each mouse. For particle rolling in intravital microscopy, each group represents at least 4 mice, with at least 5 video locations per mouse. For the ALI and circulation time study, each data point represents N=4 mice, as with the circulation time data.

Chapter 3: Exploring Deformable Particles in Vascular-Targeted Drug Delivery: Softer is Only Sometimes Better

3.1 Publication Information

The majority of the work in this chapter is published as: **Fish, Margaret B.**, Catherine A. Fromen, Genesis Lopez-Cazares, Alexander W. Golinski, Timothy F. Scott, Reheman Adili, Michael Holinstat, and Omolola Eniola-Adefeso. "Exploring deformable particles in vascular-targeted drug delivery: Softer is only sometimes better." *Biomaterials* 124 (2017): 169-179.

3.2 Abstract

The ability of vascular-targeted drug carriers (VTCs) to localize and bind to a targeted, diseased endothelium determines their overall clinical utility. Here, we investigate how particle modulus and size determine adhesion of VTCs to the vascular wall under physiological blood flow conditions. In general, microparticles (MPs) outperformed nanoparticles (NPs) in all experimental conditions tested. Our results indicate that MP modulus enhances particle adhesion in a shear-dependent manner. In low shear human blood flow profiles *in vitro*, low modulus particles showed favorable adhesion, while at high shear, rigid particles showed superior adhesion. This was confirmed *in vivo* by studying particle adhesion in venous shear profiles in a mouse model of mesenteric inflammation, where MP adhesion was 127% greater ($p<0.0001$) for low modulus particles compared to more rigid ones. Mechanistically, we establish that particle collisions with leukocytes drive these trends, rather than differences in particle deformation, localization, or detachment. Overall, this work demonstrates the importance of VTC modulus as

a design parameter for enhanced VTC interaction with vascular walls, and thus, contributes important knowledge for development of successful clinical theranostics with applications for many diseases.

3.3 Introduction

VTCs are particles designed to exploit differential surface protein expression in diseases involving the endothelium, for an increase in drug localization and corresponding decrease in off-target toxicity. The development and clinical approval of VTC systems could revolutionize the treatment of many common but therapeutically challenging diseases, including cancer and cardiovascular diseases. Recent consideration of VTC physical properties, including size, shape, and surface charge[1,11,37,127,128] has improved historically low targeted drug delivery efficiency. More recently,[15,104,129] The work presented here integrates these two lines of research to present a comprehensive study of the critical role of particle modulus on VTC targeting efficiency.

As VTCs traverse the vasculature, they must navigate complex blood flow to contact the endothelium, otherwise all targeting functionalities are negated. In blood flow, cells segregate into a concentrated red blood cell (RBC) core in the center, while white blood cells (WBCs) and platelets are excluded to the RBC-free layer (RBC-FL) to interact with endothelial cells (ECs). Hydrodynamic, heterogeneous collisions between blood components drive this segregation in flow.[40,130–132] The differences in cellular size and stiffness are often used to explain WBC and platelet margination, which, by definition, is the localization to ECs from bulk blood flow. RBCs have a Young's modulus of 26 ± 7 kPa; WBCs are an order of magnitude stiffer than RBCs and platelets are 2-5 times more rigid than RBCs.[133–136] It is vital that VTCs mimic this cellular margination process to interact with the designated endothelium and target effectively *in vivo*.

One way to achieve this is to control VTC size. Previous work has shown that optimal VTC size depends on the physical blood properties[43,137]; in human blood, 3 μm is the ideal diameter for spherical, rigid particles to maximally marginate to ECs as determined in *in vitro* flow assays.[46,113] Furthermore, rigid NPs demonstrate inefficient margination compared to MPs due to decreased localization to the vessel wall, resulting in low adhesion overall to targeted ECs.[46,138] Unfortunately, rigid MP VTCs may cause deleterious capillary occlusions and are impractical for clinical use. Thus, there is strong motivation to explore a modulus range of both MPs and NPs, with interest to circumvent possible capillary occlusions by MPs and to improve the poor margination dynamics of rigid NPs. Recent studies with varying modulus particles focus on the impact of particle modulus on *in vivo* circulation time, which does not necessarily translate to targeted adhesion.[39] There is a lack of research directly comparing an entire range of particle sizes and physiologically relevant VTC moduli for vascular targeting; there is a critical need for well-designed experiments to fill this gap.

To address this deficiency in the research field, we explore two sizes of four poly(ethylene glycol) (PEG)-based VTCs with a range of Young's moduli, spanning an order and a half of magnitude, including one modulus similar to that of WBCs and one to that of RBCs. We explore how particle modulus and size collectively dictate VTC efficacy based on a range of physiological blood flow conditions, by using particles fabricated with well-controlled surface ligand properties. Our data demonstrate that VTCs cannot be designed as "one size fits all", but rather, require the deliberate selection of VTC modulus based on known hemodynamics of the disease state. Importantly, this is the first study to report how VTC modulus directly affects the final, targeted adhesion of particles both *in vitro* and *in vivo*, providing an exciting and unique perspective on VTC engineering with potential to influence the future VTC system

development.

3.4 Results

Characterization of PEG-based hydrogel particles

We systemically varied fabrication conditions to synthesize hydrogel particles of varying modulus, as detailed in Figure 3.1. Reaction conditions for the PEG hydrogels are detailed here; we decreased the moduli from A to D by decreasing the hydrogel cross-linking density. The synthetic scheme for hydrogel polymerization is shown in Figure 3.1A-B. The *in situ* polymerization of hydrogel conditions B-D is shown in Figure 3.1C. Hydrogel condition A was omitted, as it was too rigid for the *in situ* rheometry. Complete polymerization for each condition, determined from the plateaus in the *in situ* polymerization curves, was achieved within several seconds; indeed, the onset of gelation was so rapid that the precise gel point, as determined by the crossover of the storage (G') and loss (G'') moduli,[139] could not be ascertained (Figure 3.2). We utilized a large excess of photoinitiator to ensure maximal polymerization; any unpolymerized monomer was washed out of the swollen hydrogels bulk samples and particles. As VTCs are employed in aqueous conditions of media or blood, the most relevant particle parameter is the swollen shear modulus, which varied over 1.2 orders of magnitude from 170,000 ± 40,000 Pa for condition A to 7,700 ± 300 Pa for condition D (Figure 3.1D). By design, hydrogel C closely matches WBC moduli while hydrogel D matches that of RBCs. The equilibrium swelling ratio (ESR, Figure 3.1E) is the characterization of the swelling properties of each bulk material type, is shown in both water and human blood plasma. When comparing hydrogel ESR in plasma and water, only hydrogel D showed a significant difference with $p<0.0001$. There were significant differences in ESR when comparing A with B-D. Figure 3.1F

details the calculated density, pore size, and young's modulus of each hydrogel type.[112]

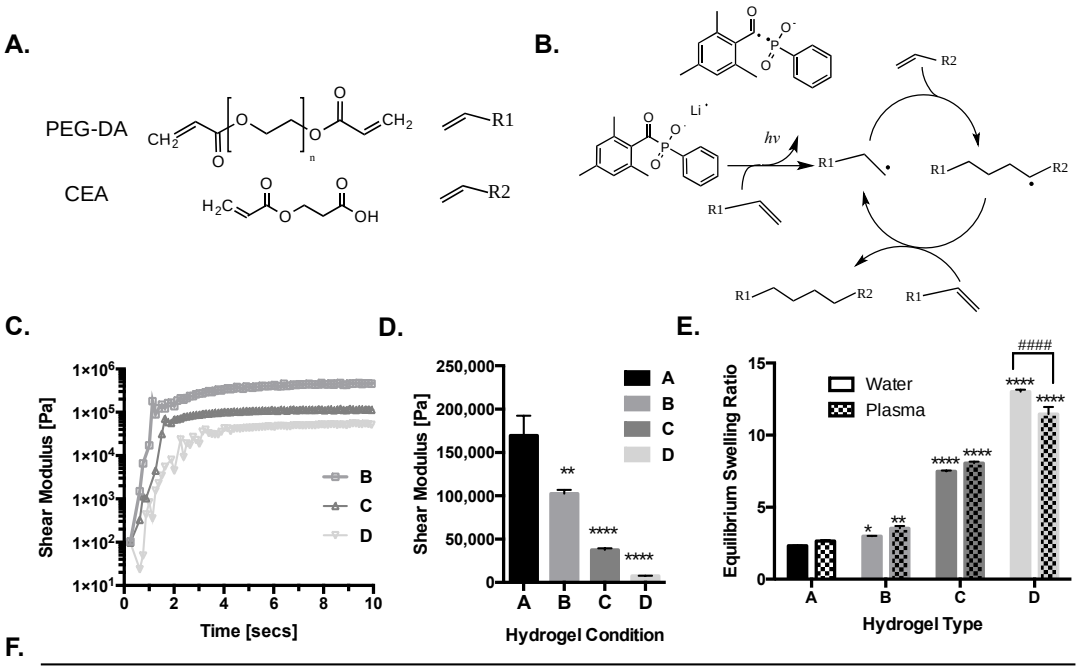

F.

Type	% Solids	% MeOH	% PEGDA	% CEA	% PI	Density (kg/m^3)	Pore Size (nm)[27]	Young's Modulus (Pa)
A	50 %	50 %	89	10	1	1051	0.376	508,300
B	40 %	60 %	89	10	1	1039	0.527	307,700
C	20 %	80 %	87	10	3	1017	1.318	113,000
D	15 %	85 %	86	10	4	1007	3.539	23,000

Figure 3.1 Hydrogel material properties.
(A) Designation of chemical moieties for synthetic scheme. (B) Synthetic scheme for lithium phenyl-2,4,6-trimethylbenzoylphosphinate photoinitiated polymerization of (poly)ethylene glycol diacrylate (PEGDA) and 2-carboxylethyl acrylate (CEA) as described in more detail in the SI. (C) *In situ* rheometry of particle conditions B, C, and D. Condition A too rigid to be tested *in situ*. (D) Swollen shear moduli of particle conditions A-D, statistics displayed represent comparison to A. (E) Equilibrium swelling ratios of particle conditions A-D, where (*s) indicate significance within hydrogel types to A and (#s) indicate difference between water and plasma. (F) Synthesis compositions and calculated bulk material properties of hydrogels.[112] Statistical analyses were performed using one- and two-way ANOVA with Fisher's Least Significant Difference (LSD) test, where (*) indicates $p<0.05$, (**) indicates $p<0.01$, and (***) indicates $p<0.001$, (****) indicates $p<0.0$-01 and (####) indicates $p<0.0001$. Error bars represent standard error.

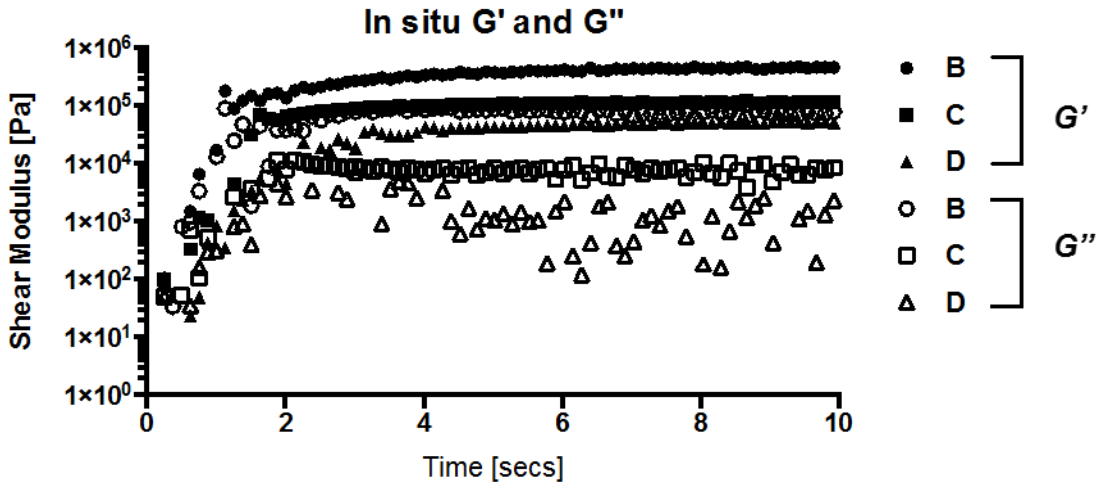

Figure 3.2 Additional rheological data.
Representative G' and G'' curves for *in situ* polymerization. G' is the storage modulus and relates to elastic modulus (closed symbols), while G'' is the loss modulus, and relates to the viscosity of the fluid being polymerized (open symbols).

Having characterized the bulk materials, hydrogel particles of either 2 μm or 500 nm in diameter were fabricated, using the conditions shown in Figure 3.1F. Figure 3.3 is a schematic of the hydrogel particle fabrication protocol as further explained in the methods chapter. Resulting particles were sized using dynamic light scattering (DLS) and scanning electron microscopy (SEM). Figure 3.4A details the resultant zeta potential (ZP) for all particle conditions, ranging from -23 mV to -32 mV, attributable to the 2-carboxyethyl acrylate (CEA) incorporated into the polymer backbone. Figure 3.4B-C show representative scanning electron microscopy (SEM) images of hydrogel particles; the clustering is a function of being dried for imaging. Particles within both size groups were found to be spherical and reasonably monodisperse after purification. There were no notable differences observed between particle A and D morphology as demonstrated in the scanning electron micrographs in Figure 3.4D-E.

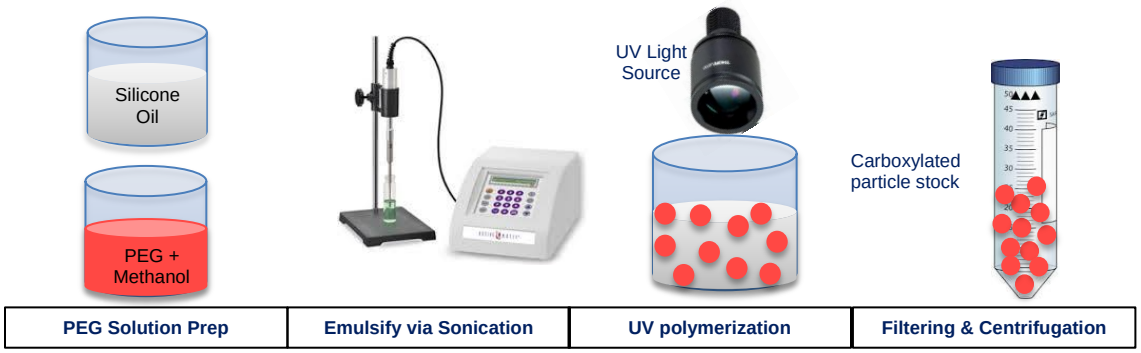

Figure 3.3 Schematic of hydrogel particle fabrication technique.
PEG precursor solution dissolved in methanol is emulsified using a probe sonicator. The emulsion is exposed to 365 nm light to initiate photopolymerization. Filtering and centrifugation, as detailed in materials and methods, completed the synthesis of monodisperse hydrogel particles.

A.

Particle	Label	D Actual	PDI	ZP (mV)
A	2 µm	2.14 µm	0.11	-32.97 ± 2.01
B	2 µm	2.02 µm	0.05	-27.76 ± 0.65
C	2 µm	1.86 µm	0.14	-23.07 ± 0.60
D	2 µm	1.94 µm	0.08	-29.67 ± 0.72
A	500 nm	519.2 nm	0.21	-27.33 ± 0.96
B	500 nm	483.7 nm	0.24	-25.60 ± 0.52
C	500 nm	505.4 nm	0.14	-29.47 ± 0.91
D	500 nm	487.1 nm	0.16	-27.67 ± 0.91

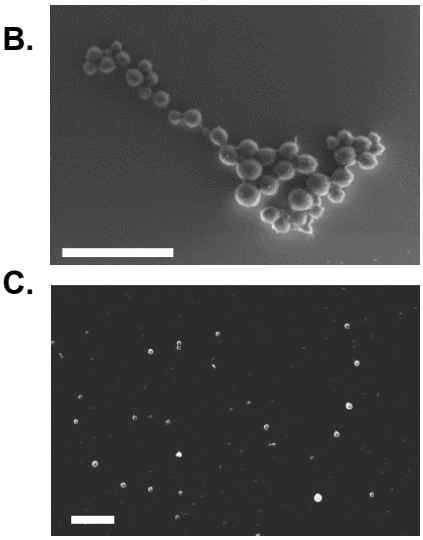

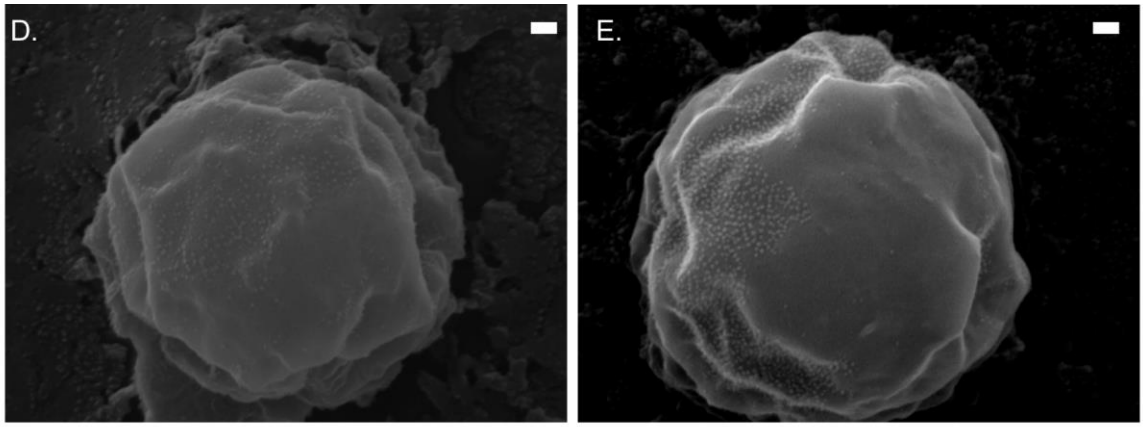

Figure 3.4 Hydrogel particle properties.
(A) Diameter, PDI and ZP measurements for fabricated hydrogel particles +/- standard deviation. Representative scanning electron microscopy (SEM) image of dried (B) 2 µm and (C) 500 nm hydrogel condition A particles, scale bars are 5 µm. Representative scanning electron micrographs at 50,000 X magnification of (D) Hydrogel particle type A and (E) D. Scale bars are 100 nm in length.

Phagocytic uptake of particles *in vitro* is a predictive technique of particle clearance rate *in vivo.* In general, cells phagocytose rigid particles more rapidly than more deformable counterparts. THP-1 uptake of both 500 nm and 2 µm hydrogels of all particle conditions confirmed previously observed trends in the literature,[39,129] specifically that rigid particles were

more readily phagocytosed, and thus, the rate of particle uptake by THP-1 cells decreased from particle A through particle D (Figure 3.5).

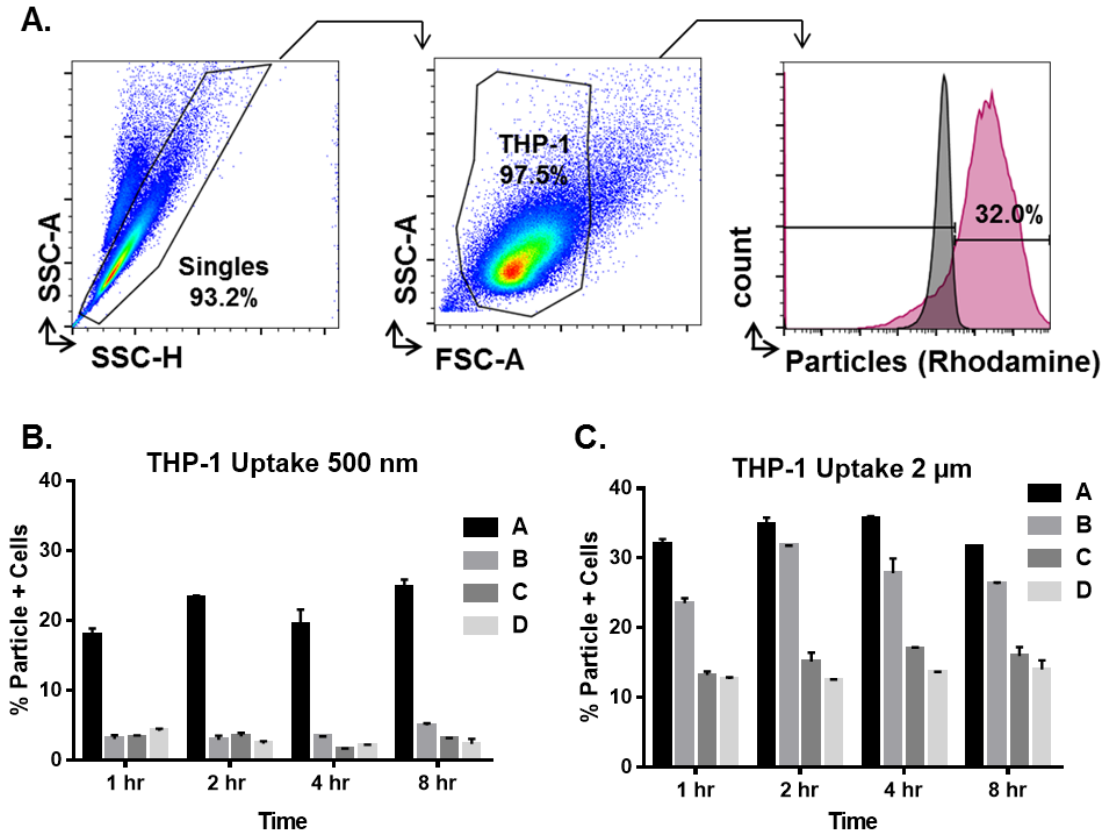

Figure 3.5 Cell uptake of hydrogel particles over time.
THP-1 cell uptake of particles over time as determined by % particle positive cells via flow cytometry. (A) Representative gating of THP-1 uptake. Single cells identified by forward (FSC) and side (SSC), and positive signal in the BL2 Rhodamine/PE channel greater than the untreated (gray) identified particle positive cells (red). Cellular uptake of 500 nm (B) and 2 µm (C) hydrogel particles; error bars represent the standard error.

Modulus dictates hydrogel particle binding under shear in vitro

We first evaluated the impact of VTC deformability on adhesion to an inflamed EC monolayer from human blood flow in a parallel plate flow chamber (PPFC) to mimic binding in a human blood vessel. Human umbilical vein EC (HUVEC) monolayers were prepared and

activated with Interleukin-1β (IL-1β). Hydrogel (A-D) and control polystyrene (PS) particles were conjugated with ~1,000 sialyl Lewis^A (sLe^A) sites/μm^2. SLe^A is a carbohydrate that has high affinity for E-selectin, a molecule that is upregulated on EC monolayers during inflammation and is minimally expressed on healthy ECs. Particle adhesion density was evaluated at varying wall shear rates (WSRs) that represent a physiological range encountered in human vasculature.

Particle adhesion of targeted sLe^A 2 μm rigid PS and varied modulus hydrogel particles in human blood flow is shown in Figure 3.6A - C for WSRs of 200, 500, and 1,000 s^{-1}, respectively, with a particle concentration of 1x10^7 particles/mL. At 200 s^{-1}, 2 μm particle adhesion significantly increased with decreasing hydrogel modulus, with particles C and D showing a significant increase in adhesion (p=0.037 and 0.029, respectively) relative to the most rigid hydrogel particle, A. Adhesion of all hydrogel particles was not significantly different when compared to the PS control. At the intermediate WSR of 500 s^{-1}, there was no significant trend amongst the 2 μm hydrogel particles or PS control. However, at the high WSR of 1,000 s^{-1}, the 2 μm hydrogel adhesion trend flipped relative to the low shear trend; the more rigid hydrogel MPs adhered better than low modulus MPs. Hydrogel A showed significant 2.8 and 4.8 fold increases over C and D, with p=0.005 and 0.0008, respectively.

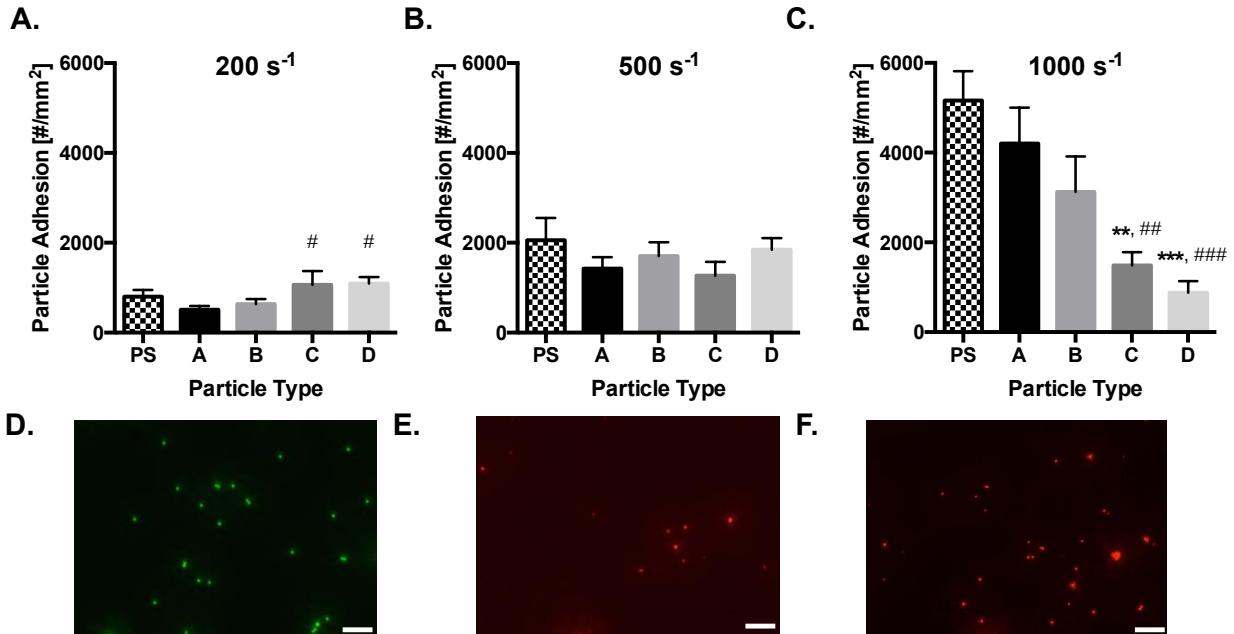

Figure 3.6 Particle adhesion to inflamed HUVEC monolayer as a function of particle modulus.

Quantified adhesion of 2 μm hydrogel particles at a wall shear rate of (A) 200 s^{-1}, (B) 500 s^{-1}, and (C) 1,000 s^{-1} by modulus after 5 minutes of laminar blood flow over an IL-1β activated HUVEC monolayer. N=3-6 human blood donors per particle condition. Statistical analysis of adherent density was performed using one-way ANOVA with Fisher's LSD test between all particle adhesion conditions. (*) Represent comparison to PS and ($^{\#}$) represents comparison to particle type A. (*) indicates $p<0.05$, (**) indicates $p<0.01$, and (***) indicates $p<0.001$. Error bars represent standard error. Representative fluorescent images of 2 μm (D) PS, (E) Hydrogel A, and (F) Hydrogel D particles bound to IL-1β activated HUVEC under a WSR of 200 s^{-1} *in vitro*. Scale bars are 20 μm.

We then probed the importance of size on the observed trends in our PPFC adhesion assays. Particles of the equivalent moduli, but of 500 nm diameter, were evaluated in the same manner. Notably, a concentration of $1x10^8$ particles/mL was evaluated in order to observe significant particle adhesion, which is an order of magnitude larger than the concentration evaluated for 2 μm particles. At all WSRs, the rigid PS control performed significantly better than all hydrogel particle types (Figure 3.7). There were no significant differences amongst the 500 nm hydrogel particles.

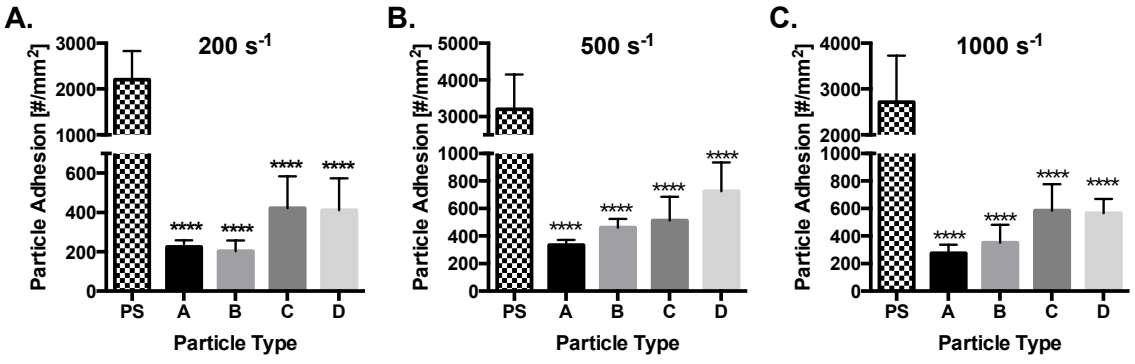

Figure 3.7 500 nm particle adhesion to inflamed HUVEC monolayer as a function of particle modulus.
Quantified adhesion of hydrogel particles at a wall shear rate of (A) 200 s^{-1}, (B) 500 s^{-1}, and (C) 1,000 s^{-1} by modulus after 5 minutes of laminar blood flow over an IL-1β activated HUVEC monolayer at 1×10^8 particles/mL. N=3-6 human blood donors per particle condition. Statistical analysis of adherent density was performed using one-way ANOVA with Fisher's LSD test between all particle adhesion conditions. (*) Represent comparison to PS where (*) indicates $p<0.05$, (**) indicates $p<0.01$, and (***) indicates $p<0.001$. There were no significant differences amongst hydrogel particle types A-D within any wall shear rate. Error bars represent standard error.

For both particle sizes, increasing the WSR resulted in increased total particle adhesion. However, at higher WSR, more particles travel through the PPFC in the fixed 5 minute experiment time, thus, adhesion trends were normalized by the total number of particles perfused thorough the PPFC, resulting in adhesion efficiency shown in Figure 3.8. From these results, we observe that even at a lower particle concentration, 2 μm particles were significantly more efficient in PPFC experiments compared to 500 nm particles, as was previously shown with PS.[46] For MPs, more rigid particles maintained their adhesion efficiency with increased WSR, while adhesion efficiency statistically significantly decreased for the low modulus conditions at higher WSRs. Together, these data indicate that targeted vascular wall adhesion of low modulus hydrogel MPs is heavily dependent on the imposed local blood flow WSR, which is physiologically pertinent, as blood shear varies widely throughout the body.

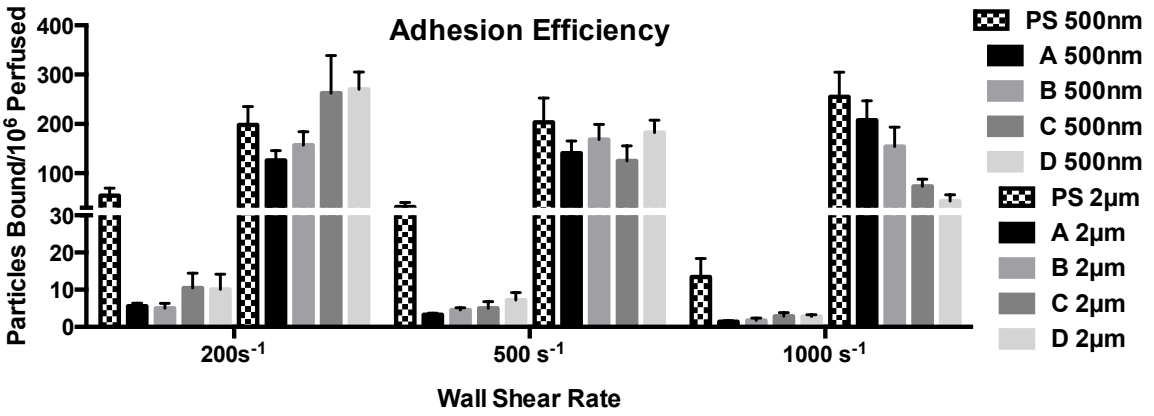

Figure 3.8 Particle adhesion normalized to the number perfused.
Data from Figure 3.6 and 3.7 normalized between particle concentration and shear rate. Data scaled by the number of particles perfused in human whole blood through the PPFC in 5 minutes and is represented as the number of particles bound per 10^6 particles perfused through the PPFC in whole blood. Error bars represent the standard error.

Low modulus particles produce superior adhesion in vivo

To confirm our *in vitro* trends, we next visualized actual targeted particle adhesion, in real time, to inflamed endothelium *in vivo* using a model of acute mesentery inflammation. Topical TNF-α results in inflammation and corresponding P-selectin expression within minutes of stimulation.[140,141] We explored extreme modulus conditions A and D and both particle diameters, 2 µm and 500 nm. All particles types were conjugated with the same surface density of anti-CD62P to ensure rapid, firm adhesion to the inflamed endothelium. Fluorescent hydrogel particles were dosed by equivalent mass and tracked real-time with fluorescent intravital microscopy. An experimental schematic is shown in Figure 3.9A, with representative images of 2 µm particle binding in mouse mesenteric veins shown in Figure 3.9B. All particles observed were firmly adhered to the inflamed mesenteric vein ECs due to the chosen ligand kinetics. Figure 3.9C shows the adhesion number of each particle type, scaled by the number of particles injected and the surface area of the examined vessels. Minimal adhesion of targeted hydrogels

was observed in non-inflamed vasculature, as shown in Video 3.1. Overall, the 2 µm particles adhered significantly more than the 500 nm particles, in line with our *in vitro* adhesion efficiencies. Figure 3.10 shows the number of each bound scaled by just the vessel surface area; particles were dosed by mass, corresponding to 64.5 times more NPs than MPs, yet NP particle adhesion by number was at most only 14 times more than MP adhesion by number. Thus, MPs demonstrated superior targeted particle adhesion than NPs for targeted applications *in vivo*. Interestingly, for both particle sizes, hydrogel D significantly outperformed hydrogel A, with observed 2.3 fold ($p<0.0001$) and 7.3 fold increases ($p=0.002$) for 2 µm and 500 nm, respectively. These results correspond to the trend observed *in vitro*; in the low WSR of the mesentery vein, particle D of lower modulus resulted in improved adhesion over stiffer particle A. High shear arteries were not evaluated *in vivo*, as the flow is pulsatile, and hence, not comparable to the *in vitro* laminar studies. Additionally, large high WSR arteries are not amenable to real-time intravital imaging, and thus, can only be evaluated posthumously, which represents widely varying conditions from those studied *in vitro*.

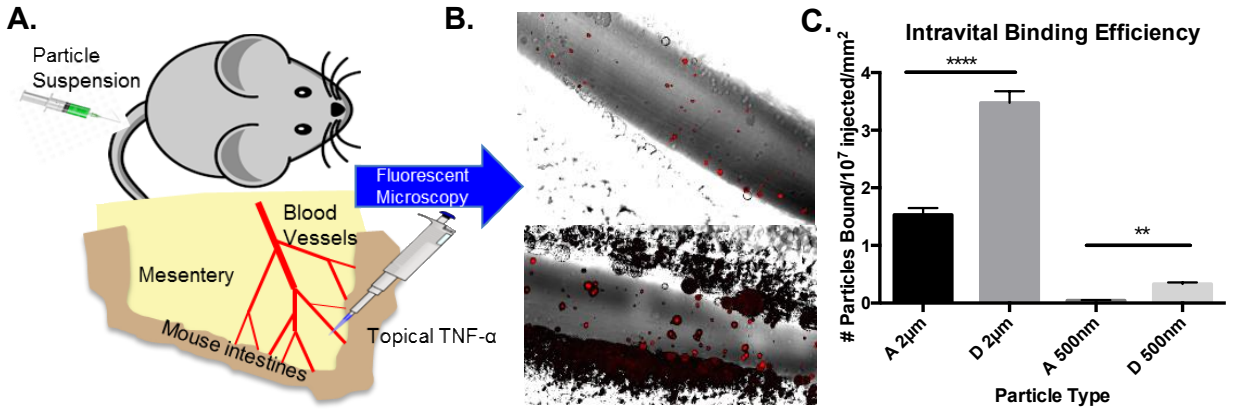

Figure 3.9 Particle adhesion to inflamed mesentery endothelium as a function of modulus and size.
(A) Schematic of mouse surgical technique for intravital imaging, as described in the methods. (B) Representative fluorescence images of particle adhesion to inflamed mesentery, images

correspond particles A-2µm and D-2µm (top to bottom). Particle fluorescence shown in red, overlaid on the bright field image. Scale bar is 50 µm. (C) Quantified adhesion efficiency of hydrogel particle conditions A-2µm, D-2µm, A-500nm, and D-500nm, scaled by vessel area, n = 4 mice per group. Statistical analysis was performed using one-way ANOVA with Fisher's LSD test within particle sizes. (**) indicates $p<0.01$ and (****) indicates $p<0.0001$. Error bars represent standard error.

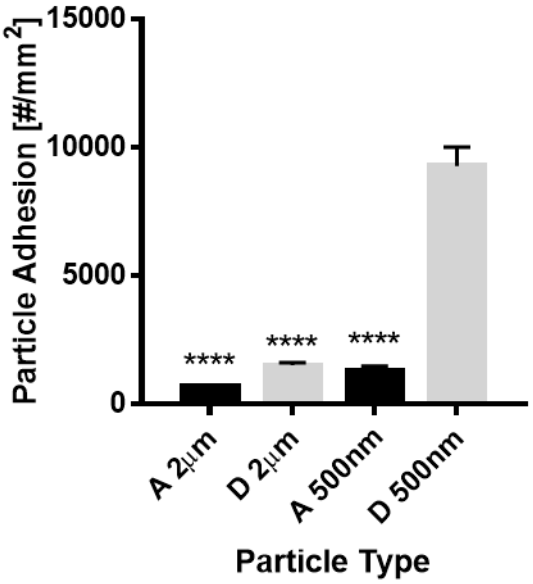

Figure 3.10 Mesentery particle adhesion by number.
Quantified adherent density by number of hydrogel particle conditions A-2µm, D-2µm, A-500nm, and D-500nm, n = 4 mice per group. Statistical analysis was performed using one-way ANOVA with Fisher's LSD. (*) Represent comparison to D 500nm and (****) indicates $p<0.0001$. Error bars represent standard error.

Evaluation of hydrogel deformability under physiological shear forces

We next sought to identify the major interactions driving the observed particle adhesion trends. Given that NPs showed low adhesion efficiency both *in vitro* and *in vivo* compared to MPs, we focused the subsequent evaluation to 2 µm particles. We investigated the bulk properties of each hydrogel material (A-D) under controlled rheometry shear inputs to estimate changes in hydrogel particle deformation produced by blood flow (Figure 3.11A). The input forces translate to the WSRs of our PPFC experiments, where 0.8 Pa and 4.0 Pa correspond to

WSR 200 s^{-1} to 1,000 s^{-1}, respectively. Figure 3.11A shows deformation responses linearly increasing with applied force. This linearity was maintained over a larger range of shear force applied by the rheometer (Figure 3.12A). Interestingly, the percent difference in strain between materials remained constant; material A deformed between 12-14% of the strain of hydrogel D at all applied shears, meaning there is a difference in how these particles will deform in fluid shear near the vascular wall. However, at the most physiologically extreme condition the magnitude of the % strain was less than 0.2%, indicating minimal deformation. These bulk property results were supported by our finite element analysis (FEA). We utilized the Taylor deformability parameter (Δ, defined in SI) as a way to quantify to FEA-modeled deformations. Particles A-D demonstrate minimal deformation within physiological fluid shear profiles, with FEA results showing indiscernible differences in particle shape and height (Figure 3.11B, force diagram in Figure 3.12B). Particle deformation results in a slight shrinkage of the particle height, meaning particle D will be shorter than particle A.[142,143] FEA modeling shows that these changes in height are small compared to the overall size of the particle, with $\Delta = 0.002$ corresponding to only an 8.02 nm decrease in particle D height at a WSR of 1,000 s^{-1} (4 Pa). This is in comparison to a 7.95 nm height decrease in particle A at the same shear rate (Δ=0.001993). Shear stresses of greater than 1,000 Pa would be needed to observe larger differences in deformation between particles; the most extreme condition presented in Figure 3.11B at 10 kPa results in a Δ=0.0039 for particle A and Δ=0.05 for particle D, corresponding to a decrease in height of 12.6 and 116 nm, respectively. Thus, these particles have the potential to significantly deform in shape due to shear forces, but do not exhibit these changes during fluid flow shears in our physiological system. To visualize the degree of particle deformation, element displacement of the inset sphere has been amplified by 2x. Thus, the continuous hydrogel particles studied here demonstrate

surprisingly small changes in their physical dimensions due to fluid induced shears, indicating that this phenomenon does not significantly contribute to the shear-based adhesion trends.

Next, we analyzed particle localization to the vessel wall from human blood flow using confocal microscopy to determine if differential particle distribution causes the variation in wall adhesion. Figure 3.11C shows the *in vitro* localization of each 2 µm hydrogel MP type A-D. Confocal images were taken at the wall of a PPFC while a mixture of human blood and particles were perfused. Figure 3.11C shows no significant differences between the wall localization of 2 µm hydrogel particles across the four moduli and three WSRs explored. These results indicate that differences in moduli did not translate to experimentally detectable changes in particle distribution to the wall from blood flow.

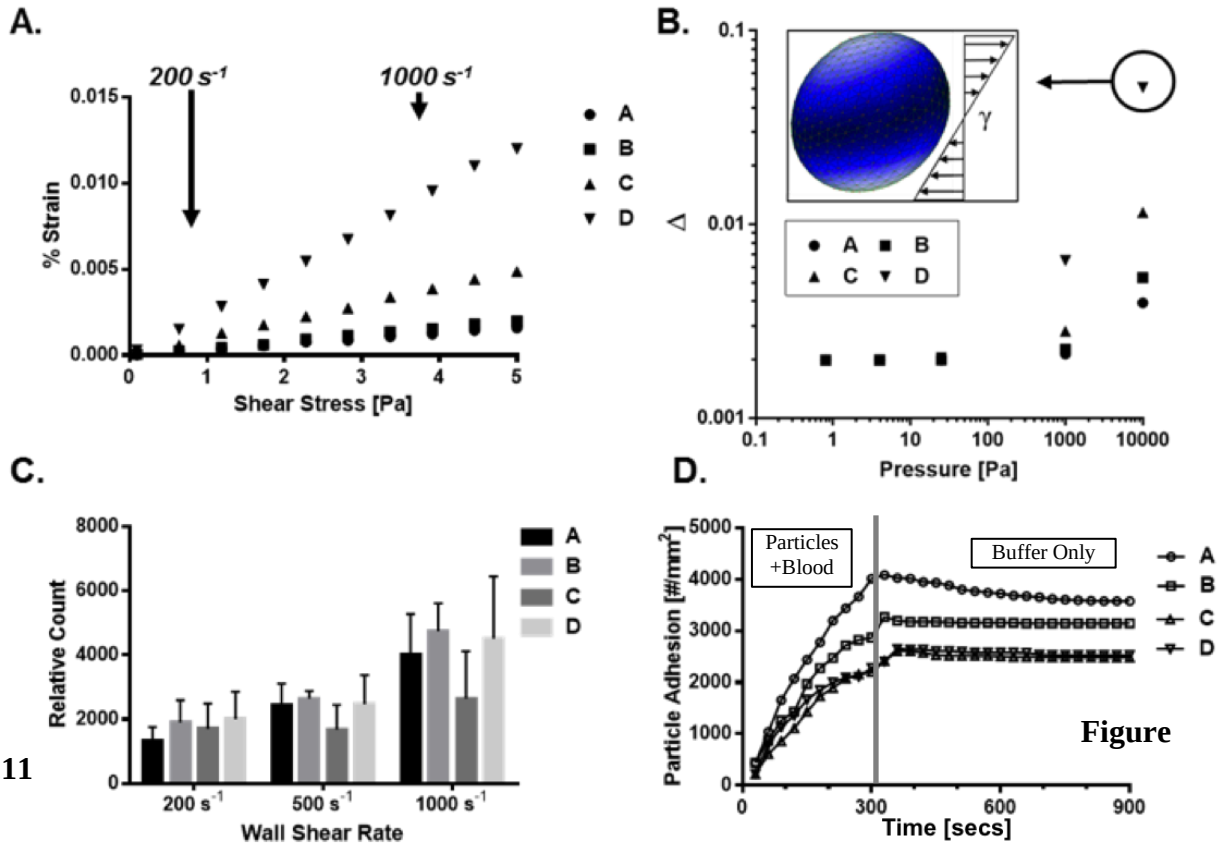

Figure 3.11

Hydrogel particle behavior under shear forces.
(A) Strain response of bulk hydrogels A-D at controlled, applied shear stress. Arrows represent corresponding wall shear rates. (B) Deformability parameter (Δ) determined by FEA for particles A-D under a range of shear forces. Inset shows applied shear force directions and representative particle deformation of particle D under the largest shear (circled) with an amplification factor of 2 to visualize deformation. (C) Localization of fluorescent hydrogel particles from human whole blood flow to the chamber wall. N = 3 human blood donors per particle condition. Statistical analysis was performed using two-way ANOVA with Fisher's LSD test between groups, resulting in non-significant differences at all shear rates. Error bars represent the standard error. (D) Representative rate of attachment and detachment to inflamed HUVECs at wall shear rates of 1000 s^{-1}. The first 300 seconds represent perfusion of whole human blood and hydrogel particles, while the remaining time represents perfusion of buffer without particles.

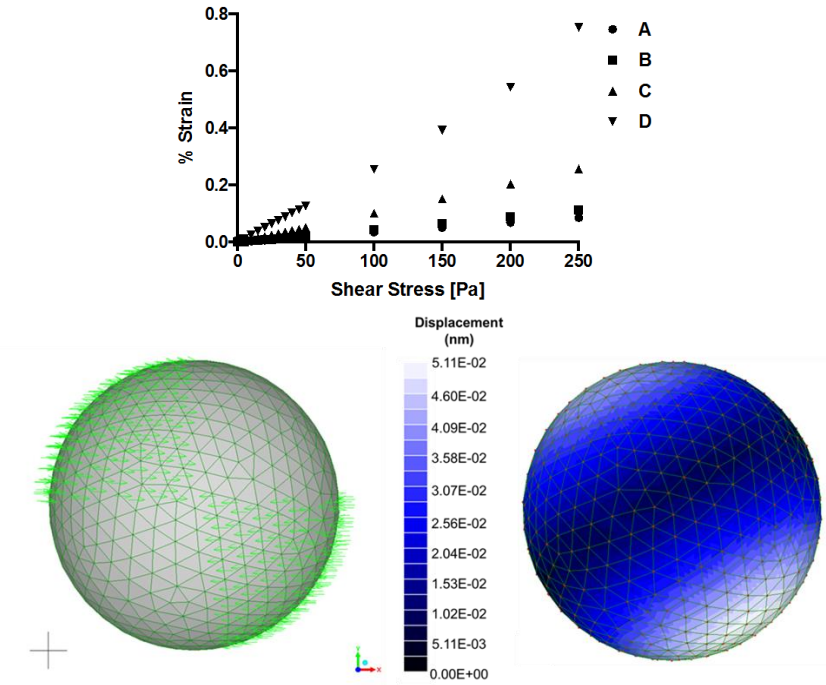

Figure 3.12 Strain response and FEA particle deformation under controlled shear stress.
Strain response of bulk hydrogels A-D over an extended range of controlled, applied stress. Stress responses remain linear far past physiologically relevant shear stresses. Schematic of applied pressure to deformable particle before and after applied forces. Sphere shown is 2 μm particle condition D with a Young's modulus of 23,000 Pa. Applied shear to indicated elements was $4x10^{-12}$ N/μm^2 (~WSR 1,000 s^{-1}) in +/- X direction. Shading represents surface element displacement, amplification factor 0.

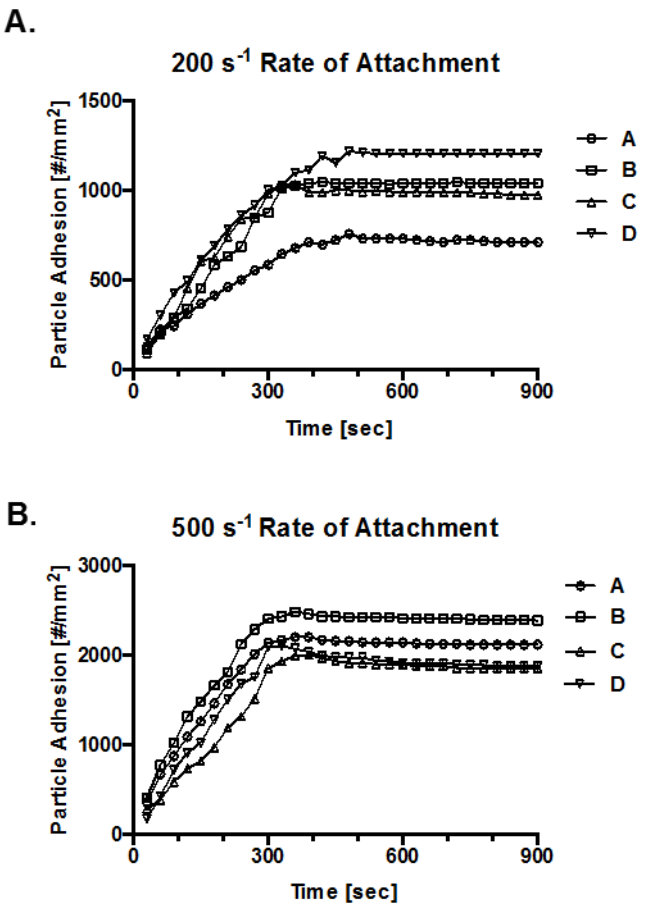

Figure 3.13 Rate of attachment in PPFC assay.
Representative displays of 2 µm particle rate of attachment and detachment to inflamed HUVECs at WSRs of (A) 200 s^{-1} and (B) 500 s^{-1}. The first 300 seconds represent perfusion of whole human blood and hydrogel particles, while the remaining time represents perfusion of buffer without any particles.

Another possible mechanism that could drive trends in PPFC adhesion by modulus is the adhesive force of hydrogel particles once present on the EC monolayer. This is indirectly represented in our data by the rate of attachment of 2 µm particles (Figure 3.11D). This plot displays the adhesion over time, captured every 30 secs, for each particle A-D at 1,000 s^{-1} WSR. A mixture of particles and blood were perfused through the PPFC for the first 5 minutes, after which, solely buffer was perfused. Figure 3.11D shows that for all 2 µm hydrogel particles A-D, there was a linear region of attachment, with only particle A showing detectable detachment in

the 10 minutes of buffer only flow. The rates of attachment for the other two WSRs are shown in Figure 3.13. The linear rate of attachment indicates dominating adhesion forces. Furthermore, this data demonstrates that even at our highest WSR, no significant number of hydrogel particles detached once adhered to the inflamed EC monolayer.

Removal of white blood cells eliminates adhesion trends

Given that discrepancies in particle deformation, localization, and rate of attachment did not together account for the observed significant trends in particle adhesion, we hypothesized that collisions with WBCs within the RBC-FL may contribute to the experimental phenomena. Importantly, WBCs will be present for all clinically relevant applications of VTCs, yet, we explored their removal from blood flow to better explain the shear dependence of hydrogel adhesion. We repeated PPFC experiments for 2 μm particles as in Figure 3.6, but with WBC depleted blood (RBC+plasma). With this blood medium, particle margination remains the same, while interactions between cells and particles within the RBC-FL are removed. As shown in Figure 3.14A-C, there were no significant differences in adhesion amongst the hydrogel particle types at any one WSR. This lack in adhesion trend compared to the whole blood experiments indicates that WBCs in the RBC-FL have a clear impact on targeted particle adhesion. To determine whether WBCs enhance or reduce particle adhesion, we subtracted RBC+plasma particle adhesion from that in whole blood (Figure 3.14D-F). In these plots, positive values denote that particle adhesion was greater in whole blood than in RBC+plasma, indicating that WBCs enhance particle adhesion; negative values indicate that WBCs reduced particle adhesion. WBCs in the RBC-FL had minimal to no impact on PS particle adhesion in low to intermediate shear but significantly enhanced PS adhesion at high WSR of 1,000 s^{-1}. WBCs in the RBC-FL

had either a neutral or enhancing impact on hydrogel particle adhesion. At 200s^{-1} (Figure 3.14D), WBCs had limited influence on hydrogels A and B, but enhanced particle adhesion for hydrogel particles C and D. At 500 s^{-1} (Figure 3.14E), WBCs enhanced particle adhesion for all hydrogel particles in a similar magnitude. A trend becomes pronounced at high shear (1,000 s^{-1}; Figure 3.14F), where collisions with WBCs in the RBC-FL helped rigid particles more than low modulus particles. Overall, the impact of WBCs in the RBC-FL was similarly shear dependent as adhesion trends in whole blood medium. Therefore, we can conclude that collisions with WBCs in the RBC-FL prescribe VTC adhesion trends by modulus.

To confirm that this effect was due to the presence of WBCs, and not the blood processing required to obtain RBCs+plasma, we compared the adhesion of 2 μm particles in 2 different blood media: whole blood and reconstituted blood. The reconstituted blood is simply whole blood processed as it would be to obtain RBCs+plasma, then recombined to have the WBCs present. For all particle types at 1000 s^{-1}, there was no significant difference between whole blood and reconstituted blood as show in Figure 3.15, further confirming that collisions with WBCs are producing the particle adhesion trends by modulus.

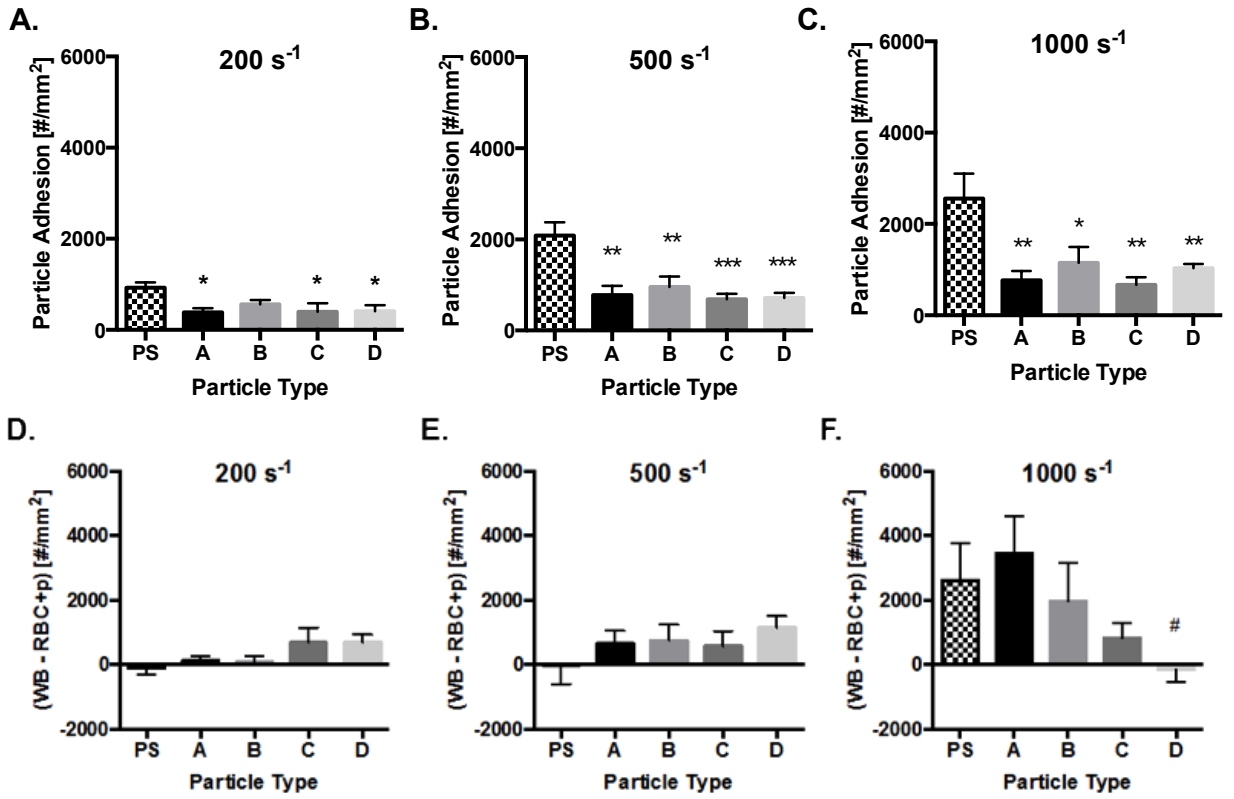

Figure 3.14 Particle adhesion in WBC depleted, RBC+plasma medium to inflamed HUVEC monolayer.

Quantified adhesion of 2 µm hydrogel particles in RBC+plasma at a wall shear rate of (A) 200 s^{-1}, (B) 500 s^{-1}, and (C) 1,000 s^{-1} by modulus after 5 minutes of laminar flow over an IL-1β activated HUVEC monolayer. N=3-6 human blood donors per particle condition in WBC depleted RBC+plasma medium. Particle adhesion in whole blood minus adhesion in RBC+plasma is quantified for (D) 200 s^{-1}, (E) 500 s^{-1}, (F) 1,000 s^{-1} by modulus. Positive values signify WBCs enhance particle binding in shear flow. Statistical analysis of adherent density was performed using one-way ANOVA with Fisher's LSD test between all particle adhesion conditions. (*) Represent comparison to PS and ($^{\#}$) represents comparison to particle type A. (*) indicates $p<0.05$, (**) indicates $p<0.01$, and (***) indicates $p<0.001$. Error bars represent standard error.

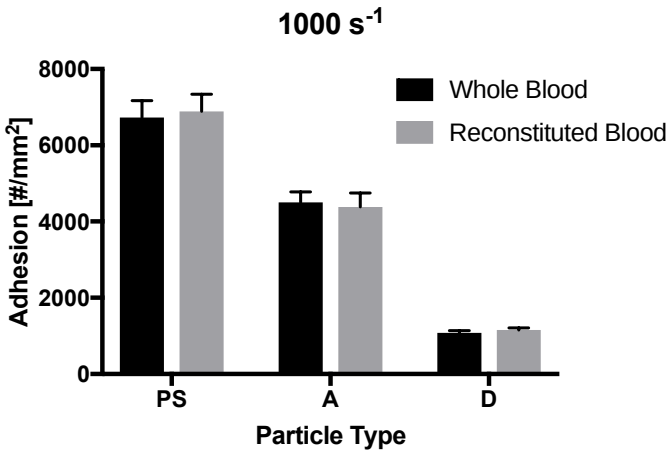

Figure 3.15 Particle adhesion in whole blood and reconstituted blood to inflamed HUVEC monolayer.
Quantified adhesion of 2 μm hydrogel particles in whole blood or reconstituted blood at a wall shear rate of 1000 s^{-1}. This data ensures that the processing of blood to obtain RBCs+plasma does not inherently alter particle behavior in the blood medium. All are non-significant between blood types.

3.5 Discussion

To date, no study has extensively evaluated the mechanism by which particle modulus affects vascular targeting and adhesion, especially for particles in the MP size range. As a crucial physical property of VTCs, this work suggests the importance of tuning the particle modulus based on local hemodynamics and provides exciting insights aimed at improving translation of VTC systems from the bench top to bedside. Our findings demonstrate the significance of fluid shear in prescribing the ideal modulus for micron-sized particles, shedding light on the importance of understanding physical transport mechanisms in the design of a VTC system. Previous computational work has predicted that the margination dynamics of particles of varying moduli will differ greatly.[135] While varied moduli particles have been explored for theranostic delivery applications *in vivo*[38,105,144–149], no study has directly evaluated the experimental margination and adhesion propensity of VTCs of varied moduli. Moreover, many previous

studies focus on a comparison between two particle moduli and the impact of particle modulus on *in vivo* circulation time, cellular uptake, and tissue biodistribution, which do not necessarily translate to targeted adhesion.[39] There is a critical need to thoroughly evaluate the impact of VTC modulus on the relevant biological transport and adhesion processes to maximize the benefits of vascular-targeted drug delivery.[128,150,151]

In this work, a range of particles (A-D) was fabricated using varied amounts of crosslinked PEG. PEG is routinely utilized in a wide range of biomedical applications for its known resistance to protein fouling, hydrophilicity, biocompatibility, and modularity for fabricating scaffolds with a custom range of moduli and functionalities.[96,97] Of note, covalently polymerized PEG particles are known to be highly stable under physiologic conditions.[152] Many studies have utilized PEG or derivatives to develop drug delivery vehicles, ranging in diameter from 30 nm[153] to over 10 μm and with Young's moduli as low as 200 Pa to as high as 3 MPa.[38,39,103] Furthermore, others have demonstrated that measurements of bulk hydrogel modulus is representative of the corresponding individual MP moduli, hence, our bulk rheometry can be used as a representation of our particle properties.[112] The bulk materials are well characterized in Figure 3.1 showing *in situ* rheometry, swollen rheometry, ESRs, and calculated bulk properties. Shown in Figure 3.1E, hydrogel D was the only material to exhibit differences in swelling between blood plasma and water, likely due to both the fact that D is the least cross-linked material and blood plasma has a higher osmolarity than water, thereby producing less swelling.[154] Our particles have well-characterized surface ligand densities, ensuring that all conclusions made here are due to physical properties rather than discrepancies in VTC surface ligand presentation. PS was included as an extremely rigid control for the varied moduli hydrogel particles, with an Elastic modulus of about 2 GPa, over 4 orders of magnitude more

rigid than hydrogel A.[155] However, we recognize that PS has different material properties than PEG, including increased hydrophobicity,[156] ZP, and more; it is well known that PS particles rapidly associate with and are taken up by phagocytes. Furthermore, these extremely rigid particles are known to occlude capillaries, particularly in the lung.[157] Lack of biocompatibility and these differences led to our exclusion of PS from *in vivo* experiments, where this would be most pronounced.

Our *in vitro* and *in vivo* adhesion results indicate that hydrogel MP VTCs are better suited for vascular adhesion than equivalent NP carriers. This corresponds to previously published studies with rigid particles, finding that micron-sized VTCs provide significantly superior vessel wall localization and EC adhesion compared to nano-sized. This is explained by superior exclusion of micron-sized particles out of the RBC-FL, similar to the reported near wall excess of white blood cells,[40,131] while nano-sized particles are suggested to co-localize with RBCs in the center of flow.[10,46] Previous work has demonstrated that deformable MPs can lead to increased circulation time and safe navigation of the vasculature.[38] Indeed, *in vivo* we did not observe tissue entrapment or capillary occlusion of 2 μm hydrogel particles, as has been shown with PS particles in the past.[157] Thus, our results demonstrate the utility of hydrogel MPs specifically for vascular targeting applications, combining improvements in both safety and efficiency. Overall, our results indicate that contributions of particle deformability and size, as well as the hemodynamics in the target vessel, dictate VTC targeting success.

For both sizes *in vivo*, particle D provided significantly elevated adhesion to the inflamed mesentery wall, compared to more rigid particle A (Figure 3.9C). Video 3.1 shows minimal adhesion of targeted particles to non-inflamed mesenteric vasculature via fluorescent intravital microscopy. These results align with a recent comparison of 200 nm targeted particles with

moduli of 10 kPa and 3 MPa, which showed improved targeting *in vivo* of the softer formulation.[39] A prevailing explanation for these trends suggests softer particles exhibit longer circulation time, leading to more opportunities to adhere to the target site. Indeed, it has been widely shown that lower modulus particles circulate longer *in vivo*, for their ability to avoid filtration and phagocytosis, as confirmed by our THP-1 uptake trends.[7,8,11,42,43] From our *in vivo* results alone, we cannot rule out this theory, as it is inherently challenging to decouple circulation time from particle modulus. However, our *in vitro* PPFC assay enables isolation of other physical factors, and supports the role of other contributing mechanisms at play.

Our *in vitro* work exposes an interesting phenomenon that the optimal modulus for 2 μm VTC adhesion is heavily dependent on the local shear profile. We utilized WSRs of 200, 500, and 1000 s^{-1}, which represent a physiological range of blood flow found in human post capillary venules and arterioles.[158,159] Namely, lower modulus PEG particles adhere with a higher efficiency compared to more rigid counterparts at low WSRs (200 s^{-1}), which was observed both *in vivo* in the inflamed mesentery model (Figure 3.9C) and *in vitro* in the PPFC assay (Figure 3.6A, 3.7A). However, at high shear, the softer particles lose this adhesion advantage. Interestingly, the lower modulus particles, C and D, behave like adherent WBCs, which also adhere less efficiently under high WSR compared to low WSR conditions.[160] These results are anticipated to be highly valuable for the engineering of VTCs; improving targeted adhesion by deliberately electing a particle modulus will facilitate the development of more efficient VTC systems.

We hypothesized that a mix of different phenomena, such as individual particle deformation at the wall, localization efficiency, particle adhesion strength, and collisions with WBCs may each contribute to collectively determine the VTC efficacy by modulus. Minimal

particle deformation under fluid shear flow unifies many of these results. According to our FEA simulations, minimal changes in particle deformation and height occurred for the hydrogels in flow, on the order of 8 nm or 0.4% of total diameter for particle D at the highest physiological WSR. This maximal deformation is small, with differences lacking between particle types. This indicates that particle deformation while in flow was not responsible for driving observed differences in vascular wall adhesion *in vitro*. Furthermore, the minimal deformation explains the lack of difference in localization amongst all particle types.[135,143] Deformable particles anti-marginate towards the centerline of flow, while more rigid particles marginate towards the chamber wall.[135,161] To produce observable differences in margination, particles must be highly deformable with capillary number (*Ca)* on the order of 0.3. Notably, a large *Ca* denotes a deformable particle, while smaller denotes a rigid particle; most computational papers assign Ca=0.3-0.5 for the "deformable particle" and Ca<0.2 for rigid particles.[135,142] The *Ca* for particle D, presumed as the largest, is 5.2×10^{-4}, a full 3 orders of magnitude smaller than the commonly studied and simulated range of modulus, indicating that particle deformation drives margination.

These results were initially unexpected; we had hypothesized that particles C and D would behave like WBCs and highly deformable RBCs, respectively, because of their matched bulk moduli. Yet, our particle C did not outperform particle D in all conditions studied. While cells are highly deformable, they are typically characterized by surface moduli and internal viscosity, rather than a uniform modulus. Conversely, hydrogel particles are considered as a continuous polymerized matrix and much better represented with a bulk, elastic modulus. This physical difference leads to particles, which, while not rigid, do not deform to the same extent as cells in fluid shears alone. However, other aspects of our study, in line with others' previous results, demonstrate that this range of particle modulus still has a considerable impact on cellular

interactions and dynamics in flow. Continuous hydrogel particles of this moduli range have considerably increased circulation time *in vivo*,[38,162] indicating the capacity to deform through narrow capillaries, as well as avoid immune clearance. Indeed, in our work, THP-1 phagocytic cells showed slower uptake rate of lower modulus particles, despite having proved that their shape does not significantly change in fluid flow (Figure 3.5). Furthermore, we observed evidence of particle deformation following adhesion at the vascular wall; the most rigid hydrogel A was the only particle that experienced noticeable detachment, designating weaker adhesive forces versus the other hydrogel particle types. Elongated, bound particles experienced a lower removal shear force once wall contact is made, as they were able to minimize their profile protruding in the direction orthogonal to blood flow and capitalize on increased adhesive bonds. Notably, the ligand-receptor pair chosen for these experiments is considered a catch-bond, which prolongs bond lifetime under increased shear force conditions.[163]

Interestingly, when WBCs were depleted from the blood medium, there were no clear particle adhesion trends as a function of WSR or VTC modulus (Figure 3.14A-C), matching the observations of particle localization. Though this result is surprising, it is key to note that WBCs will always be clinically present; these experiments simply provide insight into the mechanism of hydrogel particle behavior. We determined that the presence of WBCs in the RBC-FL overall increased hydrogel MP adhesion, even after the blood processing required to obtain reconstituted blood. We hypothesize that these results are a combination of competing effects between the frequency of collisions between WBCs and particles, and the force balance of the resulting collisions. The frequency of collisions will, in part, be dependent on the RBC-FL thickness, which increases with increasing WSR.[164] A larger RBC-FL means a decrease in number of collisions given a constant number of particles and WBCs. Following a collision, the

displacement of the colliding cell and particle will be dependent on the moduli, relative size of the two bodies, and the momentum involved in the collision. At low shear, the momentum of the collisions is not enough to produce differences in final particle adhesion to inflamed ECs compared to whole blood experiments. At intermediate WSR, collisions between more rigid hydrogels and WBCs result in larger lateral displacements towards the vessel wall, thus evening out overall adhesion in whole blood. At 1,000 s^{-1} WSR, the RBC-FL is largest, producing fewer collisions between particles and cells. Additionally, both the cells and particles have maximal momentum, resulting in larger translational displacements following each collision. As this transition to higher shear occurs, the increased displacement becomes a benefit for all hydrogel particles, but exceptionally more so for the rigid particles. More rigid particles conserve kinetic energy best and have the most elastic collisions. Though we showed that lower moduli particles do not significantly deform under fluid shear, they still produce more inelastic collisions due to viscous energy dissipation, and therefore, displace less efficiently to the vascular wall for targeted particle adhesion. Future analysis, including a computational evaluation of cell-particle collisions within the RBC-FL, are needed to verify the details of this mechanism; however, our data clearly support the hypothesis that collisions with WBCs can contribute to 2 μm particle adhesion as a function of the particle modulus.

3.6 Conclusions

The presented here is the first demonstration that the impact of VTC modulus depends on particle size and WSR. In combination with previous work from others demonstrating that low VTC modulus can increase circulation times, navigate capillaries, avoid immune clearance, and squeeze through pores, this work presents a comprehensive study of the role that particle

modulus and size play on key transport mechanisms required for targeted particle adhesion with direct applications in VTC systems. We show that MPs are more efficient than NPs in all *in vitro* and *in vivo* experimental conditions, regardless of modulus. The presented data show that for our particle conditions A-D, there is a small difference in particle deformation under prescribed shear forces, no detectable change in particle localization to the vascular wall, and relatively linear rate of attachments. Importantly, the presence of collisions with WBCs in the RBC-FL has a dramatic role in particle lateral margination, contact with the wall, and subsequent adhesion. Our findings indicate that the ideal modulus is highly dependent on local WSR, and that superior particle adhesion to inflamed venous ECs *in vivo* can be achieved with low modulus, hydrogel MP VTCs. These VTCs simultaneously overcome margination limitations of NP VTCs and occlusive potential of rigid micron-sized VTCs. Hydrogel particles capable of localizing to the endothelium have implications for a wide range of applications, including cancer, inflammation, and cardiovascular disease. Furthermore, the trends of hydrogel modulus varying with local WSR offers potential for customized therapeutics, based on disease and tissue hemodynamics; using these findings, VTC modulus can be tuned to target a plaque in a high shear vessel or venous disease in a low shear vessel. This unique work stresses the importance of modulus on targeted drug delivery, and strikingly demonstrates that one physical property can greatly alter VTC success, with possible implications for a wide range of diseases.

Chapter 4: Interplay of Ligand Kinetics and Particle Modulus for Understanding Adhesion Dynamics Under Physiological Flow Conditions

4.1 Publication Information

This data is not yet published. This chapter has been composed as a manuscript, which will be submitted to Langmuir in the coming weeks. The title will be as above, with the author list: **Fish, Margaret B.** and Omolola Eniola-Adefeso.

4.2 Abstract

The ability of vascular-targeted drug carriers (VTCs) to localize, interact with, and bind to a targeted, diseased endothelium determines the overall therapeutic functionality of the system. Nonetheless, little work has been done that simultaneously combines the study of the particle physical properties and surface ligand characteristics. Therefore, in this work, we investigate how particle modulus, ligand kinetics, ligand surface density, and hemodynamics (blood shear rate) interplay to determine the adhesion of VTCs to the vascular wall under physiological blood flow conditions. Specifically, we evaluated the adhesion of sialyl Lewis^A (sLe^A) and anti-intercellular adhesion molecule-1 (anti-ICAM-1)-coated rigid and deformable particles to activated endothelium from whole human blood flow. Of great clinical importance, utilizing an optimized ratio of these two targeting ligands equilibrated adhesion for particles of all moduli, signifying that particle modulus is no longer the dominating factor in determining VTC adhesion. This offers a route to improve the binding of low modulus particles at high shears

and that of high modulus particles at low shears. In general, as the wall shear rate and the corresponding shear removal forces increase, the site density for both sLe^A and anti-ICAM-1 particles becomes more deterministic in the final adhesion of the particles; the role of anti-ICAM-1 site density is more significant, likely due to different kinetics between the ligand types. The removal of leukocytes highlights how they interact with VTCs in hemodynamic flow to produce adhesion trends: for both ligands, lower site density particles are hindered by competition with leukocytes at the vascular wall, while higher site density particles are aided by the presence of leukocytes. Overall, this is the first work to demonstrate the interplay between ligand type, ligand density, and VTC modulus as critical design parameters for enhanced VTC adhesion to inflamed vascular walls. This information shows the importance in understanding the interplay of multiple VTC characteristics in the engineering of clinical theranostics with applications in inflammatory diseases.

4.3 Background

The concept of particulate drug delivery is to package systemically toxic drugs into biocompatible particle carriers capable of preferentially releasing active cargo to a diseased target cell population. VTCs are injectable particles designed to harness the differential expression of surface proteins on endothelial cells, and are engineered to have a high affinity for diseased areas of vasculature and low affinity elsewhere.[11] Ideally, this allows for both the protection of the cargo from degradation and clearance from the bloodstream *in vivo*, thereby lengthening the overall pharmacokinetic release profile from a single dose, while also increasing the total local therapeutic payload versus systemic exposure. The concept of VTCs has existed for decades, and yet, few systems have proven clinically viable;[165,166] VTCs, as a particulate

system, must deliver a significant benefit versus free drug in a therapeutic outcome to be clinically approved. There is still much work needed to fully understand and inform the engineering of each targeted system for maximal clinical utility.

Many critical biological processes need to take place for VTCs to provide tangible benefits over traditional free drug administration. Researchers have shown that size, shape, and surface charge of VTCs prescribe the blood circulation time and final biodistribution of both targeted and non-targeted systems, thereby altering the resulting treatment efficiency.[1,11,37,127] However, an additional critical requirement for VTCs is the ability to navigate complex blood flow to contact the endothelium; otherwise, targeted ligand-receptor adhesions cannot engage. Much work has been done to identify the properties of VTCs that directly affect the ability to localize and adhere from human blood flow, which is defined as margination, to produce targeted adhesion – this previous work highlights VTC size and shape as the most important parameters. Specifically, microparticles (MPs) having a diameter or equivalent spherical diameter, for rods and disks, in the 2-5 μm range are shown to marginate significantly better than those 500 nm and smaller.[46,113,138] Unfortunately, rigid MPs of this size may cause deleterious capillary occlusions, and thus, may be clinically impractical. This fact, combined with established benefits of deformable drug delivery particles, including increased circulation times and decreased immune recognition,[38,39] provides a strong motivation to explore a range of moduli for deformable MPs as VTCs. Recent work has shown that the binding of deformable particles is highly shear dependent, with more deformable particles adhering better at low blood shears and more rigid particles binding significantly better under high wall shears.[106] However, only one ligand-receptor system at one constant site density was utilized on the VTCs in this previous work. As such, it is conceivable that the previously reported deformable VTC adhesion trends are linked to

the specific ligand system explored. This work aims to elucidate how particle modulus and ligand kinetics interplay as critical VTC physical properties to prescribe resulting adhesion efficacy in physiological human blood flow, for application in the engineering of improved VTC systems with a multitude of clinical applications. More specifically, we aim to understand if at high shears, deformable VTC adhesion can be increased via ligand kinetics to match that of rigid particles. To date, no study has extensively evaluated the mechanism by which particle modulus affects vascular targeting and adhesion for different ligand types and kinetics, especially not for particles in the micron-size range. While many characteristics of VTCs have been individually studied, it is imperative to understand how multiple physical properties interplay to determine the final, targeted adhesion of deformable VTCs, to work toward more clinically translatable systems. Overall, there is a critical need to thoroughly understand the relevant biological transport and adhesion processes of VTCs to maximize the benefits of vascular-targeted drug delivery.[128,150,151]

In this study, we evaluated the coupled importance of ligand-receptor kinetics and particle deformability by targeting with sLe^A and anti-ICAM-1 antibody, which bind P/E-selectin and ICAM-1, respectively, on particles with a wide variation in bulk material modulus. These ligand-receptor systems are amongst ones that have been previously explored with rigid drug carriers to determine targeted adhesion *in vitro*.[167,168] We specifically chose these two ligand-receptor pairs because they represent different ligand kinetics. The forward (k_f) and reverse (k_r) rate constants of the association between sLe^A to E-selectin are approximately 27,000 $M^{-1}s^{-1}$ and 3 s^{-1}, respectively.[169] Those same rate constants for association between anti-ICAM-1 and ICAM-1 are known to be 156,000 $M^{-1}s^{-1}$ and 1.13 x 10^{-4} s^{-1}.[170] We used polystyrene (PS) and poly (ethylene glycol) (PEG)-based hydrogels to represent a range of rigid to deformable VTCs.

PS is often a model particle for targeted drug delivery research, used to study different particle parameters such as particle size, shape, and ligand kinetics.[46,113,122,171] Here we used it as a very rigid particle type. We found that as the blood wall shear rate (WSR) increases, more sites are needed in general to combat the blood shear removal forces. Deformable particles are more sensitive to increases in sLe^A surface site density whereas rigid particles are more sensitive to anti-ICAM-1 site density. White blood cell (WBC) involvement in dynamic blood flow is a major driver of particle adhesion, and has varying impacts based on both the wall shear rate and ligand kinetics. Overall, our work highlights the importance of understanding the interplay between physical properties of VTCs for successful translation into clinical applications.

4.4 Results and Discussion

Characterization of PEG-based hydrogel materials and particles

We varied hydrogel fabrication conditions to obtain particles with a broad range of moduli. Poly(ethylene glycol) diacrylate (PEGDA) comprised most the hydrogel, and 2-carboxylethyl acrylate (CEA) was added for its functional carboxylic acid handle. We fabricated and characterized a range of PEG-based particles (15%, 50% and 100% PEG) as previously described, with PS as an ultra-rigid control.[106] Figure 4.1A shows scanning electron micrographs of hydrogel particle types (i) 100% PEG, (ii) 50% PEG, and (iii) 15% PEG, which all look morphologically similar. We chose PEG because it is approved by the FDA and is routinely utilized in biomedical applications for its known biocompatibility, produced by its hydrophilicity and resulting resistance to protein adsorption.[96,97] Additionally, PEG is highly modular and allows fine control over material and end group properties; covalently polymerized PEG particles are highly stable under physiologic blood conditions.[152] Swollen modulus is the most

physiologically relevant measurement of these PEG-based materials. We fabricated bulk samples of each hydrogel type and probed the swollen shear modulus of each on an AR-G2 rheometer at 37°C. The shear moduli of these materials vary widely, as shown in Figure 4.1B. We fabricated particles of the same composition using an emulsion method, and Table 4.1 summarizes the fabrication conditions of each particle type and the resulting material properties, such as pore size.[112] Polystyrene (PS) is not included in the material characterization portion of this work because its material properties are widely known. For reference, the approximate shear modulus of bulk PS is 667,000 kPa, which is by far the most rigid particle utilized in this study.[155]

Table 4.1 Hydrogel Formulation and Calculated Material Properties

Label	% MeOH	% PEGDA	% CEA	% PI	Density (kg/m^3)	Pore Size (nm)[27]	Young's Modulus (Pa)
100% PEG	0	89	10	1	1228	0.139	2,526,800
50% PEG	50	89	10	1	1051	0.376	508,300
15% PEG	85	86	10	4	1007	3.539	23,000

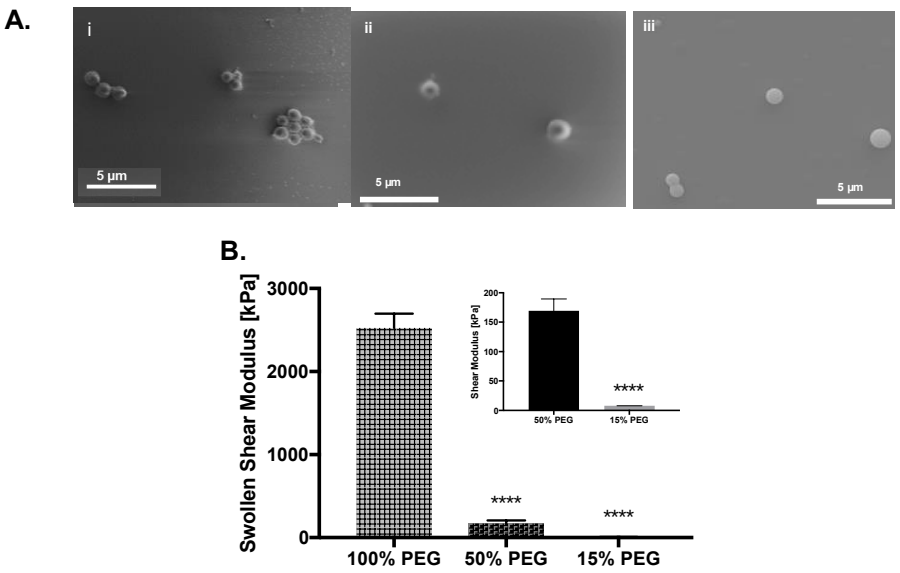

Figure 4.1 Hydrogel material and particle properties.
(A) Representative scanning electron micrographs of 2 µm hydrogel particles with (i) 100%, (ii) 50%, and (iii) 15% PEG composition respectively. Scale bars are 5 µm in length. (B) Swollen shear moduli of all hydrogel particle conditions; the inset better represents the difference between 50% and 15% PEG. Statistical analyses were performed using one-way ANOVA with Fisher's LSD test, where (****) indicates $p<0.0001$ versus 100% PEG for the main figure and versus 50% PEG for the inset. Error bars represent standard error.

Characterization of inflammatory markers on human umbilical vein endothelial cells (HUVECs)

A quantitative understanding of the EC expression of surface receptors is crucial to discern the ligand-receptor (LR) adhesion dynamics of VTCs, so we evaluated the leukocyte adhesion molecule (LAM) expression by HUVECs upon activation with Interleukin-1β (IL-1β). We quantified changes in E-selectin and ICAM-1 expression over time with flow cytometry, and the calculated site densities are shown in Figure 4.2A. Representative fluorescent staining of HUVEC monolayers is shown in Figure 4.2B. Maximal expression of E-selectin and ICAM-1 occurs at 4 hours and 24 hours, respectively, which is in line with previous reports of these molecules on HUVEC.[114,172,173] Of note, ICAM-1 is expressed approximately at double the surface density of E-selectin at these maximal activation times, providing a potential for more LR interactions per surface area. We used these time points of activation to evaluate the targeted

particle adhesion in a parallel plate flow chamber (PPFC) assay with human blood flow. *In vivo*, it is known that ICAM-1 is expressed at basal levels throughout the vasculature, and especially in the lung,[174,175] while E-selectin is not.[176,177] This is represented in our data in Figure 4.2A and is important to keep in mind the design of VTCs for applications *in vivo*.

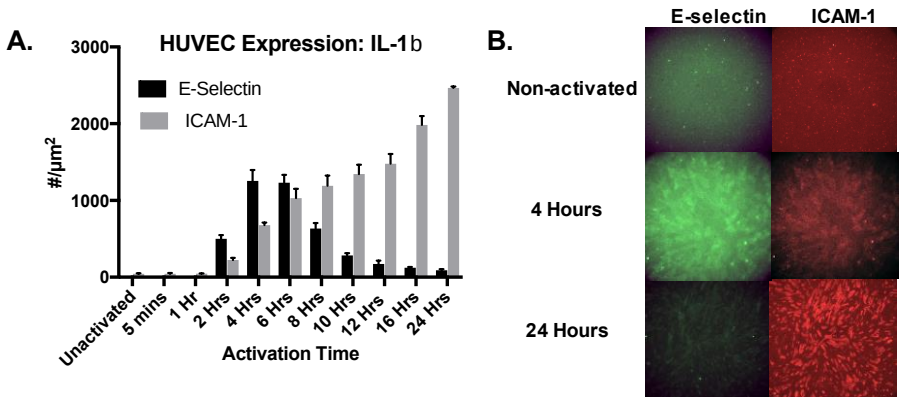

Figure 4.2 HUVEC expression profiles *in vitro*.
(A) Expression of E-selectin and ICAM-1 by endothelial cells in vitro upon activation with 1 ng/mL IL-1β, as quantified by flow cytometry. To calculate site density in # molecules/μm^2, we used D=15 μm for the cells and a calibration curve of standard beads. (B) Representative images of endothelial cells after activation and fluorescent staining. Statistical significances not shown.

Interplay of sLe^A density, particle modulus, and wall shear rate (WSR) dictates particle adhesion

Our previous work investigated the dynamics of sLe^A (a carbohydrate ligand to selectins)-coated hydrogels at a single site density, which showed some interesting dynamics regarding particle modulus. Deformable particles were more efficient at binding at low WSR, while rigid particles were significantly better at high WSR. [106] In this work, we explore the impact of ligand density on each of the four particle types to determine whether the same trends hold. We aim to determine if deformable particle binding can be increased to match that of rigid particles at high WSR by adding more adhesive forces. Specifically, we utilized our previously described PPFC blood flow assay to investigate the intersection of two particle physical properties on targeted adhesion, deformability and ligand kinetics. We did this by evaluating the

influence of sLe^A density in combination with bulk particle modulus on adhesion efficiency under physiological blood flow conditions. WSR was dictated by the blood volumetric flow rate, as detailed in the experimental section, and the concentration of particles was kept constant at 1 x 10^7/mL, so the total number of particles perfused through the chamber in the 5-minute experiment time inherently increased with WSR. Thus, we represented the data as adhesion efficiencies, which we defined as the number of particles bound per 10^6 perfused through the chamber per mm^2, so that we can compare adhesion with different WSRs head to head. In Figure 4.3, and in general, as the particle site density increases the potential adhesive force between the particle and HUVEC increases. As the WSR increases, the shear removal force on any bound particles increases. It is the balance of these two competing forces that determines the final adhesion efficiency of particles *in vitro*. Others have designated the point where the adhesive interaction of the particle is no longer sufficient to maintain binding adhesion with increasing WSR as the "critical WSR".[46] We define the "critical WSR" similarly, where the adhesion efficiency significantly decreases with increasing WSR, meaning the shear removal forces dominate the adhesive forces.

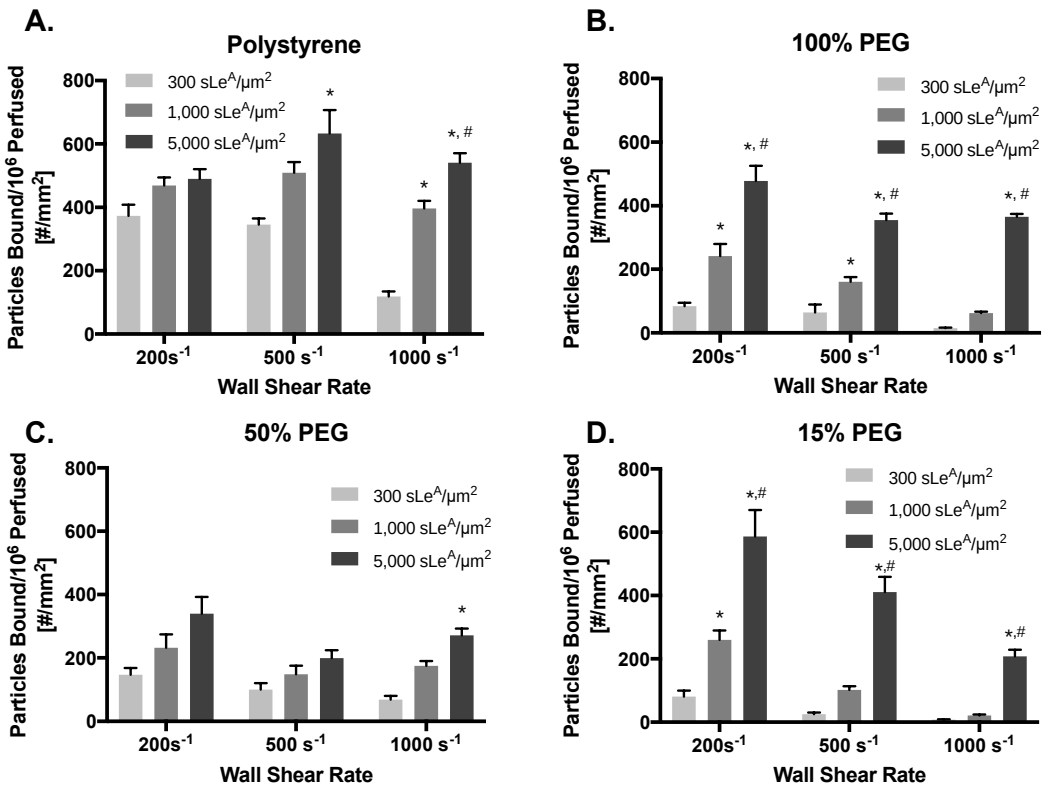

Figure 4.3 Particle adhesion efficiency to inflamed HUVEC monolayer as a function of particle sLe^A site density and modulus.
Quantified VTC adhesion grouped at 3 wall shear rates (200 s^{-1}, 500 s^{-1}, and 1,000 s^{-1}) by sLe^A site density and particle type: (A) PS, (B) 100% PEG, (C) 50% PEG, and (D) 15% PEG. Adhesion quantified after 5 minutes of laminar blood flow over a HUVEC monolayer activated with IL-1β for 4 hours. N=3 human blood donors per particle condition. Statistical analysis of adherent density was performed using one-way ANOVA with Fisher's LSD test. (*) indicates $p<0.01$ versus 300 sites/μm^2 and ($^{\#}$) indicates $p<0.01$ versus 1,000 sites/μm^2. Error bars represent standard error.

Figure 4.3 shows the adhesion efficiency of sLe^A-coated VTCs as a function of particle modulus, sLe^A density, and WSR. Importantly, there was minimal non-specific binding of non-targeted particles after 4 hours of activation, as shown in Figure 4.4A; though the HUVEC were activated, particles lacking targeting ligand showed minimal binding after 5 mins of perfusion in human blood flow. Therefore, it can be concluded that non-targeted adhesion is minimal in this experimental system. Here, in Figure 4.3, we directly compare how adding sLe^A site density affects overall adhesion at a constant WSR; in other words, we investigated how much more

adhesion could be obtained by increasing the adhesive force, with a constant shear removal force. This is of key interest for deformable particles at high WSR, as we aim to increase the adhesion to that of rigid VTCs with higher site densities.

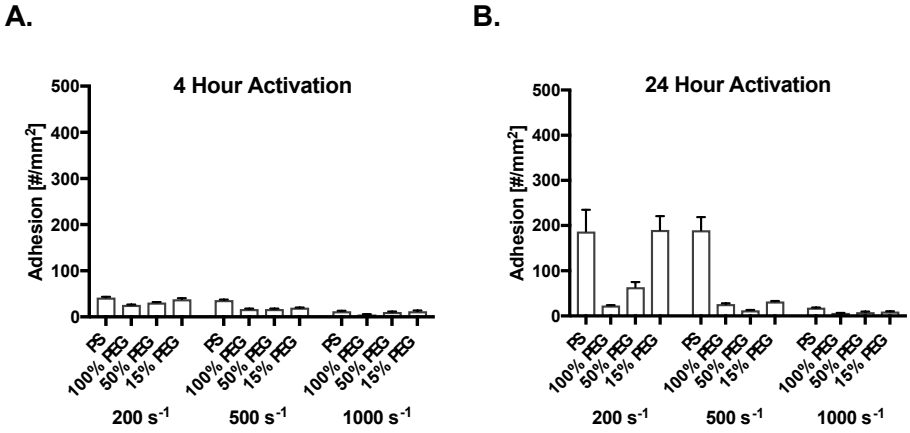

Figure 4.4 Non-targeted particle adhesion.
Quantified non-targeted VTC adhesion at 3 wall shear rates (200 s^{-1}, 500 s^{-1}, and 1,000 s^{-1}) by particle type after (A) 4 hours and (B) 24 hours of activation with IL-1β. Adhesion quantified after 5 minutes of laminar blood flow over an IL-1β activated HUVEC monolayer. N=3 human blood donors per particle condition.

We started with the most rigid PS particles, where increasing the sLe^A site density on particles did not significantly increase binding at the 200 s^{-1} WSR. At the intermediate WSR of 500 s^{-1}, an increase in site density from 300 to 5,000 sites/μm^2 delivered the only significant increase in binding. We also see that specifically at 1000 s^{-1}, this system is reaction-limited, rather than transport limited, because the overall adhesion efficiency continues to increase through the site densities tested. The data from Figure 4.3 is regrouped and plotted in Figure 4.5 to highlight different trends. In Figure 4.5, looking across different WSRs within each site density on PS, with 300 sLe^A sites/μm^2, the binding efficiency significantly decreased from the WSR of 500 s^{-1} to 1000 s^{-1}, suggesting a lack of adequate adhesive force at this site density, and

designating a critical WSR between 500 s^{-1} to 1000 s^{-1} (Figure 4.3A). With the boost of adhesive force delivered by increasing the site density from 300 sLe^A sites/μm^2 to 1,000 and 5,000 sLe^A sites/μm^2, the PS particles were able to maintain their adhesion efficiency with increasing WSR; no critical WSRs were identified for our experimental conditions.

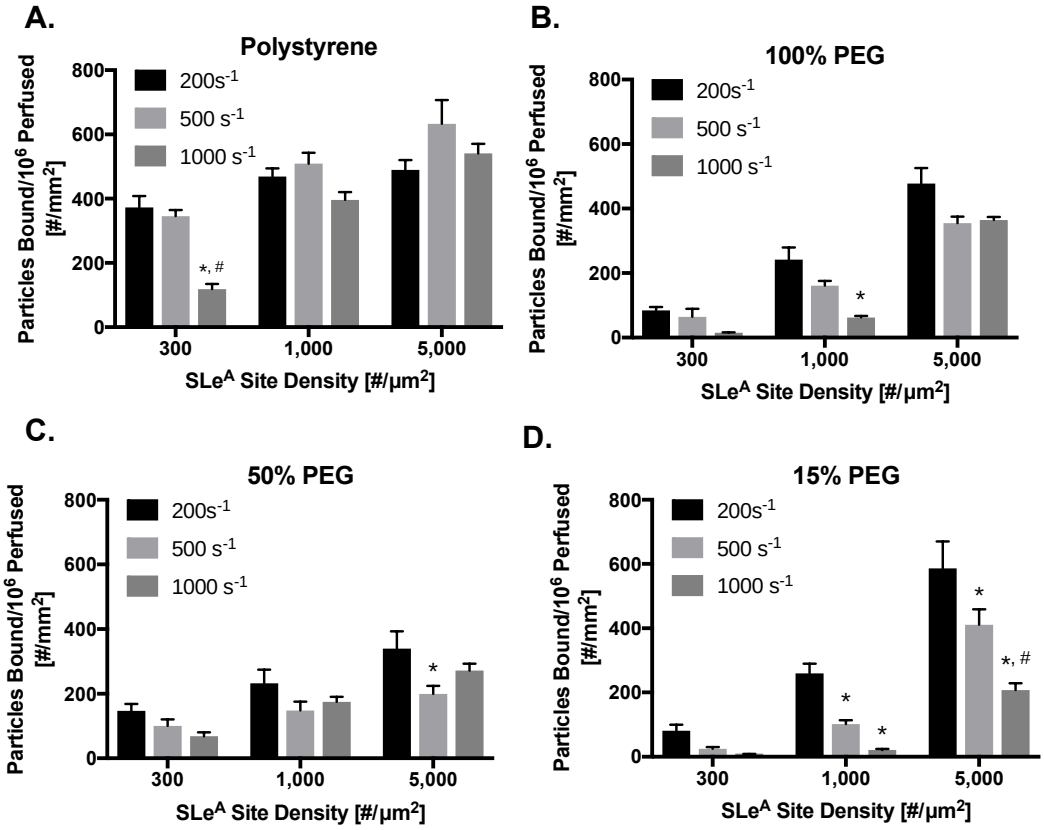

Figure 4.5 Particle adhesion efficiency to inflamed HUVEC monolayer as a function of particle sLe^A site density and modulus.
Quantified VTC adhesion at 3 wall shear rates (200 s^{-1}, 500 s^{-1}, and 1,000 s^{-1}) by sLe^A site density and particle type: (A) PS, (B) 100% PEG, (C) 50% PEG, and (D) 15% PEG. Adhesion quantified after 5 minutes of laminar blood flow over a HUVEC monolayer activated with IL-1β for 4 hours. N=3 human blood donors per particle condition. Statistical analysis of adhesion efficiency was performed using one-way ANOVA with Fisher's LSD test. (*) indicates $p<0.01$ versus 200 s^{-1} within each site density, while ($^{\#}$) indicates $p<0.01$ versus 500 s^{-1} within each site density. Error bars represent standard error.

For the 100% PEG particles (Figure 4.3B), each increase in site density at a constant WSR produced more binding, except for the increase to 1,000 sLe^A sites/μm^2 at 1000 s^{-1}, where more adhesive force was needed to combat shear removal forces. Compared to PS, the 100% PEG particles bound minimally at sLe^A low site densities. In Figure 4.5B, for the 100% PEG particles with 300 sLe^A sites/μm^2, the binding efficiency was generally low across all WSRs; thus, increasing WSRs did not reduce binding efficiency. At the 1,000 sites/μm^2, the 100% PEG particles binding efficiency decreased with increasing WSR, with a critical WSR between 500 s^{-1} and 1000 s^{-1} (Figure 4.5B). For 100% PEG particles, 5,000 sLe^A sites/μm^2 was enough adhesive force to maintain higher binding efficiency across WSRs

In Figure 4.3C, increasing the sLe^A site density for 50% PEG particles resulted in non-significant increases in particle adhesion for the 200 and 500 s^{-1} WSRs. At 1000 s^{-1} only the increase to 5,000 sLe^A sites/μm^2 resulted in significantly more binding. When considering one site density across different WSRs, for the 50% PEG particles in Figure 4.5C, the adhesion efficiency only decreased significantly with the 5,000 sites/μm^2 density for the WSR increase from 200 s^{-1} to 500 s^{-1} (Figure 4.5C).

Finally, in Figure 4.3D, on 15% PEG particles increasing site density to 5,000 sLe^A sites/μm^2 produced significantly more binding than both 300 and 1,000 sLe^A sites/μm^2. 300 sLe^A sites/μm^2 delivered minimal targeted binding, and at only 200 s^{-1} was 1,000 sites/μm^2 enough to significantly increase binding. The adhesion efficiency of 15% PEG particles decreased with increasing WSR for 1,000 and 5,000 sites/μm^2 site densities, as shown in Figure 4.5D. Therefore, for 15% PEG particles, a critical WSR exists between 200 s^{-1} and 500 s^{-1} for all 1,000 and 5,000 sites/μm^2 site densities.

In general, the more deformable the particles, the more detrimental increasing the WSR were for particle binding efficiency at the same site density, except one key deviation of 100% PEG particles with a site density of 1,000 $sLe^A/\mu m^2$, which were outperformed by the more deformable 50% PEG particles. Of note, this deviation does not arise with the anti-ICAM-1 targeted particles. We speculate that 50% PEG particles outperformed 100% PEG particles for a few possible different reasons. We previously concluded that particles are preferentially aided by WBCs under high WSR by more inelastic collisions which translate them towards the vascular wall; it is possible that such rigid particles with sLe^A on the surface may easily bounce away from the wall when translated in that direction, due to the further increased inelasticity of these particles compared to those in Chapter 3. Alternatively, it is possible that leukocytes more rapidly associate with and sweep away the more rigid hydrogel MPs under these hemodynamic conditions, and with 1000 $sLe^A/\mu m^2$, there is simply not enough adhesive force to counteract this process. Finally, as this is specific to sLe^A, it is key to note the catch-slip bond nature of the interaction between sLe^A and selectin receptors, often produces what is called the shear threshold effect, determining when cells bind firmly or roll.[178] For the 1,000 $sLe^A/\mu m^2$ at 1000 s^{-1}, the modulus of 50% PEG particles could offer an optimal interaction between the sLe^A and the selectin receptors, as compared to the 100% PEG particles, resulting in more firm adhesion.

Other than for this deviation, lower critical WSRs generally exist for more deformable particles. Overall, the more deformable particles, 15% PEG, require higher site densities to achieve significant binding at higher WSRs, in line with our previous data with a range of hydrogels from 15% PEG to 50% PEG that found that more rigid particles bind better at high WSRs (Figure 4.5).[106] While higher site density allows more 15% PEG particles to bind with near the efficiency of rigid, 50% and 100% PEG particles, adding more sLe^A was not enough to

equilibrate binding across all particle types. With higher sLe^A site densities these deformable particles are able to lessen the gap in adhesion at high WSR, though rigid particles remain significantly better except for the one deviation noted.

From previous work in Chapter 3, specifically Figure 3.11C, we know that particles of a broad range of moduli localize to the vascular wall equivalently;[106] therefore, the residence times of the particles on the vascular wall should be nearly equivalent for a fixed WSR. Thus, the trends in adhesion across particle moduli must be due other biophysical forces. We have previously shown that dynamic interactions with WBCs drive shear-dependent trends *in vitro*, where more rigid particles are preferentially collided towards the vessel wall.[106] There are a few different physical phenomena that could explain the observed trends. Particles of varying moduli have varying abilities to stretch once enough LR pairs are bound on the vessel wall to initiate adhesion. In the context of rigid VTC shape, it is widely known that elongated particles interact more efficiently with their target site in the presence of shear forces compared to spherical or non-elongated particles.[138,168,179,180] The smaller cross-sectional area normal to flow reduces the shear removal force imparted by blood flow that would remove a particle already adhered to the endothelial wall. Additionally, the larger, stretched footprint would allow for more LR pair interactions total to adhere. We know that particles of these moduli do not significantly deform in free blood flow,[106] but stretching could occur once bound to an inflamed wall. This data directly contradicts this argument. Indeed, these phenomena should lead to higher adhesion efficiencies for more deformable particles with the same or fewer targeting ligands. Clearly, this is not the case for 300 $sLe^A/\mu m^2$ across WSRs, or all site densities for that matter. Other possible phenomena that could produce these trends include the transport of particles to the vessel wall or varying rates of detachment of particles once adhesive contact is initiated. According to

computational literature, mechanical force imparted by blood shear on a LR bond would be less on a deformable particle, as the particle is able to stretch to absorb some of the force.[181] So if anything, rigid particles should detach more quickly, again contrary to our observed trends. Finally, it has been shown that leukocytes are able to roll effectively because of their deformable nature, whereas more rigid entities do not roll and have the tendency to wash away under flow. All of these possible physical explanations are contrary to our observed trends. We hypothesize and experimentally explore that this may arise due to the complex involvement of leukocytes, which are often overlooked in computational models. To elucidate the governing dynamics at play, we continued to explore the kinetics and hemodynamics of the VTC adhesion.

Interplay of anti-ICAM-1 density, particle modulus, and WSR dictates particle adhesion

To elucidate the importance of the kinetics on the particle surface, we investigated how utilizing anti-ICAM-1, with a significantly slower kinetic off rate than sLe^A, affects the adhesion efficiency of all four particle types. We sought to understand if deformable particles performed significantly worse than rigid VTCs with different ligand kinetics. Like the sLe^A experiments, PS and PEG particles were fitted with anti-ICAM-1 under the same physiological flow and total site densities (300, 1,000 and 5,000 sites/μm^2). We evaluated the adhesion efficiency of particles as the adhesive forces were fixed (site density) while the disruptive forces increased (WSR). Figure 4.6 shows the adhesion efficiency for 2 μm PS particles at a variety of anti-ICAM-1 site densities at a fixed WSR. HUVEC monolayers were activated for 24 hours for maximal ICAM-1 expression. There was minimal non-specific binding of non-targeted particles after 24 hours of activation as shown in Figure 4.4B, except for a few points at 200 s^{-1} and one at 500 s^{-1}. It is known that there are key differences in the cell surface protein expression after 24 hours, versus

4 hours, of activation by inflammatory cytokine, as detailed and quantified in Figure 4.2A. Therefore, we hypothesize that the higher non-targeted binding after 24 hours of activation is due to the higher affinity of our particles to this cell surface protein composition. This non-targeted adhesion highlights even further the diminished capacity for low site density of anti-ICAM-1 to produce any targeted binding.

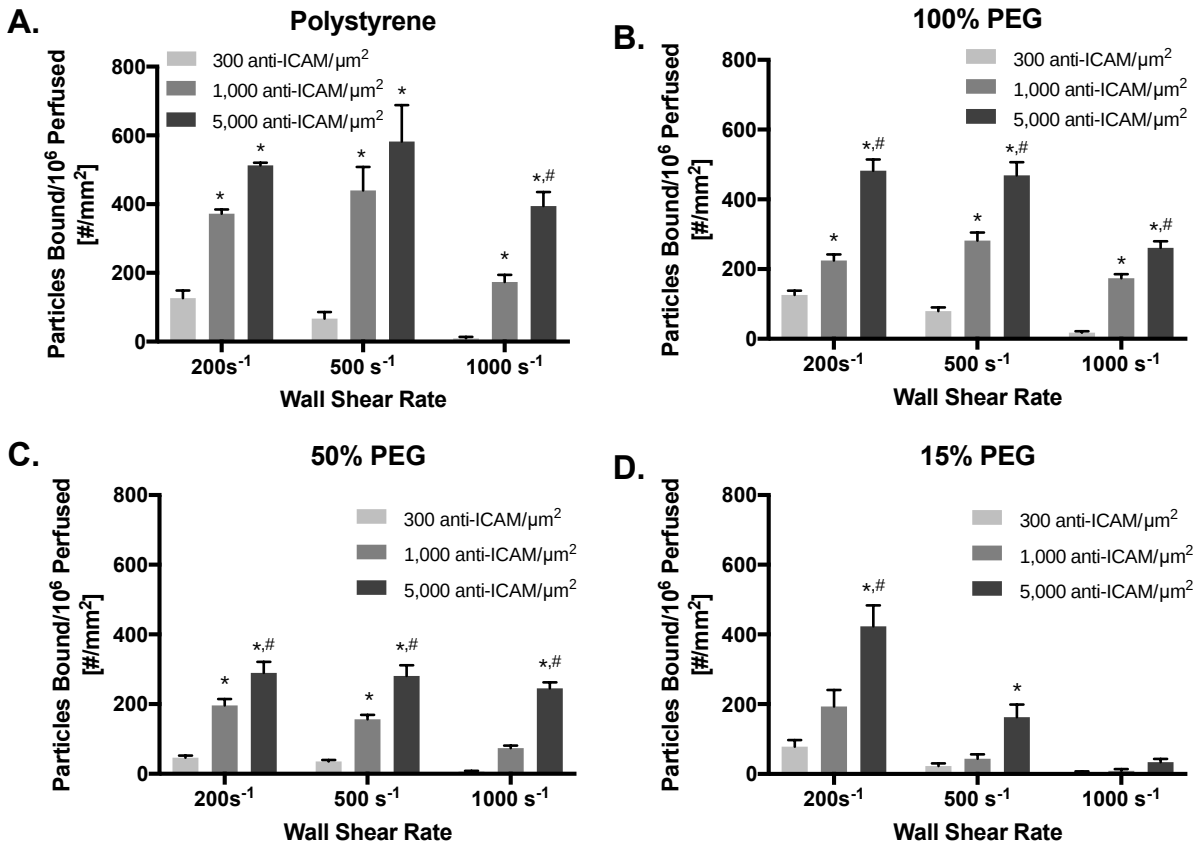

Figure 4.6 Particle adhesion efficiency to inflamed HUVEC monolayer as a function of particle anti-ICAM-1 site density and modulus.
Quantified VTC adhesion at 3 wall shear rates (200 s^{-1}, 500 s^{-1}, and 1,000 s^{-1}) by anti-ICAM-1 site density and particle type: (A) PS, (B) 100% PEG, (C) 50% PEG, and (D) 15% PEG. Adhesion quantified after 5 minutes of laminar blood flow over a HUVEC monolayer activated for 24 hours with IL-1β. N=3 human blood donors per particle condition. Statistical analysis of adherent density was performed using one-way ANOVA with Fisher's LSD test. (*) indicates $p<0.01$ versus 300 sites/μm^2 and ($^{\#}$) indicates $p<0.01$ versus 1,000 sites/μm^2. Error bars represent standard error.

The data is plotted and grouped by WSR in Figure 4.6. At 200 s^{-1}, PS adhesion increased significantly with increasing anti-ICAM-1 site density, which was not the case for the same particles with sLe^A, highlighting a key difference in ligand kinetics. Even at the low WSR of 200 s^{-1} more than 300 anti-ICAM-1/μm^2 is required to produce firm adhesion. The gain in adhesion efficiency by adding more sites onto PS increased with WSR; at 500 s^{-1}, both 1,000 and 5,000 sites/μm^2 were statistically higher than 300 anti-ICAM-1/μm^2. Overall, this demonstrated how as the shear removal force imparted by physiological blood flow increased, more adhesive force was required to achieve firm VTC binding. The same data as in Figure 4.6 is regrouped and plotted in 4.7. In Figure 4.7A, with both 300 anti-ICAM-1 sites/μm^2 and 1,000 anti-ICAM-1 sites/μm^2, as the WSR increases to 1000 s^{-1}, the binding significantly decreases, meaning the shear removal force dominated the adhesion forces and a critical WSR existed between 500 and 1000 s^{-1}. At the maximum site density of 5,000 anti-ICAM-1 sites/μm^2, PS adhesion efficiency is maintained through 1000 s^{-1}; this amount of adhesive force was never overcome by the increase in WSR and no critical WSR was identified.

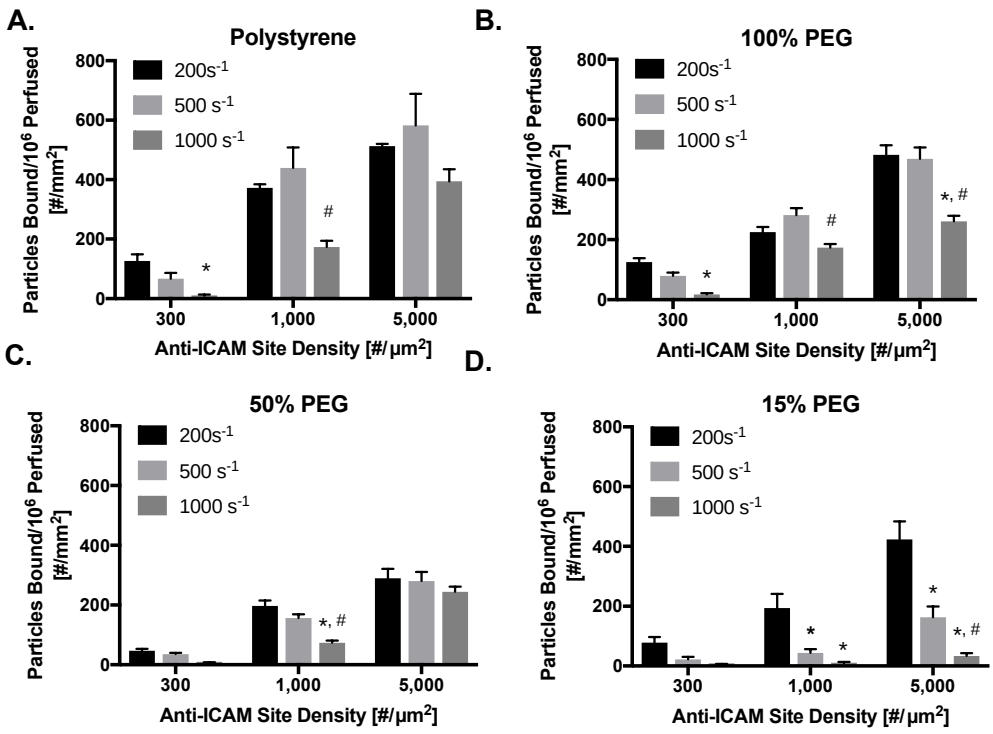

Figure 4.7 Particle adhesion efficiency to inflamed HUVEC monolayer as a function of particle anti-ICAM-1 site density and modulus.
Quantified VTC adhesion at 3 wall shear rates (200 s^{-1}, 500 s^{-1}, and 1,000 s^{-1}) by anti-ICAM-1 site density and particle type: (A) 100% PEG, (B) 50% PEG, and (C) 15% PEG. Adhesion quantified after 5 minutes of laminar blood flow over a HUVEC monolayer activated for 24 hours with IL-1β. N=3 human blood donors per particle condition. Statistical analysis of adherent density was performed using one-way ANOVA with Fisher's LSD test. (*) indicates $p<0.01$ versus 200 s^{-1} within each site density and ($^{\#}$) indicates $p<0.01$ versus 500 s^{-1} within each site density. Error bars represent standard error.

For the 100% PEG particles (Figure 4.6B), 5,000 sites/μm^2 were significantly more efficient than both 300 and 1,000 sites/μm^2 for all WSRs. This suggests that the addition of more sites was of a larger benefit to the 100% PEG particles than the PS particles, due to low adhesion efficiencies with 300 sites/μm^2. The 100% PEG particles in Figure 4.7B behaved similarly to the rigid PS particles, with a critical WSR identified for both 300 and 1,000 anti-ICAM-1/μm^2 between 500 s^{-1} and 1000 s^{-1}. The main deviation of 100% PEG from PS is with 5,000 anti-ICAM-1 sites/μm^2, we identified a critical WSR between 500 and 1000 s^{-1}.

The 50% PEG particles in Figure 4.6C exhibited similar statistical trends to 100% PEG particles across WSR and anti-ICAM-1 site densities, with the exception being at 1000 s^{-1} for 50% PEG particles, where the 1,000 sites/μm^2 density did not produce adhesion that was significantly better than 300 sites/μm^2. For 50% PEG particles in Figure 4.7C, there were no statistical changes in adhesion efficiency across WSR for both 300 and 5,000 anti-ICAM-1 sites/μm^2; for 300 sites/μm^2 this was due to low overall binding. For 1,000 anti-ICAM-1 sites/μm^2, binding efficiency decreased upon increase of WSR to 1000 s^{-1}, designating another critical WSR between 500 and 1000 s^{-1}. For the 5,000 sites/μm^2, there was no statistical change in binding obtained with increased WSR, due to the overall higher adhesive force between the particle and endothelial monolayer counteracting increases in shear removal forces.

In Figure 4.6D for 15% PEG particles, there were only statistical differences in adhesion between 300 and 5,000 anti-ICAM-1 sites/μm^2 at 200 and 500 s^{-1} and between 1,000 and 5,000 anti-ICAM-1 sites/μm^2 at 200 s^{-1}. At 1000 s^{-1} this most deformable particles minimally adhered across all antibody site densities evaluated. In Figure 4.7D, on 15% PEG particles there was no drop in adhesion efficiency with increased WSR with 300 anti-ICAM-1 sites/μm^2, again due to the very low adhesion efficiency at all WSRs. At the two higher anti-ICAM-1 densities of 1,000 and 5,000 sites/μm^2, adhesion efficiencies significantly decreased with each increased WSR, resulting in extremely low binding efficiencies observed at the 1000 s^{-1}, and critical WSRs between 200 s^{-1} and 500 s^{-1}.

As expected, more rigid particles adhered better at higher shear, as was observed with sLe^A conjugated particles in Figure 4.3. Increased anti-ICAM-1 site densities lessened the gap at high WSR, but did not fully equalize binding for all particle moduli; rigid particles remained superior at high WSRs as they did with sLe^A.[106] For all particle types and all WSRs, 300 anti-

ICAM-1 sites/μm^2 produced very low adhesion efficiencies, especially in comparison to particles targeted with the same ligand surface density, but with sLe^A. Again, this means that there is not sufficient adhesion force established to counteract the shear force of blood flow over the endothelial wall. Overall, the interplay of VTC modulus with targeting ligand site density was most prominent at the high WSR of 1000 s^{-1}, where generally more rigid particles adhered more efficiently. The raw adhesion of each particle type, not scaled to adhesion efficiency, can be found in Figures 4.8 and 4.9, for sLe^A and anti-ICAM-1 particles, respectively.

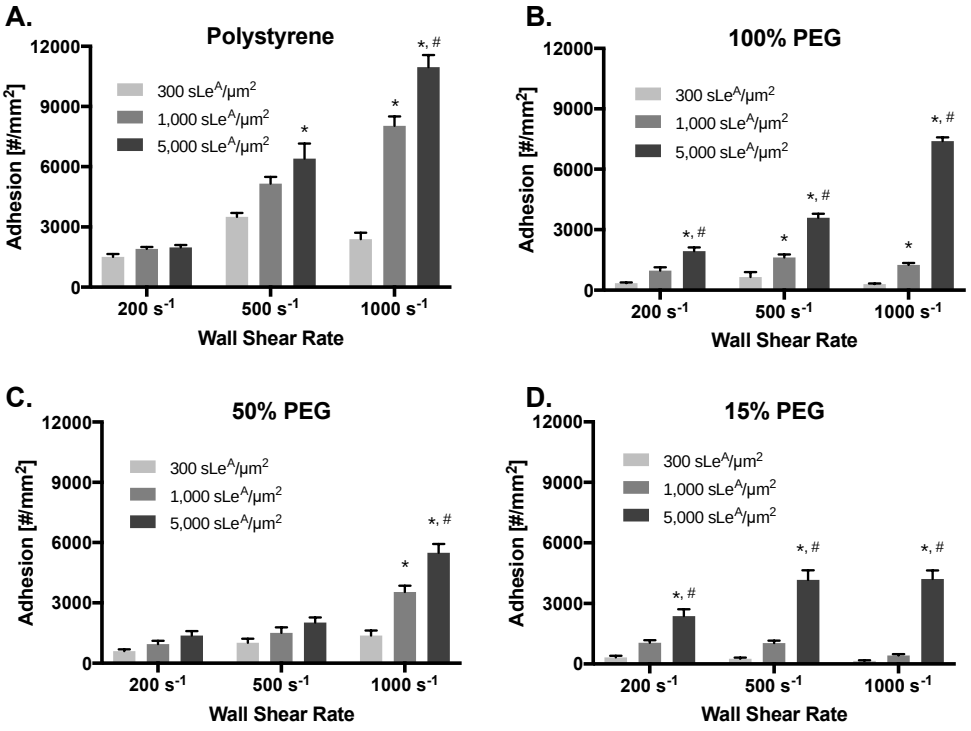

Figure 4.8 Raw particle adhesion to inflamed HUVEC monolayer as a function of particle sLe^A site density and modulus.
Quantified VTC adhesion at 3 wall shear rates (200 s^{-1}, 500 s^{-1}, and 1,000 s^{-1}) by sLe^A site density and particle type: (A) PS, (B) 100% PEG, (C) 50% PEG, and (D) 15% PEG. Adhesion quantified after 5 minutes of laminar blood flow over a HUVEC monolayer activated with IL-1β for 4 hours. N=3 human blood donors per particle condition. Statistical analysis of adherent density was performed using one-way ANOVA with Fisher's LSD test. (*) indicates $p<0.01$ versus 300 sites/μm^2 and ($^{\#}$) indicates $p<0.01$ versus 1,000 sites/μm^2. Error bars represent standard error.

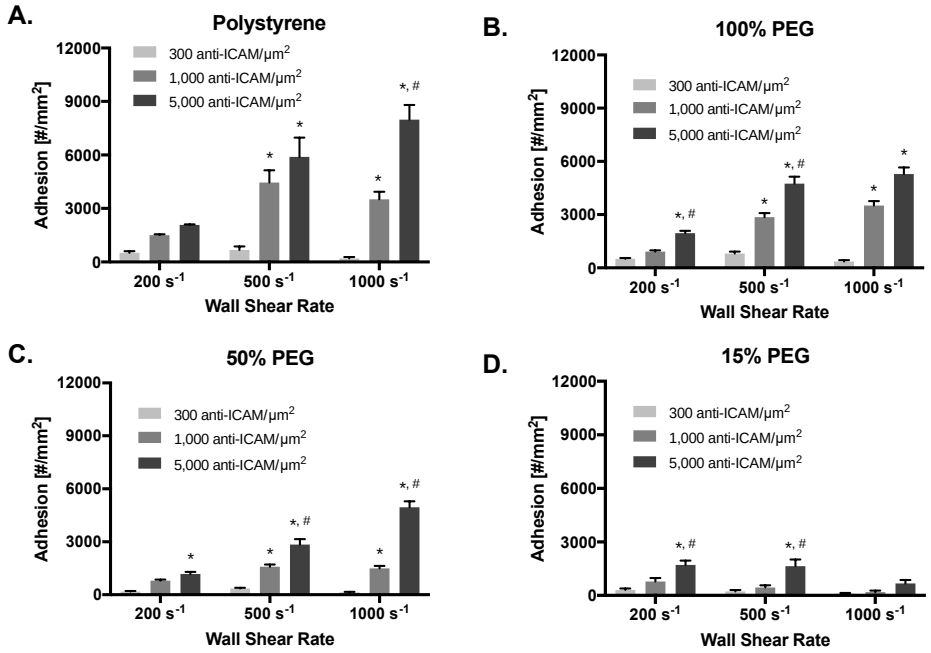

Figure 4.9 Raw particle adhesion to inflamed HUVEC monolayer as a function of particle anti-ICAM-1 site density and modulus.
Quantified VTC adhesion at 3 wall shear rates (200 s^{-1}, 500 s^{-1}, and 1,000 s^{-1}) by anti-ICAM-1 site density and particle type: (A) PS, (B) 100% PEG, (C) 50% PEG, and (D) 15% PEG. Adhesion quantified after 5 minutes of laminar blood flow over a HUVEC monolayer activated for 24 hours with IL-1β. N=3 human blood donors per particle condition. Statistical analysis of adherent density was performed using one-way ANOVA with Fisher's LSD test. (*) indicates $p<0.01$ versus 300 sites/μm^2 and ($^{\#}$) indicates $p<0.01$ versus 1,000 sites/μm^2. Error bars represent standard error.

Researchers have investigated increasing site densities on VTCs, but typically with just one particle type and one ligand type. For instance, 10 μm latex particles were functionalized with increasing amounts of sLe^X, which produced significantly slower rolling speeds in buffer flow over a protein-coated plate.[182,183] This work had a maximum site density of 90 sites/μm^2, thus rolling velocity was a better metric than firm adhesion. In comparison, our minimum site density of 300 sites/μm^2 produced minimal to no rolling adhesion, therefore we focused on binding efficiencies. Researchers have also shown that the rolling of 4.6 μm poly(lactic-co-glycolic acid) (PLGA) spheres over P-selectin coated plates decreases with increasing sLe^X site

density, indicating increased adhesive forces, again focused on rolling speeds.[184] In order to emphasize clinical utility, final adhesion is the best metric. Our previous work with sLe^A on 500 nm PS spheres in blood flow determined diminishing returns for adding more ligand *in vitro*;[122] our work here corroborates those findings on 2 μm PS and PEG spheres in Figures 4.3 and 4.6. Any non-linearity in the graphs represents a diminishing return of adding more targeting ligand- the diminishing return is most apparent and present at the lower WSRs (200 s^{-1} and 500 s^{-1}). Researchers speculate that this is due to the steric crowding of ligands and the inability to initiate more adhesive contacts.[185,186] Others have shown the interplay of size and ligand density, noting that 10 μm PS particles are in a transport-limited regime in which adding more sLe^A increased adhesion, whereas the 5 μm PS particles were in a reaction limited regime as adding more ligand did not increase the final binding. Shifting to more complex *in vivo* models with anti-ICAM-1, it has been shown that decreasing particle avidity increases the specificity of the treatment, but not the overall accumulation at the site of inflammation.[187] This is likely due to the baseline expression of ICAM-1 in the lungs. Our work, by investigating both ligand kinetics and particle modulus, aims to elucidate how these trends change based on the physical properties of the particles.

Particle binding kinetics determined by observed attachment rate $k_A C_W$

To better explain the adhesion trends, we investigated the kinetics and complex hemodynamics of our VTCs. No correlation has been established between molecular LR kinetics and those of a whole particle onto a coated plate or cell surface. This is the case because of the differences in size as well as the presence of hemodynamic blood flow. To better understand the adhesion efficiency data, the observed attachment rate, $k_A C_W$, was determined by the linear least-

squares regression of rate of attachment data and plotted in Figure 4.10. We plot this to represent how rates of attachment of different particle types change with changes in site density and ligand type. We investigated the adhesion kinetics, with sLe^A targeted particles to discern how increasing the site density of each particle type increases the attachment rate. At 200 and 500 s^{-1}, the rate of attachment for all particle types begins to saturate, designated by the lack of linearity of $k_A C_W$ with increasing site density. This means at these lower WSRs, with smaller shear removal forces, there is a diminishing return for adding more sLe^A between 1,000 and 5,000 sites/μm^2. At the higher WSR of 1000 s^{-1}, under larger shear removal forces, increasing site densities delivers higher returns than at lower WSRs; in other words, when targeting high shear vessels, higher adhesive forces are required to produce firm adhesion. Overall in Figure 4.10, we clearly see that PS particles have larger observed rates of attachment, especially at 500 s^{-1} and 1000 s^{-1}. For all particle types, with more $sLe^A/\mu m^2$, the larger the rate of attachment, as expected. With these particle kinetics findings in mind, we decided to explore how changing the kinetics of the LR pair would alter the trends in adhesion efficiencies. To date, all our work with deformable particles *in vitro* has been with sLe^A as the targeting ligand, which begs the investigation of different targeting ligands to see if the binding trends hold.

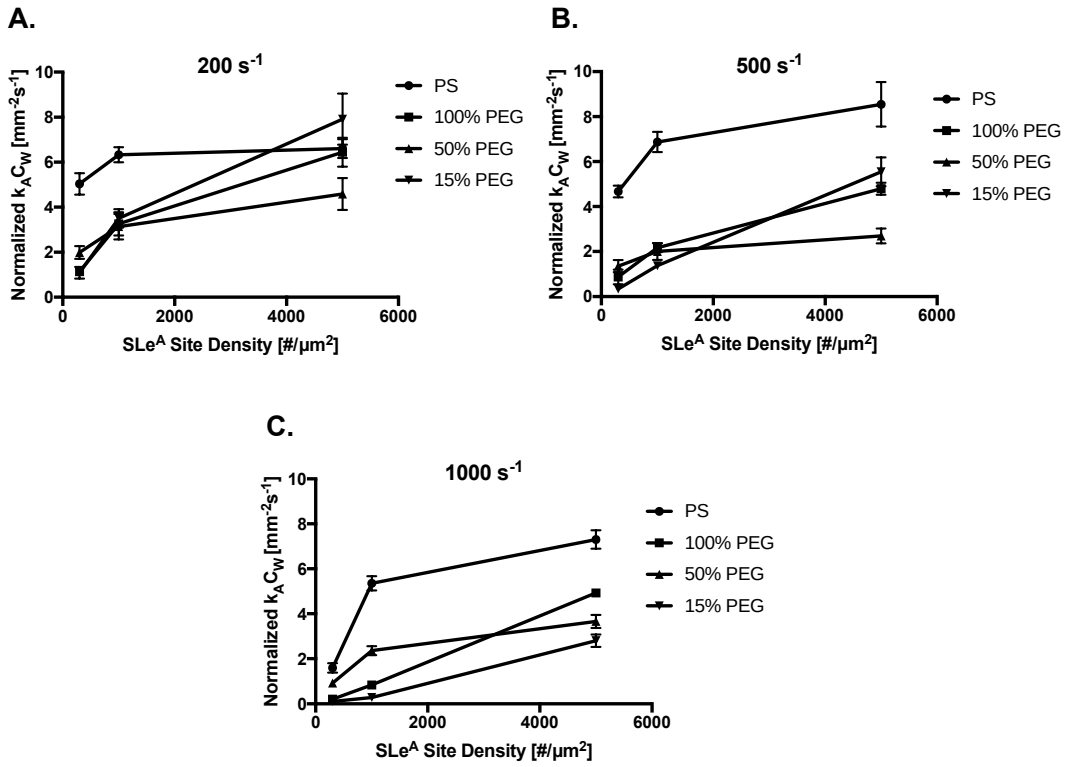

Figure 4.10 Rate of attachment constant by particle sLe^A site density.
The normalized observed attachment rate for particles of varying moduli with varying amounts of sLe^A (300, 1,000, and 5,000 sites/μm^2) at varying WSRs of (A) 200 s^{-1}, (B) 500 s^{-1}, and (C) 1000 s^{-1}. Error bars represent standard error for N=3.

In Figure 4.11 we investigated the adhesion kinetics, with anti-ICAM-1 targeted particles to discern how increasing the site density of each particle type increases the attachment rate. These were again normalized because more particles were perfused at higher WSRs. Figure 4.11A shows the trend by modulus and anti-ICAM-1 site density at 200 s^{-1}; at the low WSR the benefit of adding more sites begins to saturate between 1,000 and 5,000 sites/μm^2, as designated by the lack of linearity. At 500 s^{-1}, the rate of attachment is slower at 300 sites/μm^2 than it was for those at the 200 s^{-1}, because the higher shear removal force demands more adhesive force. At 1000 s^{-1} this is even more extreme, where the observed attachment rate saturates less than the other WSRs and there are huge benefits to adding more anti-ICAM-1 on the surface of the

particles. At this WSR, the rigid particles have a higher observed rate of attachment than deformable particles, for all site densities tested. This aligns with our previous publication, that rigid particles outperform deformable counterparts in whole blood medium at high WSR.[106] The fact that this holds true with a different ligand-receptor system at a range of site densities, points to the transport of deformable particles as the dominant mechanism controlling adhesion.

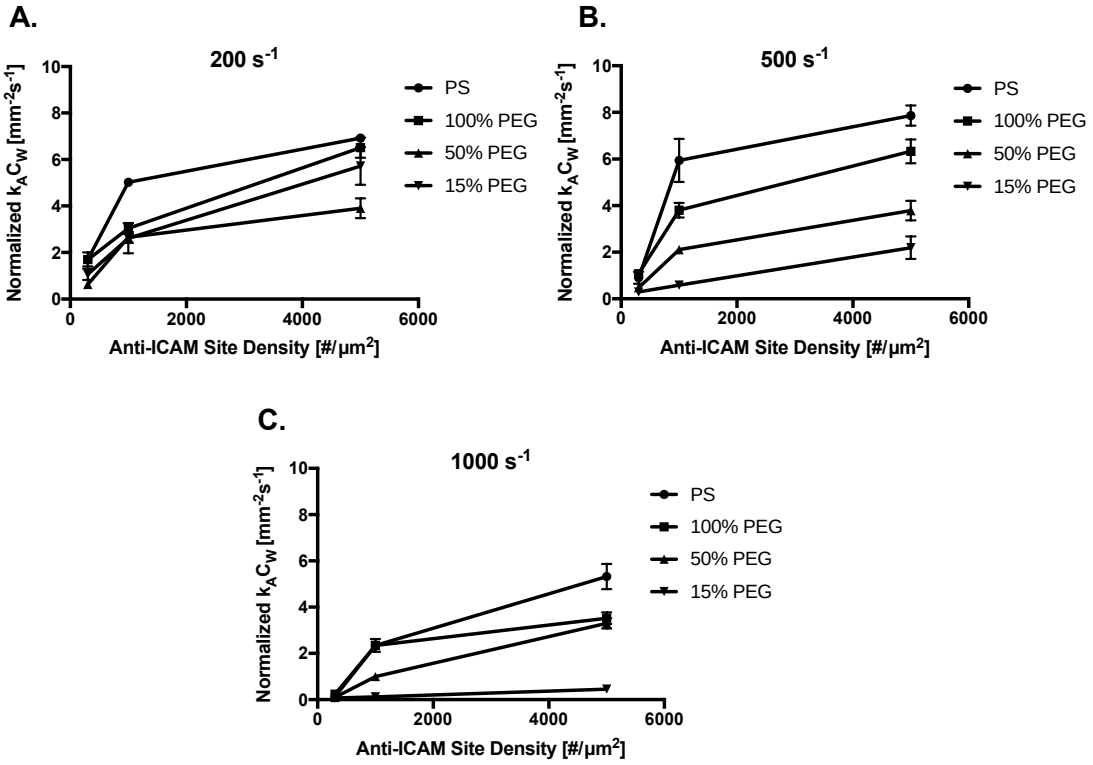

Figure 4.11 Rate of attachment constant by particle anti-ICAM-1 site density.
The normalized observed attachment rate for particles of varying moduli with varying amounts of anti-ICAM-1 (300, 1,000, and 5,000 sites/μm^2) at varying WSRs of (A) 200 s^{-1}, (B) 500 s^{-1}, and (C) 1000 s^{-1}. Error bars represent standard error for N=3.

The impact of ligand type on final particle adhesion

We explored the differences that arose directly from varying ligand receptor kinetics of sLe^A and anti-ICAM-1. We specifically chose these two ligand-receptor pairs because they

represent very different ligand kinetics. The forward (k_f) and reverse (k_r) rate constants of the association between sLe^A to E-selectin are approximately 27,000 $M^{-1}s^{-1}$ and 3 s^{-1}, respectively, and for anti-ICAM-1 and ICAM-1 they are known to be 156,000 $M^{-1}s^{-1}$ and 1.13 x 10^{-4} s^{-1}, respectively.[169,170] The kinetic rate constants for the anti-ICAM-1/ICAM-1 interaction are similar to that of the endogenous activated integrin, LFA-1/ICAM-1.[170] The k_f values are in the similar in magnitude, while the k_r values of the sLe^A/selectin is 4 orders of magnitude higher. This clear difference in reverse reaction rates explain the well-established, distinct roles of these receptors and their ligands in the leukocyte adhesion cascade.[188] Namely, binding to selectins, with large reverse rate constants, promotes rolling and slowing of WBCs, while binding to ICAM-1, with a smaller reverse constant, promotes firm adhesion.

While the quantitative kinetic values above describe the adhesive interactions at a molecular level, more macroscopic kinetics have been studied in the context of targeted drug delivery. Haun and Hammer coined the term "transport-reaction" model as a way to explain the kinetics of entire particles associating and dissociating with coated plates, rather than single molecular ligand-receptor interactions.[189] There is a big difference between molecular and particulate kinetics, namely, particles have immobilized ligands on the surface, which can be sterically hindered and are inherently coupled to the location of other ligands. Additionally, the massive difference in size scale and the presence of fluid flow have made it impossible to determine a direct correlation between molecular kinetics and particulate binding kinetics.[189] While much of this pioneering work determined how particle size and kinetics determine overall binding to a receptor-coated plate, translation to the clinic requires development into more physiological realms, such as using primary human cells and human blood. Therefore, we

compared how particles with all else constant, beside the type of ligand, bound to and inflamed endothelium.

The importance of ligand type is presented in more detail in Figures 4.12A and B. The data shown is that of the most extreme moduli particles, PS and 15% PEG. Both Figure 4.12A and B are adhesion efficiency of anti-ICAM-1 targeted particles subtracted from sLe^A targeted particles at the equivalent site density and WSR. For all but one condition, sLe^A targeted particles outperformed the anti-ICAM-1 targeted counterparts, even though about twice as much ICAM-1 is expressed on activated HUVECs than E-selectin at corresponding maximal activation times. A similar trend has been shown in the past, where significantly more anti-ICAM-1 is required to obtain a comparable amount of binding *in vitro*.[113,122,167] Of key importance, the interaction between sLe^A and selectins is considered a catch bond, which strengthens over time under increased shear force.[163,190] Thus, our result of sLe^A targeted particle outperforming anti-ICAM-1 particles at high WSRs aligns with this previously published work and known behavior of catch bonds. For rigid particles like PS, across all WSR, the benefit of sLe^A targeting decreased with increased total surface site density, meaning anti-ICAM-1 was closing the adhesion gap. The inverse is true with the most deformable, 15% PEG particles, meaning that the higher the site density, the better sLe^A targeted particles perform versus their anti-ICAM-1 targeted counterparts.

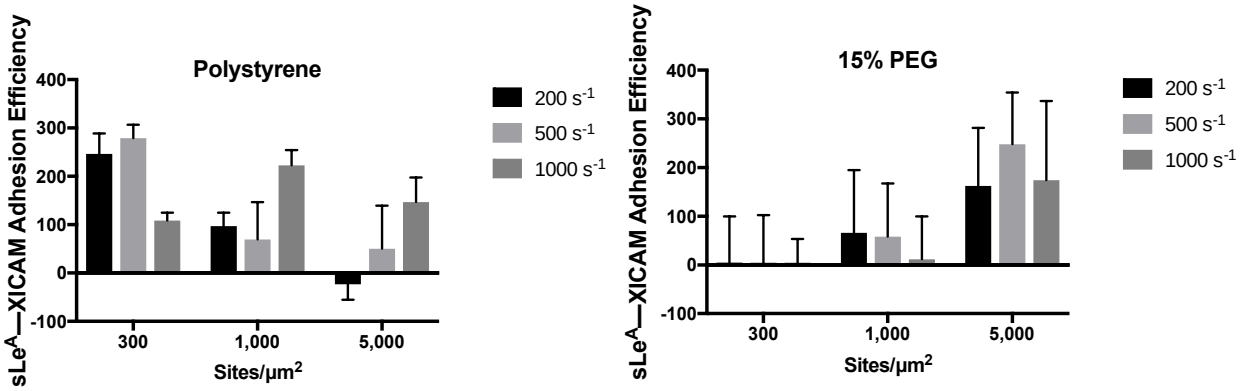

Figure 4.12 Difference in adhesion by ligand type.
(A) Differential particle adhesion efficiency, as defined by subtracting the anti-ICAM-1 adhesion efficiency from that of sLe^A adhesion efficiency (number bound/10^6 perfused), shown for the two extreme particle types (A) PS and (B) 15% PEG. In general, sLe^A adhesion efficiency is higher than that of anti-ICAM-1.

The contribution of WBCs to particle binding trends

Our previous work with sLe^A at one site density highlighted collisions with WBCs in the cell free-layer as the reason for modulus and WSR dependent binding. This was demonstrated when WBCs were removed from the blood flow medium and the sLe^A mediated particle binding was uniform across all particle moduli. Whereas in the presence of WBCs, deformable particles bound best at low WSR and rigid particles bound better than deformable at high WSRs.[106] We expanded on this to determine whether WBCs play a similar role for our particles with varying amounts of ligand, with two distinct sets of kinetics. We investigated how removing WBCs from hemodynamic blood flow affected binding *in vitro*. We hypothesized that WBCs would still be a major player, as they were in our previous work, even with different ligand kinetics. In Figure 4.13 we show adhesion efficiencies for the four particle types with either high or low site densities anti-ICAM-1, at high and low WSRs, all without WBCs (sLe^A shown in Figure 4.14). We designate this blood medium RBCs+plasma, as the other main component, WBCs, have been removed.

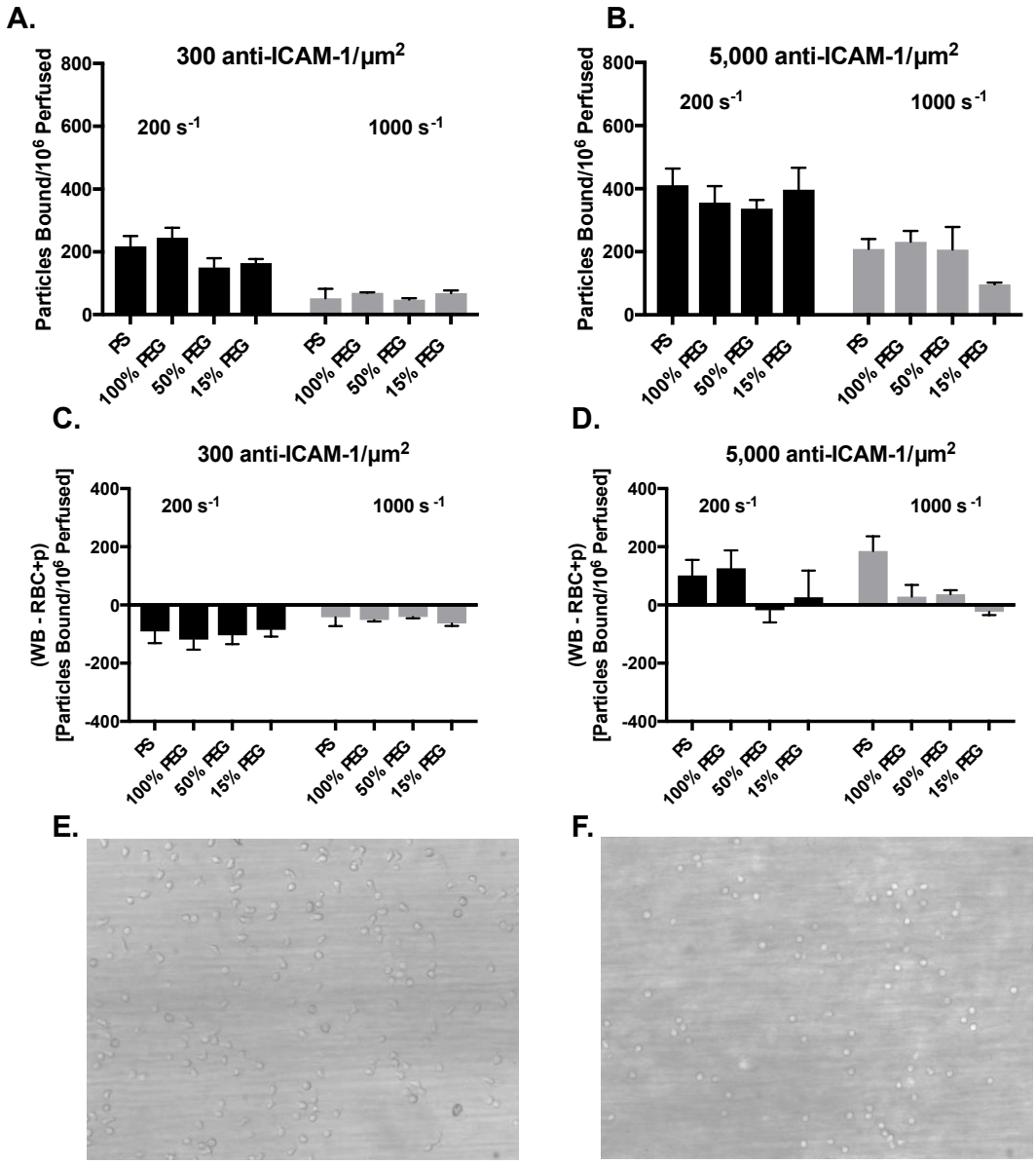

Figure 4.13 Anti-ICAM-1 particle adhesion to an inflamed HUVEC monolayer in WBC-removed, RBC+plasma medium.

Adhesion efficiency shown for all particle types at both 200 and 1000 s^{-1} WSRs with (A) 300 anti-ICAM-1/μm^2 and (B) 5,000 anti-ICAM-1/μm^2. Change in particle adhesion between whole blood (WB, from Fig. 4) and RBC+plasma (RBC+p, from Fig. 7) trials. Adhesion efficiency shown for all particle types at both 200 and 1000 s^{-1} WSRs with (C) 300 anti-ICAM-1/μm^2 and (D) 5,000 anti-ICAM-1/μm^2. All adhesion shown after 5 minutes of laminar RBC+plasma flow over a HUVEC monolayer activated with IL-1β for 24 hours. N=3 human blood donors per particle condition. Error bars represent standard error. Representative images of adhesion of leukocytes to an inflamed HUVEC monolayer at (E) 200 s^{-1} and (F) 1000 s^{-1}, after 5 mins of laminar whole blood flow.

Figure 4.13A shows how particles with 300 anti-ICAM-1/μm^2 adhere in RBCs+plasma. This data follows the trend of our previous work,[106] in that the binding is equivalent across all particle types when WBCs are removed, at both 200 and 1000 s^{-1} WSR. Interestingly here we see that removing the WBCs from the blood medium again eliminates the adhesion efficiency trends observed earlier (Figures 4.6 & 4.7), except for one condition. The 15% PEG particles with 5,000 anti-ICAM-1/μm^2 maintain low binding at 1000 s^{-1}. Other than that data point, all binding is similar within each of the low and high site densities of anti-ICAM-1, regardless of particle modulus. Figures 4.13C and D are the adhesion efficiency in RBCs+plasma subtracted from that in whole blood. Therefore, a negative value means binding is more efficient in RBCs+plasma, and that WBCs disrupt the binding of the particle to the vascular wall. A positive value means binding is higher in whole blood and WBCs aide in the binding of the VTC. For the 300 anti-ICAM-1/μm^2 the adhesion efficiency in RBCs+plasma is significantly higher than that in whole blood for both 200 s^{-1} and 1000 s^{-1}. Because this occurs predominantly at low WSR, this is likely not due to collisions in blood flow, but rather due to the adhesive competition between WBCs and VTCs at the low WSR. It is well known that WBCs adhere significantly more at lower WSRs;[191] we corroborated this known fact with qualitative images in Figure 4.13E and F, showing significantly more WBCs bound in a WSR of 200 s^{-1} versus 1000 s^{-1}. We then investigated how this trend would translate to higher site density particles. For the particles with 5,000 anti-ICAM-1/μm^2, the adhesion efficiency in RBCs+plasma is lower than that in whole blood without WBCs present, binding at this site density is statistically similar across all particle moduli tested. WBCs hinder binding at low site densities whereas they encourage high site density binding. Unlike the lower site density, the particles with higher adhesive force bind less in the absence of WBCs, though not statistically. This means, like in our previous work, that with

higher site densities, the WBCs help push the particles to the vessel wall;[106] the larger adhesive forces of these particles can bind to the endothelium in the crowded, hemodynamic environment. The more rigid particles are aided maximally by WBCs because of their inelasticity; rigid particles will displace further after each collision than deformable, elastic particles, increasing the probability that contact with the vessel wall occurs. For both site densities, WBCs have a key impact on sLe^A targeted particles *in vitro*; for the low site density WBCs competitively disturb the area of binding, whereas for the high site density particles, WBCs increase the binding of VTCs of varying moduli with anti-ICAM-1 by pushing them to the vessel wall.

In Figure 4.14 we show the same data, but for sLe^A particles. A similar trend versus the whole blood data exists as does with anti-ICAM-1 targeted VTCs. Figure 4.14A shows how particles with 300 $sLe^A/\mu m^2$ adhere in RBCs+plasma. Interestingly at 200 s^{-1} these adhesion efficiencies are significantly higher than those with WBCs, meaning that at low WSR, WBCs hinder binding of 300 $sLe^A/\mu m^2$ particles, except for PS at a low WSR. We again attribute this to the inability of particles with lower site density to bind in a crowded, competitive vessel wall environment. In Figure 4.14B, the adhesion efficiencies were also equivalent for all particle types with 5,000 $sLe^A/\mu m^2$- without WBCs present, binding at this site density is statistically similar across all particle moduli tested. We again attribute this to the increased ability of high site density particles to adhere rapidly in a dynamic, collision-filled blood vessel. Overall the sLe^A binding without WBCs is higher than that with anti-ICAM-1, continuing the trend found in the whole blood data.

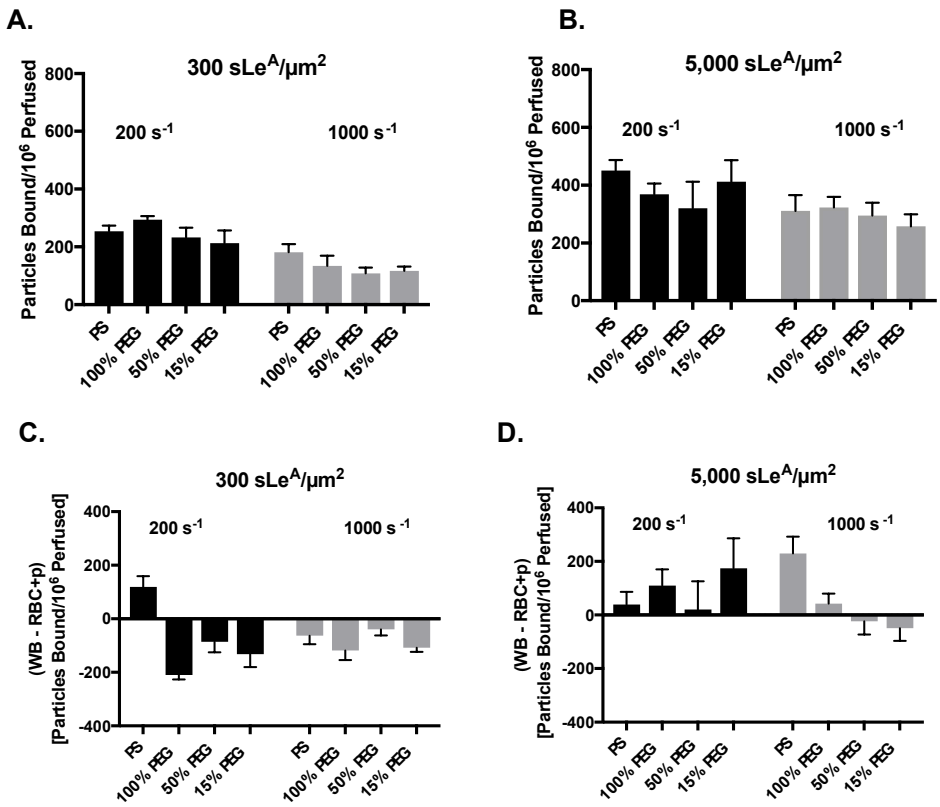

Figure 4.14 SLe^A particle adhesion to an inflamed HUVEC monolayer in WBC-removed, RBC+plasma medium.
Adhesion efficiency shown for all particle types at both 200 and 1000 s^{-1} WSRs with (A) 300 $sLe^A/\mu m^2$ and (B) 5,000 $sLe^A/\mu m^2$. Change in particle adhesion between whole blood (WB, from Fig. 2) and RBC+plasma (RBC+p, from Fig. 7) trials. Adhesion efficiency shown for all particle types at both 200 and 1000 s^{-1} WSRs with (C) 300 $sLe^A/\mu m^2$ and (D) 5,000 $sLe^A/\mu m^2$. All adhesion shown after 5 minutes of laminar RBC+plasma flow over a HUVEC monolayer activated with IL-1β for 4 hours. N=3 human blood donors per particle condition. Error bars represent standard error.

The data in Figures 4.13 and 4.14 are key for elucidating and explaining the mechanism by which adhesion trends arise in whole blood, but we note that WBCs will always be present in physiological conditions. Provided equal transport of particles to the vessel wall as we have previously shown,[106] and only a varying amount of site density, the particles respond differently to the removal of WBCs. With low site densities, WBCs hinder the binding of particles with both ligands tested, likely by crowding the vessel wall that they must bind too. Higher site density

particles can more rapidly adhere firmly, so that they are less affected by this phenomenon. At high site densities, the WBCs push or crowd the VTCs to the vessel wall, where the larger adhesive force can combat collisions with WBCs. Essentially, once VTCs with higher site density contact the vascular wall, they will bind and are not as easily disrupted by collisions or shear forces. Whereas the low site density particles are still transported to the vessel wall but simply cannot counteract the crowding on the vessel wall. Interestingly in RBCs+plasma, the gap in adhesion efficiency between the high and low site densities decreases, as the removal of WBCs aids low site density VTCs while hindering high site density VTCs. In light of these findings, and recognizing that WBCs are always present in physiological conditions, we next investigated if we could increase the binding of all particle types under the same whole blood conditions by employing an optimized mix of the two targeting ligands.

Dual targeting standardizes final adhesion across particle moduli

We utilized a mix of both targeting ligands, with the same total site density of 5,000 sites/μm^2, with a ratio known to produce maximal adhesion with 4 hours of activation.[122] Increasing the site density of either single ligand, sLe^A or anti-ICAM-1, was not enough to increase the deformable particle binding at high WSR, so we investigated if optimal dual targeting could equilibrate the binding across all moduli. It has been previously shown that ICAM-1 facilitated binding is greatly increased with the involvement of selectins; upon particles rolling via the selectin LR pair, ICAM-1 facilitated binding engages more completely.[170] Figure 4.15A is a schematic of the particle surface composition, which was 25% sLe^A and 75% anti-ICAM-1. The same PPFC flow experiments were conducted with all experimental variables the same except the targeting ligand composition. All four particle types with this dual targeting

ligand regime adhered equivalently at 200 s^{-1}, as shown in Figure 4.15B. At low WSR, the optimal mix of targeting ligands produces equivalent binding independent of particle modulus. At a high WSR of 1000 s^{-1}, the same holds true in Figure 4.15C; dual targeting with the optimal mix of ligand based on HUVEC expression equilibrated all binding patterns based on modulus. Of note, the binding efficiencies were nearly equivalent from 200 s^{-1} to 1000 s^{-1}, meaning that this dual targeting regime provides sufficient adhesive force to bind equivalently in the WSRs tested. Clearly, the interplay of the two different ligand types produced this trend; sLe^A slowed the particles rolling along the surface while anti-ICAM-1 facilitated the firm adhesion, negating any other possible WBC effects once bound to the endothelium. These results emphasize the importance of understanding the targeted particle surface, in that particle modulus no longer dictated adhesion trends at any WSR. This work is paramount in understanding how to maximize the binding of low modulus particles at high WSRs. While deformable particles are often highlighted for ability to circulate for long times *in vivo*, previous results suggested they may not produce efficient adhesion at high WSRs.[106] This work shows that by designing a dual targeting regime that is optimal for the targeted endothelium, particle modulus is no longer the dominating factor in determining VTC adhesion. Therefore, if in the development process there is a concern about particle adhesion efficiency, especially with deformable particles at high WSRs, it can be addressed with dual targeting.

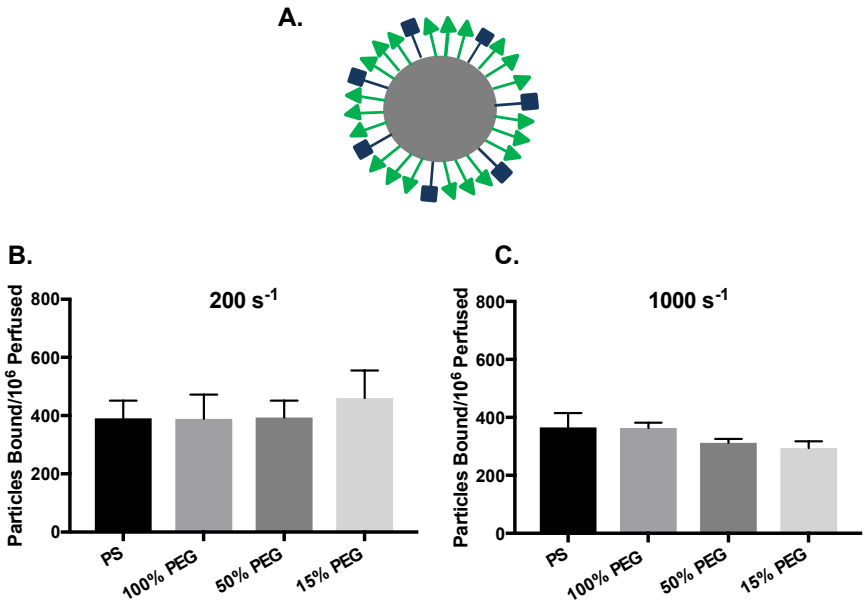

Figure 4.15 Particle adhesion efficiency of dual targeted particles to an inflamed HUVEC monolayer as a function of particle modulus.
(A) Schematic of dual targeted particle with 5,000 sites/μm^2 total, 25% of which is sLe^A, 75% of which is anti-ICAM-1. This composition has been previously determined to produce maximal binding for 4 hour activation with IL-1β. Quantified adhesion of hydrogel particles at a WSR of (B) 200 s^{-1} and (C) 1000 s^{-1} by modulus after 5 minutes of laminar blood flow over a HUVEC monolayer activated with IL-1β for 4 hours. N=3 human blood donors per particle condition. Error bars represent standard error. All conditions are not significant as determined by using one-way ANOVA with Fisher's LSD test.

Previous work evaluating the ligand-dependent binding of VTCs under flow conditions are typically targeted to protein-coated plates in buffer flow. Based on our work, WBCs alone play an integral role in the binding of targeted VTCs. Therefore, it is key to utilize increasingly physiological systems for the future development of VTC systems, while continuing to use simplified systems to elucidate the mechanisms at play.

4.5 Conclusions

The work presented here is the first demonstration that the impact of VTC ligand type and surface density depends on both VTC modulus and blood WSR. Previous work from others

demonstrated that low VTC modulus can increase circulation time, ability to navigate capillaries, and avoidance of immune clearance, making low modulus VTCs attractive for clinical applications. This work presents a comprehensive study of the role that particle ligand kinetics, ligand density, and VTC modulus play on adhesion mechanisms required for targeted particle adhesion in VTC systems. Deformable particles with a single ligand, regardless of site density or ligand type, were not able to match the binding of rigid particles in high shear environments. Importantly, WSR plays a dramatic role in determining the adhesion efficiency of all VTCs, regardless of modulus, ligand type, or ligand surface density. Our findings indicate that rigid particles are able to achieve more binding with increases in site density at the same WSR, due to the increased adhesion force. The removal of WBCs elucidates their key role in altering VTC adhesion from blood flow-with low site densities WBCs disrupt particle binding via competition at low WSRs, whereas with high site densities WBCs increased particle binding via productive collisions in the red blood cell-free layer. Interestingly, and of huge clinical importance, our study shows that by employing the most efficient dual targeting ligand composition, adhesion is completely equilibrated across all particle moduli tested at one WSR, offering a route to improve binding of rigid particles at low WSR and deformable particles at high WSR. This unique work teases out the importance of multiple crucial physical properties of VTCs and targeted components to demonstrate the clear interplay of particle modulus, ligand kinetics, and ligand density to produce trends in particle adhesion. Using these findings, in conjunction with well-defined disease hemodynamics and targeted disease receptor profiles, VTC systems can be more intelligently engineered for higher clinical efficacy and improved translation of VTC systems from the bench top to bedside.

Chapter 5: Evaluation of Receptor-Ligand Mechanisms of Dual-Targeted Particles to an Inflamed Endothelium

5.1 Publication Information

This work is a collaboration with Dr. Catherine Fromen, all parts presented here are a direct result of my work. All the data in this chapter is published as: Fromen, Catherine A., **Margaret B. Fish**, Anthony Zimmerman, Reheman Adili, Michael Holinstat, and Omolola Eniola-Adefeso. "Evaluation of receptor-ligand mechanisms of dual-targeted particles to an inflamed endothelium." *Bioengineering & translational medicine* 1, 1 (2016): 103-115.

5.2 Abstract

Vascular-targeted carriers (VTCs) are designed as leukocyte mimics, decorated with ligands that target leukocyte adhesion molecules (LAMs) and facilitate adhesion to diseased endothelium. VTCs require different design considerations than other targeted particle therapies; adhesion of VTCs in regions with dynamic blood flow requires multiple ligand-receptor (LR) pairs that provide particle adhesion and disease specificity. Despite the goal of leukocyte mimicry, the specificity of multiple LAM-targeted VTCs remains poorly understood, especially in physiological environments. Here, we investigate particle binding to an inflamed mesentery via intravital microscopy using a series of particles with well-controlled ligand properties. We find that the total number of sites of a single ligand can drive particle adhesion to the endothelium, however, combining ligands that target multiple LR pairs provides a more effective

approach. Combining sites of sialyl Lewis A (sLe^A) and anti-intercellular adhesion molecule-1 (anti-ICAM-1), two adhesive molecules, resulted in ~3-7-fold increase of adherent particles at the endothelium over single-ligand particles. At a constant total ligand density, a particle with a ratio of 75% sLe^A: 25% anti-ICAM-1 resulted in more than 3-fold increase over all over other ligand ratios tested in our *in vivo* model. Combined with *in vitro* data, we find the best dual-ligand design of a particle is heavily dependent on the surface expression of the endothelial cells, producing better adhesion with more particle ligand for the lesser-expressed receptor. These results establish the importance of considering LR-kinetics in intelligent VTC ligand design for future therapeutics.

5.3 Background

Particulate drug delivery was developed to package systemically toxic drugs into inert particle carriers, thereby selectively releasing active cargo to a diseased target. This approach should dramatically increase treatment efficacy by delivering more drug into the diseased tissue while eliminating systemic release, thereby mitigating toxic side effects. While this concept has not yielded a true "magic bullet" to date, packaging small molecule drugs into particles dramatically alters their pharmacokinetic/dynamic behavior and provides opportunities to direct drugs into diseased targets depending on their size, shape, and composition.[1,11,37,127] Many diseases manifest in the upregulation or overexpression of certain cellular surface receptors; therefore, tissue specificity can be enhanced with use of LR pairs. Particulate drug carriers can be coated with ligands complimentary to these receptors, providing a lock and key approach to disease-specific delivery. In principle, the concept of LR pairs seems straightforward, however, implementation of actively targeted particles has proved challenging.[87] Nanoparticle therapeutics

with applications in cancer have driven research in the field. Despite conflicting results in overall success,[87,192,193] a handful of candidates are currently in the clinical trial pipeline for cancer applications.[192,194]

VTCs are an emerging area of research within particulate drug delivery. We define VTCs as particles designed with surface adhesive ligands that mimic those of leukocytes. During inflammation, activated endothelial cells (ECs) upregulate surface LAMs, including selectins, intercellular adhesion molecule-1 (ICAM-1), and vascular cell adhesion molecule-1 (VCAM-1).[78] Importantly, ECs shed their glycocalyx barrier, enabling leukocytes to interact directly with the EC surface.[195] Surface ligands on circulating leukocytes facilitate rolling on and firm capture to activated ECs, and assist in extravasation into tissue to perform various immune functions.[79] This leukocyte adhesion cascade (LAC) is an important mechanism for normal immune function, but is also indicative of excessive cell recruitment that occurs early in many diseases.[78,79] Overexpression of LAMs represent potential targets for the design of particulate therapeutics; VTCs have been designed utilizing a wide range of LAM-LR pairs for novel therapeutic approaches in atherosclerosis,[196,197] and cancerous tumors,[198] among others.[192,199–202]

Success of VTCs relies heavily on LR interactions with overexpressed LAMs on diseased ECs. VTCs are unique in that they must adhere to diseased ECs under rapid blood flow conditions, unlike other particles targeted to tissue spaces. Once localized to the endothelium, the interactions between LR pairs dictate adhesion and ultimate drug carrier efficacy. VTC and EC surface bonds must form rapidly to overcome particle momentum in flow. Capture and firm arrest at the surface will depend on the kinetics of the LR engaged pair and the aggregate strength of those interactions. Particle ligand total receptor avidity and specificity must be balanced; excessive avidity can lead to off target binding and immune responses due to rapid

opsonization of non-native proteins, while insufficient LR avidity can result in minimal binding.[86] The design of VTC ligands must correspond with receptors in the targeted disease state; a ligand for the immediate onset of disease may not function efficiently in a chronic response.[203,204] Given the fluctuation of receptors on ECs and the presence of blood flow, leukocytes achieve adhesion with multiple LR pairs, where each LR pair provides a unique benefit of capture, firm adhesion or transmigration, based on spatiotemporal expression on the diseased ECs. Notably, selectin receptors facilitate leukocyte capture and rolling, yet physiological levels of this LR pair are not enough to achieve firm adhesion on inflamed ECs. Firm adhesion requires secondary LR pairs, usually involving cell adhesion molecules (CAMs), which are expressed at a lower EC surface density with more favorable kinetics for firm adhesion.[78,79] Through the synergistic effects of these two LR pairs, leukocytes efficiently respond to inflammation on diseased tissues *in vivo.*

Despite the goal of LAC mimicry, the use of multiple LAM ligands on VTCs remains poorly understood. Most studies of VTCs have focused on particle designs with a single LR pair, with emphasis on the final disease outcome due to the delivered drug. Efficacy studies that have probed dual ligands are largely qualitative, comparing multi-ligand particles to the single ligand counterparts with minimal control over the total particle ligand presentation.[85–89] Additional studies have probed the importance of ligand ratios between two LR pairs in static conditions, which fail to capture LR pair dynamics under physiologically relevant flows.[85,90] To study LR kinetics under flow, multiple research groups have used protein-coated plates to study the adhesion and rolling of dual-targeted particles *in vitro.*[205–210] However, these studies lack the complexity of a true diseased endothelium, as spatiotemporal LAM expression varies widely.[211]

To address these gaps in understanding, we have designed particles with controlled ligand densities and evaluated particle adhesion in physiological environments. We investigated both single and dual LR pairs, exploiting selectin and β_2 integrin mediated paths of adhesion by designing particles with sLe^A and anti-ICAM-1. These two LR pairs drive leukocyte adhesion during inflammatory events, representing a synergistic therapeutic target for nanoparticle delivery.[78] Furthermore, the carbohydrate-selectin LR pair and antibody-CAM LR pair have drastically different rates of interaction, which enables us to evaluate the role of LR pair kinetics in the nanoparticle design.[169,170] Notably, we evaluated these particles in a model of inflamed mesentery using intravital microscopy to capture a dynamic *in vivo* environment. Our results show that controlling the design of particle ligand presentation is critical in optimizing delivery of VTCs.

5.4 Results

Density of sLe^A dictates particle adhesion in vitro *and* in vivo

We utilized a parallel plate flow chamber (PPFC) assay to investigate the role of sLe^A density on particle adhesion under physiological blood flow conditions. A series of four particle types (A-D) was prepared with increasing sLe^A surface density (Figure 5.1A). SLe^A site densities were quantified by flow cytometry (Table 5.1), with representative gating shown in materials and methods (chapter 2) and reaction conditions are detailed in Figure 5.2. Human umbilical vein endothelial cell (HUVEC) monolayers were prepared and activated with TNF-α for 4 hours prior to experiments. Representative fluorescent images of particle binding in the PPFC assay are shown in Figure 5.1B. Minimal non-specific particle binding was observed for particles functionalized with an IgG-isotype control of varied densities, as shown in Figure 5.3. Particle

adhesion from sLe^A targeted particles was determined and non-specific binding from control particles at corresponding site densities were subtracted out to quantify target-specific adhesion (Figure 5.1C). Increasing the sLe^A density on 500 nm particles from 5,000 sites/μm^2 to 40,000 sites/μm^2 resulted in increased particle adhesion. We observed a 2-fold increase in particle binding from A to B; additional sLe^A on C and D resulted in further increased adhesion (3- and 6-fold increases over A, respectively).

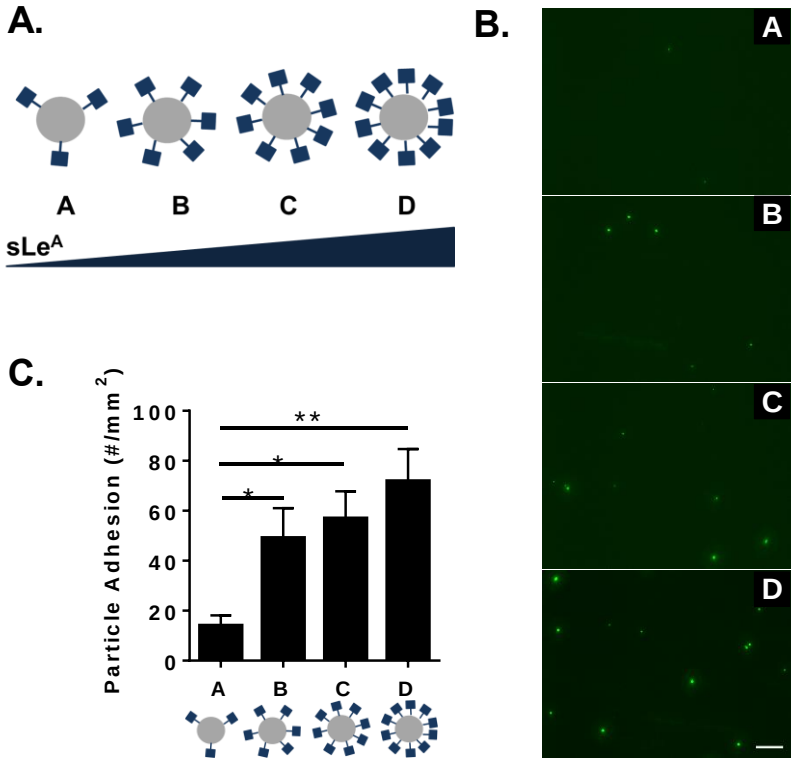

Figure 5.1 Particle adhesion to inflamed HUVEC monolayer as a function of total sLe^A sites.
(A) Diagram of four particle conditions A-D with increasing sLe^A ligand density (5,000, 10,000, 20,000, and 40,000 sLe^A sites). (B) Representative fluorescence images of particle adhesion to *in vitro* inflamed HUVEC monolayer, corresponding to particles A-D from top to bottom. HUVEC activation was achieved via 4 hour TNF-α incubation. (C) Quantified particle adhesion. Statistical analysis was performed using one-way ANOVA with Fisher's LSD test (*) indicates $p<0.05$, N=3 donors. Error bars represent standard error, scale bar 50 μm.

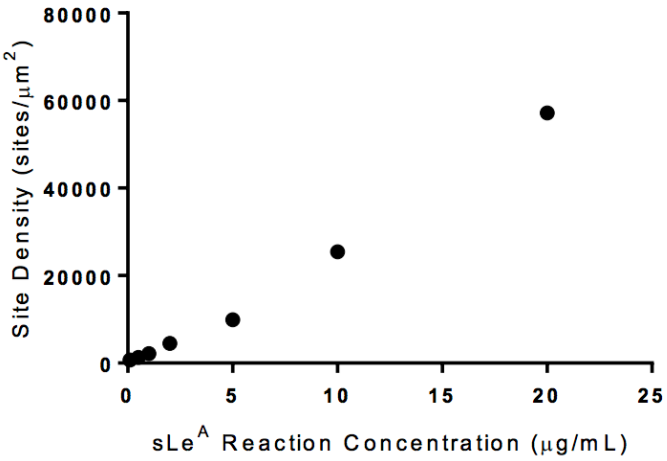

Figure 5.2 Reaction conditions for biotinylated ligand attachment of sLe^A.
Our highest site density used in subsequent studies was 40,000 ligands/μm^2; further increases in the ligand reaction concentration resulted in increased in ligand site density. This indicates that the active avidin sites were never saturated. At 40,000 sites/μm^2, the ligand occupies a parking area of 25 nm^2 per targeting ligand. This is five times larger than hydrodynamic radius of avidin (5.4 nm), thus implying a distributed ligand landscape.[212]

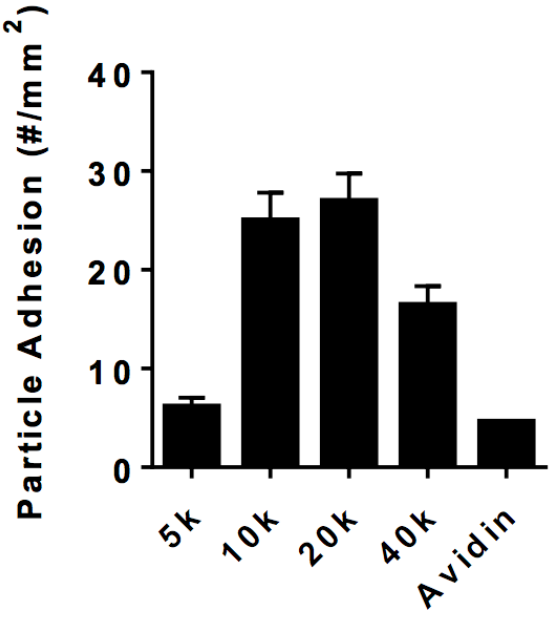

Figure 5.3 Non-specific particle adhesion to an inflamed HUVEC monolayer.
Isotype control IgG (biotin-rat IgG2b, Biolegend) sites were varied on particles ranging from 5,000, 10,000, 20,000, to 40,000. Using a PPFC, particle adhesion to *in vitro* inflamed HUVEC monolayer was determined HUVEC activation was achieved via 4 hour TNF-α incubation, N=3 donors. Error bars represent standard error.

Table 5.1 Particle Ligand Quantification, Target Values Shown in Grey, with Actual Values Determined via Flow Cytometry

Particle	sLe^A Site Density (#/μm^2)	ICAM-1Site Density (#/μm^2)	Total Site Density (#/μm^2)
A	5,000	0	5,000
	5.642 +/- 929	0	5.642
B	10,000	0	10,000
	10,374 +/- 1,369	0	10,374
C	20,000	0	20,000
	19,623 +/- 1.920	0	19,623
D	40,000	0	40,000
	41,040 +/- 2,225	0	41,040
E	0	5,000	5,000
	0	4,526 +/- 1,892	4,526
F	5,000	5,000	10,000
	3,866 +/- 487	4,717 +/- 1,006	8,583
G	0	10,000	10,000
	0	10,938 +/- 2,536	10,938
H	10,000	10,000	20,000
	11,495 +/- 4,631	10,987 +/- 2,466	22,482
I	7,500	2,500	10,000
	6,792 +/- 911	2,976 +/- 675	9,768
J	2,500	7,500	10,000
	2,910 +/- 127	8,891 +/- 220	11,801

We were interested if the increase in sLe^A site density could produce a similar increase in particle binding *in vivo,* which we observed with real-time intravital fluorescence microscopy. Fluorescent particle types A-D were visualized at the surface of the inflamed blood vessel *in vivo,* with qualitative differences in particle adhesion shown in representative still images of Figure 5.4A. The vessel walls of selected veins are indicated with black arrows; particles found

in other vessels, including adjacent capillaries, were not included in the adhesion analysis. Particle adhesion and rolling densities were determined (Figure 5.4B) and the rolling velocities of corresponding particles are shown (Figure 5.4C). No particle binding or adhesion was observed for control particles with isotype-control IgG (Video 5.1). Movies of particles B & C rolling *in vivo* can be seen in Videos 5.2 and 5.3.

Particles A-D successfully adhered to the inflamed endothelium via both rolling and firm arrest. Particle A exhibited the fastest rolling velocity, which corresponded to the lowest occurrence of particles firmly arrested or rolling at the wall. Particle B exhibited a decreased rolling velocity compared to particle A ($p<0.0001$), which corresponded to an increased presence of particles at the wall. Particles C and D had similar low rolling velocities ($p=0.2$), which resulted in more firmly bound particles; Particle C was the most effective, with a ~30-fold increase of total adherent particles over A ($p=0.014$). This corresponded to a ~30-fold increase in rolling particles and a ~20-fold increase in firmly arrested particles ($p=0.012$ and $p=0.042$, respectively). Additionally, particle C produced a ~9-fold increase in total adherent particles over B ($p=0.019$), with a 7.5-fold increase in number of rolling particles and a ~10-fold increase in firmly arrested particles ($p=0.019$ and $p=0.051$ respectively). We observed no statistical difference between particles C and D for either rolling or firmly arrested particles, however the average number of adherent particles was less for particle D ($p>0.05$ for all interactions). As the average velocity of rolling particles decreased, more particles of that type firmly adhered to the inflamed vessel. Particle types C and D had the highest sLe^A surface densities and yielded the highest amount of firmly arrested and rolling particles. This suggests a sLe^A saturation point *in vivo.*

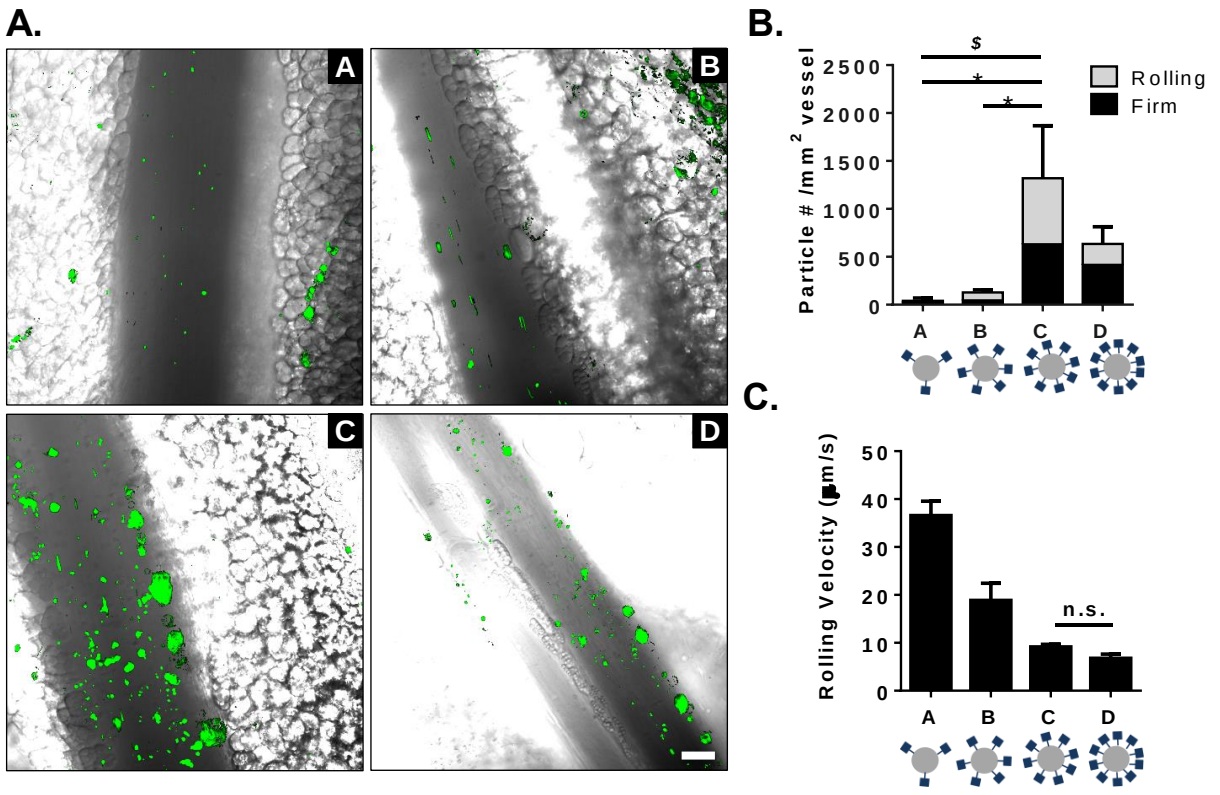

Figure 5.4 Particle adhesion to inflamed mesentery endothelium *in vivo* as a function of total sLe^A sites.
(A) Representative fluorescence images of particle adhesion to inflamed mesentery, top images correspond particles A and B (left to right), bottom images correspond to particles C and D (left to right). Particle fluorescence shown in green, overlaid on the bright field image. (B) Quantified adherent density of firmly bound and rolling particles per representative # second imaging segment, n = 3 mice. Statistical analysis was performed using one-way ANOVA with Fisher's LSD test between total adherent particles, where (*) indicates $p<0.05$, and two-way ANOVA with Fishers LSD test between groups ($) indicates $p<0.05$ between rolling groups, with all else non-significant (n.s.). (C) Velocity of rolling particles found at mesentery wall, $n \geq 50$ particles from n = 3 mice. Statistical analysis was performed using one-way ANOVA with Fisher's LSD test, with all interactions $p<0.001$ except where indicated. Error bars represent standard error, scale bar 50 μm.

Use of dual-targeting ligands enhances particle binding in vivo

We next explored how a mix of targeting ligands could further improve VTC adhesion *in vivo.* We compared a series of particles with varied sLe^A and anti-ICAM-1 ligand densities, as shown in Figure 5.5, to determine if particle adhesion from a dual-targeted particle is merely the

sum from the two individual ligands. The adhesion and rolling propensity of these particles were evaluated in the *in vivo* model of acute mesentery inflammation, as before.

As shown in Figure 5.5A, particles A and E had 5,000 sites/μm^2 of sLe^A or anti-ICAM-1, respectively, while particle F was the direct sum of the two ligands, for a total site density of 10,000 sites/μm^2 (Table 5.1). At a constant ligand density of 5,000 sites/μm^2, varying the ligand type from sLe^A (A) to anti-ICAM-1 (E) resulted in a statistically insignificant increase in particles rolling or firmly arrested on the vessel wall (p=0.5). However, combining sites of sLe^A and anti-ICAM-1 on the same particle (F) resulted in a significant increase of adherent particles at the wall (~7-fold increase over A, p=0.005, and ~3-fold increase over E, p=0.012). For particle F, the number of firmly arrested particles was a ~5-fold (p=0.034) and ~3-fold (p=0.049) increase over A and E, respectively. No differences were observed in the number of rolling particles between groups, however, there were differences in rolling velocities. Particle A had the fastest rolling velocity, while particle F had the slowest rolling velocity, corresponding to the most effective adhesion at the wall. A video of particle type F adhering *in vivo* can be found in Video 5.4. With particle types A, E, and F, a decrease in observed particle rolling velocity corresponded to more particle adhesion at the vessel wall *in vivo.*

To probe the effect of total site density, we investigated particles B, G, and H, which each had twice the site densities of particles A, E, and F, respectively (Figure 5.5B). At these higher total site densities, varying the ligand from sLe^A (B) to anti-ICAM-1 (G) produced a minimal increase of particle presence at the wall, in either firmly arrested or rolling numbers, neither of which were significant from observation for particles A and E. Again, combining sites of sLe^A and anti-ICAM-1 on the same particle (H) resulted in a significant increase of adherent particles at the wall (~2-fold increase over B, p=0.039, and ~3-fold increase over G, p=0.030). The

number of firmly arrested particles of type H resulted in a ~4.3-fold (p=0.007) and ~3-fold (p= 0.011) increase over E and G, respectively. The relationship between rolling velocity and total particle adhesion was not linear in Figure 5.5B, owing to the fact that no particles were detected rolling for particle type G. Interestingly, increasing the total site density of dual-targeted particles from 10,000 (F) to 20,000 (H) sites/μm^2 did not provide a significant increase in adhesion (p=0.5).

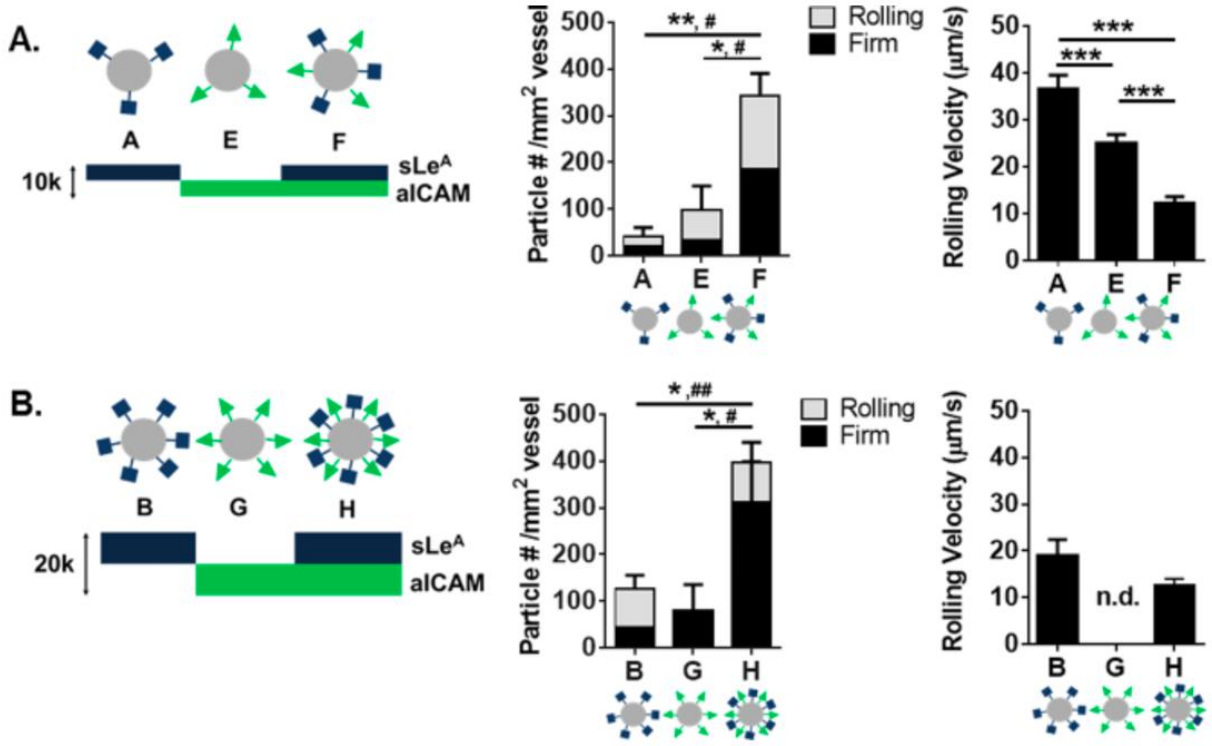

Figure 5.5 Particle adhesion to inflamed mesentery endothelium *in vivo* as a function of combined sLe^A and anti-ICAM-1 sites.
Comparison of dual-targeted particle designs with single ligand densities of (A) 5,000 sites/μm^2 and (B) 10,000 sites/μm^2. *Left*: Diagram of particle conditions with varied amounts of sLe^A and anti-ICAM-1 ligand density. *Middle*: Quantified adherent density of firmly bound and rolling particles per representative imaging segment, $n = 3$ mice. *Right:* Velocity of rolling particles found at mesentery wall, $n \geq 50$ particles from $n = 3$ mice. Statistical analysis of adherent density was performed using one-way ANOVA with Fisher's LSD test between total adherent particles: (*) indicates $p < .05$, (**) $p < .01$ and two-way ANOVA with Fishers LSD test between groups, (#) indicates $p < .05$, (##) $p < .01$ between firm groups, rolling groups n.s. Statistical analysis of rolling velocity was performed using one-way ANOVA with Fisher's LSD test, (***) indicates $p < .001$. Error bars represent standard error.

Particle adhesion of both dual-targeted particle types (F, H) indicate a more than additive effect of each individual-targeting ligand. We further compared the benefit of dual-targeting ligands on a single particle by keeping the total number of sites constant to eliminate any possible enhancement due to the change in total density (as studied in Figure 5.5). We developed a series of five particles with a constant total of 10,000 sites/μm^2, given the lack of benefit when increasing to 20,000 sites/μm^2 (F, H). We varied ratios of sLe^A and anti-ICAM-1 (Figure 5.6A and Table 5.1) and tested these in the model of acute mesentery inflammation. Figure 5.6B is a representative image of the highest dual-targeted fluorescent particle binding *in vivo*. Representative movies of particle types F, I, and J can be found in Videos 5.4-6, respectively. For all five particle types, the number density of both rolling and firmly arrested particles are quantified in Figure 5.6C. The ligand combination on particle I resulted in a significantly increased number of firmly arrested particles compared to all other combinations ($p<0.001$ for all comparisons), with at least a ~3-fold increase over all other ligand combinations. Similar numbers of rolling particles were observed with all five conditions; however as shown in Figure 5.6D, slight decreases in rolling velocities were observed for particles I and F compared to B and J.

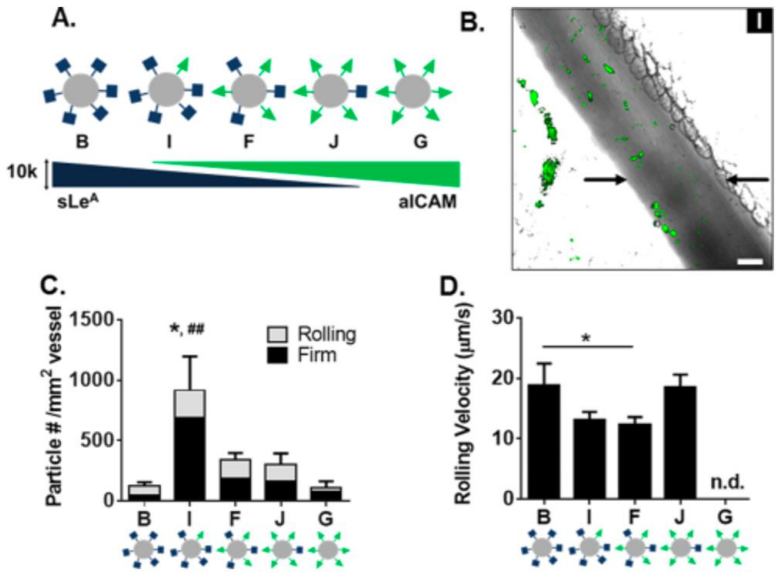

Figure 5.6 Particle adhesion to inflamed mesentery endothelium *in vivo* as a function of varied ratios of sLe^A and anti-ICAM-1 sites.
(A) Diagram of five particle conditions with varied amounts of sLe^A and anti-ICAM-1 ligand density at a constant total site density of 10,000 sites/μm^2. (B) Representative fluorescence image of particle I (7,500 sites/μm^2 sLe^A: 2,500 sites/μm^2 anti-ICAM) adhesion to inflamed mesentery, scale bar 50 μm. (C) Quantified number of fixed or rolling particles on inflamed mesentery per representative imaging segment, $n = 3$ mice. Statistical analysis of adherent density was performed using one-way ANOVA with Fisher's LSD test between total adherent particles: (*) indicates $p < .05$ and two-way ANOVA with Fishers LSD test between groups (##) $p < .01$ between firm groups, rolling groups n.s. (D) Velocity of rolling particles found at mesentery wall, $n \geq 50$ particles from $n = 3$ mice. Statistical analysis of rolling velocity was performed using one-way ANOVA with Fisher's LSD test, (*) indicates $p < .05$, n.d. indicates none detected and excluded from the analysis. Error bars represent standard error.

Optimal dual ligand ratio on particle varies with EC surface expression

Given the dramatic increase in adhesion of particle I *in vivo* over all other ligand combinations in the particle series (Figure 5.6C), we investigated the dependence of particle adhesion on the corresponding surface expression of LAMs on the endothelium. As shown in in Figure 5.7A, TNF-α activation of HUVECs resulted in elevated levels of both ICAM-1and E-selectin surface expression, albeit maximally at different times. Basal levels of ICAM-1were observed in all three conditions, while no basal E-selectin was observed. We further quantified these changes in expression level over time using flow cytometry (representative gating in Figure

5.8), with fold changes over unactivated cells shown in Figure 5.7B. Maximum E-selectin was observed between 4 and 8 hours, while maximum ICAM-1expression was observed at 24 hours. With maximum E-selectin expression, there was elevated ICAM-1expression, with the inverse true for E-selectin at time points of maximum ICAM-1expression. We explored particle adhesion of the panel of five particle types from Figure 5.6A in a PPFC with activated HUVECs at 4 hours (Figure 5.7C) and 24 hours (Figure 5.7D) to probe the importance of HUVEC surface expression on particle adhesion. At 4 hours, particle J resulted in superior particle adhesion, corresponding to ~1.5-fold more bound particles than all other particle types ($p<0.05$ between J and particles I, F, and G). At 24 hours, particle I resulted in maximal particle adhesion, with ~6-fold more bound particles over all other particle types ($p<0.0001$ between all particle types).

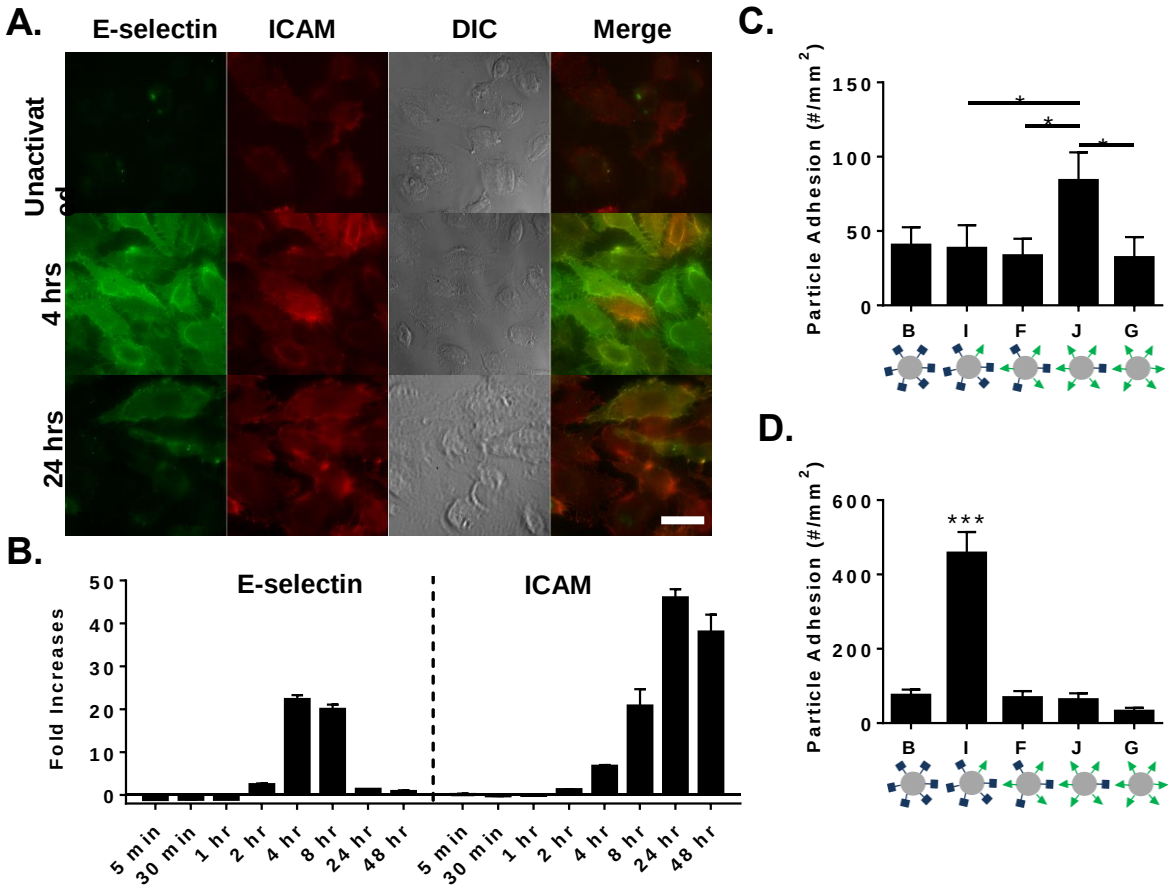

Figure 5.7 Particle adhesion to HUVEC monolayer as a function HUVEC surface expression.

(A) Representative fluorescence images of HUVEC surface expression of E-selectin and ICAM-1 at 4 hour and 24 hour post TNF-α activation. (B) HUVEC surface expression of E-selectin and ICAM-1 (left to right) over time determined via flow cytometry, representative gating in Supplemental Figure 2. Shown as fold increases of MFI over unactivated cells. Quantified particle adhesion following 5 minute PPFC assay after (C) 4 hour and (D) 24 hour TNF-α activation for particles at constant total site density but varied ligand ratios. Statistical analysis was performed using one-way ANOVA with Fisher's Least Significant Difference (LSD) test (*) indicates $p<0.05$, (***) indicates $p<0.001$ between all groups, N=3 donors. Error bars represent standard error, scale bar 10 μm.

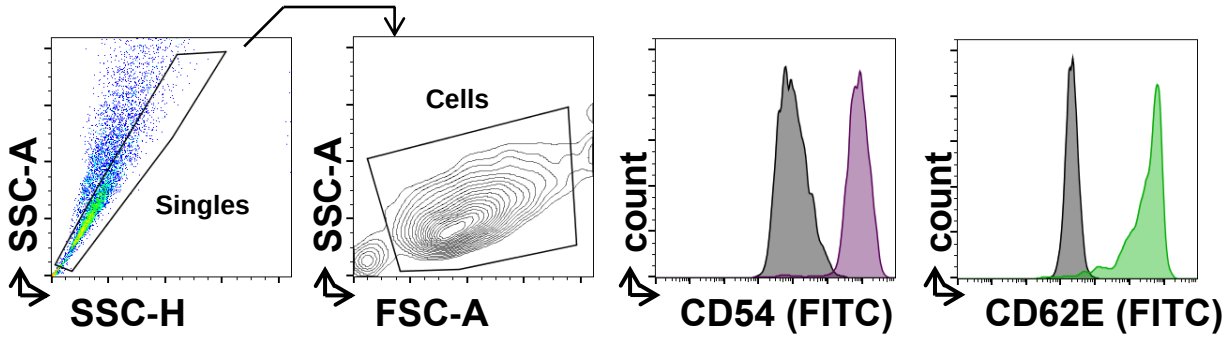

Figure 5.8 Representative gating of HUVEC surface expression.
HUVEC cells were identified as single cells by forward (FSC) and side (SSC). Surface expression of CD45 (ICAM-1) and CD62E (E-selectin) were evaluated by MFI values in the FITC channel. Untreated cells shown in black, purple curve for 24 hour TNF-α activation, green curve for 4 hour TNF-α activation.

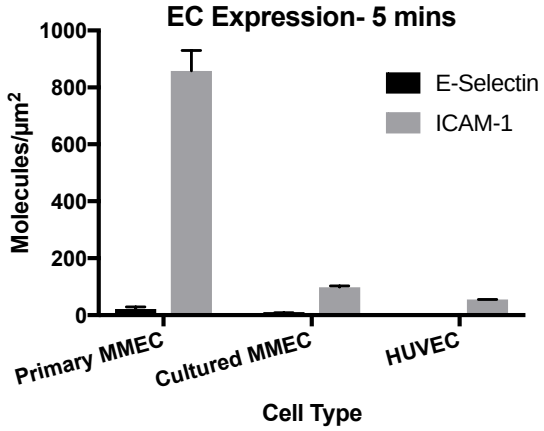

Figure 5.9 Relative E-selectin and ICAM-1 expression of different endothelial cell types after 5 minutes of TNF-α activation.
Surface expression of CD54 (ICAM-1) and CD62E (E-selectin) were evaluated via flow cytometry by comparing MFI values to standard curves. Surface expression was probed on primary mouse mesentery endothelial cells (MMEC), gated for CD106 positive cells only; cultured MMEC, gated by CD31 positive cells only; and (C) HUVEC.

In Figure 5.9 we quantified the expression of three different EC types at the short, 5-minute activation utilized in the intravital method. Of note, this time frame of activation is much shorter than the 4 and 24 hour activations utilized *in vitro* due to animal protocol limitations. Of key importance, the ICAM-1 expression dominates that of E-selectin for all 3 cell types tested. For the primary mouse mesentery endothelial cells (MMEC) this gap was the largest, with ~39

times more ICAM-1expressed than E-selectin. For both cultured cell types, MMEC and HUVEC, there was about ~10 times more ICAM-1expressed than E-selectin.

5.5 Discussion

Despite studies successfully employing dual-targeted particles for vascular delivery, gaps remain in understanding the effect of varied particle ligand densities and ratios. Here, we report a distinct interplay between endothelial receptor expression and particle ligand patterning that determines particle adhesion. To our knowledge, this is the first report of intravital microscopy investigations of dual-targeting VTCs *in vivo*, thus allowing evaluation of both particle rolling and firm adhesion. We find that increasing the number of sites of sLe^A on particles increases adhesion *in vitro* and *in vivo.* We also find that the dual-targeting particle designs result in adhesion superior to that of the linear addition of each individual ligand, indicating a multifaceted relationship in LR interactions. Overall, a 50%-50% split in ligand coverage, which is often studied, did not result in the best adhesion tendencies *in vitro* or *in vivo* under the conditions explored; rather, intermediate ligand regimes produced the best performance. Combined, these results indicate a balance required in LR kinetics, favoring particle designs with more ligands to the LAM receptor with the lower expression level.

Under flow conditions, many forces interact to prescribe the adhesion tendencies of VTCs. First, particles must marginate from bulk blood flow in order to interact with the vasculature of interest; only then does the targeting efficiency matter. Use of whole blood in our PPFC assay reproduces the conditions particles must overcome *in vivo*; particles must marginate to the surface, overcome collisions with blood cells, and be able to adhere in the presence of plasma proteins. Previous literature has demonstrated that 2-3 μm spherical particles are most

efficient at marginating from bulk human blood flow and concentrate in the cell free layer (CFL) near the wall, while 500 nm particles remain uniformly distributed.[10,46] Smaller nano-sized VTCs are appealing for the ability to safely traverse capillaries and travel through intracellular and interstitial spaces in both mouse and human circulation. While 500 nm particles were used in our study, we anticipate the adhesion properties described here to follow similar trends when applied to a range particle sizes. Furthermore, polystyrene particles serve as a model VTC carrier; we anticipate ligand kinetics described here will be applicable to translatable particle formulations, such as poly(lactic-co-glycolic acid) (PLGA). As the particles used in this study were all the same size and material, margination dynamics, and thus interaction potential with the vascular wall, can be considered uniform across all trials; all effects observed are attributable to variations in the surface ligands.

In both our *in vitro* and *in vivo* results, increasing sLe^A densities produced increased adhesion. This increase in single ligand density also slowed the rolling velocity of particles, which has previously been demonstrated for sLe^A functionalized particles over a coated surface.[182] As more LR pair interactions occur, the aggregate LR interaction forces overcome the wall shear force to establish firm adhesion. Avidin's multivalency increases the likelihood of clustered targeting ligands, yet our surface densities never saturated the available avidin sites (Figure 5.2). General increases in ligand density increases the likelihood of a viable spatial orientation that favors LR interactions. However, there were diminishing returns to adding more sLe^A on the particle surface *in vivo*. Other researchers have discussed the steric hindrance limit of antibody ligands, such that too many antibodies on a particle surface block each other from successful interaction with endothelial receptors.[185,186] Though sLe^A is a small carbohydrate unlikely to cause steric hindrance, our results indicate a similar trend, showing a clear limit of

diminishing returns of particle adhesion with increasing site density. Adding more sites of sLe^A did not significantly hinder particle adhesion over the range of densities tested, these data disprove the mantra that "the more, the better" for particle ligands.

The dual-ligand VTC particles studied here target both the selectin and β_2 integrin mediated paths of adhesion to inflamed endothelium. Most previous work in dual ligand particles explores targeting inflammatory surface molecules with mixes of antibodies.[85,86,88,213] Our work aims to explore a dynamic mixing of a carbohydrate-selectin LR pair with an antibody-CAM LR pair, which have drastically different kinetics.[170,188] We first explored the benefit of having two ligands on a single particle, to determine if particle adhesion from a dual-targeted particle is merely the sum from the two different ligands. To answer this, we evaluated the series of particles shown in Figure 5.5. *In vivo,* increasing the total ligand density of either sole ligand type from 5,000 sites/μm^2 to 10,000 sites/μm^2 resulted in non-significant increases in either firmly arrested (A-B, E-G) or rolling (A-B, E-G) particles. When we compare these individual ligand types to dual-targeted particles F and H, we can conclude that there is a more than additive effect when blending the two ligand types. For example, the total number of adhesive particles for dual-targeted particle F is more than the addition of particle A and E; this is also true when comparing particle H to the sum of adhesion from B and G. Particles F and H resulted in increased rolling and adhesive densities compared to both single-ligand particle types. As explained with the rolling velocities, this is likely due to the synergistic activity of the two ligands; sLe^A facilitates initial adhesion, but the rapid off rate guarantees some level of particle rolling,[188] while anti-ICAM-1 facilitates firm adhesion after an initial interaction.[170] When both ligands are present, the behaviors blend to allow initial rolling and eventual firm capture, similar to leukocytes. Various investigations into leukocyte adhesion *in vivo* have demonstrated the

importance of endothelial expression of both selectins and CAMs on cell rolling and adhesion.[214–217] Providing a variety in the ligand presentation on particles corresponding to physiological ratios of endothelial receptors provides additive benefits for VTCs targeting a dynamic endothelium.

As Figures 5.1 and 5.4 demonstrate, increasing the total site density can increase particle adhesion both *in vitro* and *in vivo*. To eliminate the suspicion that comparative observations in Figure 5.5 are purely due to the increased total site density, we compared particles of the same total ligand density (10,000 sites/μm^2), as shown in Figures 5.6 & 5.7. Our results show that an optimal particle ligand ratio exists based on the surface expression of the endothelium, where the most effective particle type has a blend of both ligands and a ratio favoring the least expressed receptor. These results were initially counter-intuitive. At maximum expression of E-selectin (4 hours, Figure 5.7C), we hypothesized that the sLe^A/E-selectin interaction would control particle adhesion, with greater amounts of sLe^A resulting in greater adhesion to the dominant receptor. Instead, our results show the most adhesion for particle J, with 25% sLe^A:75% anti-ICAM-1. A parallel trend was observed at maximum expression of ICAM-1(24 hours, Figure 5.7D), where the most adhesion was achieved with particle I, with 75% sLe^A:25% anti-ICAM-1. Furthermore, the *in vivo* results shown in Figure 5.6C match this adhesion trend in Figure 5.7D. Initially, the receptor profile was not explicitly quantified in the mesentery, but it was known that rapid inflammation induced by topical TNF-α results in P-selectin expression within minutes of stimulation, in addition to omnipresent basal levels of ICAM.[140,141] SLe^A binds non-specifically to all selectins, facilitating the adhesive sLe^A-selectin LR pair interaction. Though initially uncharacterized, the total number of ICAM-1receptors is likely higher than selecting within our short, 5 minute activation.[218] In order to confirm this hypothesis, Figure 5.9 shows that in all 3

live cell types tested, ICAM-1expression far outweighs that of E-selectin, from 10 to 39 times, depending on the cell type. Indeed, basal levels of ICAM-1expression dominate at short, 5 minute activation times, as hypothesized. Combined, these *in vitro* and *in vivo* data support the conclusion that the best ligand design of a particle is dependent on the surface expression of the ECs, showing better adhesion with more ligand for the lesser-expressed receptor. Fewer ligands to the more abundant receptor are required to maximize the benefit of that LR pair (rolling or firm adhesion, for sLe^A and ICAM, respectively). Additionally, more ligands lesser-expressed receptor increases the likelihood that the ligands find the LR pair for an adhesive interaction.

Few studies have delved deeply into the direct effect of each LR pair on multi-targeted particles.[170,210,213] Of those, there has been *in vitro* research corroborating that particle adhesion and rolling velocities depend on both the receptor density, as represented by coated plate coverage, and the particle ligand density.[170,219] In these coated plate studies, particles with increasing amounts of anti-ICAM-1 provided improved firm binding regardless of dominant plate receptor composition.[208] Particles functionalized in these studies had ligand site densities typically less than 1,000 sites/μm^2.[170] Our *in vitro* findings differ in three key ways: utilizing TNF-α activated ECs rather than receptor coated plates, 500 nm particles instead of 6 μm, and whole blood in place of buffer flow, all of which more closely capture the physiological dynamics at the surface of the vascular wall. Our *in vitro* findings are also supported by recent work with 2 μm particles coated with variable ratios of the antibody ligands anti-ICAM-1 and anti-E-selectin, where optimal binding was achieved by a particle of 70:30 anti-ICAM-1:anti-E-selectin ligand composition following 4 hour HUVEC activation.[213] Unfortunately, the total ligand site density was not evaluated in this study. Here, we attribute the success of this particle combination to the surface receptor expression, rather than the cited geometry of the flow

channel. This work on larger, 2 μm particles suggests that the same optimal presentation of ligands on the particle can be extended to particles of different sizes.

Optimization of VTC particle designs that utilize dual targeting is expected to provide improved delivery to the vascular wall. As demonstrated via intravital microscopy, the dual-targeted VTCs studied here rapidly and efficiently adhere to the inflamed endothelium. Importantly, these combinations of ligands provided minimal off target adhesion, resulting in high targeting specificity. Our work suggests that cargo-loaded VTCs with these ligand decorations can provide highly efficient binding to the vascular endothelium, especially when optimized towards the known receptor profiles of the target disease. In addition to this application towards drug delivery, there are possible diagnostic applications of this work. Particle adhesion with dual-targeted particles could help determine the surface expression of diseased endothelium, providing a diagnostic tool to determine stage of a disease with a simple IV injection of a blend of dual-targeted particles.

5.6 Conclusions

Overall, the work presented here represents a truly novel demonstration of particle binding to an inflamed mesentery via intravital microscopy. We have shown that the adhesive abilities of 500 nm particles, which are not preferentially excluded to the vascular wall from blood flow, can be significantly improved by targeting ligand design. While the total number of sites of a single ligand can drive particle adhesion to the endothelium, combining LR pairs from multiple LAM interactions provides a more powerful approach. These dual-targeted ligand designs should be optimized based on the surface endothelium, with ligand coating densities favoring the less-predominant adhesive receptor, as driven by the LR pair kinetics. The

knowledge presented here about the importance of the LR pair matching will help in the intelligent particle ligand design for future applications in all diseases benefitting from VTCs, including atherosclerosis, cancer, inflammation, and many more.

Chapter 6: Impact of Targeting Ligands on Circulation Time and Accumulation at Inflammatory Sites

6.1 Publication Information

This data is not published. This chapter has been merged with chapter 7 into a manuscript, which will be submitted in the coming weeks. It will be entitled: "A Paradigm Shift in Vascular-Targeted Drug Delivery: Hydrogel Microparticles as Carriers for Nanoparticles to the Vascular Wall." The author list will be as follows: **Fish, Margaret B.,** Catherine A. Fromen, Margaret Braunreuther, William J. Kelley, Alison L. Banka, and Omolola Eniola-Adefeso.

6.2 Abstract

Vascular-targeted drug delivery aims to increase the amount of drug that arrives at the disease site, while decreasing side effects that arise due to systemic exposure. In order to achieve this intended objective, the particle carriers with targeting ligands must evade immune uptake and circulate in the vasculature long enough to establish firm adhesion in the diseased area. After adhering, the particles must stay bound sufficiently long enough to release their cargo and achieve a therapeutic effect. We have previously shown that targeted hydrogel particles are able to bind to inflamed mesentery *in vivo.* In this work, we directly compare the pharmacokinetic (PK) behavior of hydrogel particles both with and without targeting ligand. We then determined the capacity of targeted hydrogels to stay adhered over time *in vivo* with two different models of inflammation. We show that for polymerized poly(ethylene glycol) (PEG)-based particles, deformable hydrogels maintain targeted adhesion over an hour in the mesentery, while rigid

hydrogel adhesion drops to less than 50% in this time frame. Over longer time windows, deformable microparticles are able to achieve a targeting window of up to 8 hours, significantly longer than nanoparticles. All PEG-based particles have similar plasma circulation times, regardless of the presence of a targeting ligand. This work directly investigates how adding targeting ligand affects particle PK parameters and the direct translation into targeted particle adhesion and accumulation. Overall, this work demonstrates the importance of particle modulus and size as design considerations for controlling the targeting timeline of different hydrogel systems. These results emphasize the importance of choosing the particle size and modulus for maximizing the targeting time horizons, and has the potential to improve treatments for a variety of diseases, including cardiovascular disease, cancer, diabetes, and more.

6.3 Background

Free pharmaceutical agents, whether administered orally or intravenously, distribute throughout the human body in a pharmacokinetically problematic manner; minimal amounts of drug reach the intended tissues and cells. Depending on the drug properties, there tends to be a small therapeutic window, also known as therapeutic index, between the dose-limiting toxicity and the minimal therapeutically effective concentration.[220,221] This issue initially inspired the field of particulate drug carriers, with hopes to skew the pharmacokinetic parameters of drug delivery.[222–224] As an additional benefit, particles have the ability to protect free drug from degradation in the blood stream while shifting the drug biodistribution and interaction with the immune system versus free drug dosing. Over decades many research groups have investigated particles of widely varying physical properties with a whole host of proposed disease applications, resulting in surprisingly little clinical success.[225] Particles include but are not

limited to liposomes, micelles, hydrogels, polymeric particles, dendrimers, and polymersomes.[226] Unfortunately, even though these carriers are proposed as magic bullets, it has been shown that in cancer specifically, less than 1% of the particles arrive at the intended site of accumulation, the tumor.[166,227,228] Intravenously administered particles must navigate complex blood flow to arrive at the site of disease. Particle size and modulus have been firmly established as important particle properties that determine the transport, circulation time, immune interactions, and biodistribution of these carriers. Briefly, more deformable particles evade immune uptake and circulate longer than rigid counterparts. Additionally, microparticles (MPs) have been shown to be more efficient at binding from whole blood flow, but are more readily phagocytosed than nanoparticles (NPs).[29,38,39,46,106,229] Another crucial property of particulate drug delivery systems is the presence or absence of surface-bound ligands that target particles, thereby changing the whole particle biodistribution and potential accumulation at the targeted site.

Vascular-targeted drug carriers (VTCs) are particulate carriers that have targeting ligands on the surface that specifically bind to receptors on endothelial cells, which line the luminal side of all blood vessels. By strengthening the affinity of particles preferentially to inflamed cells, the field has aimed to increase the local therapeutic exposure while decreasing systemic exposure and toxicity. However, it is debated in the literature whether these targeting ligands can provide a benefit versus bare particle surfaces; the ligands are often proteins, which significantly decrease the circulation time of certain types of particles.[32,33,94] Some use this fact alone as rationale to abandon the targeted particle strategy- these researchers tend to focus on extending the circulation time of particles, even if they lack targeting ligands to direct them to the specific disease site. Those in the targeting camp have thought that if particles rapidly bind, the circulation time should not be considered the only defining particle characteristic. Yet, many

targeting studies look at final time points of less than an hour, which is not long enough to address whether targeting produces the sustained adhesion required to outperform the dosing of free drug and non-targeted particles. These competing paradigms have yet to be tested experimentally in an extended clinical window, meaning we do not know the true potential that VTCs have to deliver sustained release in comparison to untargeted particle and free drug administration.

To address this deliberation in the literature, we explore the behavior of both targeted and untargeted particles for their ability to specifically adhere to cells or tissues, using a range of inflammatory models. We explore how particles of varying moduli and size can adhere to a targeted tissue and how that targeting evolves over time. We approach the question of whether it is worth it to target polymeric PEG-based particles by looking at the circulation time, adhesion in intravital microscopy (IVM) for an hour, and targeting to the lung in an acute lung injury (ALI) model for 24 hours. Our data demonstrate that for polymerized PEG particles, the circulation times are very short, independent of particle modulus, size, and targeting state. However, we found that larger particles bind more in general, as shown by comparing VTCs of 2 μm and 500 nm diameters. Furthermore, rigid VTCs begin to detach within an hour, whereas the deformable counterparts stay bound. Finally, we found that targeting to the lung in an ALI model is dependent on the PEG particle size and modulus; we define clear targeting windows, when targeted particles outperform non-targeted counterparts, of up to 8 hours depending on the combination of VTC modulus and size. This work is the first to approach the question of whether particulate drug carriers, after having minimal success clinically for decades, should be developed as targeted entities, based on how long they sustain targeting after being cleared from circulation. Overall, our results provide an unprecedented perspective on the length of time that

targeted PEG particles, based on size and modulus, are able to maintain adhesion for targeted drug delivery.

6.4 Results

Targeting time IVM: larger, softer particles are best at maintaining adhesion for 1 hour

We first evaluated the ability for targeted particles to adhere at an inflammation site and stay bound for up to 1 hour, using real-time imaging of an inflammation model: mesentery vein IVM. Four PEG-based, spherical particle types were utilized throughout this work, including 2 different sizes and 2 different moduli. 2 μm diameter particles of 15% PEG and 100% PEG composition were designated as MPS and MPH, respectively. 500 nm diameter particles of 15% PEG and 50% PEG composition were designated as NPS and NPH, respectively, designating both the size and either "soft" or "hard" modulus. The "T" at the end designate the targeted status of the particle type. Anti-P-selectin antibody was used as the targeting ligand to bind P-selectin induced by topical application of TNF-α on the mesentery vessels. All particle types were conjugated with the same targeting ligand density of 30,000 anti-P-selectin/μm^2 so that trends were independent of ligand effects. These site densities were confirmed via flow cytometry and have been previously shown to produce firm particle adhesion in this model.[106]

We dosed all four particle types by equivalent mass, 30 mg particles/kg mouse (~0.6 mg of particles), and captured the adhesion in five distinct locations of the mesentery veins every five minutes for an hour. Figure 6.1A and 6.1B shows representative images of the adhesion to an inflamed mesenteric vein 5, 30, and 60 minutes after particle injection for 2 μm and 500 nm particles, respectively. Figure 6.1C shows the adhesion of MP of both moduli over 60 minutes, displayed as both the number per vessel area and that scaled to the mass of particle per vessel

area. Figure 6.1D shows the same but for NP of both moduli, with the y-axis zoomed in to highlight the trend. Two very clear trends emerged, one by size and one by modulus. First, 2 μm diameter MPs bound significantly better than 500 nm diameter NPs for all moduli tested, as highlighted by the different y-axes, varying by a full order of magnitude. In fact, the adhesion over the entire hour was significantly better for both MPs than for both NPs tested; NPs never matched or surpassed MPs in targeted adhesion efficiency in this time frame. Interestingly, both hard particle sizes began to detach within 20 minutes of the particle injection, dropping to about half of the maximal adhesion achieved by the final hour time point (38.6% of max for MPHT and 49.3% of max for NPHT). All the while, soft particles of both sizes were able to at least maintain the adhesion; the soft MPs maintained adhesion while the soft NPs adhesion increased through the hour time frame. Therefore, the superiority of soft particles versus the hard counterparts increased over the hour time window tested. Despite the uniform ligand density employed on the particle surfaces, there are key differences in the ability of particles to sustain targeted adhesion in the acute mesentery vein inflammation model based on both particle size and modulus.

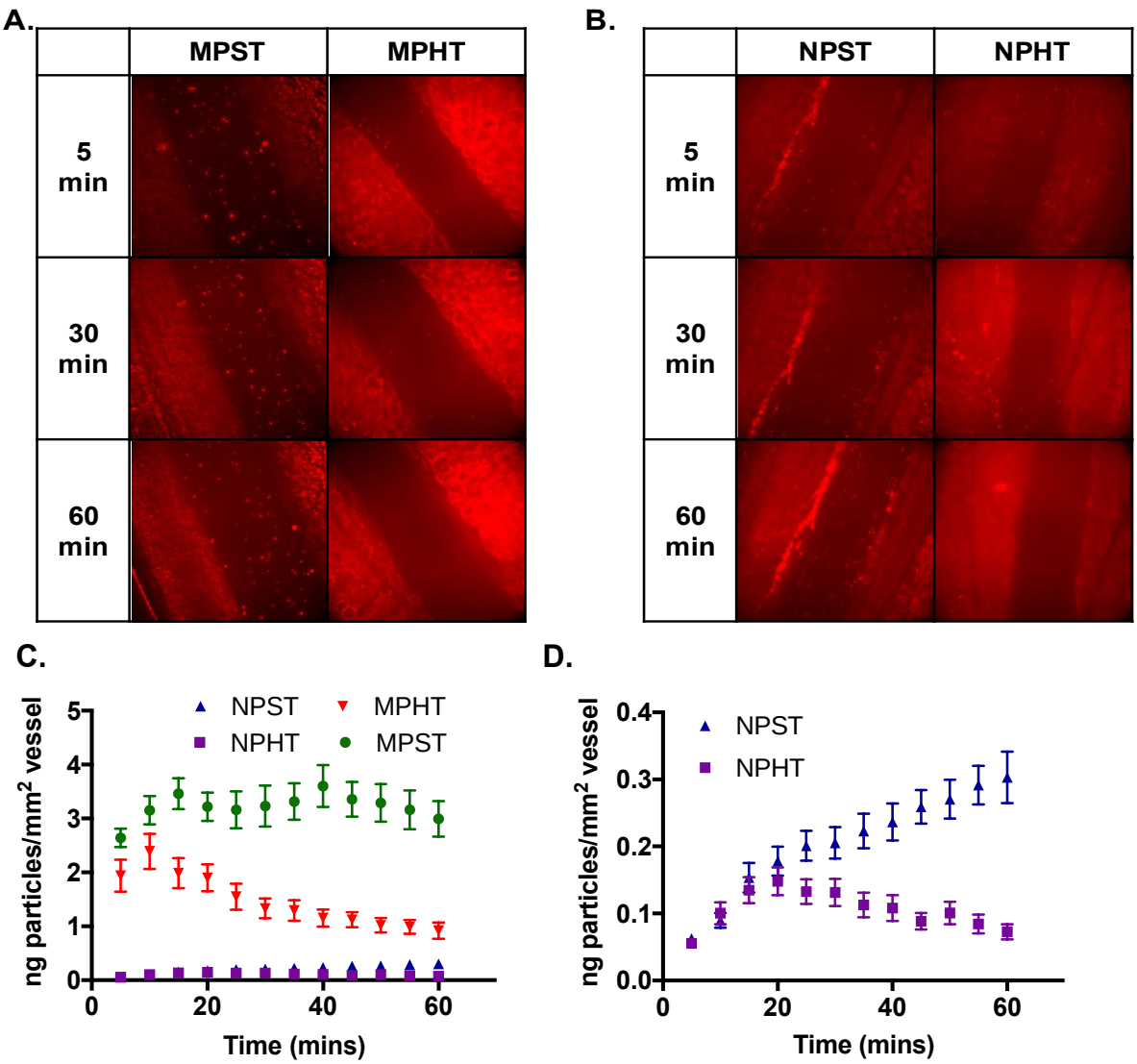

Figure 6.1 IVM to evaluate MP and NP adhesion over time.
(A) Representative images of MPST and MPHT at 5, 30, and 60 minutes post particle injection. (B) Representative images of NPST and NPHT at 5, 30, and 60 minutes post particle injection. The adhesion of particles on an inflamed mesentery vein of both (C) 2 µm and 500 nm diameters over a full hour. (D) Is the same data as (C), but for just the 500 nm particle data zoomed in on the y-axis. Error bars represent standard error for N=3.

Lung accumulation of VTCs in ALI mice

To extend the time window of targeting experiments, we shifted to a different inflammation model, known as the acute lung injury (ALI) model. For this, lipopolysaccharide (LPS) was instilled into the mouse airways to induce a local inflammation event, and one hour

later an equivalent mass of particles (30 mg particles/kg mouse, ~0.6 mg of particles), were injected via the tail vein. We then quantified accumulation in the targeted organ of interest, the lung. The same particles were as used for IVM, excluding MPH for its known short circulation times in the literature, poor performance versus MPS in IVM, and increased risk of producing pulmonary embolism.[38,150] The "T" or "U" at the end of each particle type designates the targeting status of the particle, either targeted or untargeted; anti-intercellular adhesion molecule-1 (anti-ICAM-1) was employed as the targeting ligand for these experiments. ICAM-1 is highly upregulated by the lung endothelium through 48 hours post instillation with LPS, producing a more sustained inflammatory response compared to the IVM method,[75,173,175,230] whereas P-selectin was the VTC target of choice in the IVM because of the rapid expression of P-selectin within minutes of exposure to agonists.[140,141] All particle types were loaded with near-infrared dye to quantify the lung accumulation over time.

Of note, the average vessel size in the lung is much smaller than that evaluated via mesentery IVM method in Figure 6.1. Additionally, higher shear is expected in the lung capillaries versus the mesentery due to physiological differences between capillaries and veins, including vessel diameter and blood flow rate.[117] The particle accumulation in the lung is reported as µg particles/mg lung tissue for Figure 6.2A-C. Figure 6.2A shows a direct comparison between MPSU and MPST to elucidate any benefits of targeting the exact same particle type. Targeting the MPS particle induced statistically increased accumulation in the lung for both the 2 and 4 hour time points, which was resolved by the 8 hours after the particle injection. Thus, the targeting window, which we define here as the time when targeted particles accumulate significantly more in the lung versus the untargeted counterparts, was established between 4-8 hours. Figure 6.2B shows the same comparison for NPS between targeted and

untargeted particles. There was a statistically increased amount of NPST as compared to NPSU for 2 hours after the initial particle injection, which resolved by the 4 hour time point, establishing a targeting window of 2-4 hours. We then investigated NPHT and NPHU, as shown in Figure 6.2C; in line with the results from Figure 6.1D, the hard NPs did not deliver any targeting benefit at the initial 2 hour time point, designating no targeting window in this model. Figure 6.2D-F shows this same data and particle comparisons but represented at % of total fluorescence recovered rather than a particle mass per lung tissue mass. With this representation of the data, the benefit of targeting looks smaller in magnitude overall, but is still maintained statistically through 4 hours in Figure 6.2D.

Area under the curve (AUC) is a PK parameter typically used in the context of blood circulation to compare the exposure of particles to the body; in Figure 6.2G we applied this concept to particle mass accumulation in the lung, representing the particle exposure of each type to the targeted organ. The AUC of MPST is significantly higher than that of MPSU, designating an overall higher exposure of particles in the lung over the time window tested. The same is true of NPST versus NPSU, whereas for NPH there is no increased exposure to the lung by adding targeting functionality. These data establish the difference between targeted and untargeted particles, as a way to measure targeting specificity over time. These results are consistent with the findings of Figure 6.1, where deformable VTC adhesion persisted over time and more rigid VTC adhesion decreased to about 50% in one hour. Yet, we are interested in how the overall biodistribution and circulation of these particles in blood compares to targeted adhesion in both inflammation models over time.

VTCs in ALI mice: circulation time, biodistribution and PK parameters

The experimental setup of Figure 6.2 was repeated, with the same LPS instillation, dosing schedule, and same particle types, but evaluated in the context of blood circulation and biodistribution over 24 hours. Shown in Figure 6.3A-C, the data was collected as the actual concentration in blood by particle mass (mg/mL), which was also represented as the % of the total particle dose in the blood, shown in Figure 6.3D-F. From Figure 6.3, we show that the circulation of all particles is short-lived and qualitatively similar across particle types. By the 30 minute time point, less than 1% of all particle types were still circulating in the blood (Figure 6.3D-F), and MPST and MPSU dropped the fastest, to less than 0.1% in 30 minutes.

The pharmacokinetic parameters of AUC and initial concentration (C_0), obtained from fitting bi-exponential curves using PKSolver to the particle concentrations in blood over time, are shown in Table 6.1. Data was evaluated with both one- and two-compartment models, with comparison of the Akaike information criterion (AIC) determining the two-compartment model as the best fit for all particle types. The AUC is a representation of the body exposure to the injected VTCs, the higher the AUC, the more opportunity for the particles to interact with the targeted vasculature. AUCs ranged from 0.011 to 0.141 [(mg*hour)/mL], for MPST and NPSU, respectively, with the AUCs of untargeted particles are all marginally larger than their targeted counterparts. The C_0 calculated by the model was smaller than the actual injection of 0.6 mg for all particle types, as shown in Figure 6.4, with a significant disparity between the targeted and untargeted of each particle type. The initial concentrations of the targeted particles were calculated as lower by the bi-exponential model, given the blood concentration inputs in Figure 6.3A-C, due to the targeted particle's more rapid clearance in the first 5 minutes prior to the first blood draw. Because of this, the absolute value of the concentrations of the targeted particles were lower at the initial time point of the circulation plots in Figure 6.3. The model uses C_0 as the

initial concentration, even though a uniform, and higher concentration of all particle types were dosed.[231,232]

After determining pharmacokinetic parameters for PEG-based spherical particles, we analyzed overall biodistribution of all particle types at all time points (2, 4, 8, and 24 hours) in the organs of interest as shown in Figure 6.5. The head to head comparisons of MPST and MPSU, NPST and NPSU, NPHT and NPHU are shown consecutively in Figure 6.5A, 6.5B, and 6.5C in units of μg particle per mg of organ tissue. This measure gives a good idea of a hypothetical drug density delivered in each organ. Over time, all particle types increasingly accumulate in organs of the reticuloendothelial system, namely the liver and spleen, after they have been cleared out of circulation. Any accumulation in the lung in the early time points later shifts to that in the liver and spleen. There is little accumulation in the kidney and heart for all particle types and all time points; by 24 hours there is little accumulation in either. For all time points and all organs, except MPST at 2 hours, most of the particles accumulate in the liver than any other organ due to its sheer size. The relative amount in the spleen is significantly less than how the data was presented in Figure 6.5 because of the spleen's small size. Finally, as expected based on the circulation curves and PK parameters, there were few particles remaining in the blood across all time points tested here.

Figure 6.6 is focused on the accumulation of particles into the liver over time in the ALI model, with all time points included in A-C for all particle types, in units of μg particles per mg of liver. As expected, over time the accumulation of all particle types increases as they are cleared out of the blood stream and from the lungs to the liver. There is a clear trade off in accumulation in the liver and lung; as particles leave the lung they traffic to the liver as a

clearance mechanism. The micron-sized particles accumulated in the liver the most by the final time point of 24 hours. Figure 6.7 is a head to head comparison of two different methods of the ALI model 2 hours post particle injection, either with lung perfusion or without before evaluating the amount of particle fluorescence in the lungs. All comparisons between the two methods for one particle type are non-significant, indicating the similarity between the results obtained with the different methods. Figure 6.7 shows the raw differences in adhesion between the two methods; again, all were non-significant, but the MPSU were most affected by the perfusion of the lungs, designating some amount of non-specific entrapment in the lung that is eliminated by perfusion.

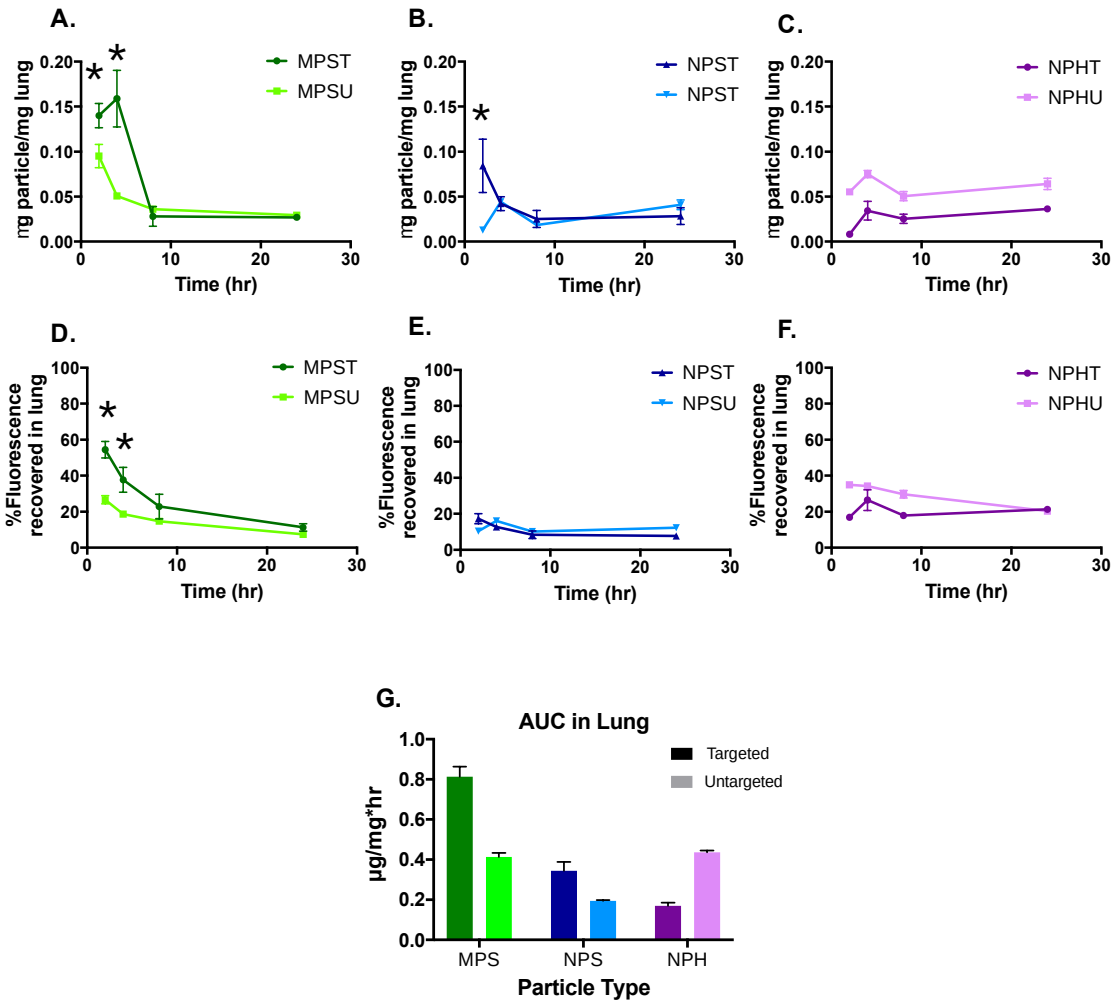

Figure 6.2 Accumulation of PEG-based particles in the lungs of ALI mice.
2 hours, 4 hours, 8 hours, and 24 hours post particle injection. Left to right: (A) MPS (B) NPS (C) NPH. (D-F) Is the same particle sequence, but the data is represented at the % of total dose recovered in the lungs. (G) The Area Under the Curve (AUC) represents the exposure of the organ to each particle type by mass, in units of (µg particles/mg lung tissue)*hour. Bars represent the standard error for N=4 for all plots. Statistical analysis was performed using one-way ANOVA with Fisher's Least Significant Difference (LSD) test (*) indicates $p<0.05$ with targeted lung accumulation over non-targeted lung accumulation.

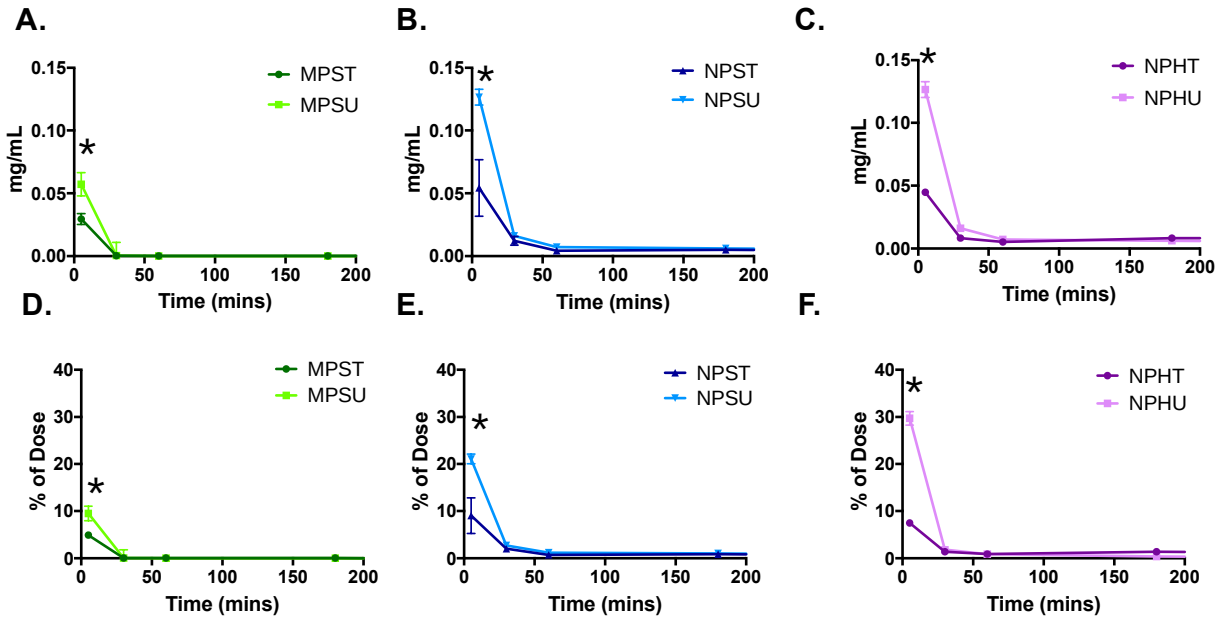

Figure 6.3 Blood circulation profile of PEG-based particles over time in ALI mice.
The concentration of particles remaining in the blood stream of C57BL/6 mice after orotracheal instillation with LPS. Plots are shown for (A) MPS, (B) NPS, and (C) NPH both targeted (T) and untargeted (U). (D-F) Is the same particle sequence, but the data is represented at the % of total dose recovered in the blood. Blood samples were collected at 5, 30, 60 and 180 minutes after the particle injection. Bars represent the standard error from N=4. Statistical analysis was performed using one-way ANOVA with Fisher's Least Significant Difference (LSD) test (*) indicates a higher untargeted concentration in the blood versus targeted, with $p<0.05$.

Table 6.1 Pharmacokinetic Parameters from Two-Compartment Model Fit of Blood Concentration Data in ALI Mice

Particle	C_0 (mg/mL)	AUC_{0-t} (hr*mg/mL)
MPSU	0.156	0.013
MPST	0.093	0.011
NPSU	0.206	0.141
NPST	0.077	0.097
NPHU	0.335	0.099
NPHT	0.083	0.122

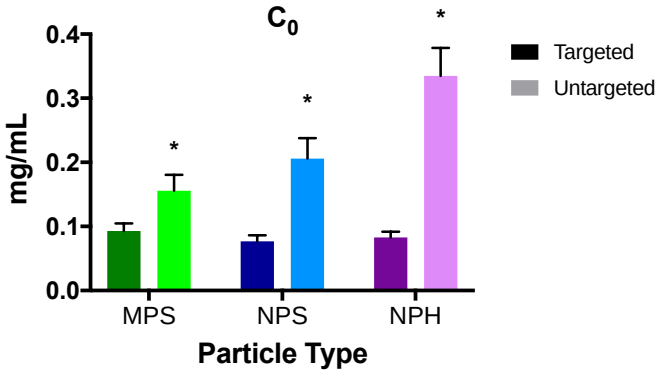

Figure 6.4 The fit parameter C_0, as determined by PKSolver, in the ALI model.
The calculated initial concentration of particles in the blood, based on the biexponential fit of the two-compartment model. N=4 for all circulation plots used to fit this model. Statistical analysis was performed using one-way ANOVA with Fisher's Least Significant Difference (LSD) test (*) indicates $p<0.05$ versus targeted of the same particle group.

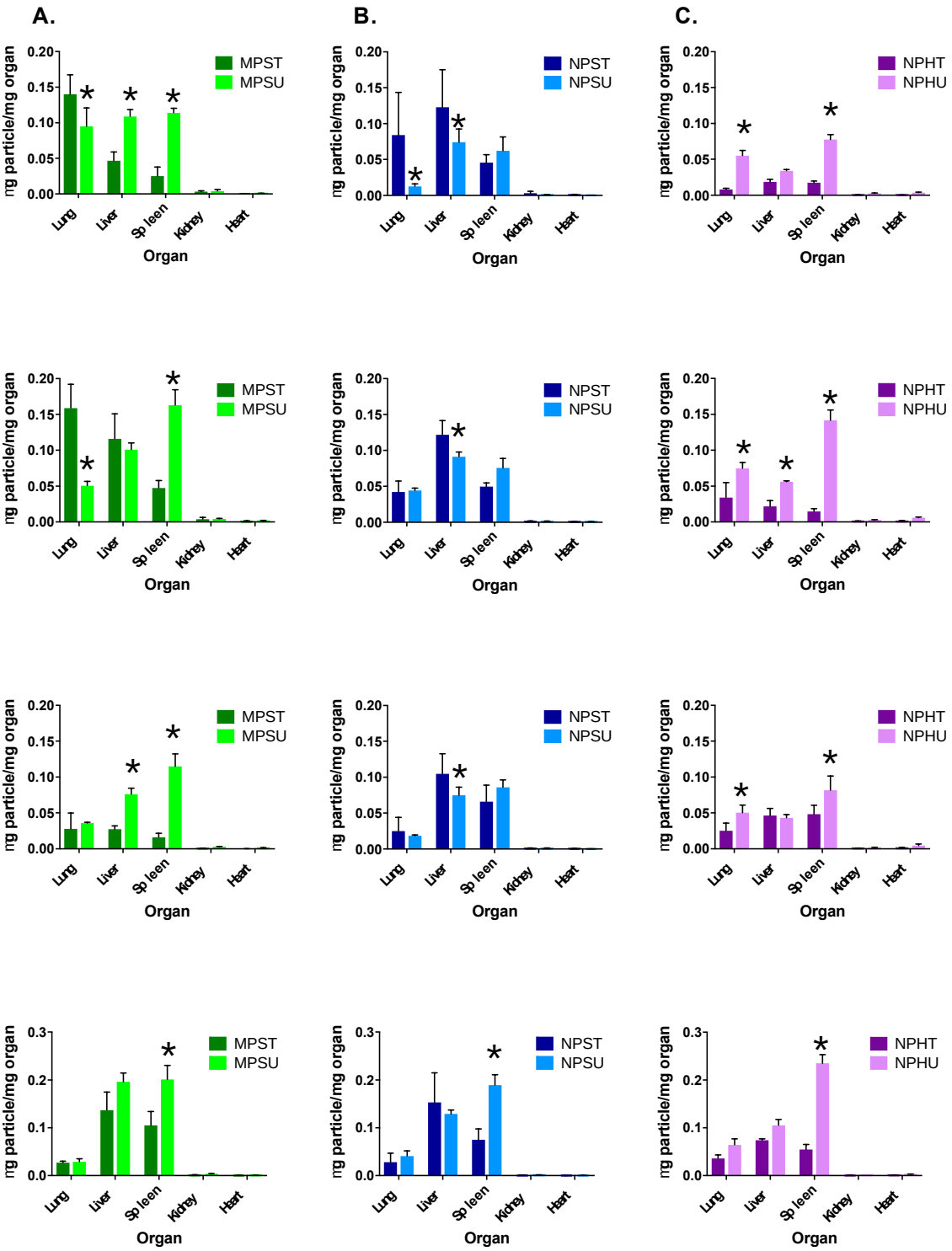

Figure 6.5 Biodistribution of PEG-based particles in ALI mice by mass.
Each row represents a different time point after particle injection: 2 hours, 4 hours, 8 hours, and 24 hours, respectively. The columns represent the different particle types, from left to right: (A) MPS (B) NPS (C) NPH. Bars represent the standard error for N=4. Statistical analysis was

performed using one-way ANOVA with Fisher's Least Significant Difference (LSD) test (*) indicates $p<0.05$ versus targeted particle of the same type.

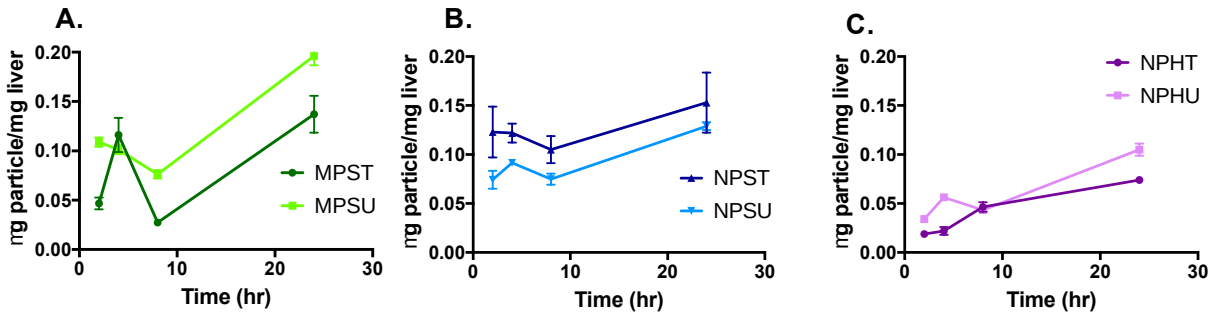

Figure 6.6 Accumulation of PEG-based particles in the livers of ALI mice over time. 2hours, 4hours, 8hours, and 24 hours post particle injection. Left to right: (A) MPS (B) NPS (C) NPH. Bars represent the standard error for N=4.

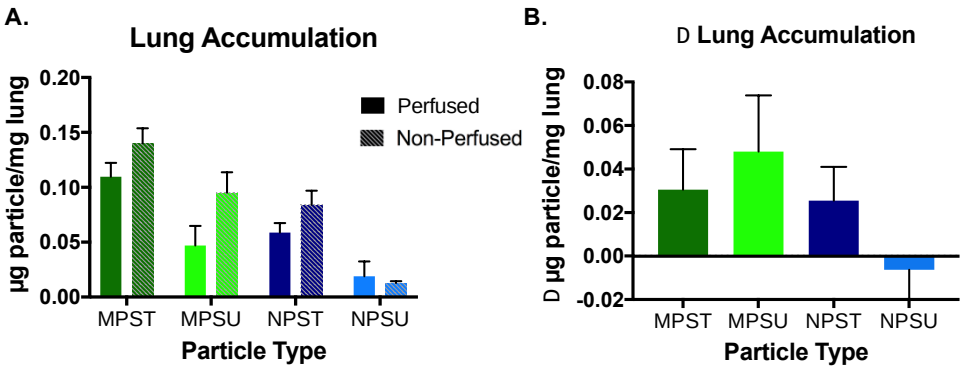

Figure 6.7 Impact of lung perfusion on particle lung accumulation in ALI model. (A) Head to head comparison of particle accumulation in the lung obtained when the lungs are perfused or not perfused, 2 hours post injection. Within each particle type, there is no statistical difference between perfused and non-perfused; statistical analysis of lung accumulation was performed using one-way ANOVA with Fisher's LSD test between perfusion conditions. (B) Difference in µg particles/mg lung tissue from non-perfused to perfused. The particle types MPST, MPSU, NPST, and NPSU are included. N=3 for all and error bars represent the standard error.

6.5 Discussion

To date, no study has extensively evaluated the time horizon of targeting functionality for biocompatible PEG-based particles, especially for VTCs in the MP size range. For vascular

targeting to deliver a clear benefit over free drug administration, targeted particles must be able to bind to inflamed vasculature and stay bound longer than untargeted particles, to release the loaded cargo. This work confirms the ubiquitous superiority of MPs over NPs for targeting efficiency, as found in our previous *in vitro* and *in vivo* work.[122,138,229] Additionally, we found that in two different models of inflammation, including blood vessels of varying diameter, soft VTCs were better than rigid counterparts at maintaining targeted adhesion, and soft MPs delivered the largest targeting window of all, up to 8 hours. Others' have utilized a large range of hydrogel moduli for drug delivery applications,[38,105,144–149] but have not established a true targeting window to inform VTC and dosing design. There is a critical need to determine and understand the targeting windows of particles developed with the intention to translate into the clinic; this information is vital in the engineering of particles, their loading, release, and dosing schemes.

In this work, we utilized a range of particle size and modulus, including 2 μm and 500 nm diameters and 15%, 50%, or 100% PEG compositions. We wanted to know how both targeted particles interact with inflamed endothelium in real time. In our IVM results in Figure 6.1, the MPs adhere better than all NPs because of the superior ability of MPs to marginate to vessel wall versus NPs in hemodynamic conditions.[10,46,106] A range of mechanisms could explain the difference in adhesion behavior after particles of different moduli are bound to the vessel wall. Of note, the differences in circulation time between rigid and soft PEG particles is not enough to explain these differences; all particle types are cleared in a statistically similar fashion and the phenomena is removal of rigid particles after initially bound. Leukocytes have the potential to disrupt particles in two ways: by physically colliding with them on the vascular wall and dislodging them, or by actively phagocytosing them off the vessel wall. Alternatively, the

surface receptors of endothelial cells are extremely dynamic and the constant recycling and resolution of expression could affect particle binding over time.[75,233,234] This would decrease the number of ligand-receptor pairs engaged, decreasing the adhesive force holding the particle on the wall, allowing the hemodynamic force of flow to shear the particles off. In looking at Figure 6.1, the soft particles maintain their binding, therefore we do not expect that the recycling of surface receptors is the dominant mechanism driving this behavior. Yet, these less rigid particles are able to deform once bound, allowing more ligand receptor interactions per particles and lessening the stress on each bond due to particle deformation.[181,235] As for the contribution of leukocytes, it is likely a combination of both physical collisions and phagocytosis; indeed, leukocytes are known to be a substantial player in particle clearance,[236,237] and rigid particles are more readily removed by phagocytic cells.[39,106] The trend of particle targeting over an hour was clear by both size and modulus in IVM, but to evaluate VTC behavior for clinically-relevant, longer time windows we moved to a different experimental method. Overall, these results indicate that softer particles have maximal potential to maintain any adhesion achieved, with MPs significantly better than NPs.

The lung ALI model was introduced to investigate longer time points to overcome the protocol-imposed time constraints of IVM. There are significant differences between the IVM and ALI models; most importantly are the inflammatory prompt of TNF-α versus LPS and the difference in targeted vessel size. In the mesentery we selected veins of about 150-250 μm in diameter, whereas in the lung the majority of the vasculature is capillaries with diameters less than 20 μm.[238] This difference in vessel size dictates different forces experienced by particles in blood flow and bound to the vessel wall. Figure 6.2 highlights the key results from this ALI study, the accumulation of particles in the inflamed lung over a 24-hour time frame. MPST are

again better than all NP conditions, like the IVM model in Figure 6.1, especially in the 2 to 8-hour time window; for these times, MPST are the best performers.

We define the targeting window in the ALI study as the time frame where the targeted particles result in significantly more lung accumulation than the untargeted counterparts. In line with the mesentery IVM, the hard particles, down-selected to NPHT and NPHU for this inflammation model from a combination of safety and performance perspectives, showed no ability to target in the 2 to 24-hour time window; this aligns with the particles binding being reduced to only 50% of the max binding within 1 hour after injection in the IVM method. MPH resulted in significantly less adhesion than MPS previously, so was not included here for its poor performance and increased risk of causing lung emboli and non-specific accumulation in capillaries, which would confound results. Together, these data suggest that rigid PEG-based hydrogel particles, though orders of magnitude less rigid than often-used biocompatible materials such as poly(lactic-co-glycolic acid) or polycaprolactone,[239] are still not soft enough to deliver targeting over an extended time window needed to make intravenous particle drug delivery clinically viable. We show a difference for the soft particles of the same modulus but two different sizes, 2 μm and 500 nm. The NPST particles deliver a targeting window between 2 and 4 hours, whereas MPST deliver an extended targeting window between 4 and 8 hours. Again, the same possible mechanisms can be driving the reduction in targeted particle accumulation in the lung as were in the mesentery. We know that in the ALI model the targeted receptor, ICAM-1, persists and increases in EC density through 24 hours, longer than the time frame of our experiments.[125,240] Therefore, the decrease in targeting over time must be due to the physical collision and phagocytic action of leukocytes in the inflamed lung vasculature. Additionally, neutrophils, a particular subset of leukocytes, are known to be hyperactive in ALI models with

regards to accumulation and action such as phagocytosis in the lung in response to inflammation.[125] Therefore, we hypothesize that the behavior seen in lung accumulation and clearance is heavily correlated to the behavior of neutrophils occupying and functioning in the same vascular and tissue space as our PEG-based particles. In the context of phagocytosis, researchers have shown that deformable particles are phagocytosed significantly slower than rigid particles of the same composition,[101,104,150,241] which bolsters the argument that leukocyte phagocytosis is the driving mechanism that creates the key differences between soft and rigid particles.

For all particle types tested through the longer 24 hour experimental time window, we found extremely short circulation times. The known benefit of "PEGylation" is manifested when it is grafted onto the surface, either in mushroom or brush conformation, to resist protein opsonization.[32,33] Of note, our particles are composed of polymerized PEG, which has been previously shown to have short circulation times *in vivo*, even at relatively low moduli and corresponding crosslinking densities.[38] Additionally, our targeted particles had either anti-P-selectin or anti-ICAM-1 on the surface; proteins on the surface of particles are known to increase immune recognition and therefore decrease circulation times.[32,33,91] Since the circulation time of our untargeted particles is short to begin with in Figure 6.3, the addition of targeting ligands keeps these values low, but does not significantly change the amount circulating. It is key to remember that particles may exit the blood stream with two different destinations: the targeted lung, which is a positive event, or the RES, which is still considered negative clearance. The removal of MPs from the blood stream and into the lungs likely dropped the MP concentrations in the blood, as seen in Figure 6.3.

The predicted initial concentrations are significantly lower for those targeted particles, as shown in Table 6.1 and plotted in Figure 6.4. This C_0 can be thought of a representation of what happens before the first experimental blood draw at 5 minutes; the lower the C_0 value, the more that is cleared in the short 5 minute window. Namely, more of the targeted particles are cleared faster, as corroborated by the smaller C_0 values. This could be due to a phenomenon known as target-mediated drug disposition, where the pharmacokinetics of an entity with high affinity is affected by binding to the targeted site.[242] Even with these very short circulation times, the recirculation time of a whole mouse is only 6 seconds, meaning the particles have multiple passes through the targeted vasculature before clearance.[243] Our short circulation times align with values of crosslinked PEG in the literature, where Merkel noted that a 10% crosslinked hydrogel particles had a half-life of 0.038 hours *in vivo*.[38] It is important to note that large differences in circulation times arise between particles that are either targeted or surface grafted with PEG, rather than simply bare.[33,91] Overall, our intravenously injected particles circulate for short times whether there or not there is targeting ligand on the surface. Thus, any targeted accumulation found after a few minutes is overcoming the rapid clearance mechanisms found *in vivo*.

Our work provides an interesting perspective on the ability of PEG-based particles of different sizes and moduli to target inflamed tissue and the resulting quantitative benefit of this targeting over time. Importantly, the circulation times of particles is not the most significant indication of particle accumulation, rather, the targeting and retention in the organ of interest is more indicative of VTC system success. Again, even though our particles were cleared within the order of 10 minutes, they were able to stay bound in the targeted organ for up to 8 hours. This conclusion will inform the intelligent engineering of VTCs for intravenously delivery and will

allow further development of particle systems that have short circulation times. Researchers have shown that the targeted adhesion and resulting biodistribution heavily depends on the targeting ligand density and mix of multifunctional targeting ligands.[33,46,122,244] For each engineered system, our work builds a framework of expected targeting window, but this and the biodistribution will undoubtedly change with changes in ligand number, ligand type, disease, and endothelium expression. Thus, future work in the field should investigate each VTC system carefully in the best disease models possible. We hypothesize that multifunctional targeting would simultaneously increase the initial targeting specificity achieved and the immune recognition, thereby slightly decreasing the circulation time but allowing for the possibility of more targeted accumulation in the first 5 minutes that has the potential to stay for hours. Lessening the amount of targeting ligand would decrease the overall adhesion in the areas of inflammation, thereby skewing the targeted biodistributions closer to those of the untargeted particles.

This study provides clear guidelines for and conclusions about the resulting timeline of particle adhesion once adhered to the vessel wall. In general, using particles instead of free intravenous drug alters this pharmacokinetic profile in the blood serum. In the context of maintaining a drug dose in the therapeutic window in the body, between the minimally effective dose and toxicity threshold, our work gives detailed biodistribution and circulation data that will help inform and predict systemic and organ-specific toxicity. Of course, all of this is very drug molecule and release mechanism dependent. Particles can be designed to degrade in the time window of targeting via mechanisms such as ester hydrolysis,[245,246] or enzymatic release,[247–249] thereby maximizing the amount of drug that reaches the target cell before the majority is trafficked to the liver and spleen. Indeed, the information presented here will allow much tighter

control of future VTC systems and better pharmacokinetic understanding. We highly encourage this sort of work be expanded for many other types of VTCs in development today.

6.6 Conclusions

The work presented here is the first demonstration that the ability of particles to maintain targeting to inflamed vasculature is heavily dependent on both the particle size and bulk modulus. For VTCs to deliver the theorized benefit of extended release profiles over free drug, the particles must stay bound near the disease site. This work represents a comprehensive study of PEG-based particles, with and without targeting ligand, to understand the true targeting benefit delivered *in vivo*. First, our findings confirm that micron-sized particles of all moduli are significantly better than all of our nano-sized particles tested at maintaining adhesion once bound, which ultimately controls the amount of cargo that is delivered to the vessel wall. The circulation time of all polymerized PEG particles employed is low, and yet, in both models, a significant number of particles remain bound after most the particle dose is cleared, indicating that circulation time is not the deterministic parameter. These modular hydrogel particles can target the vasculature in a variety of diseases, and have the potential to be utilized for a range of treatments in widespread diseases such as cardiovascular disease, cancer, diabetes, and more. This work emphasizes the importance of choosing the particle size and modulus for maximizing targeting over long time horizons and encourages the continued examinations of VTC systems in this manner.

Chapter 7: A Paradigm Shift in Targeted Drug Delivery: Hydrogel Microparticles as Carriers for Nanoparticles to the Vascular Wall

7.1 Publication Information

This data is not published. This work has been merged with chapter 6 into a manuscript, which will be submitted in the coming weeks. It will be entitled: "A Paradigm Shift in Vascular-Targeted Drug Delivery: Hydrogel Microparticles as Carriers for Nanoparticles to the Vascular Wall." The author list will be as follows: **Fish, Margaret B.,** Catherine A. Fromen, Margaret Braunreuther, William J. Kelley, Alison L. Banka, and Omolola Eniola-Adefeso.

7.2 Abstract

Vascular-targeted drug carriers (VTCs) must localize and bind to a targeted, diseased endothelium to achieve clinical utility. There is a great need to improve the proportion of injected particle dose that ultimately reaches the targeted tissue. Frequently used nanoparticles (NPs) are limited in their ability to marginate to the vessel wall from blood flow versus microparticles (MPs). However, NP drug carriers remain attractive as they can better take advantage of the enhanced permeation and retention (EPR) effect for uptake by targeted cells and intracellular drug delivery, and can also more easily transcytose into key tissue spaces compared to MPs. Here, we propose the use of biocompatible hydrogel MPs as carriers for smaller NPs to the vessel wall. We previously showed that hydrogel MPs adhered significantly more efficiently than NPs, and that deformable MPs adhered best in low shears, while rigid MPs adhered best at high shears. The engineered VTC system in this work leverages the size and modulus of two

particle types to increase NP delivery. We investigate how bulk hydrogel properties and NP loading determine the adhesion of VTCs to the vascular wall under physiological blood flow conditions and the resulting NP payload delivered. In general, deformable hydrogel MPs bound better under low shear and more rigid MPs under high shear, with the hydrogel modulus being the key variable. More importantly, at a fixed dose of NPs *in vitro*, deformable particles delivered a larger NP payload at the low wall shear rates and rigid particles delivered more NPs at the high wall shear rate tested. *In vivo*, the deformable particles far outperformed free 50 nm NPs, where the loading density into hydrogel MPs did not change the overall number of NPs delivered. Overall, this work is a key paradigm shift in targeted drug delivery: hydrogel MPs can be used to more efficiently traffic smaller NPs to the inflamed endothelium of interest, proposing a new way to greatly improve clinical theranostics with applications for many diseases.

7.3 Background

VTCs are engineered to adhere and accumulate at sites of disease, producing localized delivery of drugs with the goal of increasing the local therapeutic payload and decreasing systemic toxicity. Current research in the targeted drug delivery field has established that physical properties of the carriers, including size, and modulus, affect the ability of particles to marginate from bulk blood flow to adhere at the site of disease or inflammation.[10,106] These physical parameters can greatly impact the final performance of a VTC system, as successful margination from bulk blood flow is a prerequisite for the final adhesion of the particles; active ligand-receptor interactions must occur for the particle to adhere. Upon firm interaction, VTCs can release their drug payload to the diseased endothelium and into the adjacent tissue.

Biocompatible, biodegradable NPs are often cited as appealing drug delivery candidates for both targeted and non-targeted applications for a variety of reasons. Non-targeted particles in the 20-80 nm range avoid immune recognition and clearance, minimizing cellular phagocytosis and enabling long circulation half lives in the bloodstream.[250,251] Their high surface area to volume ratio makes them ideal drug carriers, with drug loading near the particle surface enabling rapid release from the carrier,[252] and allowing for a more finely tuned pharmacokinetic release versus a single intravenous dose. Once near the vascular wall, although NPs are typically too large for paracellular diffusion, they are able to transcytose more readily than MPs into the adjacent tissues beneath endothelium.[71,253,254] Furthermore, NPs in the 20-80 nm range are able to passively diffuse through disordered vasculature often present in tumors, taking advantage of the EPR effect.[255,256] However, recent work and reviews have revealed that less than 1% of injected doses make it to the tumor site, far from the "magic bullet" name so often used.[166,227,228] A main issue with this is the diminished ability of nano-sized particles to marginate and bind to a vessel wall from whole blood.[10,46] Instead, research has shown that 2-5 μm particles marginate much more effectively than NPs.[10] However, rigid, polymeric particles in the micrometer size range optimal for margination could produce dangerous capillary occlusions *in vivo* and lack many of the benefits detailed for NPs. In parallel to the VTC size work, researchers have established particle modulus as a key physical property and shown that lower VTC modulus both decreases non-specific particle entrapment and increases circulation time *in vivo*, due to slower filtration rates and phagocytosis by immune cells.[38,39,104,150,153] Furthermore, we have recently demonstrated that the targeting ability of MPs is dependent on both the MP modulus and the local shear rate. Soft, more flexible particles are more efficient at margination under low shear

conditions found typically in veins, while stiffer, more rigid MPs are more efficient under higher shear conditions found in arteries or partially blocked, diseased vessels.

In this work, we sought to leverage the benefits of two different sizes and different moduli, by loading rigid NPs into deformable hydrogel MPs for delivering NPs to the endothelial cell (EC) wall. Recent studies have explored the use of bulk hydrogels loaded with NPs for a broad range of applications, including the controlled release of insulin,[257] bone tissue proteins,[258,259] glaucoma therapeutic,[260] local anti-inflammatories,[261–263] oral anti-inflammatories,[264] and antibacterials[265,266]. In these studies, NPs were released from bulk hydrogels via a variety of mechanisms, including non-specific hydrolysis, pH and thermos-specific hydrolysis, and infrared light-triggered release. A few others have loaded NPs into larger MPs in the range of 100 μm diameter, and studied the resulting encapsulation[267] mainly for increased solubility of poorly soluble drug-loaded NPs.[268,269] Some work has developed NP-embedded MPs for treatment of lung disorders via inhalation,[270,271] while others have shown favorable release kinetics via oral delivery,[272] while some have only tested on the bench top.[273] Most of these formulations involve spray drying of powders, which results in polydisperse collections of non-spherical MPs. Some call these methods a type of "Trojan Horse", in that NPs can be covertly delivered to the tissue of interest without recognition by the immune system.[269] While these studies demonstrate the feasibility of loading NPs into a hydrogel carrier, to date, no one has loaded NPs into hydrogel MPs in the 2 μm size range for intravenously administrated vascular-targeted drug delivery and evaluated the system both *in vitro* and *in vivo*. This is the first known work that proposes the use of deformable hydrogel MPs as carriers for rigid NPs to directly improve margination to the vessel wall. We propose the exploitation and sequential harnessing of complementary characteristics of the different particle types employed for the

increased trafficking of rigid NPs to inflamed endothelium. To address this deficiency in the research field, we investigate 2 μm hydrogel particles of varying moduli loaded with polystyrene (PS) NPs (500 nm and 50 nm). We explore how modulus and the molecular weight of highly biocompatible, FDA-approved poly(ethylene glycol) (PEG) used in the fabrication of the hydrogel MPs affect loading efficiency by comparing relative fluorescence of the loaded MPs under controlled fabrication conditions. We investigate the impact of two different variables: the bulk material modulus and the number of loaded NPs, on margination and adhesion both *in vitro* in human blood flow assays and *in vivo* via intravital microscopy. Our data demonstrate that the loading of rigid NPs into deformable MPs slightly affects the modulus of the MPs, but in a way that would not alter the *in vivo* circulation time of low modulus VTCs. Importantly, our work shows that head to head, delivering NPs loaded into hydrogel MPs is between 630% and 5,450% more efficient than free NPs alone, depending on the hemodynamic conditions. For small NPs that do not marginate well, we report a dramatic increase in NP delivery to the inflamed vessel wall. This is the first study to examine the possibilities of loaded MPs as a method to increase margination and adhesion of NPs, and therefore offers important insight into utility of loaded MPs as carriers for NPs, and exciting improvements for many therapeutic applications.

7.4 Results

NP loading dictated by NP size, PEG molecular weight, and % solids in composition

We first investigated how different parameters in the emulsion fabrication system impacted the loading of PS NPs into spherical hydrogel MPs of 2-μm diameter. Loading of NPs into hydrogel MPs was evaluated by flow cytometry; all PS NPs utilized were fluorescent green and the number of NPs per particle directly correlated to the quantified median fluorescent

intensity (MFI). Fabrication of PEG-based hydrogel MPs was as previously reported,[106] using PEG diacrylate (PEGDA) of 700 Da molecular weight (MW), with the addition of varying amounts of PS NPs, except where the PEG MW is noted as varied. Lyophilized NPs were suspended in predetermined volumes of PEG hydrogel precursor solution so that upon photopolymerization, the NPs were physically entrapped in the hydrogel matrix. Reaction conditions for the PEG hydrogels are detailed with the resulting physical properties in Figure 7.1; the hydrogel pores are only 3.5 nm and 0.3 nm for the 15% and 50% PEG conditions, respectively; thus, we do not expect any diffusion of the NPs out of the MPs. Flow cytometry gating ensured characterization of only hydrogel MPs, with exclusion of free NPs based on their small diameter.

To determine how different parameters affected NP loading, we evaluated the importance of PS NP size, PEGDA MW and PEGDA composition in the final NP loading into hydrogel MPs. We tested both 500 nm and 50 nm NPs diameter in Figure 7.2A, fabricated at initial equivalent volume fractions as specified in the methods. The 50 nm particle loading increased linearly with increased volume percent of NPs. The 500 nm particle loading also increased with the volume percent of NPs, except for the 15.6% v/v, where the MFI dropped significantly and fewer hydrogel MPs total were formed. We hypothesize that this was due to the larger NPs inhibiting the end group proximity required to initiate the crosslinking and formation of hydrogel MPs. In summary, we successfully loaded a range of NPs into 2 μm hydrogel MPs. We found the saturation limit for the 500 nm particles at 15% v/v. Conversely, we achieved a linear loading for 50 nm particles across the studied range. Next, we were interested if varying the PEGDA MW would increase NP loading due to different crosslinking dynamics of varying length monomers. Figure 7.2B shows the importance of PEGDA MW in the loading of 50 nm NPs with

250, 700, and 10,000 Da PEG monomer. Higher MW PEGDA delivered the highest loading efficiencies, followed by the low MW PEGDA, and the intermediate PEGDA MW produced the least loading. In all cases, loading of the 50 nm NPs increased with increased % v/v NPs, indicating that loading saturation had not been reached for any conditions tested. Next, we explored whether the number of NPs loaded changes with MP modulus by varying the PEGDA composition within the emulsion to achieve MPs with varied crosslinking density and modulus, but the same loading of NPs. Figure 7.2C shows a plot of NP loading into hydrogels MPs with varying amounts of PEG composing the hydrogel matrix. In Figure 7.2C, the higher % solids on the x-axis means more PEGDA and crosslinking present during fabrication, which resulted in higher modulus particles. We found that with the same number of NPs in the formulation prior to polymerization, more heavily crosslinked particles loaded and retained more NPs in the hydrogel MP. This is likely because with a set volume of NPs and increasing amount of polymer present, more end groups are readily available to polymerize together and encapsulate more NPs.

From this work, we elected to study delivery of 50 nm NPs, as both a larger number and more volume can be loaded into a single hydrogel MP. Additionally, the 50 nm size is more amenable to endothelial transcytosis, intracellular delivery, and the EPR effect than the 500 nm diameter NPs.[71,253–256] We focused our evaluation on two different % solids of PEGDA, to determine how the overall MP modulus may impact NP delivery to the vascular wall. All MPs were fabricated using the 700 Da MW PEGDA monomer. Finally, for each of the MP of varied moduli, we evaluated different NP loading to assess if more NPs per MP was more efficient at delivering NPs to the vessel wall. In Figure 7.2D, we report the MFI of the particles selected and utilized for the remainder of this work. We find that with the loading and PEG formulations employed, we obtained a range of NPs/MP. Subsequent *in vitro* and *in vivo* experiments will be

performed with “soft” 15% PEG particles with 2 different amounts of NPs loaded, and one “hard” 50% PEG particle with NP loading. A schematic of these particles is shown in Figure 7.2E, along with designations of how they will be discussed moving forward. This set of different particle types will help determine what level of loading and which hydrogel bulk modulus are optimal for each hemodynamic condition tested.

A.

Label	% MeOH	% PEGDA	% CEA	% PI	Density (kg/m^3)	Pore Size $(nm)^{27}$	Young’s Modulus (Pa)
50% PEG	50	89	10	1	1051	0.376	508,300
15% PEG	85	86	10	4	1007	3.539	23,000

B.

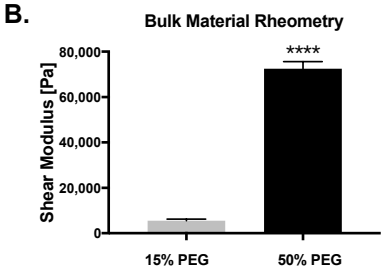

Figure 7.1 Hydrogel fabrication conditions and characterization.
(A) Tabulated fabrication conditions and calculated bulk material properties of unloaded hydrogel materials. (B) Swollen shear moduli of hydrogel particle conditions without loaded NPs.

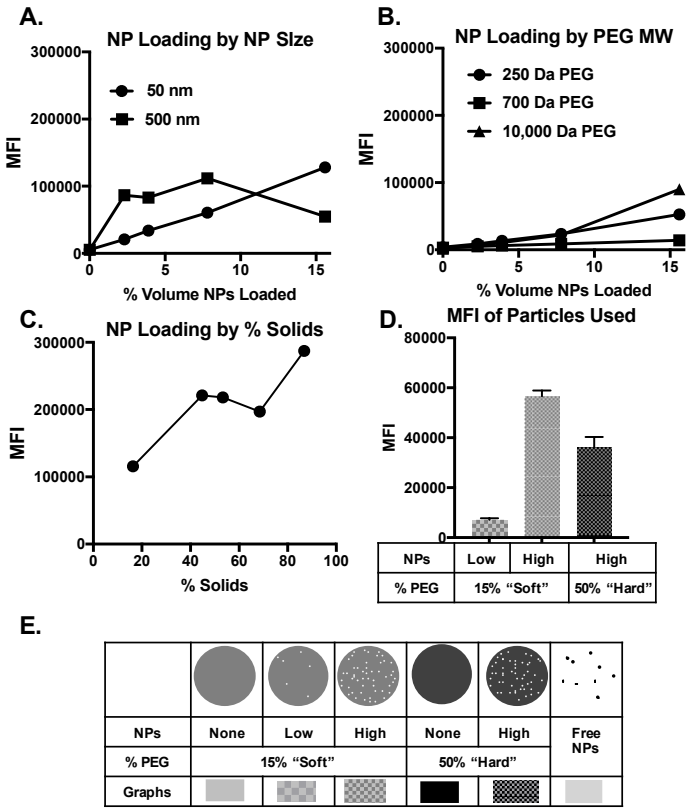

Figure 7.2 Characterization of PS NP loading into hydrogel MPs by emulsion.
PS NPs were loaded into hydrogel MPs under varying conditions. All other variables held constant, the NP loading is represented by the median fluorescent intensity (MFI) and plotted by varying (A) NP size with constant "hard" hydrogel and 700 Da PEG, (B) PEGDA MW with constant "soft" hydrogel and 50 nm PS NPs, (C) % Solids PEG with 500 nm PS NPs and 700 Da PEG. The MFI of the NP-loaded hydrogel MPs used throughout the remainder of the paper is shown in (D). (E) Schematic of five hydrogel particles and free nanoparticles utilized throughout this work.

Loading of NPs into hydrogels alters the bulk modulus

Figure 7.3A shows fluorescent images of hydrogel MP (in red), 50 nm PS NPs (in green) and the two overlain to show both the co-localization of the NPs into the PEG and the varying amount of NP loading by condition. VTC modulus has been shown to affect particle adhesion efficiency *in vitro* and *in vivo*, as well as circulation time *in vivo*.[38,39,149] Therefore, we tested

how the physical loading of PS NPs affected the bulk material modulus of the hydrogels used in this work. We hypothesized that loading of rigid NPs would impact the overall modulus of the hydrogel MPs because PS is very rigid with an elastic modulus of about 2 GPa.[155] We fabricated bulk hydrogels with same composition as the MPs utilized for the *in vitro* and *in vivo* experiments and tested them via rheometry. The bulk conditions correspond to 0, 3, or 25 of the 50 nm PS NPs loaded into each 2 μm hydrogel MP, which we defined as unloaded, low, and high NP loading, respectively. In Figure 7.3B, we show that both amounts of NP loading into "soft" hydrogels significantly increased the shear modulus versus the unloaded hydrogel, as measured on swollen bulk hydrogels via an AR-G2 rheometer. Specifically, the shear modulus increased from 5600 +/- 700 Pa for unloaded hydrogel to 8600 +/- 420 Pa for the low NP loading to 9800 +/- 290 Pa for the high NP loading. Thus, at high NP loading, we observe a 75% increase in the bulk shear modulus. We then fabricated "hard" 50% PEG hydrogels both unloaded and with high NP loading, corresponding to 16 PS 50 nm NPs per 2 μm hydrogel MP. Physically loading 50 nm PS NPs into a bulk hydrogel for this composition did not significantly increase the bulk shear modulus (72,500 +/- 300 Pa to 78,400 +/- 280 Pa), as shown in Figure 7.3C, corresponding to an only 8% increase in shear modulus. Overall, despite the significant impact of NP loading on the rigidity of the "soft" hydrogel, these hydrogels are still considerably more deformable than the "hard" hydrogels.

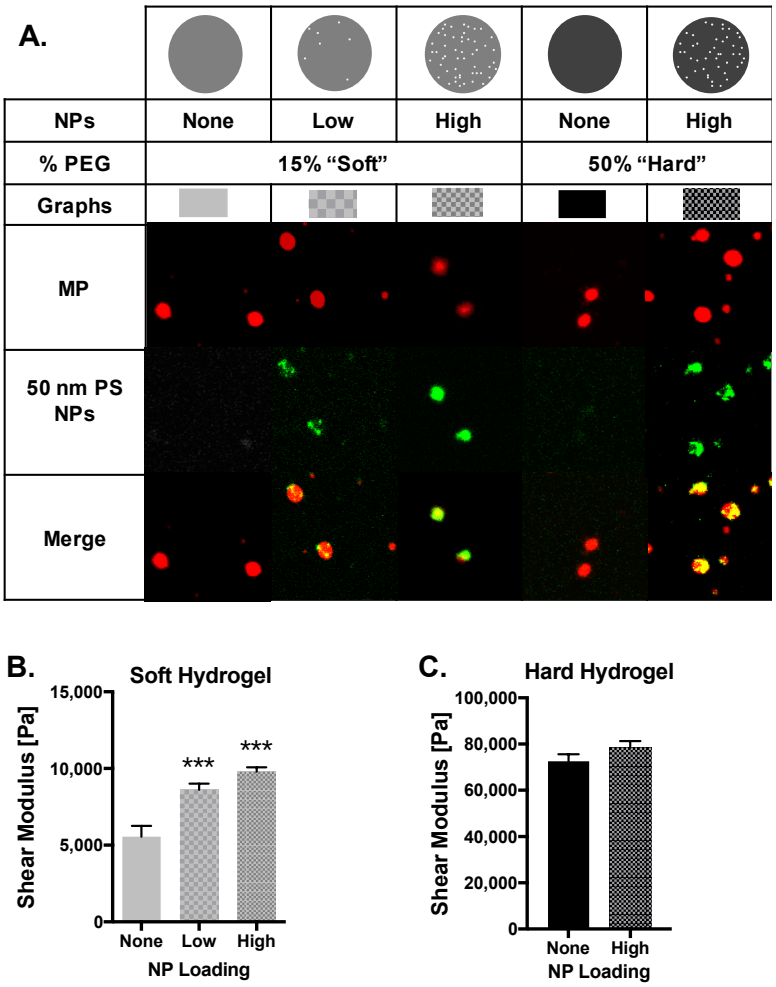

Figure 7.3 Material properties of NP-loaded hydrogel MPs.
(A) Schematic of five hydrogel MP with varied modulus and NP loading, with representative fluorescence images of each particle type via confocal microscopy. Red is MP hydrogel, green is 50 nm PS NPs, and the two are overlaid to show co-localization of NPs and hydrogel MPs. Swollen shear moduli of all hydrogel particle conditions; influence of adding different amounts of NPs on bulk material rheometry for (B) 15% PEG and (C) 50% PEG hydrogels. Statistical analyses were performed using one-way ANOVA with Fisher's LSD test, where (***) indicates $p<0.001$ in comparison to the non-loaded hydrogels. Error bars represent standard error for N=3.

Hydrogel MPs outperform free NPs in an experimental blood vessel model

Next, we evaluated the ability of our NP-loaded hydrogel MPs to bind to an inflamed vessels wall in blood flow via an *in vitro* model of blood flow in a parallel plate flow chamber (PPFC) with activated human umbilical vein endothelial cell (HUVEC) monolayer serving as the inflamed vessel wall. Our key interest here is to determine if MPs can deliver a better NP load to

the vascular wall than free NPs. Using the PPFC assay,[106] we are able to quantify the number of both MP and NPs trafficked to the vessel wall. We evaluated the adhesion of our particles in two different dosing schemes. First, we maintained a fixed hydrogel MP concentration in human blood and characterized the resulting adhesion of anti-ICAM-1 targeted particles in Figure 7.4A. The surface of each particle type was characterized to ensure a constant 5,000 sites of anti-ICAM/μm^2 and all experiments were at a low WSR of 200 s^{-1}. This shear rate represents that of veins and venules, which is often where leukocytes are captured for rapid response to inflammation.[117] The "soft" 15% PEG particles adhered equivalently independent of NP loading (unloaded, low, and high), whereas the "hard" 50% PEG MPs adhered less than all "soft" conditions. Thus, the difference in modulus produced by loading of NPs within each of the "soft" and "hard" particle groups did not produce significant differences in adhesion of hydrogel MPs, as shown in Figure 7.4A.

The MFIs, representing the number of 50 nm PS NPs loaded per hydrogel MP, were used to scale from the number of hydrogel MPs bound to the inflamed HUVEC to the number of NPs delivered. More specifically, we compared the loaded hydrogel MPs to free NPs on a plate reader to determine the average number of NPs loaded per hydrogel MP. We translated results from Figure 7.4A to the number of 50 nm NPs delivered in NPs/mm^2 vessel wall using the MFIs, with the results shown in Figure 7.4B. In these experiments, the concentration of hydrogel MPs was fixed in blood, therefore those with higher NP loading delivered a significantly higher NP payload to the vessel wall. In order to determine which particle type is most efficient at delivering NPs, we next dosed MPs by a fixed concentration of NPs in the flow, i.e. more hydrogel MPs/mL for those loaded with fewer NPs. The adhesion of hydrogel MPs in the fixed NP concentration dosing scheme are shown in Figure 7.4C; the 15% PEG particles with low

loading adhere significantly more because the concentration was much higher per mL of human blood perfused. The unloaded hydrogel conditions were excluded as no NPs were loaded, so there was no logical dosing equivalent. We again translated these results to the delivery of NPs to the vessel wall in Figure 7.4D and compared to adhesion quantified from experiments which utilized free 50 nm PS particles of the same concentration in flow. We find that the low loading of "soft" 15% PEG particle delivered significantly more NPs to the vessel wall than any other condition tested, including the soft hydrogel MPs with higher loading. This is in line with the softer particles adhering significantly better at low WSRs. Of note, the free NPs were significantly worse than all other particle types tested at delivering 50 nm PS NPs to the vessel wall. Quantitatively, in the order that they are presented in Figure 7.4D, the hydrogel MPs delivered 5,450%, 3,300%, and 630% increases in number of NPs delivered to the vessel wall versus free NPs themselves, all massive increases.

After determining the most efficient combination of hydrogel formulation and NP loading at a low WSR of 200 s^{-1}, we then evaluated the particles in a high WSR of 1000 s^{-1} in the same PPFC assay. This shear rate represents the higher end of the range that occurs in the body, typically found in healthy arterioles and stenotic large arteries in atherosclerosis.[117] We again employed the two different dosing schemes of fixed hydrogel MP concentration (Figure 7.5A-B) and fixed NP concentration (Figure 7.5C-D). At a fixed hydrogel MP concentration under high shear conditions, the "hard" 50% PEG particles adhered significantly more than the "soft" 15% PEG particles, consistent with previous results from our lab that find hydrogel binding is heavily shear dependent *in vitro* (Figure 7.5A).[106] The difference in modulus produced by loading of NPs within each of the "soft" and "hard" particle groups again did not produce significant differences in adhesion. We translated these hydrogel MP adhesion results to the delivery of NPs to the

vessel wall in Figure 7.5B and the “hard” 50% PEG particle delivered the most NPs under high WSR. Like the low shear assays, we then dosed a fixed number of NPs by altering the number of hydrogel MPs per mL of human blood in the PPFC assay. Again, shown in Figure 7.5C, the lowest loaded hydrogel MP, composed of 15% PEG, adhered the best due to being dosed with more hydrogel MPs per mL of human blood. However, the 50% PEG “hard” particles, though dosed at a significantly lower concentration, achieved similar binding under these conditions. We then translated this adhesion to the NPs delivered to the vessel wall in Figure 7.5D and found that at a high WSR of 1000 s^{-1}, the rigid particles delivered significantly more NPs to the vessel wall then all other conditions tested, including free NPs. Within the soft hydrogel MPs, the low loading again produced more NP delivery to the wall versus the high loading equivalent. Again, every NP-loaded hydrogel MP condition was significantly better at delivering NPs to the vessel wall than free NPs perfused at the same concentration. Quantitatively, in the order that they are presented in Figure 7.5D, the hydrogel MPs delivered 310%, 170%, and 1,550% increases in number of NPs delivered to the vessel wall versus free NPs themselves. In summary, the adhesion efficiency is the driving variable of final NP delivery.

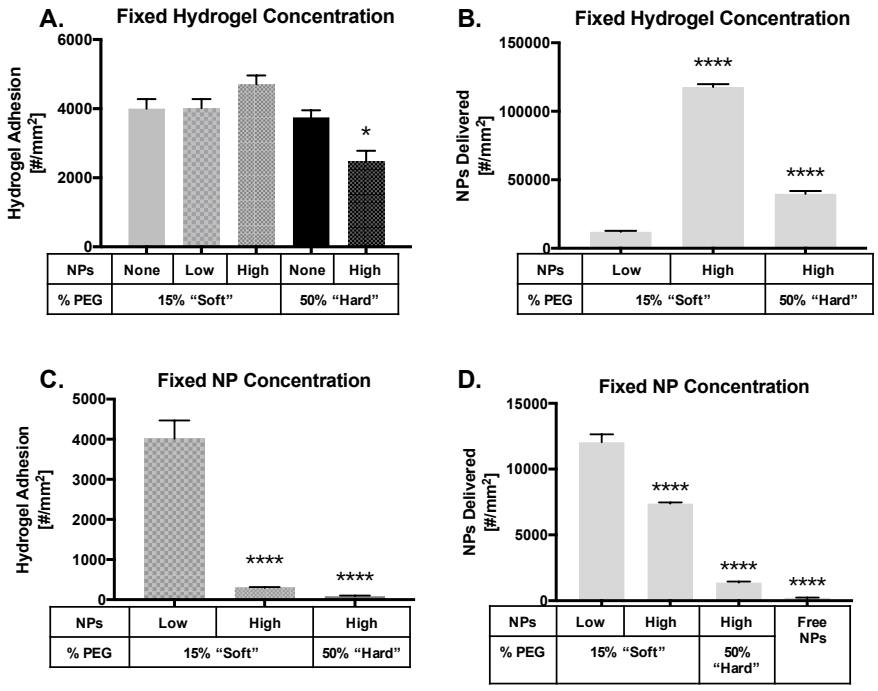

Figure 7.4 Adhesion of NP-loaded hydrogels to an inflamed HUVEC monolayer at 200 s^{-1} wall shear rate.

Quantified VTC adhesion for all particle types with a (A) fixed concentration of hydrogel MPs and scaled in (B) to the number of NPs delivered by this hydrogel adhesion. (C) Shows hydrogel MP binding at a fixed NP concentration, scaled in (D) to the number of NPs delivered. For all, adhesion was quantified after 5 minutes of laminar blood flow over an IL-1β activated HUVEC monolayer. N=3 human blood donors per particle condition. Statistical analysis of adherent density was performed using one-way ANOVA with Fisher's LSD test where (*) indicates $p<0.05$ and (****) indicates $p<0.0001$ versus the first bar in each plot. Error bars represent standard error.

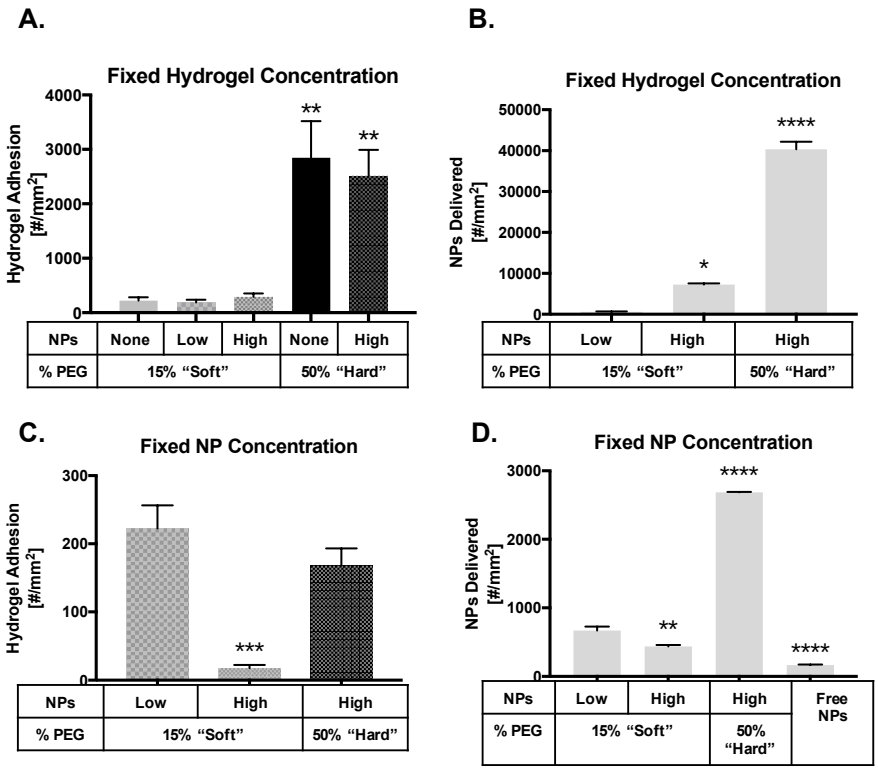

Figure 7.5 Adhesion of NP-loaded hydrogels to an inflamed HUVEC monolayer at 1000 s^{-1} wall shear rate.
Quantified VTC adhesion for all particle types with a (A) fixed concentration of hydrogel MPs and scaled in (B) to the number of NPs delivered by hydrogel adhesion. (C) Shows hydrogel MP binding at a fixed NP concentration, scaled in (D) to the number of NPs delivered. For all, adhesion was quantified after 5 minutes of laminar blood flow over an IL-1β activated HUVEC monolayer. N=3 human blood donors per particle condition. Statistical analysis of adherent density was performed using one-way ANOVA with Fisher's LSD test where (*) indicates $p<0.05$, (**) indicates $p<0.01$, (***) indicates $p<0.001$ and (****) indicates $p<0.0001$ versus the first bar in each plot. Error bars represent standard error.

Hydrogel MPs deliver significantly more NPs to an in vivo *vessel wall than free NPs alone*

To better understand how these results may translate into the clinical setting, we evaluated the vessel wall adhesion of "soft" 15% PEG particles of both high and low NP loading in direct comparison to free 50 nm NPs *in vivo* in mouse mesenteric veins. We down-selected the particle types to those that were the most efficient at delivering NPs to the vessel wall *in vitro* at low WSR in Figure 7.4D, which is the expected mesenteric venous WSR *in vivo*. Additionally, it

has been shown previously that more rigid hydrogel MPs have shorter circulation times *in vivo* and are significantly worse than deformable hydrogels at adhering to inflamed endothelium.[106] Therefore, we directly compared our "soft" hydrogels MPs with two different amounts of NPs to free NPs. We utilized an intravital microscopy method to facilitate live imaging of inflamed mesentery veins in an anesthetized mouse. We dosed the mice with a fixed number of NPs, meaning a variable number of hydrogel MPs, all with a constant surface targeting ligand site density of 30,000 anti-P-selectin/μm^2. Anti-P-selectin has been previously shown to ensure rapid, firm capture of particles *in vivo*.[106] Figure 7.6A is representative images of each hydrogel particle type used, broken out by hydrogel MP binding in red, NP binding in green, and all merged to observe the overlap. Of note, there is no red image for free 50 nm particles because there was no hydrogel material. Figure 7.6B shows the hydrogel adhesion to a mesentery vein, after 3 minutes of TNF-α activation, followed by the injection of particles, and 5 minutes of circulation time. The results portrayed as the adhesion of hydrogel MPs per mm^2 of vessel *in vivo*. As with Figures 7.4C and 7.5C, the low loaded hydrogel MP produced the best hydrogel MP adhesion simply because more particles were injected into the mouse than the other hydrogel MP type. In Figure 7.6C we then translated these results to the number of NPs delivered, and found that *in vivo*, the loading density of NPs does not significantly change the number of NPs trafficked to the vessel wall within the "soft" 15% PEG particle type. Free 50 nm PS NPs resulted in significantly less adhesion versus both high and low loading into 15% PEG particles after 5 mins of particle circulation *in vivo*. Specifically, the two hydrogel conditions delivered at minimum a 3,630% increase in the number of NPs that arrive on the vessel wall. Overall, it is very clear that *in vivo*, 15% PEG particles are significantly more efficient at delivering 50 nm PS

NPs to an inflamed mesentery versus free NPs, within the experimental window that we dosed, regardless of the number of NPs loaded and small variations in bulk modulus.

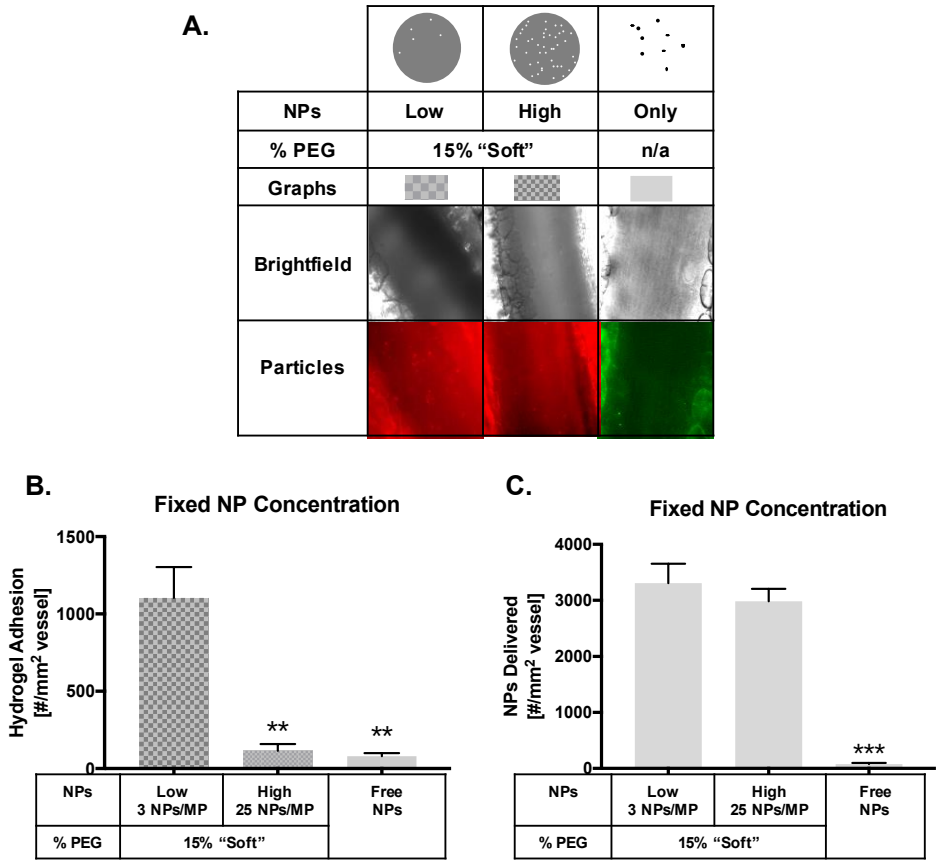

Figure 7.6 Delivery of NPs to an inflamed mesentery endothelium as a function of loading into hydrogel MPs.
(A) Representative brightfield and fluorescence images of particle adhesion to inflamed mesentery. (B) Quantified adherent density of three different particle conditions, 15% PEG low loading hydrogel MP, 15% PEG high loading hydrogel MP, and free NPs. Particles were dosed by equivalent NP payload, therefore a different number of hydrogel MPs for each bar. (C) Data scaled by the number of NPs to show efficiency of NP delivery by each VTC system. N = 3 mice per group and statistical analysis was performed using one-way ANOVA with Fisher's LSD test. (**) indicates $p<0.01$ and (***) indicates $p<0.001$ compared to the low NP loaded 15% PEG particle binding. Error bars represent standard error.

From Figure 7.6 it is clear that after 5 mins of particle circulation *in vivo*, 50 nm NPs are significantly worse at trafficking to the vessel wall than 2 μm hydrogels. In Chapter 6 we showed

that binding of particles to a vessel wall depended heavily on both size and modulus of the particles. Therefore, we next evaluated whether the binding of 50 nm NPs increased over time to approach the binding of NP-loaded hydrogels. We utilized the same method as in Figure 6.4 and quantified the binding of 50 nm NPs, targeted with anti-P-Selectin, to an inflamed mesentery wall with IVM. In Figure 7.7, the binding of 50 nm particles increases slightly over an hour time frame, but does not come near closing the gap in Figure 7.6. Therefore, we can be sure that the adhesion of 50 nm NPs will not catch that of hydrogel MPs over time; after an hour binding increased 54% from the initial, 5 minute time point, but leveled off and stopped increasing after 25 minutes. Figure 7.7B shows a head to head comparison of the two particle types, scaled to the mass of particles delivered to the vessel wall. The binding of 50 nm NPs is nominal compared to that of 2 µm hydrogels.

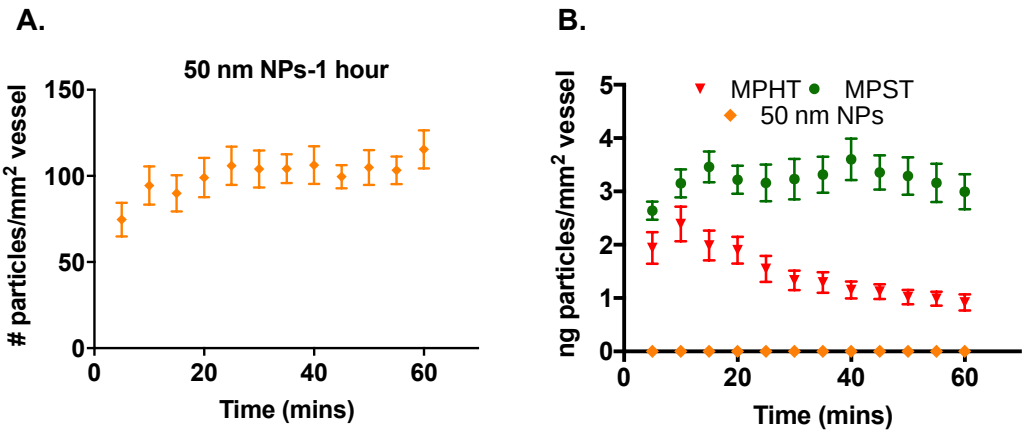

Figure 7.7 Delivery of NPs to an inflamed mesentery endothelium as a function of loading into hydrogel MPs.
(A) The adhesion of 50 nm PS particles targeted with anti-P-Selectin to an inflamed mesentery vein of over a full hour. (B) Is the same data as (A), but with data from Figure 6.4C to give an idea about the difference in binding between hydrogel MPs and 50 nm PS NPs. Error bars represent standard error for N=3.

7.5 Discussion

To date, no study has extensively evaluated how loading NPs into targeted hydrogel MPs affects the overall transport and adhesion of NPs in vascular targeting. It has been shown that a very small percent, about 0.7% on average, of intravenously delivered VTCs arrive at the targeted tissue or vasculature of interest in cancer applications, where the VTCs are labeled as "magic bullets".[166,227,228] It is imperative that VTCs make adhesive contact with the endothelium of interest, otherwise all potential benefits of targeting are negated. While different NP-embedded MP systems have been developed for proposed theranostic applications,[267–273] none have targeting moieties, nor are they tailored in modulus and NP loading to optimize targeted NP delivery and adhesion. In this work, we show that targeted hydrogel MPs deliver significantly more NPs to the vessel wall than free NPs themselves, for all hemodynamic conditions tested, and for up to an hour. This suggests that there are major improvements yet to be made in the delivery of NPs to disease sites in vascular-targeted drug delivery. Our findings shed light on hydrogel modulus as the key physical property that controls the number of loaded NPs delivered to the vessel wall. There is a critical need to thoroughly evaluate the ability of smaller NPs to bind to the vessel wall in inflammatory disease, and to understand how loading into hydrogel MPs directly affects their transport to the vessel wall. This work elucidates the untapped potential of smaller NPs loaded into hydrogel MPs for clinical treatment of many diseases involving with inflammatory responses, including cancer, diabetes, atherosclerosis, and many more.

Motivated by others' results showing that NPs of different compositions and sizes can be loaded into varying types of MPs, we engineered a simple emulsion system to fabricate NP-loaded hydrogel MPs and then target inflamed vascular wall. By loading rigid NPs into hydrogel

MPs, we have developed a system that exploits the benefits of each respective size and modulus in two subsequent steps. The larger, deformable MP has improved margination dynamics in blood flow versus 50 nm PS NPs. Upon release, the loaded rigid NPs can more readily transcytose into the tissue, travel intracellularly to deliver a therapeutic, or diffuse through leaky vasculature via EPR effect more rapidly than a MP.[71,253–256] Thus, this proposed 2 step vascular targeting strategy has the potential to revolutionize the efficiency and overall targeted delivery efficacy of NPs for broad applications in difficult to treat diseases. Many studies have investigated the loading of NPs into bulk hydrogels for varied applications,[257–266,274] but haven't exploited the potential of using a PEG-based hydrogel MP as a Trojan horse through blood to transport rigid NPs to the vessel wall. This work is a paradigm shift in the way to think about VTC size; namely, two different particle sizes are used for two different transport length scales. Larger particles are used to traffic smaller particles to the vessel wall from bulk blood flow, and then the smaller particles can perform their functionality more efficiently at the cellular level.

We chose to work with PEG because it is highly biocompatible due to its hydrophilicity and is a highly modular building block for VTCs. We show in this work that a variety of PEG hydrogel formulations may be employed to load different numbers of NPs into the crosslinked VTC. Our previous work has shown the overall particle modulus controls the final binding of hydrogel MPs, thus, loading NPs has the potential to alter the particle modulus and therefore the final adhesion.[106] Overall, we find that the physical properties of the emulsion system, PEG, and NPs determine the final encapsulation of PS NPs into the hydrogel crosslinked matrix (Figure 7.1). The 50 nm NPs were more easily encapsulated in MPs than the 500 nm NPs, which is likely due to inability of the PEG to crosslink around high concentrations of the larger NPs; this limit was not reached for the conditions tested with 50 nm NPs, highlighting the fact that a higher %

v/v of 50 nm NPs can be loaded versus 500 nm NPs. As for the influence of PEG properties, PEGDAs of varying MW have very similar chemical properties, including solubility and hydrophilicity, but the solution viscosity can increase greatly with increasing MW, which has the potential to affect emulsion dynamics.[275] In Figure 7.2B, the higher PEG MW loaded significantly more NPs than the lower MWs, due to both the higher viscosity droplets retaining more of the solid NPs and the flexibility of the much longer PEGDA monomers that can bend around NPs to make covalent bonds. Within the two lower MWs, which were very similar in size, the crosslinking was likely controlled by crosslinking dynamics; with 250 Da PEG, there are significantly more acrylate groups, which increases the probability that polymerization around the particle is completed. The 700 Da PEG is also small, but has significantly fewer end groups, making it harder to polymerize around the NPs, leading to the lowest amount of loading. The higher loading of NPs with increasing amount of PEG in the formulation can be attributed to a tighter hydrogel matrix that again allows less diffusion out during and after loading. As anticipated, adding NPs to the PEG formulations has an overall larger effect on modulus of softer hydrogels than that of rigid hydrogels (Figure 7.3). Since the NPs are physically entrapped rather than covalently crosslinked into the hydrogel backbone, even though they are very rigid PS NPs, they move with the material under shear force. Importantly, these differences in modulus produced by NP loading are not enough to produce difference in circulation time *in vivo*.[38]

We hypothesized that by loading small NPs into larger 2 μm hydrogel MPs, we would be able to deliver significantly more to a vessel wall, based on our previous work studying particle size and margination. We know that particles of different sizes respond differently to the presence of the RBC core in flow; micron-sized particles present a near-wall excess whereas NPs do not, meaning NPs have a diminished probability of binding compared to MPs.[46] We designed

this study to compare the importance of two different variables on determining the final NP delivery to inflamed vasculature: NP loading, and PEGDA crosslinking (baseline modulus without loading). We varied NP loading because researchers have shown that VTCs surprisingly deliver more total drug, when less drug was loaded per particle, and more particles were dosed *in vivo*. This is due to saturation of the mononuclear phagocyte system (MPS) with a larger number of particles,[276] therefore, we explored different amounts of loading in our system to see if we produced the same effect. We explored bulk hydrogel modulus, controlled by PEGDA crosslinking, as it has been extensively shown that particle modulus controls the overall circulation time of drug delivery particles, with deformable particles circulating significantly longer than rigid counterparts.[38,39,104,150,153] In addition, particle modulus has been established as a physical property that dictates VTC adhesion, a vital step in overall targeted cargo delivery.[39,106] Between these two variables, we worked to optimize the delivery of NPs under physiological, hemodynamic conditions.

Both these and previous results show that rigid particles adhered better at high WSR while more deformable particles were better at low WSR.[106] At low WSR this behavior by modulus directly produced most efficient NP delivery with the most deformable hydrogel, with the inverse being true at high WSR. These results are clear evidence that hydrogel modulus is the most important property to consider when designing a NP loaded hydrogel system. *In vivo*, the soft 15% PEG particles loaded with different amounts of NPs delivered statistically the same number of NPs to the vessel wall, 3,630% more than free NPs, meaning the disparity in hydrogel number dosed was mostly equilibrated by the different number of NPs per particle. We hypothesize that this difference between *in vitro* and *in vivo* results, where the lower loaded particles produced better adhesion, arises due to the complexity of the *in vivo* environment; the

higher loaded particles were only slightly more rigid than the low loading, likely not enough to alter circulation times. Therefore, the same number of NPs were delivered by both systems because all MPs had a similar number of opportunities to bind to the inflamed endothelium.

We applied concepts and experimental methods from Chapter 6 to this project, and evaluated how long 50 nm NPs could target a vessel wall. Of importance, 50 nm particles are known to circulate for longer times, due to their ability to evade uptake by the liver and spleen, or organs of the reticuloendothelial system. Therefore, one could conceive that 50 nm NPs may continue to accumulate on a vessel wall *in vivo*, like the NPS in Chapter 6. Our findings showed the opposite- 50 nm NPs maintained and slightly increased their adhesion over an hour, but this leveled off after 25 mins. Therefore, it is possible to conclude that the transport of 50 nm NPs to the vessel wall will always be significantly better when loaded into hydrogel MPs, rather than free NPs. This data allows extrapolation to longer time points and allows us to definitively conclude that the superiority of NP-loaded hydrogels over free NPs will be maintained for long times *in vivo*, in clinical settings.

By showing that the loading density into deformable hydrogel MPs does not change the overall delivery of NPs to the inflamed vessel wall *in vivo*, we propose that this system can be engineered to have tailored release kinetics based on the design parameter of NP loading density. For instance, higher loading could facilitate a burst release while lower loading could produce a depot-like NP extended release. As an example, chronic inflammation implicated in cardiovascular disease could be treated with low loaded hydrogel MPs while a more acute disorder, such as sepsis, could benefit from the release profile produced with higher loading of NPs. If the active pharmaceutical ingredient is poorly loaded into the NPs, as is often then case,[11,277,278] then loading more NPs into the MPs would facilitate higher overall dosing. In order

to release these NPs additional functionality will need to explored in these particles. In addition to non-specific hydrolysis to degrade MPs, researchers have utilized materials functionalized to impart the triggered degradation of hydrogel-based materials upon exposure to changes in pH,[245] certain wavelengths of light,[274] and certain enzymes.[11,249] Future work to tune the hydrolytic or protease-induced degradation of PEG-based hydrogels is will further optimize the clinical functionality of these particles.

Our work is not the first to conceive the general idea of loading NPs into MPs for drug delivery, yet, our particles vary from previous studies in a few key ways. Rather than focusing on synthesis and characterization,[267,268,270,273] our research is highly comprehensive, starting with fabrication and continuing through both *in vitro* and *in vivo* applications. Rather than suggesting certain clinical outcomes in certain animal models,[269,271,272] we propose that this system is widely applicable to diseases involving inflammation for systems dosed intravenously. We use MPs of a size that will not cause dangerous capillary occlusions after intravenous administration, especially because they are deformable. Others' have shown that hydrogels with similar moduli are able to navigate small capillary diameters.[38] Because we chose an emulsion method of fabrication, our particles are highly spherical and smooth, in stark contrast to particles that are spray dried.[269–271] Overall, in the context of other work, we are able to provide a holistic view of the potential of NP-loaded PEG based hydrogel systems.

7.6 Conclusions

The loading of NPs into hydrogel MPs has great potential to revolutionize the delivery of smaller NPs for the many broad clinical situations amenable to targeted drug delivery. Loading NPs can impact the resulting bulk materials, but not in a way that impacts the final delivery of

NPs. The hydrogel composition is the driver dictating final adhesion both *in vitro* and *in vivo*. For all experiments hydrogel MPs were significantly better than free NPs, by at least an order of magnitude, if not two, designating a massive advantage gained by loading NPs into hydrogels in trafficking them to the vessel wall. This advantage was maintained for over an hour time window, indicating a sustained advantaged delivered by hydrogel MPs. An immense improvement over free NPs that has potential to revolutionize the clinical delivery of NPs. A very thorough review shows that less than 1% of NPs dosed intravenously ever make it to the intended site of delivery;[227] if the same number of NPs were encapsulated into hydrogel MPs, this efficacy could be increased over 10%, and our study suggests, to up to 25% of the dose. Overall, this work will inform the engineering of VTCs moving forward such that smaller NPs may be tremendously more efficiently delivered to the site of disease.

Chapter 8: Conclusions and Future Directions

8.1 Overall Dissertation Conclusions

This dissertation embodies a few important projects that highlight the potential of vascular targeted carrier (VTC) development into the clinic. Understanding the properties and dynamics that control VTC behavior in physiological blood flow is key to contributing fundamental knowledge to the field, that can then be used to engineer next generation VTCs for clinical use. It is imperative that the characteristics of the target tissue and cells are well-understood, including the local hemodynamics, vessel geometry, and diseased surface protein expression pattern. In addition, the physical properties of VTCs can be manipulated to alter their behavior, including the size, shape, modulus, targeting ligand regime, composition, surface coating, density, and much more. Our original hypothesis, that multiple physical properties of particles interplay with physiological considerations to determine specific optimized conditions for each disease state, was confirmed by our experiments. The body of work presented here, which accomplishes the original goal of establishing how different particle properties interact with physiological parameters of disease to produce VTC adhesion, delivers the key knowledge that working together, particle modulus, size, and ligand regime have a massive impact on the final efficacy of VTCs in blood flow.

In chapter 3, we found a coupled influence of particle modulus and size in determining VTC adhesion both *in vitro* and *in vivo*. In our experimental work, 2 μm particles were significantly better than all 500 nm particles when tested head to head, regardless of modulus.

For 2 μm hydrogel particles of varying deformabilities, a shear-dependent adhesion trend arose. At a low wall shear rate (WSR), more deformable particles performed better, whereas at a high WSR, more rigid particles delivered maximal adhesion. We find that this trend primarily arose due to collisions with leukocytes, where rigid particle produced more elastic collisions, which push them preferentially toward the vessel wall for enhanced adhesion.

In chapter 4 we expanded the work from chapter 3 and investigated how ligand kinetics intersect with particle modulus to determine overall adhesion. We found consistency with the overarching trend of rigid particles performing better at higher WSR, with more targeting ligand unable to equilibrate the binding across all moduli. Deformable particles with a single ligand, regardless of site density or ligand type, were not able to match the binding of rigid particles in high shear environments. The complex involvement of leukocytes drove the observed trends at both low (300 sites/μm^2) and high (5,000 sites/μm^2) site densities, and for both ligands sialyl $Lewis^A$ (sLe^A) and anti-intercellular adhesion molecule-1 (anti-ICAM-1). The removal of white blood cells (WBCs) elucidates their key role in altering VTC adhesion from blood flow. With low site densities and adhesive forces, WBCs disrupted particle binding via competition at low WSRs, whereas with high site densities WBCs increased particle binding via productive collisions in the red blood cell-free layer. Interestingly, optimal dual targeting of the particles resulted in uniform adhesion across all particle moduli.

In chapter 5, we aimed to enhance the poor margination and adhesion of 500 nm polystyrene (PS) spheres by comparing different ratios of two targeting ligands, sLe^A and anti-ICAM-1. We found that by adding more sLe^A, adhesion increased both *in vitro* and *in vivo*, but with overall diminishing returns. The mixing of the two ligand types provided a more than linear addition boost in the adhesion produced by the two individual ligands alone. For all experimental

conditions tested, particles with a 25%-75% mix of the two ligands performed best; with the 75% as the ligand of the lesser expressed receptor. For the more prevalent receptor present on the targeted cells, less ligand was needed to achieve the benefit of that ligand receptor (LR) interaction. We confirmed these findings *in vivo* in our mesentery inflammation model. Therefore, given a known cell surface protein pattern, we suggested a ligand configuration to maximize the binding of 500 nm PS spheres.

In chapter 6, we combined the findings from the previous chapters and investigated the duration for which VTCs can stay bound *in vivo.* We examined the circulation times in mice plasma for a rigid and soft NP and MP, all composed of PEG. All particles had extremely short plasma circulation times in a mouse, independent of size, modulus, or presence of targeting ligand. Over the time frame of an hour, the soft MP and NP maintained or increased binding over time in our mesentery inflammation intravital method, whereas the rigid MP and NP detached to about half the maximum binding after an hour. In line with the intravital results, only the soft MP and NP showed significant targeting in our acute lung injury model, and the soft MP delivered the maximum particle dose and specificity to the lung for up to 8 hours. Therefore, we experimentally demonstrated that the ability of particles to target and stay bound to a vessel wall does not require extremely long circulation times *in vivo*, which was achieved with particles used in previous chapters.

In chapter 7, we proposed the use of 2 μm PEG hydrogel MPs as Trojan Horses for the delivery of 50 nm NPs to the vascular wall. Physical entrapment of the NPs in to the PEG hydrogel did not alter the material modulus enough to expect a change in MP behavior, such as adhesion *in vitro* or circulation time *in vivo.* We found that in terms of the number of NPs delivered to the vascular wall, it was significantly more efficient to load these NPs into the

hydrogel MPs versus direct NP dosing in the free blood stream, both *in vitro* and *in vivo*. When dosed by a constant number of NPs, it did not matter if many hydrogel MPs were used with low loading, or fewer with high loading, a similar number of NPs were transported to the vessel wall. Overall, the driving characteristic of this system was the bulk modulus of the hydrogel MP, in line with our previous findings. This suggested that loading density of NPs could be tailored to desired release kinetics.

In conclusion, we found that particle modulus is a key physical property to consider in the engineering of particulate drug delivery systems, especially for MP VTCs. We found that the adhesion of VTCs was often limited by ligand kinetics, which could be tuned to improve final binding efficiency based on known surface protein patterns. We proposed the use of hydrogel MPs as Trojans Horses for smaller NPs, with great success . This work contributes to the fundamental knowledge base that is necessary to design modular, optimized VTCs for broad applications in clinical settings. With this, we hope to provide continually better vascular-targeted therapies for challenging-to-treat diseases.

8.2 Impact and Future Directions

This dissertation lays the ground work for many more potential projects, both experimental and computational in nature. Given the status of and improvements needed in the vascular targeted drug delivery field, we highlight the impact of our work and propose the following are areas of interest to pursue.

The work presented in chapter 3 is the first study to systematically investigate a broad range of particle moduli, in conjunction with size, for targeted adhesion both *in vitro* and *in vivo.* With all the work around deformable, biocompatible, PEG-based particles,[150] it is imperative to

understand exactly how modulus dictates different physiological processes necessary for vascular-targeted drug delivery. Our work delivers well-controlled particle and physiological conditions, including pertinent blood flow, to shed valuable insight into how modulus affects particle binding.

Chapter 3 emphasizes the importance of modulus, and how that interplays with WSR to dictate final adhesion. In my mind, the follow up on this chapter is three-fold. First, would be to push the lower limits of deformability to more completely explore the modulus parameter space. Second, while our *in vitro* results were corroborated under low shear conditions *in vivo*, the high shear trend has not been confirmed *in vivo.* Therefore, an experimental method should be developed to image the targeted adhesion of hydrogels in high shear arteries in real time. Of note, the blood flow in large arteries is pulsatile rather than laminar in nature, making the arteries more challenging to image. The pulsatility of the blood flow can produce differences in targeted adhesion versus equivalent laminar conditions.[46,168] High shear areas are the most relevant for targeting in atherosclerosis and cardiovascular disease, meaning this work would be high impact and extremely pertinent. A model could be developed to image the carotid artery of anesthetized mice; methods are currently being explored in the literature to establish stabilization of the artery sufficient to facilitate imaging.[279,280] Other arteries could be explored, again, so long as they can be sufficiently stabilized for imaging. For these experiments, the endothelial cells should be characterized to provide as much physiologically pertinent information as possible. Finally, in chapter 3 we showed computationally via finite element analysis that hydrogels MPs in the modulus range we tested did not deform in the physiological shear forces of free blood flow. It would be of key interest to model the deformation of these same particles, but anchored to a vascular wall via LR pairs. It is expected that more deformation will arise, as the shear forces are

larger in magnitude near the vessel wall, especially if the anchored velocity of the particle is zero.[119] These simulations would contribute to the understanding and expectations of how deformable VTCs should behave once bound to a blood vessel wall. Overall, these three projects would continue to build key knowledge about deformable hydrogel VTCs.

Chapter 4 is a unique study that combines the investigation of key physical VTC properties including modulus, targeting ligand type, and ligand amount, to deliver insight into how two different VTC properties work together to deliver targeted adhesion. This kind of work is key for developing understanding of how all VTC properties must be engineered in concert to produce maximal adhesion and specificity. The work in chapter 5 is the first systematic variation of the ratio of two different ligands on VTCs for adhesion to cells under truly physiological blood flow conditions. It is imperative to design studies that mimic physiological conditions, otherwise results may differ when translated from an oversimplified system to an animal model. Overall, these studies deliver key knowledge that will impact the engineering of VTC systems targeted to many common diseases.

In chapters 4 and 5, we look at ligand kinetics, and in chapter 5 we focus on the dual targeting of 500 nm PS spheres. While this was a good model drug carrier to establish the importance of ligand kinetics, more work should be done with biocompatible particles. The dual targeting work should be expanded to larger particles still relevant for drug delivery (2 μm) and across the parameter space of particle moduli, using a range of materials. It is well known that particles composed of different materials absorb different plasma protein opsonins, which alter the way in which the VTCs bind.[92,281] Additionally, larger particles will experience more efficient margination and offer a larger surface for adhesive contact, but will experience greater shear removal forces.[37,65,229] Therefore, it is of key interest to investigate at how size and material

interact with targeting ligand composition and blood vessel size to produce maximal targeted adhesion. Additionally, our conclusion of more ligand is needed to the lesser expressed receptor should be tested for different LR pairs, relevant to disease, with different individual kinetics. It is imperative to keep in mind that the over-expressed receptor or protein must be expressed on the luminal side of the blood vessel, otherwise known as on the endothelial cells, or else the ligand will never find the intended counter receptor. For example, folic acid and hyaluronic acid, ligands to folate receptors and CD44 on cancer cells, respectively, may seem attractive for intravenous drug delivery, but will require that the cancerous cells protrude into the vasculature, which is not a given; the receptors are not present at high levels on endothelial cells.[248,282] As one example, platelet mimetics have arisen as targeted therapeutic particles in the recent years, but the ratio of ligands to collagen and von Willebrand factor could be studied in more detail to optimize the clotting capabilities of the VTCs.[283]

Chapter 6 is the first work to investigate how the circulation time of particles *in vivo* produces targeted adhesion over time. We were able to show that circulation time is not indicative of how long particles will stay bound at an intended inflammatory site, but rather, deformable particles are able to maintain adhesion for hours despite short circulation times for all particle types. Indeed, we are the first to show that once particles bind to endothelial cells *in vivo*, which happens within minutes, they no longer need to circulate for targeted adhesion to be maintained. This work has an immense impact, indicating that circulation time should not be used as a proxy for the possible success of a VTC system, but rather, accumulation at the target site over time is key.

In chapter 6, we investigate the duration for which VTCs maintain targeted adhesion once injected intravenously. This chapter can certainly be expanded to more particle moduli

and different biocompatible materials. While our "rigid MP" was the most rigid condition tested, it is nowhere near the rigidity of other polymeric materials such as poly(lactic-co-glycolic acid) (PLGA) or polycaprolactone, therefore this study could continue in this direction. This work can also be expanded to investigate targeting duration in pulsatile, high shear vessels *in vivo*, which may prove very different environments for particle adhesion than the low shear mesenteric veins. In addition to looking at targeting time, this project can be extended into a model with more complete clinical relevance, including drug loading and optimized release mechanisms to compare the clinical outcomes are over time. We hypothesize that deformable MPs will deliver the best clinical outcome in most disease models, because it has the longest targeting window, and therefore time to release the drug locally. Proteins such as hemoglobin have been loaded into PEG-based particles with high loading capacities and non-specific release mechanisms.[102] Other drugs have been loaded into hydrogels, such as insulin,[257] bone tissue proteins,[258,259] glaucoma therapeutics,[260] and anti-inflammatories.[261–263]

To fully understand the possible clinical impacts of these loaded VTC systems, it is critical that the drug loading capacity and release kinetics be studied in the context of multiple disease models. Then the targeting ligand regime on the deformable PEG-based particle should be optimized to the known diseased endothelium, to maximize adhesion at the disease site and minimize accumulation in healthy tissue. I propose tracking the development of atherosclerotic plaque over time in apolipoprotein E–deficient ($ApoE^{-/-}$) mice dosed daily with statin-loaded PEG particles.[284] Statins lower the amount of lipids present and accumulating *in vivo*, thereby decreasing the development cardiovascular disease. This class of medications has a dose limiting toxicity due to the systemic side effects such as muscle pain, fever, and digestive problems.[285] With the proposed targeting of particles loaded with statins to areas inflammation,

which manifests due to high lipid levels in ApoE$^{-/-}$ mice, I hypothesize that a higher level of local statin concentration can be maintained with decreased systemic side effects. All results with targeted, loaded particles should be compared head to head with the same free drug dosage. A higher local statin concentration would decrease the size of atherosclerotic plaque developed, which should be evaluated histologically at the end of the experiment. If the targeted statin treatment functions more locally than free statin dosing, fewer inflammatory cytokines should be detected circulating in the blood stream, which can be sampled more regularly throughout the experiments on the same mice and quantified via ELISA kits. I suggest the testing of interleukin-1β, interleukin-6, tumor necrosis factor-α and interferon-γ, due to the known involvement in development and modulation of cardiovascular disease.[286] Additionally, the concentrations of different lipids and lipid by-products can be monitored for their ability to mediate chronic inflammation.[287] This model will give a complete picture of the clinical utility of statin-loaded hydrogel MPs and will show the importance of maintaining particle adhesion to the disease vessel site.

Chapter 7 is the first study to explore the parameter space of NP loading into hydrogel MPs for targeted delivery to an inflamed vascular wall. We employed well-controlled ligand kinetics, and directly compared how delivering the same number of NPs, either in free solution or in different numbers of 2 μm PEG hydrogels, resulted in adhesion to the vascular wall. This work highlighted the huge impact that loading smaller NPs into deformable hydrogels can have, and the untapped potential for using polymerized PEG as a Trojan horse to get NPs to the disease site. This work has the potential to impact and greatly improve the overall efficacy of VTC systems involving small NPs, including many already in development for the clinic.

Chapter 7 finds that loading 50 nm PS NPs into PEG hydrogel MPs delivers significantly more to the vessel wall than free NPs themselves. This should be developed in the direction of biocompatibility, using NPs composed of PLGA or polycaprolactone. Of interest, PLGA suffers from a significant plasma effect, where any exposure to protein opsonins in the blood significantly decreases the targeted adhesion.[92] Loading PLGA NPs into the highly hydrophilic PEG hydrogel will provide a shield to the detrimental opsonins, and decrease the overall plasma effect. Once released, the PLGA NPs will need to bind very quickly to fight the rapid opsonization, and therefore, must too be conjugated with targeting ligand. As the NPs are released from the hydrogel, they must stay bound locally, otherwise all NPs and their cargo will wash away, overturning any targeting functionality. Therefore, the MPs and NPs should both be targeted to ensure extreme proximity to the diseased cells of interest.

The next critical step in NP-loaded VTC development is to optimize a mechanism for NP release from hydrogel MPs. In the degradable polymer field, non-specific hydrolytic degradation is often utilized as a mechanism of cargo release, typically by inclusion of ester linkages in the hydrogel backbone or mesh.[288,289] However, by definition, hydrogels are comprised of a high water content, facilitating rapid hydrolysis in solution and under physiological conditions, making this strategy not feasible for targeted delivery. Other mechanisms of hydrogel degradation/release include changes in pH, temperature, or enzymatic degradation. Finally, a zymogen could be loaded into the hydrogel MP, which would be converted into an active protease for an autocatalytic approach that feeds back for amplified degradation with enzyme exposure.[290] If the delivery site is acidic in pH, such as a tumor environment, pH sensitivity can be incorporated into the hydrogels via hydrazine, acetal, or oxime bonds in the polymer mesh, which degrade in acidic pHs.[248] This body of work discusses vascular targeting, where a shift in

pH is likely not large enough to facilitate the development of site-specific degradation. Therefore, enzymatic degradability offers the best avenue for disease site-specific degradation of VTC systems.

Proteases are known to play an active role in the complex development of atherosclerotic plaques and exhibit enhanced expression and activity surrounding the associated inflamed endothelial cells (ECs).[291]Atheromas on arterial walls, have characteristically increased expression and activity of matrix metelloproteinases (MMPs), which are secreted by infiltrating macrophages, surrounding inflamed ECs, and smooth muscle cells (SMCs);[292] the high expression of these MMPs has been associated with vulnerable plaques,[293] and may offer an avenue for targeted cargo release in cardiovascular disease. MMP-9, also known as Gelatinase B, is a protease that is minimally expressed by healthy cells but is highly expressed by luminal ECs and SMCs near atherosclerotic plaques.[292] It is key that there is a sizeable increase in protease expression near the intended site of release versus healthy tissue. MMP-9 is a prime example, with the healthy serum level reported as 0.2–0.4 nM (20-40 ng/mL) in healthy tissues and cells,[294,295] and approximately 100 times that level near vulnerable regions of atherosclerotic plaques.[292] We hypothesize that upon successful inclusion of protease-degradable cross-linkers within a hydrogel matrix, loaded NPs, or any desired cargo, can be locally released at the site of disease upon contact with proteases that are upregulated by the inflamed endothelium. An ideal MP for the delivery of cargo (NP, drug, imaging agent) to the vascular wall must both specifically and rapidly degrade once in contact with the endothelium, and also stay intact in the free stream of blood flow and elsewhere in the body.

If hydrogel particles are rendered enzymatically degradable for NP release, then final NP adhesion and functionality requires that any particle and corresponding ligand system must be

stable in the presence of high concentrations of enzymes. A protocol must be established to synthesize custom peptides in house, to render our hydrogel VTCs enzymatically cleavable. Significantly more work is required to tailor the degradation kinetics for the time scales of degradation required *in vivo*. These time scales are dictated by the targeting windows established in Chapter 6; once the VTCs wash away, degradation is no longer relevant or site-specific.

It has been previously shown in the literature that the degradation kinetics of bulk materials can be tuned based on hydrogel crosslinking density, the kinetics of the degradation of the linker, and the mode of degradation, including but not limited to: non-specific diffusion, hydrolysis, enzymatic cleavage, and response to changes in pH.[257–260,262–266] The potential impact of this system lies with diseases that involve over activity of specific proteases as part of the clinical manifestation. For these systems, the specificity will be two-fold, including both the adhesion aspect and targeted degradation and release.

If pursuing enzymatically-triggered NP release, the amount of peptide in the hydrogel back bone should be optimized to allow the particle to stay intact everywhere, except with atherosclerotic plaque levels of disease associated proteases, which should produce degradation. First, a quantitative method needs to be developed to determine the concentration of peptide that is crosslinked into the backbone of the hydrogel matrix. Once a reliable method is developed, well-varied amounts of peptide should be incorporated into either bulk hydrogels, hydrogel MPs, or both. I can fathom four ways of determining the rate of degradation over time. Smaller NPs, larger than the pore size of the hydrogel mesh, can be physically entrapped into the material. As the hydrogel degrades upon exposure to disease associated proteases, the NPs will be released into solution, which can be quantified with a plate reader. Else, the mass of a bulk hydrogel can be weighed over time in an enzymatic solution, with an eventual decrease in mass signifying

significant degradation. This has limitations as the hydrogel will eventually break into too small of pieces to measure. Otherwise, once enzymes cleave the peptide at a peptide bond, both a free carboxyl and amine group will be exposed. Therefore, colorimetric assays to determine the concentrations of free amines may be used with a hydrogel MP solution.[296,297] Alternatively, MP degradation can be observed by automated microscopic imaging of samples from the degradation solution, to monitor the concentration of particles in solution over time. Based on the findings in chapter 6 that VTCs can stay bound for up to 8 hours, the site specific degradation should be optimized to occur in hours, upon exposure to elevated levels of disease associated protease.

There are many formulation variables that may be altered to tune the enzymatic degradation kinetics of the hydrogels to the intended disease application. The PEG mesh will determine how quickly the bulk hydrogels or MPs degrade. The molecular weight of the PEG monomer can have a huge impact on the molecular mesh formed, and therefore, the degradation kinetics.[152] All else constant, higher molecular weight PEG increases the degradation rate of the overall gel. The number of arms on the PEG can also greatly impact degradation kinetics; more arms on each PEG molecule means a tighter hydrogel mesh and slower degradation rate.[152,298]

The work in chapter 7 establishes the ability of targeted hydrogel particles to deliver NPs to the vascular wall with much higher efficiency than free NPs. Upon determining degradation kinetics *in vitro* with disease associated proteases, the system should be evaluated in more physiological environments, which could include cultured cells or many animal models of inflammation that involve over activity of disease associated proteases.

After testing degradability, researchers should evaluate the ability of these particles to be conjugated covalently with targeting ligands. Once maximal site densities are determined via secondary staining and flow cytometry, the MPs should be tested via parallel plate flow chamber

assay to ensure that rendering hydrogel degradable does not significantly alter the adhesion characteristics of the MPs prior to degradation. At this stage in development the particles will have both degradation and targeting built in or onto the surface, and so their overall functionality can be tested in many ways. Different experimental models should be used to fully investigate this system's functionality both *in vitro* and *in vivo*, including degradation kinetics, uptake of released NPs by target cells, biodistributions of both hydrogel MPs and loaded NPs, and treatment of inflammatory models *in vivo*.

The possible success of this enzymatically-degradable system will require the tuning of many variables, including the loading density of NPs, the peptide concentration, and the MP size, to name a few. This system can be tested with many animal models, such as with atherosclerotic $ApoE^{-/-}$ mice[299] or with atherosclerotic $Ldlr^{-/-}$ $Apob^{100/100}$ mice,[300] which have both shown increased activity of disease-associated proteases such as MMPs near plaque development areas. Additionally, and more broadly, this system could be applied to a range of cancer models, as specific proteases are highly active in tumor environments.[290] The entire design of the enzymatically-degradable hydrogel system would need to be tailored to each, unique tumor environment. The concentration of disease associated enzymes will be different in a tumor versus and atherosclerotic plaque, and hence, the kinetics should be tailored to the local concentrations and desired rate of overall hydrogel particle degradation. The intersection of all three chapters (6-8) should deliver a well-developed system with high clinical utility for a broad application of diseases.

These last chapters should be combined to deliver a fully optimized system *in vivo*. By this, I mean that enzymatically degradable, NP-loaded hydrogel MPs should be injected intravenously and evaluated for delivery of small NPs to target endothelial cells. Of key interest,

an assay should be developed to determine the rate of retention on the vascular wall when the NPs are released. This should give an idea of how many are being swept back into the bloodstream, which will determine the true viability of this system. This can be visualized in real time, using intravital microscopy, as demonstrated throughout my dissertation. If most of the NPs rinse away from the vessel wall back into the blood stream, then the added complexity of adding NPs into hydrogel MPs did not deliver a significant benefit and the system must be reevaluated for clinical utility.

8.3 Overall Outlook

I maintain a strong scientific conviction that targeted drug delivery will have an immense impact on many diseases in the not-so-distant future. Here, I give my insight on the current state of the art in vascular-targeted drug delivery, and my outlook as to where the field is going from here. I also propose a few more creative ideas to help propel the field forward with the ultimate goal of clinical translation.

Regarding the deformability of particles in blood flow, there is a crucial need to better understand how particles will behave in the dynamic environment of blood vessels *in vivo*, full of different cell types, constant collisions, varying vessel geometries, and variable shear forces and profiles. Atomic force microscopy has been used to study the different components of blood extensively, including RBCs, WBCs, and platelets.[133,134,178,301] This work with blood cells helped elucidate the mechanics that govern the development of a RBC core *in vivo*. While rheometry has proven a good way to compare different elastic materials, it has been difficult to dive into the more micro-mechanics and hemodynamics of micro-sized particles in complex blood flow. I propose that the development of atomic force microscopy methods to better characterize the

detailed mechanics of deformable VTCs, would better inform computational models to more accurately predict the margination and adhesion of hydrogel VTCs in blood flow. Recent computational work has begun to elucidate the transport mechanisms of cell types with different physical properties in blood flow,[40,135,302] yet there are many challenges to modeling such highly complex fluid flow, such as human blood, accurately. Recent computational work has underlined the major impact of cell size and rigidity on blood margination, however, little experimental work focuses on the effects particle physical properties in full blood flow. In summary, I propose a concerted effort to much more expansively use atomic force microscopy to better inform simulations involving complex, whole blood dynamics. This would allow for the better screening of particle behavior *in vivo*.

There has been a surge in clinical nanomedicines recently, with 40% of all current clinical trials involving particles having started in the last three years.[13,14] The term "nanomedicine" is defined rather loosely, and can apply to systems from polymer-drug conjugates to bare or targeted, polymeric particles.[14] While there are many clinical trials involving either particle or antibody drug candidates, there are very few that involve antibody targeting on a particle. BIND therapeutics has one of the fastest developing platforms of PLGA/PEG targeted particles, with indications for many cancer types showing promising results.[13] Some of the key hurdles remaining for VTCs, from my perspective, are regulatory and manufacturing in nature. The US Food and Drug Administration has stringent clinical trial requirements, such as exact control over the number of antibodies per warhead on an antibody-drug conjugate. That is easy to manage when there are only one or two active sites for linking between the two. When particles have the potential for thousands or millions of targeting ligands, controlling the exact number of molecules on the surface has proven either too costly (top-down

manufacturing) or generally impossible in the window required (bottom up manufacturing). In terms of the particles themselves, methods that are the highest throughput typically offer the least amount of control over particle size, shape, and morphology. Well-designed top-down manufacturing is cost prohibitive on a clinical trial or commercial scale. Taken together, there is not quite a happy medium between manufacturing capabilities and the US Food and Drug Administration clinical trial requirements. In my opinion, once we are able to tweak those requirements for particle systems, rather than trying to apply those in place from molecular systems to VTCs, the field will take off rapidly into the clinic.

In general, there are still creative emerging concepts when it comes to targeted drug delivery. For instance, researchers have proposed the use of zwitterions as either particle coatings or as the bulk particle material itself to evade immune recognition. Zwitterions have shown massively successful initial results, delivering huge increases in circulation times versus conventional polymers such as PEG and PLGA.[303,304] More creative methods to control cargo release, including enzymatically cleavable hydrogels, has allowed for more finely tuned, and even sequential release,[305] of different active molecules. There are hugely comprehensive reviews that cover all of the different physical and chemical design parameters to be considered in the design of a particulate drug carrier.[6,11] Based on my experience, I believe that the key is to keep it simple. Not to stop innovating, but to drive towards the most elegant solutions that provide the required outcomes to translate into the clinic, rather than racing to a new idea that adds an undue level of complexity. For example, the complex synthesis of zwitterions has slowed the research and development of such molecules. That said, to the high levels of success with zwitterions, I propose that the field collaborate with chemists to find the simplest, most stable synthesis route possible. I strongly believe that these collaborations will produce the

elegant solutions required in academic research to accomplish the maximal impact in the medical world.

In general, it is key that work in the vascular-targeted drug delivery field becomes more systematic and concerted across research groups, to be able to establish guiding principles for designing VTCs with entire physiological process in mind. Far too much work is conducted in a scientific silo, when a more collaborative effort would inform the development of more efficacious VTCs. By working together, there is potential to provide working guidelines for what to consider when choosing a VTC system for a specific disease. To date, many studies evaluate one specific parameter of VTCs in only one experimental model *in vitro* or *in vivo*, making it difficult to see the big picture of how the biology interfaces with all the different design parameters of VTCs. Moving forward, the intersection of all the different physical properties of VTCs must be combined and studied, to create understanding that will propel both the general field and clinical trials forward.

References

1. Brannon-Peppas, L. & Blanchette, J. O. Nanoparticle and targeted systems for cancer therapy. *Adv. Drug Deliv. Rev.* **6,** 206–212 (2012).

2. Faraji, A. H. & Wipf, P. Nanoparticles in cellular drug delivery. *Bioorg. Med. Chem.* **17,** 2950–62 (2009).

3. Misset, J. L. *et al.* Original article Dose-finding study of docetaxel and doxorubicin in first-line treatment of. *Ann. Oncol.* **10,** 553–560 (1999).

4. Perhamon Press, L. *The Collected Papers of Paul Ehrlich, vol III*. (1960).

5. Strebhardt, K. & Ullrich, A. Paul Ehrlich's magic bullet concept: 100 years of progress. *Nat. Rev. Cancer* 1–8 (2008). doi:10.1038/nrc2394

6. Torchilin, V. P. Multifunctional nanocarriers. *Adv. Drug Deliv. Rev.* **58,** 1532–55 (2006).

7. Santos, L. A. & Akil, E. M. Drug Delivery Formulations of Ordered and Nonordered Mesoporous Silica: Comparison of Three Drug Loading Methods. *J. Pharm. Sci.* **100,** 3294–3306 (2011).

8. Zhang, L. *et al.* Nanoparticles in Medicine : Therapeutic Applications and Developments. *Clin. Pharmacol. Ther.* **83,** 761–769 (2008).

9. Mehta, D. & Malik, A. B. Signaling Mechanisms Regulating Endothelial Permeability. *Physiol. Rev.* **86,** 279–367 (2006).

10. Charoenphol, P. *et al.* Targeting therapeutics to the vascular wall in atherosclerosis-Carrier size matters. *Atherosclerosis* **217,** 364–370 (2011).

11. Torchilin, V. P. Multifunctional nanocarriers. *Adv. Drug Deliv. Rev.* **64,** 302–315 (2012).

12. Cheng, Z., Zaki, A. Al, Hui, J. Z., Muzykantov, V. R. & Tsourkas, A. Multifunctional Nanoparticles : Cost and Versus Benefit of Adding Targeting and Imaging Capabilities. *Science (80-.).* **338,** 903–910 (2012).

13. Anselmo, A. & Mitragotri, S. Nanoparticles in the clinic. *Bioeng. Transl. Med.* **1,** 10–29 (2016).

14. Bobo, D., Robinson, K. J., Islam, J., Thurecht, K. J. & Corrie, S. R. Nanoparticle-Based Medicines: A Review of FDA-Approved Materials and Clinical Trials to Date. *Pharm.*

Res. **33,** 2373–2387 (2016).

15. Mitragotri, S. & Lahann, J. Physical approaches to biomaterial design. *Nat. Mater.* **8,** 15–23 (2009).

16. Tao, L. *et al.* Shape-specific polymeric nanomedicine: emerging opportunities and challenges. *Exp. Biol. Med. (Maywood).* **236,** 20–9 (2011).

17. Decuzzi, P., Pasqualini, R., Arap, W. & Ferrari, M. Intravascular delivery of particulate systems: does geometry really matter? *Pharm. Res.* **26,** 235–43 (2009).

18. Nel, A. E. *et al.* Understanding biophysicochemical interactions at the nano-bio interface. *Nat. Mater.* **8,** 543–57 (2009).

19. Owens, D. E. & Peppas, N. a. Opsonization, biodistribution, and pharmacokinetics of polymeric nanoparticles. *Int. J. Pharm.* **307,** 93–102 (2006).

20. Jiskoot, W., van Schie, R. M. F., Carstens, M. G. & Schellekens, H. Immunological risk of injectable drug delivery systems. *Pharm. Res.* **26,** 1303–14 (2009).

21. Fromen, C. *et al.* Neutrophil–Particle Interactions in Blood Circulation Drive Particle Clearance and Alter Neutrophil Responses in Acute Inflammation. *ACS Nano* (2017).

22. Longmire, M., Choyke, P. L. & Kobayashi, H. Clearance properties of nano-sized particles and molecules as imaging agents: considerations and caveats. *Nanomedicine (Lond).* **3,** 703–17 (2008).

23. Boulikas, T. Clinical overview on Lipoplatin: a successful liposomal formulation of cisplatin. *Expert Opin. Investig. Drugs* **18,** 1197–1218 (2009).

24. Pinto-Sietsma, S.-J. *et al.* Urinary Albumin Excretion Is Associated with Renal Functional Abnormalities in a Nondiabetic Population. *J Am Soc Nephrol* **11,** 1882–1888 (2000).

25. Smith, D. A., Waterbeemd, H. van de & Walker, D. K. *Pharmacokinetics and Metabolism in Drug Design*. (2006).

26. Mebius, R. E. & Kraal, G. Structure and function of the spleen. *Nat. Rev. Immunol.* **5,** 606–16 (2005).

27. Cesta, M. F. Normal structure, function, and histology of the spleen. *Toxicol. Pathol.* **34,** 455–65 (2006).

28. Moghimi, S. M. Mechanisms of splenic clearance of blood cells and particles: towards development of new splenotropic agents. *Adv. Drug Deliv. Rev.* **17,** 103–115 (1995).

29. Merkel, T. J. *et al.* The effect of particle size on the biodistribution of low-modulus hydrogel PRINT particles. *J. Control. Release* **162,** 37–44 (2012).

30. Tomlinson, E. Theory and practice of site-specific drug delivery. *Advanced Drug Delivery*

Reviews **1,** 87–198 (1987).

31. Bilzer, M., Roggel, F. & Gerbes, A. L. Role of Kupffer cells in host defense and liver disease. *Liver International* **26,** 1175–1186 (2006).

32. Perry, J. L. *et al.* PEGylated PRINT nanoparticles: the impact of PEG density on protein binding, macrophage association, biodistribution, and pharmacokinetics. *Nano Lett.* **12,** 5304–10 (2012).

33. Reuter, K. G. *et al.* Targeted PRINT Hydrogels: The Role of Nanoparticle Size and Ligand Density on Cell Association, Biodistribution, and Tumor Accumulation. *Nano Lett.* **15,** 6371–6378 (2015).

34. Goldberg, M., Langer, R. & Jia, X. Nanostructured materials for applications in drug delivery and tissue engineering. *J. Biomater. Sci. Polym. Ed.* **18,** 241–268 (2007).

35. Yoo, J.-W., Doshi, N. & Mitragotri, S. Adaptive micro and nanoparticles: temporal control over carrier properties to facilitate drug delivery. *Adv. Drug Deliv. Rev.* **63,** 1247–56 (2011).

36. Doane, T. & Burda, C. Nanoparticle mediated non-covalent drug delivery. *Adv. Drug Deliv. Rev.* **65,** 607–21 (2013).

37. Albanese, A., Tang, P. S. & Chan, W. C. W. The effect of nanoparticle size, shape, and surface chemistry on biological systems. *Annu. Rev. Biomed. Eng.* **14,** 1–16 (2012).

38. Merkel, T. J. *et al.* Using mechanobiological mimicry of red blood cells to extend circulation times of hydrogel microparticles. *Proc. Natl. Acad. Sci. U. S. A.* **108,** 586–91 (2011).

39. Anselmo, A. C. *et al.* Elasticity of Nanoparticles Influences Their Blood Circulation, Phagocytosis, Endocytosis, and Targeting. *ACS Nano* **9,** 3169–3177 (2015).

40. Kumar, A. & Graham, M. D. Mechanism of Margination in Confined Flows of Blood and Other Multicomponent Suspensions. *Phys. Rev. Lett.* **109,** 108102 (2012).

41. Crowl, L. M. & Fogelson, A. L. Computational model of whole blood exhibiting lateral platelet motion induced by red blood cells. *Int. j. numer. method. biomed. eng.* **26,** 471–487 (2010).

42. Eckstein, E. C., Tilles, A. W. & Millero, F. J. Conditions for the occurrence of large near-wall excesses of small particles during blood flow. *Microvasc. Res.* **36,** 31–39 (1988).

43. Lee, T.-R. *et al.* On the near-wall accumulation of injectable particles in the microcirculation: smaller is not better. *Sci. Rep.* **3,** 2079 (2013).

44. Tilles, A. W. & Eckstein, E. C. The near-wall excess of platelet-sized particles in blood flow: its dependence on hematocrit and wall shear rate. *Microvasc. Res.* **33,** 211–223

(1987).

45. Namdee, K., Thompson, A. J., Charoenphol, P. & Eniola-Adefeso, O. Margination propensity of vascular-targeted spheres from blood flow in a microfluidic model of human microvessels. *Langmuir* **29,** 2530–2535 (2013).

46. Charoenphol, P., Huang, R. B. & Eniola-Adefeso, O. Potential role of size and hemodynamics in the efficacy of vascular-targeted spherical drug carriers. *Biomaterials* **31,** 1392–1402 (2010).

47. Dell'Orco, D., Lundqvist, M., Oslakovic, C., Cedervall, T. & Linse, S. Modeling the time evolution of the nanoparticle-protein corona in a body fluid. *PLoS One* **5,** e10949 (2010).

48. Mahmoudi, M. *et al.* Protein À Nanoparticle Interactions : Opportunities and Challenges. 5610–5637 (2011).

49. Lundqvist, M. *et al.* Nanoparticle size and surface properties determine the protein corona with possible implications for biological impacts. *Proc. Natl. Acad. Sci. U. S. A.* **105,** 14265–14270 (2008).

50. Monopoli, M. P., Aberg, C., Salvati, A. & Dawson, K. a. Biomolecular coronas provide the biological identity of nanosized materials. *Nat. Nanotechnol.* **7,** 779–86 (2012).

51. Zalipsky, S. Chemistry of polyethylene glycol conjugates with biologically active molecules. *Adv. Drug Deliv. Rev.* **16,** 157–182 (1995).

52. Kentworthy, A. K., Hristova, K., Needham, D. & Mcintosh, T. J. Range and Magnitude of the Steric Pressure Between Bilayers Containing Phospholipids with Covalently Attached Poly(ethylene glycol). *Biophys. J.* **68,** 1921–1936 (1995).

53. Gombotz, W. R., Guanghui, W., Horbett, T. A. & Hoffman, A. S. Protein adsorption to poly (ethylene oxide) surfaces. *J. Biomater. Res.* **25,** 1547–1562 (1991).

54. Gref, R. *et al.* 'Stealth' corona-core nanoparticles surface modified by polyethylene glycol (PEG): influences of the corona (PEG chain length and surface density) and of the core composition on phagocytic uptake and plasma protein adsorption. *Colloids Surfaces B Biointerfaces* **18,** 301–313 (2000).

55. Cui, J. *et al.* Engineering Poly (ethylene glycol) Particles for Improved Biodistribution. *ACS Nano* **9,** 1571–1580 (2015).

56. Canelas, D. A., Herlihy, K. P. & Desimone, J. M. Top-down particle fabrication : control of size and shape for diagnostic imaging and drug delivery. **1,** 391–404 (2009).

57. Fattahi, P., Borhan, A. & Abidian, M. R. Microencapsulation of chemotherapeutics into monodisperse and tunable biodegradable polymers via electrified liquid jets: control of size, shape, and drug release. *Adv. Mater.* **25,** 4555–60 (2013).

58. Discher, D. E. & Ahmed, F. Polymersomes. *Annu. Rev. Biomed. Eng.* **8,** 323–341 (2006).

59. Lahann, J. Recent Progress in Nano-biotechnology : Compartmentalized Micro- and Nanoparticles via Electrohydrodynamic Co-jetting. *Small* **7,** 1149–1156 (2011).

60. Vehring, R. Pharmaceutical Particle Engineering via Spray Drying. *Pharm. Res.* **25,** 999–1022 (2008).

61. Gonçalves, C., Pereira, P. & Gama, M. Self-Assembled Hydrogel Nanoparticles for Drug Delivery Applications. *Materials (Basel).* **3,** 1420–1460 (2010).

62. Srivastava, A. *et al.* Polymers in Drug Delivery. *J. Biosci. Med.* **4,** 69–84 (2016).

63. James, H. P., John, R., Alex, A. & Anoop, K. R. Smart polymers for the controlled delivery of drugs– a concise overview. *Acta Pharm. Sin. B* **4,** 120–127 (2014).

64. Müller, K., Fedosov, D. a & Gompper, G. Margination of micro- and nano-particles in blood flow and its effect on drug delivery. *Sci. Rep.* **4,** 4871 (2014).

65. Toy, R., Hayden, E., Shoup, C., Baskaran, H. & Karathanasis, E. The effects of particle size, density and shape on margination of nanoparticles in microcirculation. *Nanotechnology* **22,** 115101 (2011).

66. Dasgupta, S., Auth, T. & Gompper, G. Shape and orientation matter for the cellular uptake of nonspherical particles. *Nano Lett.* **14,** 687–93 (2014).

67. Champion, J. a & Mitragotri, S. Role of target geometry in phagocytosis. *Proc. Natl. Acad. Sci. U. S. A.* **103,** 4930–4 (2006).

68. Champion, J. a, Walker, A. & Mitragotri, S. Role of particle size in phagocytosis of polymeric microspheres. *Pharm. Res.* **25,** 1815–21 (2008).

69. Champion, J. a & Mitragotri, S. Shape induced inhibition of phagocytosis of polymer particles. *Pharm. Res.* **26,** 244–9 (2009).

70. Champion, J. A. & Mitragotri, S. Shape induced inhibition of phagocytosis of polymer particles. *Pharm. Res.* **26,** 244–249 (2009).

71. Kulkarni, S. A. & Feng, S. Effects of Particle Size and Surface Modification on Cellular Uptake and Biodistribution of Polymeric Nanoparticles for Drug Delivery. *Pharm. Res.* **30,** 2512–2522 (2013).

72. Chen, L. *et al.* Development and Characterization of Lecithin-based Self-assembling Mixed Polymeric Micellar (saMPMs) Drug Delivery Systems for Curcumin. *Sci. Rep.* (2016). doi:10.1038/srep37122

73. Chen, W., Palazzo, A., Hennink, W. E. & Kok, R. Effect of Particle Size on Drug Loading and Release Kinetics of Gefitnib-Loaded PLGA Microspheres. *Mol. Pharm.* **14,** 459–467

(2017).

74. Yang, L. & Fassihi, R. Zero-order release kinetics from a self-correcting floatable asymmetric configuration drug delivery system. *J. Pharm. Sci.* **85,** 170–3 (1996).

75. Muro, S., Gajewski, C., Koval, M. & Muzykantov, V. R. ICAM-1 recycling in endothelial cells : a novel pathway for sustained intracellular delivery and prolonged effects of drugs. *Blood* **105,** 650–659 (2017).

76. Granger, D. N. & Kubes, P. The microcirculation and inflammation: modulation of leukocyte-endothelial cell adhesion. *J. Leukoc. Biol.* **55,** 662–75 (1994).

77. Eldika, N., Yerra, L., Chi, D. S. & Krishnaswamy, G. Atherosclerosis as an inflammatory disease: implications for therapy. *Front. Biosci.* **9,** 2764–2777 (2004).

78. Ley, K., Laudanna, C., Cybulsky, M. I. & Nourshargh, S. Getting to the site of inflammation: the leukocyte adhesion cascade updated. *Nat. Rev. Immunol.* **7,** 678–89 (2007).

79. Schmidt, S., Moser, M. & Sperandio, M. The molecular basis of leukocyte recruitment and its deficiencies. *Molecular Immunology* **55,** 49–58 (2013).

80. Libby, P., Ridker, P. M. & Maseri, A. Inflammation and atherosclerosis. *Circulation* **105,** 1135–1143 (2002).

81. Mann, A. P. *et al.* Identification of Thioaptamer Ligand against E-Selectin: Potential Application for Inflamed Vasculature Targeting. *PLoS One* 1–14 (2010).

82. Schardt, J. S. *et al.* Engineered Multivalency Enhances Affibody-Based HER3 Inhibition and Downregulation in Cancer Cells. *Mol. Pharm.* **14,** 1047–1056 (2017).

83. Omolola Eniola, A. & Hammer, D. a. In vitro characterization of leukocyte mimetic for targeting therapeutics to the endothelium using two receptors. *Biomaterials* **26,** 7136–44 (2005).

84. Barthel, S. R., Gavino, J. D., Descheny, L. & Dimitroff, C. J. Targeting selectins and selectin ligands in inflammation and cncer. *Expert Opin. Ther. Targets* **11,** 1473–1491 (2008).

85. Gunawan, R. C., Almeda, D. & Auguste, D. T. Complementary targeting of liposomes to IL-1?? and TNF-?? activated endothelial cells via the transient expression of VCAM1 and E-selectin. *Biomaterials* **32,** 9848–9853 (2011).

86. Papademetriou, I., Tsinas, Z., Hsu, J. & Muro, S. Combination-targeting to multiple endothelial cell adhesion molecules modulates binding, endocytosis, and in vivo biodistribution of drug nanocarriers and their therapeutic cargoes. *J. Control. Release* **188,** 87–98 (2014).

87. Howard, M. *et al.* Vascular targeting of nanocarriers: Perplexing aspects of the seemingly straightforward paradigm. *ACS Nano* **8,** 4100–4132 (2014).

88. McAteer, M. A. *et al.* Magnetic resonance imaging of endothelial adhesion molecules in mouse atherosclerosis using dual-targeted microparticles of iron oxide. *Arterioscler. Thromb. Vasc. Biol.* **28,** 77–83 (2008).

89. Sun, D. *et al.* Superior sensitivity of novel molecular imaging probe: simultaneously targeting two types of endothelial injury markers. *FASEB J.* **24,** 1532–40 (2010).

90. Gunawan, R. C. & Auguste, D. T. The role of antibody synergy and membrane fluidity in the vascular targeting of immunoliposomes. *Biomaterials* **31,** 900–907 (2010).

91. McNeeley, K. M., Annapragada, A. & Bellamkonda, R. Decreased circulation time offsets increased efficacy of PEGylated nanocarriers targeting folate receptors of glioma. *Nanotechnology* **18,** (2007).

92. Sobczynski, D. J. *et al.* Plasma protein corona modulates the vascular wall interaction of drug carriers in a material and donor specific manner. *PLoS One* **9,** e107408 (2014).

93. Onyskiw, P. J. & Eniola-adefeso, O. Effect of PEGylation on Ligand-Based Targeting of Drug Carriers to the Vascular Wall in Blood Flow. *Langmuir* **29,** 11127–11134 (2013).

94. Saw, P. E. *et al.* Effect of PEG Pairing on the Efficiency of Cancer-Targeting Liposomes. *Theranostics* **5,** 746–754 (2015).

95. Garay, R. P., El-Gewely, R., Armstrong, J. K., Garratty, G. & Richette, P. Antibodies against polyethylene glycol in healthy subjects and in patients treated with PEG-conjugated agents. *Expert Opin. Drug Deliv.* 1319–1323 (2012). doi:10.1517/17425247.2012.720969

96. Peppas, N. A., Hilt, J. Z., Khademhosseini, A. & Langer, R. Hydrogels in Biology and Medicine: From Molecular Principles to Bionanotechnology. *Adv. Mater.* **18,** 1345–1360 (2006).

97. Knop, K., Hoogenboom, R., Fischer, D. & Schubert, U. S. Poly(ethylene glycol) in drug delivery: Pros and cons as well as potential alternatives. *Angew. Chemie - Int. Ed.* **49,** 6288–6308 (2010).

98. Olabisi, O. & Adewale, K. *Handbook of Thermoplastics*. (2016).

99. Yoo, J., Irvine, D. J., Discher, D. E. & Mitragotri, S. Bio-inspired, bioengineered and biomimetic drug delivery carriers. *Nat. Rev. Drug Deliv.* **10,** 521–535 (2011).

100. Meyer, R. A., Sunshine, J. C. & Green, J. J. Biomimetic particles as therapeutics. *Trends Biotechnol.* **33,** 514–524 (2015).

101. Balmert, S. C. & Little, S. R. Biomimetic Delivery with Micro- and Nanoparticles. *Adv.*

Mater. **24,** 3757–3778 (2012).

102. Chen, K. *et al.* Low modulus biomimetic microgel particles with high loading of hemoglobin. *Biomacromolecules* **13,** 2748–2759 (2012).

103. Cui, J. *et al.* Super-Soft Hydrogel Particles with Tunable Elasticity in a Microfluidic Blood Capillary Model. *Adv. Mater.* **26,** 7295–7299 (2014).

104. Beningo, K. A. & Wang, Y. Fc-receptor-mediated phagocytosis is regulated by mechanical properties of the target. *J. Cell Sci.* **115,** 849–856 (2002).

105. Modery-Pawlowski, C. L. *et al.* Biomaterials Approaches to synthetic platelet analogs. *Biomaterials* **34,** 526–541 (2013).

106. Fish, M. B. *et al.* Exploring deformable particles in vascular-targeted drug delivery: Softer is only sometimes better. *Biomaterials* **124,** 169–179 (2017).

107. Dawidczyk, C. M. *et al.* State-of-the-Art in Design Rules for Drug Delivery Platforms: Lessons from FDA-approved Nanomedicines. *J. Control. Release* 133–144 (2014). doi:10.1016/j.jconrel.2014.05.036.State-of-the-Art

108. Zhang, Y., Chan, H. F. & Leong, K. W. Advanced Materials and Processing for Drug Delivery: The Past and The Future. *Adv. Drug Deliv. Rev.* **65,** 104–120 (2014).

109. Fairbanks, B. D., Schwartz, M. P., Bowman, C. N. & Anseth, K. S. Photoinitiated polymerization of PEG-diacrylate with lithium phenyl-2,4,6-trimethylbenzoylphosphinate: polymerization rate and cytocompatibility. *Biomaterials* **30,** 6702–6707 (2009).

110. Majima, T. & Schnabel, W. Phenyl-2,4,6-trimethylbenzoylphosphinates as water-soluble photoinitiators. Generation and reactivity of O=P(C6H5)(O-) radical anions. *Makromol. Chem.* **192,** 2307–2315 (1991).

111. Anseth, K., Bowman, C. N. & Brannon-peppas, L. Mechanical Properties of Hydrogels and Their Experimental Determination. *Biomaterials* **17,** (1996).

112. Stenekes, R. J. *et al.* Pore sizes in hydrated dextran microspheres. *Biomacromolecules* **1,** 696–703 (2000).

113. Charoenphol, P., Onyskiw, P. J., Carrasco-Teja, M. & Eniola-Adefeso, O. Particle-cell dynamics in human blood flow: implications for vascular-targeted drug delivery. *J. Biomech.* **45,** 2822–8 (2012).

114. Huang, R. B. & Eniola-Adefeso, O. Shear stress modulation of IL-1-induced E-selectin expression in human endothelial cells. *PLoS One* **7,** 1–11 (2012).

115. Huang, A. D. A. J. *et al.* Effects of Human Neutrophil Chemotaxis Across Human Endothelial Cell Monolayers on the Permeability of These Monolayers to Ions and Macromolecules. *J. Cell. Physiol.* **135,** 355–366 (1988).

116. Ducusin, R. J. T., Sarashina, T., Uzuka, Y., Tanabe, S. & Ohtani, M. Phagocytic response of bovine polymorphonuclear leukocytes to different incubation conditions and following exposure to some effectors of phagocytosis and different anticoagulants in vitro. *Can. J. Vet. Res.* **65,** 38–44 (2001).

117. Papaioannou, T. G. & Stefanadis, C. Vascular wall shear stress: basic principles and methods. *Hellenic J. Cardiol.* **46,** 9–15 (2005).

118. Lipowsky, H. H., Usami, S. & Chien, S. In vivo measurements of 'apparent viscosity' and microvessel hematocrit in the mesentery of the cat. *Microvasc. Res.* **19,** 297–319 (1980).

119. Papaioannou, T. & Stefanadis, C. Vascular wall shear stress: basic principles and methods. *Hell. J Cardiol* (2005).

120. Wang, Y. *et al.* Plasma fibronectin supports hemostasis and regulates thrombosis. *J. Clin. Invest.* **124,** 4281–4293 (2014).

121. Reheman, A. *et al.* Vitronectin stabilizes thrombi and vessel occlusion but plays a dual role in platelet aggregation. *J. Thromb. Haemost.* **3,** 875–883 (2005).

122. Fromen, C. A. *et al.* Evaluation of Receptor-Ligand Mechanisms of Dual-Targeted Particles to an Inflamed Endothelium. *Bioeng. Transl. Med.* **1,** 2–41 (2016).

123. Fromen, C. A. *et al.* Controlled analysis of nanoparticle charge on mucosal and systemic antibody responses following pulmonary immunization. *Proc. Natl. Acad. Sci.* **112,** 488–493 (2015).

124. Fromen, C. A. *et al.* Nanoparticle surface charge impacts distribution , uptake and lymph node trafficking by pulmonary antigen-presenting cells. *Nanomedicine Nanotechnology, Biol. Med.* **12,** 677–687 (2016).

125. Grommes, J. & Soehnlein, O. Contribution of Neutrophils to Acute Lung Injury. *Mol. Med.* **17,** 293–307 (2011).

126. Hsu, C. W. & Chen, Y. L. Migration and fractionation of deformable particles in microchannel. *J. Chem. Phys.* **133,** (2010).

127. Fish, M. B., Thompson, A. J., Fromen, C. A. & Eniola-Adefeso, O. Emergence and Utility of Non-Spherical Particles in Biomedicine. *Ind. Eng. Chem. Res.* **54,** 4043–4059 (2015).

128. Sen Gupta, A. Role of particle size, shape, and stiffness in design of intravascular drug delivery systems: insights from computations, experiments, and nature. *WIREs* **8,** 255–270 (2016).

129. Geng, Y. *et al.* Shape effects of filaments versus spherical particles in flow and drug delivery. *Nat. Nanotechnol.* **2,** 249–55 (2007).

130. Skotheim, J. M. & Secomb, T. W. Red blood cells and other nonspherical capsules in

shear flow: Oscillatory dynamics and the tank-treading-to-tumbling transition. *Phys. Rev. Lett.* **98,** (2007).

131. Crowl, L. M. & Fogelson, A. L. Computational model of whole blood exhibiting lateral platelet motion induced by red blood cells. *Int. j. numer. method. biomed. eng.* **26,** 471–487 (2010).

132. Geislinger, T. M. & Franke, T. Hydrodynamic lift of vesicles and red blood cells in flow — from Fåhræus & Lindqvist to microfluidic cell sorting. *Adv. Colloid Interface Sci.* **208,** 161–176 (2014).

133. Dulinska, I. *et al.* Stiffness of normal and pathological erythrocytes studied by means of atomic force microscopy. *J. Biochem. Biophys. Methods* **66,** 1–11 (2006).

134. Radmacher, M., Fritz, M., Kacher, C. M., Cleveland, J. P. & Hansma, P. K. Measuring the Viscoelastic Properties of Human Platelets with the Atomic Force Microscope. *Biophys. J.* **70,** 556–567 (1996).

135. Kumar, A., Rivera, R. G. H. & Graham, M. D. Flow-induced segregation in confined multicomponent suspensions : effects of particle size and rigidity. *J. Fluid Mech.* 423–462 (2014). doi:10.1017/jfm.2013.592

136. Haga, J., Beaudoin, A., White, J. & Strony, J. Quantification of the Passive Mechanical Properties of the Resting Platelet. *Ann. Biomed. Eng.* **26,** 268–277 (1998).

137. Namdee, K., Carrasco-Teja, M., Fish, M. B., Charoenphol, P. & Eniola-Adefeso, O. Effect of Variation in hemorheology between human and animal blood on the binding efficacy of vascular-targeted carriers. *Sci. Rep.* **5,** (2015).

138. Namdee, K. *et al.* In vivo evaluation of vascular-targeted spheroidal microparticles for imaging and drug delivery application in atherosclerosis. *Atherosclerosis* **237,** 279–286 (2014).

139. Winter, H. H. & Chambon, F. Analysis of Linear Viscoelasticity of a Crosslinking Polymer at the Gel Point. *J. Rheol. (N. Y. N. Y).* **30,** 367–382 (1986).

140. Kansas, G. Selectins and Their Ligands: Current Concepts and Controversies. *Blood* **88,** 3259–3287 (1996).

141. Foreman, K. E. *et al.* C5a-induced expression of P-selectin in endothelial cells. *J. Clin. Invest.* **94,** 1147–1155 (1994).

142. Gao, T. & Hu, H. H. Deformation of elastic particles in viscous shear flow. *J. Comput. Phys.* **228,** 2132–2151 (2009).

143. Chen, Y. Intertia- and deformation-driven migration of a soft particle in confined shear and Poiseuille flow. *RSC Adv.* **4,** 17908–17916 (2014).

144. Doshi, N., Zahr, A. S., Bhaskar, S., Lahann, J. & Mitragotri, S. Red blood cell-mimicking synthetic biomaterial particles. *Proc. Natl. Acad. Sci. U. S. A.* **106,** 21495–9 (2009).

145. Modery-pawlowski, C. L., Tian, L. L., Pan, V. & Sen Gupta, A. Synthetic Approaches to RBC Mimicry and Oxygen Carrier Systems. *Biomacromolecules* **14,** 939–948 (2013).

146. Doshi, N. *et al.* Platelet mimetic particles for targeting thrombi in flowing blood. *Adv. Mater.* **24,** 3864–9 (2012).

147. Anselmo, A. C. *et al.* Platelet-like nanoparticles: mimicking shape, flexibility, and surface biology of platelets to target vascular injuries. *ACS Nano* **8,** 11243–53 (2014).

148. Brown, A. C. *et al.* Ultrasoft microgels displaying emergent platelet-like behaviours. *Nat. Mater.* **13,** 1108–1114 (2014).

149. Su, J. *et al.* Long Circulation Red-Blood-Cell-Mimetic Nanoparticles with Peptide-Enhanced Tumor Penetration for Simultaneously Inhibiting Growth and Lung Metastasis of Breast Cancer. *Adv. Funct. Mater.* **26,** 1243–1252 (2016).

150. Anselmo, A. C. & Mitragotri, S. Impact of particle elasticity on particle-based drug delivery systems. *Adv. Drug Deliv. Rev.* (2016).

151. Wang, J., Byrne, J. D., Napier, M. E. & Desimone, J. M. More Effective Nanomedicines through Particle Design. *Small* **7,** 1919–1931 (2011).

152. Zustiak, S. P. & Leach, J. B. Hydrolytically Degradable Poly (Ethylene Glycol) Hydrogel Scaffolds with Tunable Degradation and Mechanical Properties. *Biomacromolecules* **11,** 1348–1357 (2010).

153. Hu, Y., Xie, J., Tong, Y. & Wang, C.-H. Effect of PEG conformation and particle size on the cellular uptake efficiency of nanoparticles with the HepG2 cells. *J. Control. Release* **118,** 7–17 (2007).

154. Cheuvront, S. N., Kenefick, R. W., Heavens, K. R. & Spitz, M. G. A Comparison of Whole Blood and Plasma Osmolality and Osmolarity. *J. Clin. Labratory Anal.* **28,** 368–373 (2014).

155. Guo, D., Li, J., Xie, G., Wang, Y. & Luo, J. Elastic Properties of Polystyrene Nanospheres Evaluated with Atomic Force Microscopy: Size Effect and Error Analysis. *Langmuir* **30,** 7206–7212 (2014).

156. Addio, S. M. D. *et al.* Effects of block copolymer properties on nanocarrier protection from in vivo clearance. *J. Control. Release* **162,** 208–217 (2012).

157. Kutscher, H. L. *et al.* Threshold size for optimal passive pulmonary targeting and retention of rigid microparticles in rats. *J. Control. Release* **143,** 31–37 (2010).

158. Koutsiaris, A. G. *et al.* Volume flow and wall shear stress quantification in the human

conjunctival capillaries and post-capillary venules in vivo. *Biorheology* **44,** 375–386 (2007).

159. Nagaoka, T. & Yoshida, A. Noninvasive Evaluation of Wall Shear Stress on Retinal Microcirculation in Humans. *Investig. Ophthalmol. Vis. Sci.* **47,** 1113–1119 (2006).

160. Simon, S. I., Hu, Y., Vestweber, D. & Smith, W. C. Neutrophil Tethering on E-Selectin Activates β 2 Integrin Binding to ICAM-1 Through a Mitogen-Activated Protein Kinase Signal Transduction Pathway. *J. Immunol.* **164,** 4348–4358 (2000).

161. Müller, K., Fedosov, D. A. & Gompper, G. Understanding particle margination in blood flow – A step toward optimized drug delivery systems. *Med. Eng. Phys.* **38,** 2–10 (2016).

162. Yoo, J., Chambers, E. & Mitragotri, S. Factors that Control the Circulation Time of Nanoparticles in Blood: Challenges , Solutions and Future Prospects. *Curr. Pharamceutical Des.* **16,** 2298–2307 (2010).

163. Marshall, B. T. *et al.* Direct observation of catch bonds involving cell-adhesion molecules. *Nature* **423,** 190–193 (2003).

164. Kim, S., Ong, P. K., Yalcin, O., Intaglietta, M. & Johnson, P. C. The cell-free layer in microvascular blood flow. *Biorheology* **46,** 181–189 (2009).

165. Pillai, G. Nanomedicines for Cancer Therapy: An Update of FDA Approved and Those under Various Stages of Development. *SOJ Pharm. Pharm. Sci.* **1,** 13 (2014).

166. Bae, Y. H. & Park, K. Targeted drug delivery to tumors: Myths, reality and possibility. *J. Control. Release* **153,** 198–205 (2011).

167. Charoenphol, P. *et al.* Targeting therapeutics to the vascular wall in atherosclerosis-Carrier size matters. *Atherosclerosis* **217,** 364–370 (2011).

168. Thompson, A. J., Mastria, E. M. & Eniola-Adefeso, O. The margination propensity of ellipsoidal micro/nanoparticles to the endothelium in human blood flow. *Biomaterials* **34,** 5863–71 (2013).

169. Beauharnois, M. E. *et al.* Affinity and Kinetics of Sialyl Lewis-X and Core-2 Based Oligosaccharides Binding to L- and P-Selectin. *Biochemistry* **44,** 9507–9519 (2005).

170. Eniola, A. O., Willcox, P. J. & Hammer, D. A. Interplay between rolling and firm adhesion elucidated with a cell-free system engineered with two distinct receptor-ligand pairs. *Biophys. J.* **85,** 2720–31 (2003).

171. Thompson, A. J., Mastria, E. M. & Eniola-Adefeso, O. The margination propensity of ellipsoidal micro/nanoparticles to the endothelium in human blood flow. *Biomaterials* **34,** 5863–5871 (2013).

172. Bevilacqua, M. P. Enodthelial-Leukocyte Adhesion Molecules. *Annu. Rev. Immunol.* **11,**

767–804 (1993).

173. Haraldsen, G., Kvale, D., Lien, B., Farstad, I. N. & Brandtzaeg, P. Cytokine-Regulated Expression of E-Selectin, Intercellular Adhesion Molecule-1 (ICAM-1), and Vascular Cell Adhesion Molecule-1 (VCAM-1) in Human Intestinal Microvascular Endothelial Cells. *J. Immunol.* **156,** 2558–2565 (1996).

174. Kobuchi, H. *et al.* Quercetin inhibits inducible ICAM-1 expression in human endothelial cells through the JNK pathway. *Am. J. Physiol.* **304,** 403–411 (1999).

175. Panes, J. *et al.* Regional differences in constitutive and induced ICAM-1 expression in vivo. *Am. Physiol. Soc.* **269.6,** H1955–H1964 (1995).

176. Springer, T. a. Traffic signals for lymphocyte recirculation and leukocyte emigration: The multistep paradigm. *Cell* **76,** 301–314 (1994).

177. Augustin, H., Kozian, D. & Johnson, R. Differentiation of Endothelial Cells: Analysis of the constitutive and activated endothelial cell phenotypes. *BioEssays* **16,** 901–906 (1994).

178. Caputo, K. E., Lee, D., King, M. R. & Hammer, D. A. Adhesive Dynamics Simulations of the Shear Threshold Effect for Leukocytes. *Biophys. J.* **92,** 787–797 (2007).

179. Decuzzi, P. & Ferrari, M. The adhesive strength of non-spherical particles mediated by specific interactions. *Biomaterials* **27,** 5307–5314 (2006).

180. Doshi, N. *et al.* Flow and adhesion of drug carriers in blood vessels depend on their shape: A study using model synthetic microvascular networks. *J. Control. Release* **146,** 196–200 (2010).

181. Pawar, P., Jadhav, S., Eggleton, C. D. & Konstantopoulos, K. Roles of cell and microvillus deformation and receptor-ligand binding kinetics in cell rolling. *Am. J. Physiol. - Hear. Circ. Physiol.* **295,** 1439–1450 (2008).

182. Chang, K. C. & Hammer, D. a. Adhesive dynamics simulations of sialyl-Lewis(x)/E-selectin-mediated rolling in a cell-free system. *Biophys. J.* **79,** 1891–1902 (2000).

183. Brunk, D. K. & Hammer, D. A. Quantifying Rolling Adhesion with Carbohydrate Ligands Cell-Free Assay: E-Selectin and Its Carbohydrate Ligands. *Biophys. J.* **72,** 2820–2833 (1997).

184. Eniola, A. O., Rodgers, S. D. & Hammer, D. A. Characterization of biodegradable drug delivery vehicles with the adhesive properties of leukocytes. *Biomaterials* **23,** 2167–2177 (2001).

185. Fakhari, A., Baoum, A., Siahaan, T. J., Le, K. B. & Berkland, C. Controlling ligand surface density optimizes nanoparticle binding to ICAM-1. *J. Pharm. Sci.* **100,** 1045–1056 (2011).

186. Gu, F. *et al.* Precise engineering of targeted nanoparticles by using self-assembled biointegrated block copolymers. *Proc. Natl. Acad. Sci.* **105,** 2586–2591 (2008).

187. Zern, B. *et al.* Reduction of Nanoparticle Avidity Enhances the Selectivity of Vascular Targeteing and PET Detection of Pulmonary Inflammation. *ACS Nano* **7,** 2461–2469 (2014).

188. Beauharnois, M. E. *et al.* Affinity and kinetics of sialyl lewis-X and Core-2 based oligosaccharides binding to L- and P-selectin. *Biochemistry* **44,** 9507–9519 (2005).

189. Haun, J. B. & Hammer, D. A. Quantifying Nanoparticle Adhesion Mediated by Specific Molecular Interactions. *Langmuir* **24,** 8821–8832 (2008).

190. Ley, K., Laudanna, C., Cybulsky, M. I. & Nourshargh, S. Getting to the site of inflammation: the leukocyte adhesion cascade updated. *Nat. Rev. Immunol.* **7,** 678–89 (2007).

191. Lawrence, M. B. & Springer, T. a. Leukocytes Roll on a Selectin at Physiologic Flow Rates: Distinction from and Prerequisite for Adhesion through lntegrins. *Cell* **65,** 859–873 (1991).

192. Cheng, Z., Al Zaki, A., Hui, J. Z., Muzykantov, V. R. & Tsourkas, A. Multifunctional nanoparticles: cost versus benefit of adding targeting and imaging capabilities. *Science* **338,** 903–10 (2012).

193. Wang, J., Tian, S., Petros, R. a, Napier, M. E. & Desimone, J. M. The complex role of multivalency in nanoparticles targeting the transferrin receptor for cancer therapies. *J. Am. Chem. Soc.* **132,** 11306–13 (2010).

194. Wang, X. *et al.* The development of site-specific drug delivery nanocarriers based on receptor mediation. *J. Control. Release* **193,** 139–153 (2014).

195. Mulivor, a. W. & Lipowsky, H. H. Role of glycocalyx in leukocyte-endothelial cell adhesion. *Am. J. Physiol. Heart Circ. Physiol.* **283,** H1282–H1291 (2002).

196. Wickline, S. a., Neubauer, A. M., Winter, P. M., Caruthers, S. D. & Lanza, G. M. Molecular imaging and therapy of atherosclerosis with targeted nanoparticles. *J. Magn. Reson. Imaging* **25,** 667–680 (2007).

197. Winter, P. M. *et al.* Molecular Imaging of Angiogenesis in Early-Stage Atherosclerosis With αvβ3-Integrin-Targeted Nanoparticles. *Circulation* **108,** 2270–2274 (2003).

198. Neri, D. & Bicknell, R. Tumour vascular targeting. *Nat. Rev. Cancer* **5,** 436–446 (2005).

199. Torchilin, V. P. Multifunctional nanocarriers. *Adv. Drug Deliv. Rev.* **64,** 302–315 (2012).

200. Muro, S. *et al.* Control of endothelial targeting and intracellular delivery of therapeutic enzymes by modulating the size and shape of ICAM-1-targeted carriers. *Mol. Ther.* **16,**

1450–1458 (2008).

201. Garnacho, C., Albelda, S. M., Muzykantov, V. R. & Muro, S. Differential intra-endothelial delivery of polymer nanocarriers targeted to distinct PECAM-1 epitopes. *J. Control. Release* **130,** 226–33 (2008).

202. Hossain, S. S. *et al.* In silico vascular modeling for personalized nanoparticle delivery. *Nanomedicine (Lond).* **3,** 343–357 (2013).

203. Modery-Pawlowski, C. L. & Sen Gupta, A. Heteromultivalent ligand-decoration for actively targeted nanomedicine. *Biomaterials* **35,** 2568–2579 (2014).

204. Doolittle, E. *et al.* Spatiotemporal Targeting of a Dual-Ligand Nanoparticle to Cancer Metastasis. *ACS Nano* **9,** 8012–8021 (2015).

205. Robbins, G. P. *et al.* Tunable leuko-polymersomes that adhere specifically to inflammatory markers. *Langmuir* **26,** 14089–14096 (2010).

206. Hammer, D. A. & Apte, S. M. Simulation of cell rolling and adhesion on surfaces in shear flow: general results and analysis of selectin-mediated neutrophil adhesion. *Biophys. J.* **63,** 35–57 (1992).

207. Kim, M. J. & Rhee, K. Computational analysis of nanoparticle adhesion to endothelium: Effects of kinetic rate constants and wall shear rates. *Med. Biol. Eng. Comput.* **49,** 733–741 (2011).

208. Eniola, A. O. & Hammer, D. A. In vitro characterization of leukocyte mimetic for targeting therapeutics to the endothelium using two receptors. *Biomaterials* **26,** 7136–7144 (2005).

209. Haun, J. B., Robbins, G. P. & Hammer, D. A. Engineering Therapeutic Nanocarriers with Optimal Adhesion for Targeting. *J. Adhes.* **86,** 131–159 (2010).

210. Haun, J. B. & Hammer, D. A. Quantifying nanoparticle adhesion mediated by specific molecular interactions. *Langmuir* **24,** 8821–8832 (2008).

211. Huang, R. B. & Eniola-Adefeso, O. Shear stress modulation of IL-1-induced E-selectin expression in human endothelial cells. *PLoS One* **7,** 1–11 (2012).

212. Liljestro, V., Mikkila, J. & Kostiainen, M. A. Self-assembly and modular functionalization of three-dimensional crystals from oppositely charged proteins. *Nat. Commun.* **5,** (2014).

213. Lamberti, G. *et al.* Adhesive interaction of functionalized particles and endothelium in idealized microvascular networks. *Microvasc. Res.* **89,** 107–114 (2013).

214. Ley, K., Allietta, M., Bullard, D. C. & Morgan, S. Importance of E-selectin for firm leukocyte adhesion in vivo. *Circ. Res.* **83,** 287–94 (1998).

215. Simone, E., Ding, B. Sen & Muzykantov, V. Targeted delivery of therapeutics to endothelium. *Cell Tissue Res.* **335,** 283–300 (2009).

216. Mayadas, T. N., Johnson, R. C., Rayburn, H., Hynes, R. O. & Wagner, D. D. Leukocyte rolling and extravasation are severely compromised in P selectin-deficient mice. *Cell* **74,** 541–554 (1993).

217. Robinson, S. D. *et al.* Multiple, targeted deficiencies in selectins reveal a predominant role for P-selectin in leukocyte recruitment. *Proc. Natl. Acad. Sci. U. S. A.* **96,** 11452–11457 (1999).

218. Langley, R. R. *et al.* Quantification of murine endothelial cell adhesion molecules in solid tumors. *Am J Physiol Hear. Circ Physiol* **277,** 1156–1166 (1999).

219. Eniola, A. O. & Hammer, D. A. Characterization of biodegradable drug delivery vehicles with the adhesive properties of leukocytes II: effect of degradation on targeting activity. *Biomaterials* **26,** 661–70 (2005).

220. Yu, L. X. *et al.* Novel Bioequivalence Approach for Narrow Therapeutic Index Drugs. *Clin. Pharmacol. Ther.* **97,** 286–291 (2015).

221. Muller, P. Y. & Milton, M. N. The determination and interpretation of the therapeutic index in drug development. *Nat. Rev. Drug Discov.* **11,** 751–761 (2012).

222. Kai, M. P. *et al.* Evaluation of drug loading, pharmacokinetic behavior, and toxicity of a cisplatin-containing hydrogel nanoparticle. *J. Cont* **204,** 70–77 (2015).

223. Chu, K. S. *et al.* Particle Replication in Nonwetting Templates Nanoparticles with Tumor Selective Alkyl Silyl Ether Docetaxel Prodrug Reduces Toxicity. *Nano Lett.* **14,** 1472–1476 (2014).

224. Davis, M. E., Chen, Z. G. & Shin, D. M. Nanoparticle therapeutics : an emerging treatment modality for cancer. *Nat. Rev. Drug Discov.* **7,** 771–782 (2008).

225. Ulbrich, K. *et al.* Targeted Drug Delivery with Polymers and Magnetic Nanoparticles : Covalent and Noncovalent Approaches , Release Control , and Clinical Studies. *Chem. Rev.* **116,** 5388–5431 (2016).

226. Koren, E. & Torchilin, V. P. Drug Carriers for Vascular Drug Delivery. *IUBMB Life* **63,** 586–595 (2011).

227. Wilhelm, S. *et al.* Analysis of nanoparticle delivery to tumours. *Nat. Rev. Mater.* **1,** 1–12 (2016).

228. Ulbrich, W. & Lamprecht, A. Targeted drug-delivery approaches by nanoparticulate carriers in the therapy of inflammatory diseases. *J. R. Soc. Interface* 1–12 (2009).

229. Charoenphol, P. *et al.* Targeting therapeutics to the vascular wall in atherosclerosis–

Carrier size matters. *Atherosclerosis* **217,** 364–370 (2011).

230. Grommes, J. & Soehnlein, O. Contribution of Neutrophils to Acute Lung Injury. *Mol. Med.* **17,** 293–307 (2011).

231. Zhang, Y., Huo, M., Zhou, J. & Xie, S. PKSolver: An add-in program for pharmacokinetic and pharmacodynamic data analysis in Microsoft Excel. *Comput. Methods Programs Biomed.* **99,** 306–314 (2010).

232. Rosenbaum, S. *Basic Pharmacokinetics and Pharmacodynamics, an Integrated Textbook and Computer Simulations*. (2011). doi:10.1111/j.1365-2125.2011.04077.x

233. Kameda, H. *et al.* Re-expression of functional P-selectin molecules on the endothelial cell surface by repeated stimulation with thrombin. *J. Br. Hematol.* **97,** 348–355 (1997).

234. Jo, J. *et al.* Recylcing and LFA-1-Dependent Trafficking of ICAM-1 to the Immunological Synapse. *J. Cell. Biochem.* **111,** 1125–1137 (2010).

235. Dong, C. & Lei, X. X. Biomechanics of cell rolling: shear flow cell-surface adhesion, and cell deformability. *J. Biomech.* **33,** 35–43 (2000).

236. Yang, Q. *et al.* Evading Immune Cell Uptake and Clearance Requires PEG Grafting at Densities Substantially Exceeding the Minimum for Brush Conformation. *Mol. Pharm.* **11,** 1250–1258 (2014).

237. Alexis, F., Pridgen, E., Molnar, L. K. & Farokhzad, O. C. Factors Affecting the Clearance and Biodistribution of Polymeric Nanoparticles. **5,** 505–515 (2008).

238. Townsley, M. I. Structure and composition of pulmonary arteries, capillaries and veins. *Compr. Physiol.* 675–709 (2013). doi:10.1002/cphy.c100081.Structure

239. Chou, S. & Woodrow, K. A. Relationships between mechanical properties and drug release from electronspun fibers of PCL and PLGA blends. *J. Mech. Behav. Biomed. Mater.* **65,** 724–733 (2017).

240. Menden, H., Tate, E., Hogg, N. & Sampath, V. LPS-mediated endothelial activation in pulmonary endothelial cells : role of Nox2-dependent IKK-B phosphorylation. *Am J Physiol Lung Cell Mol Physiol* **304,** 445–455 (2013).

241. Yi, X., Shi, X. & Gao, H. Cellular Uptake of Elastic Nanoparticles. *Phys. Rev. Lett.* **107,** 1–5 (2011).

242. Mager, D. Target-mediated drug disposition and dynamics. *Biochem. Pharmacol.* **72,** 1–10 (2006).

243. Peters, R. H. *The Ecological Implications of Body Size*. (Cambridge University Press, 1983).

244. Calderon, A. J. *et al.* Optimizing endothelial targeting by modulating the antibody density and particle concentration of anti-ICAM coated carriers. *J. Control. Release* **150,** 37–44 (2011).

245. Kharkar, P. M., Kiick, K. L. & Kloxin, A. M. Designing degradable hydrogels for control of cell microenvironments. *Chem Soc Rev* **42,** 7335–7372 (2013).

246. Kharkar, P. M., Kloxin, A. M. & Kiick, K. L. Dually degradable click hydrogels for controlled degradation and protein release. *J Mater Chem B Mater Biol Med* **2,** 5511–5521 (2014).

247. de la Rica, R., Aili, D. & Stevens, M. M. Enzyme-responsive nanoparticles for drug release and diagnostics. *Adv. Drug Deliv. Rev.* **64,** 967–78 (2012).

248. Mura, S., Nicolas, J. & Couvreur, P. Stimuli-responsive nanocarriers for drug delivery. *Nat. Mater.* **12,** 991–1003 (2013).

249. Patterson, J. & Hubbell, J. A. Enhanced proteolytic degradation of molecularly engineered PEG hydrogels in response to MMP-1 and MMP-2. *Biomaterials* **31,** 7836–7845 (2010).

250. Nel, A. E. *et al.* Understanding biophysicochemical interactions at the nano-bio interface. *Nat. Mater.* **9,** (2009).

251. Kwon, G. & Teruo, O. Polymeric micelles as new drug carriers. *Adv. Drug Deliv. Rev.* **21,** 106–117 (1996).

252. Singh, R. & Jr, J. W. L. Nanoparticle-based targeted drug delivery. *Exp. Mol. Pathol.* **86,** 215–223 (2009).

253. Simionescu, M., Popov, D. & Sima, A. Endothelial transcytosis in health and disease. *Cell Tissue Res.* **335,** 27–40 (2009).

254. Ye, D. *et al.* Nanoparticle accumulation and transcytosis in brain endothelial cell layers. *Nanoscale* **5,** 11153–11165 (2013).

255. Maeda, H., Wu, J., Sawa, T., Matsumura, Y. & Hori, K. Tumor vascular permeability and the EPR effect in macromolecular therapeutics: a review. *J. Control. Release* **65,** 271–284 (2000).

256. Fang, J., Nakamura, H. & Maeda, H. The EPR effect : Unique features of tumor blood vessels for drug delivery, factors involved, and limitations and augmentation of the effect. *Adv. Drug Deliv. Rev.* **63,** 136–151 (2011).

257. Peng, Q. *et al.* Injectable and biodegradable thermosensitive hydrogels loaded with PHBHHx nanoparticles for the sustained and controlled release of insulin. *Acta Biomater.* **9,** 5063–5069 (2013).

258. Park, K. H., Kim, H., Moon, S. & Na, K. Bone morphogenic protein-2 (BMP-2) loaded

nanoparticles mixed with human mesenchymal stem cell in fibrin hydrogel for bone tissue engineering. *J. Biosci. Bioeng.* **108,** 530–537 (2009).

259. Chung, Y. Il *et al.* Enhanced bone regeneration with BMP-2 loaded functional nanoparticle-hydrogel complex. *J. Control. Release* **121,** 91–99 (2007).

260. Jung, H. J., Abou-Jaoude, M., Carbia, B. E., Plummer, C. & Chauhan, A. Glaucoma therapy by extended release of timolol from nanoparticle loaded silicone-hydrogel contact lenses. *J. Control. Release* **165,** 82–89 (2013).

261. Laroui, H. *et al.* Drug-Loaded Nanoparticles Targeted to the Colon With Polysaccharide Hydrogel Reduce Colitis in a Mouse Model. *Gastroenterology* **138,** 843–853 (2010).

262. Gou, M. L. *et al.* A novel injectable local hydrophobic drug delivery system: Biodegradable nanoparticles in thermo-sensitive hydrogel. *Int. J. Pharm.* **359,** 228–233 (2008).

263. Grazia Cascone, M., Zhu, Z., Borselli, F. & Lazzeri, L. Poly(vinyl alcohol) hydrogels as hydrophilic matrices for the release of lipophilic drugs loaded in PLGA nanoparticles. *J. Mater. Sci. Mater. Med.* **13,** 29–32 (2002).

264. Casadei, M. A. *et al.* Solid lipid nanoparticles incorporated in dextran hydrogels: A new drug delivery system for oral formulations. *Int. J. Pharm.* **325,** 140–146 (2006).

265. Hebeish, A., Hashem, M., El-Hady, M. M. A. & Sharaf, S. Development of CMC hydrogels loaded with silver nano-particles for medical applications. *Carbohydr. Polym.* **92,** 407–413 (2013).

266. Juby, K. A. *et al.* Silver nanoparticle-loaded PVA/gum acacia hydrogel: Synthesis, characterization and antibacterial study. *Carbohydr. Polym.* **89,** 906–913 (2012).

267. Lee, Y., Johnson, P. J., Robbins, P. T. & Bridson, R. H. Production of nanoparticles-in-microparticles by a double emulsion method : A comprehensive study. *Eur. J. Pharm. Biopharm.* **83,** 168–173 (2013).

268. Guzman-villanueva, D., El-sherbiny, I. M., Herrera-Ruiz, D. & Smyth, H. D. C. Design and In Vitro Evaluation of a New Nano-Microparticulate System for Enhanced Aqueous-Phase Solubility of Curcumin. *Biomed Res. Int.* (2013).

269. Bohr, A., Water, J., Beck-broichsitter, M. & Yang, M. Nanoembedded Microparticles for Stabilization and Delivery of Drug-Loaded Nanoparticles. *Curr. Pharamceutical Des.* **21,** 5829–5844 (2015).

270. Bakhtiary, Z. *et al.* Microparticles containing erlotinib-loaded solid lipid nanoparticles for treatment of non-small cell lung cancer. *Drug Dev. Ind. Pharm.* **43,** 1244–1253 (2017).

271. Roa, W. H. *et al.* Inhalable nanoparticles , a non-invasive approach to treat lung cancer in a mouse model. *J. Control. Release* **150,** 49–55 (2011).

272. Imperiale, J. C., Nejamkin, P., Maria, J., Lanusse, C. E. & Sosnik, A. Novel protease inhibitor-loaded Nanoparticle-in-Microparticle Delivery System leads to a dramatic improvement of the oral pharmacokinetics in dogs. *Biomaterials* **37,** 383–394 (2015).

273. Tasciotti, E. *et al.* Mesoporous Silicon Particles as a Multistage Delivery System for Imaging and Therapeutic Applications. *Nat. Nanotechnol.* **3,** 151–157 (2008).

274. Yan, B., Boyer, J., Habault, D., Branda, N. R. & Zhao, Y. Near Infrared Light Triggered Release of Biomacromolecules from Hydrogels Loaded with Upconversion Nanoparticles. *J. Am. Chem. Soc.* **134,** 16558–16561 (2012).

275. Pandolfe, W. D. Effect of Dispersed and Continuous Phase Viscosiry on Droplet Size of Emulsions Generated by Homogenization. *J. Dispers. Sci. Technol.* **2,** 459–474 (1981).

276. Chu, K. S. *et al.* Nanoparticle drug loading as a design parameter to improve docetaxel pharmacokinetics and efficacy. *Biomaterials* **34,** 8424–8429 (2013).

277. Kalepu, S. & Nekkanti, V. Insoluble drug delivery strategies: review of recent advances and business prospects. *Acta Pharm. Sin. B* **5,** 442–453 (2015).

278. Lipinski, C. Poor Aqueous Solubility – an Industry Wide Problem in Drug Discovery. *Am. Pharm. Rev.* **5,** 82–85 (2003).

279. Chevre, R. Mechanical Stabilization of Mouse Carotid Artery for In Vivo Intravital Microscopy Imaging of Atherogenesis. *Methods Mouse Atheroscler.* 349–355 (2015).

280. Megens, R. & Soehnlein, O. Intravital Microscopy for Atherosclerosis Research. *Methods Mouse Atheroscler.* 41–60 (2015).

281. Aggarwal, P., Hall, J. B., McLeland, C. B., Dobrovolskaia, M. a & McNeil, S. E. Nanoparticle interaction with plasma proteins as it relates to particle biodistribution, biocompatibility and therapeutic efficacy. *Adv. Drug Deliv. Rev.* **61,** 428–37 (2009).

282. Zwicke, G. L., Mansoori, G. A. & Jeffery, C. J. Utilizing the folate receptor for active targeting of cancer nanotherapeutics. *Nano Rev.* **3,** (2012).

283. Ravikumar, M. *et al.* Mimicking Adhesive Functionalities of Blood Platelets using Ligand- Decorated Liposomes. *Bioconjug. Chem.* **23,** 1266–1275 (2012).

284. Bot, I., Jukema, J. W., Lankhuizen, I. M., Berkel, T. J. C. Van & Biessen, E. A. L. Atorvastatin inhibits plaque development and adventitial neovascularization in ApoE deficient mice independent of plasma cholesterol levels. *Atherosclerosis* **214,** 295–300 (2011).

285. Taylor, F. *et al.* Statins for the primary prevention of cardiovascular disease. 1–76 (2014). doi:10.1002/14651858.CD004816.pub4.Statins

286. Ito, T. & Ikeda, U. Inflammatory Cytokines in Cardiovascular Disease. *Curr. Drug*

Targets- Inflamm. Allergy (2003).

287. Rogerio, A. D. P., Sorgi, C. A., Sadikot, R. & Carlo, T. The Role of Lipids Mediators in Inflammation and Resolution. *Biomed Res. Int.* 2–4 (2015).

288. Amber E. Rydholm, Kristi S. Anseth, and C. N. B. Effects of neighboring sulfides and pH on ester hydrolysis in thiol-acrylate photopolymers. *Acta Biomater.* **3,** 449–455 (2007).

289. Yun Suk Jo, Jay Gantz, Jeffrey A. Hubbell, and M. P. L. Tailoring hydrogel degradation and drug release via neighboring amino acid controlled ester hydrolysis. *Soft Matter* **5,** 440–446 (2009).

290. Kessenbrock, K., Plaks, V. & Werb, Z. Matrix Metalloproteinases: Regulators of the Tumor Microenvironment. *Cell* **141,** 52–67 (2010).

291. Garcia-Touchard, A. *et al.* Extracellular proteases in atherosclerosis and restenosis. *Arteriosclerosis, Thrombosis, and Vascular Biology* **25,** 1119–1127 (2005).

292. Galis, Z. S., Sukhova, G. K., Lark, M. W. & Libby, P. Increased expression of matrix metalloproteinases and matrix degrading activity in vulnerable regions of human atherosclerotic plaques. *J. Clin. Invest.* **94,** 2493–2503 (1994).

293. Sluijter, J. P. G. *et al.* Matrix metalloproteinase 2 is associated with stable and matrix metalloproteinases 8 and 9 with vulnerable carotid atherosclerotic lesions: a study in human endarterectomy specimen pointing to a role for different extracellular matrix metalloproteinase in. *Stroke.* **37,** 235–9 (2006).

294. Lehrke, M. *et al.* MMP-1 serum levels predict coronary atherosclerosis in humans. *Cardiovasc. Diabetol.* **8,** 50 (2009).

295. Inokubo, Y. *et al.* Plasma levels of matrix metalloproteinase-9 and tissue inhibitor of metalloproteinase-1 are increased in the coronary circulation in patients with acute coronary syndrome. *Am. Heart J.* **141,** 211–217 (2001).

296. Padovan, G. J., Leme, I. A., Fassini, P. G., Junior, N. I. & Marchini, J. S. A New O-phthaldialdeyde (OPA) Solution for Fluorescence HPLC Amine Group Detection without Boric Acid Preparation. *Chromotography Sep. Tech.* **5,** (2014).

297. Hennig, A. *et al.* Simple Colorimetric Method for Quantification of Surface Carboxy Groups on Polymer Particles. *Anal. Chem.* **83,** 4970–4974 (2011).

298. Kim, J. *et al.* Characterization of the crosslinking kinetics of multi-arm poly(ethylene glycol) hydrogels formed via Michael-type addition. *Soft Matter* **12,** 2076–2085 (2016).

299. Gough, P. J., Gomez, I. G., Wille, P. T. & Raines, E. W. Macrophage expression of active MMP-9 induces acute plaque disruption in apoE-deficient mice. *J. Clin. Invest.* **116,** 59–69 (2006).

300. Wagsater, D., Zhu, C., Bjorkegren, J., Skogsberg, J. & Eriksson, P. MMP-2 and MMP-9 are prominent matrix metalloproteinases during atherosclerosis development in the Ldlr-/-Apob100/100 mouse. *Int. J. Mol. Med.* **28,** 247–253 (2011).

301. Nandi, S. & Brown, A. C. Platelet-mimetic strategies for modulating the wound environment and inflammatory responses. *Exp. Biol. Med.* 1–11 (2016). doi:10.1177/1535370216647126

302. Kumar, A. & Graham, M. D. Margination and segregation in confined flows of blood and other multicomponent suspensions. *Soft Matter* **8,** 10536 (2012).

303. Blanco, E., Shen, H. & Ferrari, M. Principles of nanoparticle design for overcoming biological barriers to drug delivery. *Nat. Biotechnol.* **33,** 941–951 (2016).

304. Weifeng Lin, Guanglong Ma, Nir Kampf, Zhefan Yuan, and S. C. Development of Long-Circulating Zwitterionic Cross-Linked Micelles for Active-Targeted Drug Delivery. *Biomacromolecules2* **17,** (2016).

305. Jaklenec, A. *et al.* Sequential release of bioactive IGF-I and TGF-β1 from PLGA microsphere-based scaffolds. *Biomaterials* **10,** (2008).